Design and Optimization of Reconfigurable Intelligent Surfaces for Enhanced Wireless Communication Systems

Xinyi Lin

Submitted in fulfilment of the requirements for the
Degree of Doctor of Philosophy

School of Engineering
College of Science and Engineering
University of Glasgow

June 2024

University of Glasgow

College of Science & Engineering

Statement of Originality

Name: Xinyi Lin

Registration Number: XXXXX

I certify that the thesis presented here for examination for a PhD degree of the University of Glasgow is solely my own work other than where I have clearly indicated that it is the work of others (in which case the extent of any work carried out jointly by me and any other person is clearly identified in it) and that the thesis has not been edited by a third party beyond what is permitted by the University's PGR Code of Practice.

The copyright of this thesis rests with the author. No quotation from it is permitted without full acknowledgement.

I declare that the thesis does not include work forming part of a thesis presented successfully for another degree.

I declare that this thesis has been produced in accordance with the University of Glasgow's Code of Good Practice in Research.

I acknowledge that if any issues are raised regarding good research practice based on review of the thesis, the examination may be postponed pending the outcome of any investigation of the issues.

Signature: .....

Date: .....16/08/2024.....

Abstract

Reconfigurable intelligent surface (RIS) has been identified as a promising disruptive innovation to realize a faster, safer and more efficient communication system in the coming 6^{th} generation (6G) era. The RIS is a meta-material composed surface comprising a large number of passive scattering unit cell (UC) elements. Each element independently controls incident signals by dynamically adjusting their amplitude and/or phase shifts. The reflected signals from all elements are coherently combined and directed towards specified directions, enabling selective electromagnetic (EM) properties. By densely deploying RISs and intelligently coordinating them within wireless propagation environments, it is possible to achieve reconfigurable and programmable end-to-end wireless channels. This innovation has the significant potential to revolutionize wireless communication by enhancing signal quality, coverage, and capacity in a cost-effective and energy-efficient manner.

This thesis aims to systematically study the design of RIS to address potential challenges in its practical deployment for wireless communication enhancement. An overview of basic technologies that may be encountered in RIS-assisted systems has been first studied. To address the inaccurate and complex channel estimation and ensure sufficient and stable power gain, a RIS-aided broadbeam design is then proposed. The design proposed in this thesis will mainly include the RIS beamforming design of generating single and multiple flat beams to cover any arbitrary sector regions. Meanwhile, the thesis also tends to define cooperation modes of base stations (BSs) concerning whether they reach an agreement on collaboratively utilising RISs and sharing resources. The resource allocation scheme between cooperative and non-cooperative BSs will be investigated. Lastly, the thesis also aims to design a RIS codebook in the wideband system leveraging the beam squint effect. The design of a codebook can largely reduce computational complexity.

To conclude, the work presented in this thesis provides insight into the design of RIS for broadbeam design, which can be viewed as an initial step towards achieving channel estimation. The investigation of non-cooperative BSs and the design of RIS codebooks also provide guidance for further theoretical study and practical implementation of RIS for enhancing wireless communication systems.

Contents

Statement of Originality i

Abstract ii

List of Publications vi

List of Figures viii

List of Acronyms x

Nomenclature of Operators xiii

Acknowledgements xv

1 Introduction 1

1.1 The Reconfigurable Intelligent Surface 2

1.1.1 RIS Hardware Structure 2

1.1.2 RIS Model and Basic Functionalities 4

1.1.3 RIS Application Scenarios 6

1.2 Motivation 8

1.3 Objectives 11

1.4 Research Contributions 12

1.5 Thesis Outline 14

2 Background and Literature Review 16

2.1 Overview of Beamforming Techniques 16

2.1.1 Narrowband Beamforming 16

2.1.2 Wideband Beamforming 17

2.1.3 Analog Beamforming 18

2.1.4 Digital Beamforming 19

2.1.5 Hybrid Beamforming 21
2.2 Overview of Channel Model and Estimation 22
2.2.1 Channel Model 22
2.2.2 Channel Estimation 24
2.3 Overview of Convex Optimization 25
2.3.1 Linear Programming Problem 26
2.3.2 Quadratic Programming Problem 27
2.3.3 Transformation from Non-convex to Convex Problem 28
2.4 Radiation Pattern of Antenna 29
2.5 State-of-the-Art in RIS 32

3 On the Design of Broadbeam on RIS 35
3.1 Introduction 35
3.2 Generation of a Single Broadbeam 37
3.2.1 System Model 38
3.2.2 Analysis on Average Received Power 41
3.2.3 The DC-SDP Algorithm 49
3.2.4 Simulation Results 53
3.3 Generation of Multiple Broadbeams 62
3.3.1 System Model 63
3.3.2 ADMM Algorithm 65
3.3.3 Simulation Results 67
3.4 Summary 68

4 Resource Allocation in RIS-Aided Non-Cooperative BS Networks 70
4.1 Introduction 70
4.2 Resource Allocation for Single c-BS - n-BS - RIS System 71
4.2.1 System Model under Sub-6GHz Frequency Band 71
4.2.2 Sub-channel Assignment Design 75
4.2.3 Power Allocation Design 77
4.2.4 RIS Passive Beamforming Design 78
4.2.5 The Overall Solution 81
4.2.6 Simulation Results 81
4.3 Resource Allocation for Multiple c-BSs - n-BSs - RISs Network 83
4.3.1 System Model under mmWave Frequency Band 83
4.3.2 Power Allocation Design 89
4.3.3 UE Association Design 91

4.3.4 RIS Passive Beamforming Design . . . 93
4.3.5 The Overall Solution . . . 96
4.3.6 Simulation Results . . . 97
4.4 Summary . . . 100

5 A Codebook Design of RIS Leveraging Beam Squint 103
5.1 Introduction . . . 103
5.2 System Model . . . 105
5.2.1 Beam Squint Effect . . . 105
5.2.2 The Definition of W-HPBW . . . 108
5.3 The RIS Codebook Design . . . 108
5.3.1 Codebook Design with MRT Beamforming . . . 109
5.3.2 Codebook Design with Beam Broadening Technique . . . 112
5.4 Simulation Results . . . 113
5.5 Summary . . . 115

6 Conclusion and Future Work 117
6.1 Conclusion . . . 117
6.2 Future Work . . . 119
6.2.1 Extension of this work . . . 119
6.2.2 Promising Future Direction . . . 120

A Derivation of Theorems 122
A.1 Integral approximation by Riemann sum method . . . 122
A.2 Proof of Corollary 4 . . . 123
A.3 Proof of Theorem 2 . . . 123
A.4 Proof of Proposition 1 . . . 124
A.5 Proof of the convergence behaviour . . . 126

Bibliography 128

List of Publications

Journal

- **X. Lin**, L. Zhang, A. Tukmanov, Y. Liu, Q. Abbasi and M. A. Imran, "On the Design of Broadbeam of Reconfigurable Intelligent Surface," in IEEE Transactions on Communications, doi: 10.1109/TCOMM.2024.3354200.
- **X. Lin**, Y. Fan, L. Zhang, K. Ma, Y. Sun, A. Tukmanov, Q. Abbasi, and M. A. Imran, "Resource Allocation for RIS-aided mmWave System with Cooperative and Non-cooperative Base Stations," in IEEE Transactions on Vehicular Technology, under review.
- Z. Zhou, O. Onireti, **X. Lin**, L. Zhang, and M. A. Imran, ”On the Performance of Wireless PBFT-based Blockchain Network with IEEE 802.11,” in IEEE System Journal, under review.
- Z. Zhou, O. Onireti, **X. Lin**, L. Zhang, and M. A. Imran, ”Implementing Practical Byzantine Fault Tolerance Over The Cellular Network,” in IEEE Open Journal of Communications Society, under review.
- J. Kaur, **X. Lin**, O. R. Popoola, M. A. Imran, Q. Abbasi, L. Zhang, and H. T. Abbas, "Location-Based Adaptive Beamforming and Beamsteering for Mobile Communication in Multipath Environments," in IEEE Communications Letters, under review.
- Y. Fan, L. Zhang, Y. Sun, **X. Lin**, and Y. Fang, "Decentralized Autonomous Organizations (DAOs) Voting: Modeling and Analysis of Decentralization Performance," in IEEE Transactions on Network and Service Management, under review.

Conference

- **X. Lin**, Y. Liu, L. Zhang, A. Tukmanov, Q. Abbasi and M. A. Imran, "Beamforming on Reconfigurable Intelligent Surface: A Codebook Design for Spatial Coverage with Beam Squint Effect," 2023 IEEE International Conference on Communications

Workshops (ICC Workshops), Rome, Italy, 2023, pp. 1130-1135, doi: 10.1109/ICC-Workshops57953.2023.10283606.

- **X. Lin**, Z. Zhou, L. Zhang, A. Tukmanov, Q. Abbasi and M. A. Imran, "RIS-Assisted Resource Allocation under Base Stations' Non-Cooperation Scheme," GLOBECOM 2023 - 2023 IEEE Global Communications Conference, Kuala Lumpur, Malaysia, 2023, pp. 7237-7242, doi: 10.1109/GLOBECOM54140.2023.10437328.

- **X. Lin**, Z. Zhou, L. Zhang, A. Tukmanov, Q. Abbasi and M. A. Imran, "Joint Wide Illumination and Null Insertion Design in RIS-Assisted System," 2024 18th European Conference on Antennas and Propagation (EuCAP), Glasgow, United Kingdom, 2024, pp. 01-04, doi: 10.23919/EuCAP60739.2024.10501227.

- Z. Zhou, Y. Fan, **X. Lin**, L. Zhang, M. A. Imran, and O. Onireti, "Base Station-enabled PBFT Consensus Network: An Outlook and Performance Analysis," 2024 IEEE 35th Annual International Symposium on Personal, Indoor and Mobile Radio Communications (PIMRC), accepted.

List of Figures

1.1 The three-layer hardware structure of RIS [1]. 3
1.2 PIN diodes based unit cell design [2]. (A) The detailed structure of the unit cell. (B,C) The circuit models of the pin diode at the state "on" and "off ", respectively. (D,E) The scattered electric-field patterns of the unit cell at the states "on" and "off ", respectively. (F) The reflection amplitudes of the unit cell. (G) The reflection phases of the unit cell. 4
1.3 Varactor-based unit cell design [3]. (a) Equivalent circuit model of the proposed unit cell; (b) Varactor diode model in reverse bia; (c) Unit cell response versus different capacitance values of the varactor diode (C_V) at $f = 3.5$ GHz. 5
1.4 Metal plate v.s. RIS. (a) Metal plate: specular reflection ($\theta_i = \theta_r$); (b) RIS: anomalous reflection ($\theta_i \neq \theta_r$). 5
1.5 Illustration of basic functionalities of the RIS [4]. 6
1.6 RIS application scenarios [5]. 7

2.1 Illustration of a narrowband beamformer [6]. 17
2.2 Illustration of a wideband beamformer [6]. 18
2.3 Architectures of digital, analog, and hybrid beamforming. 19
2.4 Graph of a convex function [7]. 26
2.5 An example of the 2D polar radiation pattern. 30

3.1 System model of RIS-aided flat broadbeam design for K random directions. . 37
3.2 2D RIS under URA configuration in 3D geometry axis. 39
3.3 Investigation of sum rate for different generated beams. 55
3.4 Comparison between the derived upper bound and the simulation results with flat broadbeam design. 56
3.5 Comparison of the simulated and theoretical average received power. 57
3.6 Proof of convergence of the proposed algorithm. 58
3.7 The comparison under both ULA and URA configurations. 59

3.8 The power pattern under practical channel model when ULA configuration is applied. 60
3.9 The 3D power pattern under URA configuration. 62
3.10 System model of RIS-assisted joint wide illumination and null insertion design. 63
3.11 The convergence behaviour of the proposed algorithm. 68
3.12 The comparison between the target and optimized power pattern. 69

4.1 System model of BSs' non-cooperation scheme. 72
4.2 Convergence of the proposed algorithm. 82
4.3 The Sum-rate for $M = \{64, 96, 128, 256, 512\}$, and $P_{\max} = \{25, 35, 45\}$ dBm. . 83
4.4 The effects of RIS on n-BS - UEs served by n-BS links. 84
4.5 System model of RIS-aided mmWave System with Cooperative and Non-cooperative Networks. 85
4.6 Convergence behaviour of the proposed algorithm. 98
4.7 Sum rate under different numbers of RIS elements. 99
4.8 Sum rate under different transmit power. 100
4.9 Power allocation, user association, and the achievable SNR of each UE. (The color and height of each bar corresponds to the user association and allocated power level; the solid and dashed line corresponds the achieved and the threshold SNR.) 101
4.10 The effects of RISs on n-BSs-RISs-n-UEs links under different numbers of RIS elements. 102

5.1 Beam squint effect with $\theta_{in} = 90^\circ$ and $\theta_{out} = 30^\circ$. 106
5.2 Spatial domain covered by beams generated by Q group of RIS weights. Each group of RIS weights leverages the beam squint for signal coverage. 109
5.3 RIS codebook design with $N_s = 1$. 114
5.4 RIS codebook design with $N_s = 8$. 115
5.5 The W-HPBW of each sub-area regarding different size of RIS. 116

List of Acronyms

2D	Two-dimensional
3D	Three-dimensional
3GPP	the 3rd Generation Partnership Project
4G	4^{th} Generation
5G	5^{th} Generation
6G	6^{th} Generation
ADC	Analog-to-digital Converter
ADMM	Alternating Direction Method of Multipliers
AI	Artificial Intelligence
AIRS	Aerial Intelligent Reflecting Surface
AOA	Angle of Arrival
AOD	Angle of Departure
AWGN	Additive White Gaussian Noise
B5G	Beyond 5^{th} Generation
BCD	Block Coordinate Descent
BS	Base Station
CCP	Convex-concave Procedure
CDMA	Code Division Multiple Access
CR	Cognitive Radio
CS	Compressed Sensing
CSI	Channel State Information
D2D	Device-to-device
DAC	Digital-to-analog Converter
DB	Decibels
DC	Difference-of-convex
DC-SDP	Difference-of-convex-based Semi-definite Programming
DOA	Direction-of-arrival
EE	Energy Efficiency

EM	Electromagnetic
FDMA	Frequency Division Multiple Access
FP	Fractional Programming
GHz	Gigahertz
GP	Geometric Programming
HPBW	Half-power Beamwidth
ICI	Inter-cell Interference
IoT	Internet of Things
IRR	Iterative Rank Reduction
IRS	Intelligent Reflecting Surface
ISAC	Integrated Sensing and Communication
LoS	Line-of-sight
LP	Linear Programming
LTE	Long Term Evolution
MEC	Mobile Edge Computing
MEMS	Microelectromechanical Systems
MHz	Megahertz
MIMO	Multiple-input-multiple-output
MISO	Multi-input-single-output
ML	Machine Learning
m-MIMO	Massive Multiple-input multiple-output
mmWave	Millimeter Wave
MRC	Maximum Ratio Combining
MRT	Maximum Ratio Transmission
MU	Multi-user
NLoS	Non-line-of-sight
NOMA	Non-orthogonal Multiple Access
OFDM	Orthogonal Frequency-Division Multiplexing
PSD	Positive Semi-definite
PU	Primary User
QCQP	Quadratically Constrained Quadratic Program
QoS	Quality of Service
QP	Quadratic Programming
RF	Radio Frequency
RIS	Reconfigurable Intelligent Surface
Rx	Receiver

SCA	Successive Convex Approximation
SDP	Semidefinite Programming
SDR	Semidefinite Relaxation
SE	Spectral Efficiency
SIMO	Single-input-multi-output
SINR	Signal-to-interference-plus-noise Ratio
SNR	Signal-to-noise Ratio
SOCP	Second-order Cone Program
SU	Secondary User
SVD	Singular Value Decomposition
SWIPT	Simultaneous Wireless Information and Power Transfer
THz	Terahertz
TOA	Time-of-arrival
TSM	Two-sided Matching
TS-OMP	Twin-stage Orthogonal Matching Pursuit
Tx	Transmitter
UAV	Unmanned Aerial Vehicle
UE	User
ULA	Uniform Linear Array
URA	Uniform Rectangular Array
W-HPBW	Wideband-half-power Beamwidth
WiGig	Wireless Gigabit Alliance
ZF	Zero Forcing

Nomenclature of Operators

$(\cdot)^*$ The complex conjugate

$(\cdot)^\dagger$ The matrix (vector) pseudo-inverse

$(\cdot)^H$ The complex conjugate transpose

$(\cdot)^T$ The matrix (vector) transpose

$\angle$ The phase of a complex variable

$\inf\{\cdot\}$ The infimum of a set

$\langle \mathbf{Y}, \mathbf{Z} \rangle$ The inner product of two matrices

$\|\cdot\|$ The Euclidean norm of vector

$\mathbb{C}$ Complex numbers

$\mathbb{E}\{\cdot\}$ The expectation operator

$\mathbb{R}$ Real numbers

$\mathcal{L}(\cdot)$ The length of a set

$\mathcal{I}m\{\cdot\}$ The imaginary part of a complex variable

$\mathcal{R}e\{\cdot\}$ The real part of a complex variable

$\odot$ The point-wise multiplication

$\partial\|\cdot\|_2$ Sub-gradient of the matrix

$\sup\{\cdot\}$ The supremum of a set

$\text{rank}(\cdot)$ Rank of a matrix

$\text{Tr}(\cdot)$ Trace of a matrix

$Diag(\cdot)$ The vector with elements defined by the diagonal entries of the matrix

$diag(\cdot)$ The symbol for vectoring a matrix by taking its diagonal terms

$n(\cdot)$ The cardinal number

Acknowledgements

First of all, I would like to express my deepest thanks to my supervisor, Prof. Lei Zhang, who has given me unconditional support throughout my entire Ph.D. study. His indispensable support, both as a supervisor and as a friend, has been invaluable. His vast knowledge, passionate research enthusiasm, and diligent work ethic have profoundly inspired me throughout my Ph.D. journey and will continue to influence my future career. I feel incredibly fortunate to have had Prof. Lei Zhang as my supervisor.

I must also thank my supervisors Prof. Muhammad Ali Imran, Prof. Qammer Abbasi, and Dr. Anvar Tukmanov from British Telecom (BT) Group. They contribute a lot of time to provide valuable and critical comments to my work on reconfigurable intelligent surfaces from both academic and industrial insights. I could not finish these works without their endless and professional instructions.

I would also like to thank my boyfriend for unconditionally supporting me in both research and life. Without him, this journey would have been much harder and arduous. Additionally, I would like to thank my friends in the CSI group of UofG. The time we spent studying, discussing, and relaxing together will remain unforgettable.

Finally, I would like to express my heartfelt gratitude to my family. Their unwavering concern and care have been invaluable and irreplaceable in supporting me to pursue my desired life.

Chapter 1

Introduction

Over the last decades, a quantum leap has been accomplished in the development of wireless communication. The emergence of various advanced techniques, including orthogonal frequency-division multiplexing (OFDM) [8–10], massive MIMO (m-MIMO)[11–13] and non-orthogonal multiple access (NOMA) [14], etc., has been witnessed. However, with the globally accelerating penetration of smart devices, the wireless industry is facing the challenge of exploiting new services to enhance current communication systems.

Recently, both academia and industry have begun to envision and project for the forthcoming 6^{th} Generation (6G) technology, which will make up for the defects of the current wireless communication system. Specifically, some novel technologies such as terahertz (THz) communication [15] and distributed m-MIMO [16] will be developed, which effectively improves energy efficiency (EE) and spectral efficiency (SE). However, these technologies also mean huge hardware costs and energy consumption by deploying more active nodes and mounting more antennas [17]. Though capacity has been enhanced due to design on the precoder at the transmitter (Tx) side and/or the decoder at the receiver (Rx) side [18], optimization on the propagation environment has not been much explored yet. Indeed, it is the propagation environment that can significantly affect wireless transmission quality. In particular, the transmitted signals can be easily affected by blockages, extreme weather, etc., and thereby suffer from severe path loss and multipath fading. Hence, it is necessary to propose new paradigms that enable a significant reduction in hardware and energy costs, as well as a controllable and reconfigurable radio propagation environment.

1.1 The Reconfigurable Intelligent Surface

Motivated by the aforementioned issues, a new and disruptive technology — reconfigurable intelligent surface (RIS)[1], which is also referred to as Intelligent Reflecting Surface (IRS) [19] and metasurface [20], has been introduced and considered as a key enabling technology to realize challenging communication goals in the next few decades [21]. This section provides an exhaustive overview of RIS, encompassing its hardware structure, modelling techniques, basic functionalities, and application scenarios.

1.1.1 RIS Hardware Structure

RIS consists of a two-dimensional (2D) ultra-thin artificial structure made up of periodically or aperiodically arranged sub-wavelength elements [22]. These elements are engineered to manipulate the phase, amplitude, and polarization of incident electromagnetic (EM) waves, enabling dynamic control over signal propagation [23]. By adjusting the properties of individual elements, RIS can actively shape electromagnetic fields to achieve desired outcomes, such as signal enhancement, directional beamforming, or interference suppression.

Fig. 1.1 shows the RIS structure from a high-level perspective [1]. RIS consists of the metasurface layer, the configuration network layer, and the control layer, which is an upgrade of the conventional metasurface and the reconfigurable metasurface. Particularly, the control layer of RIS serves as a pivotal component in imbuing intelligence within the RIS framework. It plays a crucial role in interfacing with the broader network infrastructure, receiving configuration commands, and executing the necessary actions to adjust the RIS configuration. This involves applying configuration signals to the configuration network, as well as processing any pertinent sensor information collected by on-board sensors. By seamlessly integrating with the network and executing configuration commands, the RIS control layer enables dynamic adaptability and responsiveness to changing environmental conditions and network requirements. The configuration network provides a means of control over the individual unit cell reflection characteristics, such as the associated processing, biasing, and control circuitry. In EM-engineering, the response configuration can be obtained via different approaches such as by using liquid crystals, graphene [24], microelectromechanical systems (MEMS) [25], PIN diodes [26], or varactor diodes [27].

Fig. 1.2 gives a typical example of discrete RIS that is made up of unit cells controlled by PIN diodes [2]. The phase shift of each element is tuned in a discrete manner. The RIS is designed at approximately 9 Gigahertz (GHz). The 9 GHz frequency supports various critical applications, such as radar systems, satellite communications, and scientific research.

[1]Without loss of generality, RIS is the term that will be used in the thesis for the following discussion.

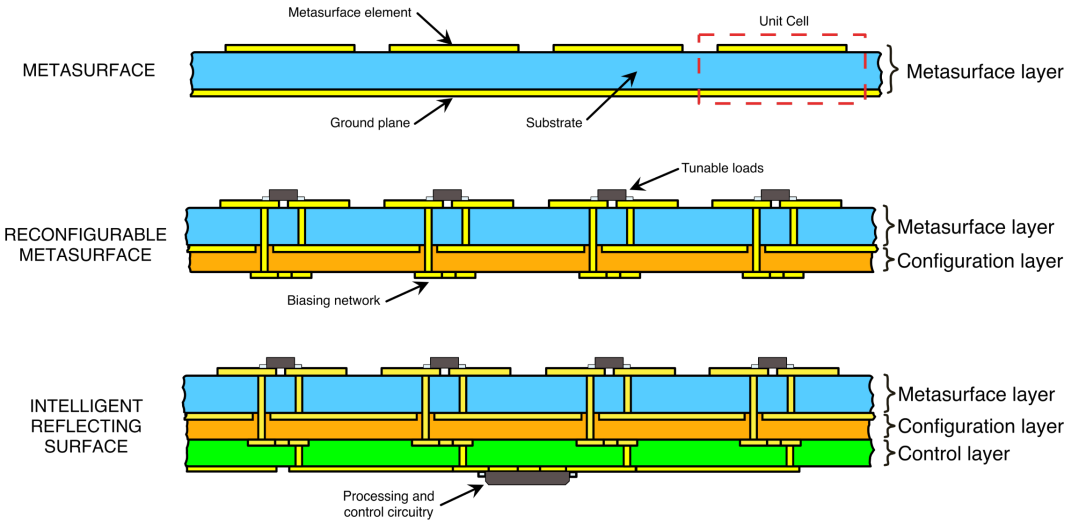

Figure 1.1: The three-layer hardware structure of RIS [1].

Its ability to balance between penetration and resolution makes it particularly valuable in environments where detailed information and reliability are required. Specifically, the authors propose a three-layer unit cell design, which is controlled through a single PIN diode. Two discrete phases can be produced on each unit cell. Fig. 1.2 (A) illustrates the structure of the binary unit, in which a PIN diode is loaded and a direct-current feeding line is introduced to switch the states of the PIN diode. Fig. 1.2 (B, C) reveals the circuit models of the pin diode at the state “on” and “off ”, respectively. The field patterns of the binary unit at the states “on” and “off ” are demonstrated in Fig.1.2 (D, E), respectively. The binary unit shows dispersive reflection characteristics as in Fig. 1.2 (F, G). With the proposed design, the best binary state occurs at 8.9 GHz, where the states “on” and “off ” possess identical reflective amplitude and the perfect opposite reflective phases.

Apart from the PIN diode-based RIS unit cell design [28], the varactor-based design is also broadly investigated, which can offer a continuous variation of surface response as the states of the scatterer on each unit cell can vary continuously. Furthermore, given the environmental changes that occur in cellular networks, the inherent properties of varactor diodes are unlikely to undergo significant alterations. Fig. 1.3 shows a varactor-based unit cell design [3] under the 3.5 GHz frequency range. The 3.5 GHz frequency band is a crucial part of modern communication infrastructure, particularly for 5G networks. Specifically, fig. 1.3(a) and fig. 1.3(b) shows the equivalent circuit model and the varactor diode model in reverse bias, respectively. For different capacitance values of the varactor diode ranging from 0.5 to 2 pF, the unit cell response is presented in Fig. 1.3(c) at the frequency of 3.5 GHz. Measurement results show that the designed unit cell can cover the required variation of phase with a low reflection loss throughout the entire range of capacitance variation, which is also consistent

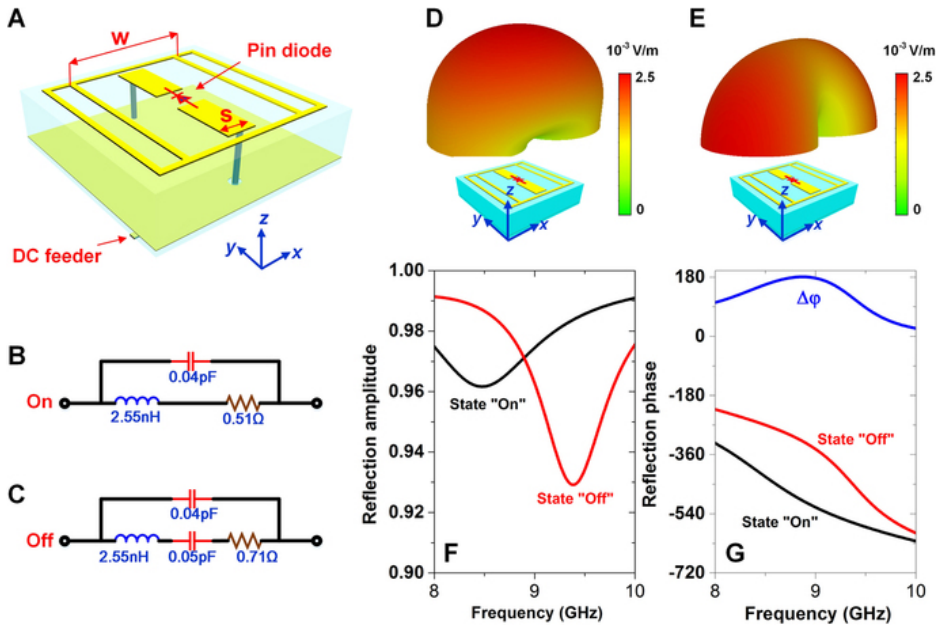

Figure 1.2: PIN diodes based unit cell design [2]. (A) The detailed structure of the unit cell. (B,C) The circuit models of the pin diode at the state "on" and "off ", respectively. (D,E) The scattered electric-field patterns of the unit cell at the states "on" and "off ", respectively. (F) The reflection amplitudes of the unit cell. (G) The reflection phases of the unit cell.

with the results obtained by CST Studio Suite and the ADS software.

1.1.2 RIS Model and Basic Functionalities

Fundamentally, for regular surfaces, such as the metal plate shown in Fig. 1.4(a), the angle of incidence is the same as the angle of reflection, which is governed by Snell's law [29]. The advancements in research on RIS have facilitated the manipulation of surface impedance and the attainment of specific phase shifts between incident and scattered waves [30]. By dividing the surface into closely-spaced elements and configuring each RIS element to induce precise phase shifts, EM waves can be directed to angles other than the symmetric reflective wave dictated by Snell's law. As shown in Fig. 1.4(b), the phase shift of each RIS element can be smartly configured within the range of 0 to 2π, a reflected beam can be sequentially formed towards any desired directions.

In addition to the intelligent tuning mechanism of the RIS phase shifts, the amplitude of each unit cell is adjustable as well [31]. The combined adjustment of both amplitude and phase shift offers diverse EM functionalities for RISs, which merit further exploration in research. Fig. 1.5 summarizes some examples of EM-based functions that can be applied on RISs. Particularly, reflection, refraction, and focusing consist of reflecting/refracting/focusing an impinging radio wave towards a specified direction, respectively. Absorption is to design

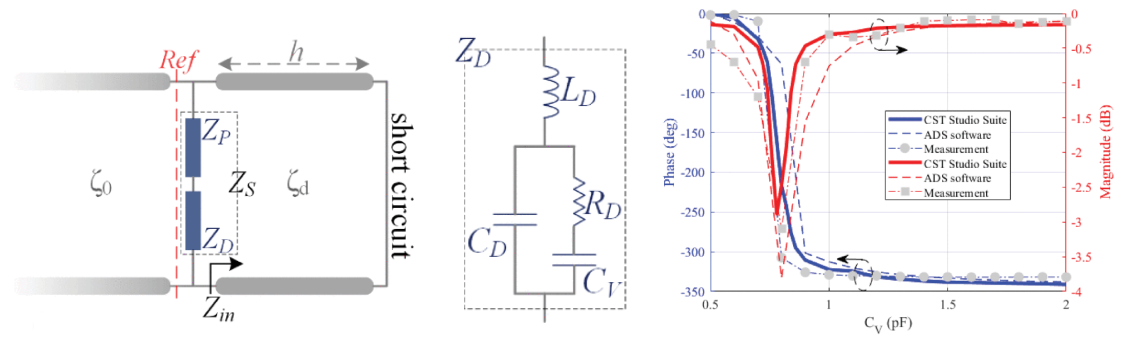

(a) (b) (c)

Figure 1.3: Varactor-based unit cell design [3]. (a) Equivalent circuit model of the proposed unit cell; (b) Varactor diode model in reverse bia; (c) Unit cell response versus different capacitance values of the varactor diode (C_V) at $f = 3.5$ GHz.

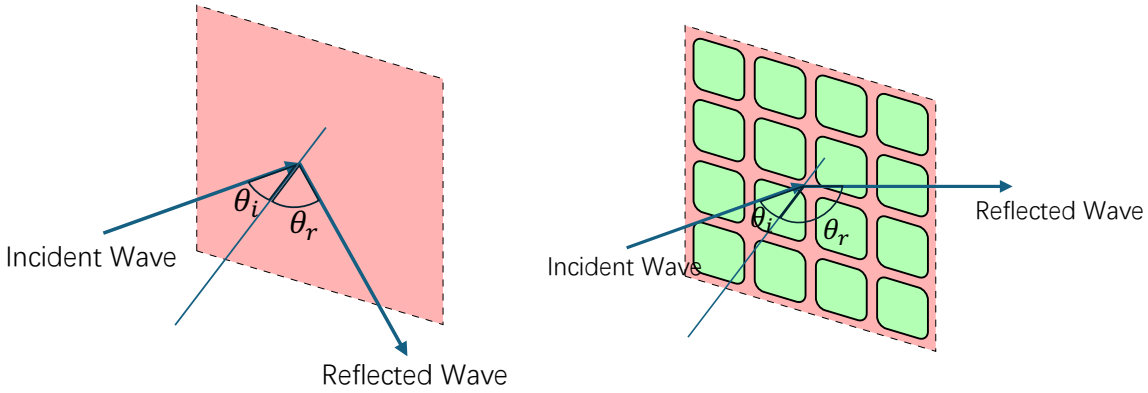

(a) (b)

Figure 1.4: Metal plate v.s. RIS. (a) Metal plate: specular reflection ($\theta_i = \theta_r$); (b) RIS: anomalous reflection ($\theta_i \neq \theta_r$).

of an intelligent surface that suppresses the reflected and refracted radio waves. The polarization of the incident radio wave can be modified by the RIS, such as from linear to circular polarization, which is particularly useful for aligning the polarization of transmitted and received signals, thereby optimizing the communication link. RIS can also enable polarization diversity by reflecting or transmitting signals with different polarizations, which enhances communication robustness as it allows the system to exploit multiple polarization channels in environments with multi-path propagation. Moreover, the RIS can also realize radio wave splitting, collimation, and analog processing. A range of selective EM functionalities can be realized on RISs leveraging the flexible phase and amplitude configuring.

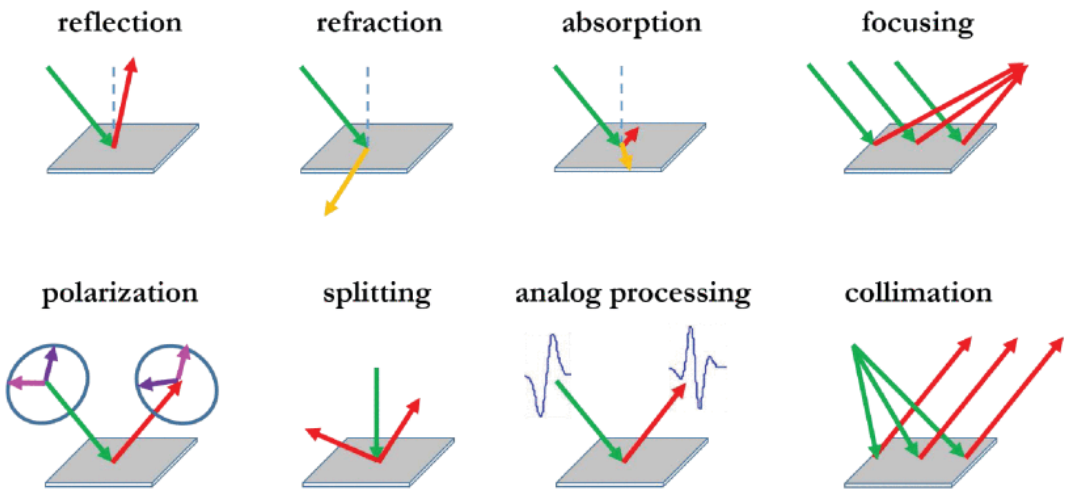

Figure 1.5: Illustration of basic functionalities of the RIS [4].

1.1.3 RIS Application Scenarios

Considering the tremendous amount of functionalities that can be realized by the RISs, several application scenarios are proposed for potential industrial implementation. Fig. 1.6 reports several applications which benefit from the use of RIS. The first application illustrates a scenario where the direct link between the user and the base station (BS) is severely blocked. Then, a virtual link could be established with the help of RIS [32]. This application is particularly useful for coverage enhancement in millimeter wave (mmWave) and THz communications systems due to the unfavourable free-space path loss in these frequency bands. The RIS could also be employed to enhance communication security by suppressing the signal towards eavesdroppers while guaranteeing the communication performance of legitimate users [33]. Moreover, as the inter-cell interference (ICI) could be challenging to mitigate in a multi-cell cellular network, especially for users at the cell edge, RIS could be a potential solution for ICI suppressing [34]. The fourth application illustrated in Fig. 1.6 focuses on device-to-device (D2D) communication, where the RIS could be used for jamming management and communication reliability augmentation [35, 36]. Since severe blockage often occurs in mmWave communications, the direct Tx-Rx channel is generally considered as negligible, and the RIS is used to build reflective virtual links between the Tx and Rx [37]. The RIS are particularly useful in the high-frequency scenario to increase the received power, the channel rank, and the spatial diversity needed for outdoor systems. The use of the RIS is also beneficial for EE improvement in Internet of Things (IoT) networks by providing additional services to IoT devices through the visible link established by the cascaded reflection of multihop RISs [38]. The RIS is also a rewarding technology to be applied in the beyond 5^{th} generation (B5G) NOMA system. By appropriately implementing the RIS and configuring each unit cell, the transmit power can be reduced, and the number of served users increases

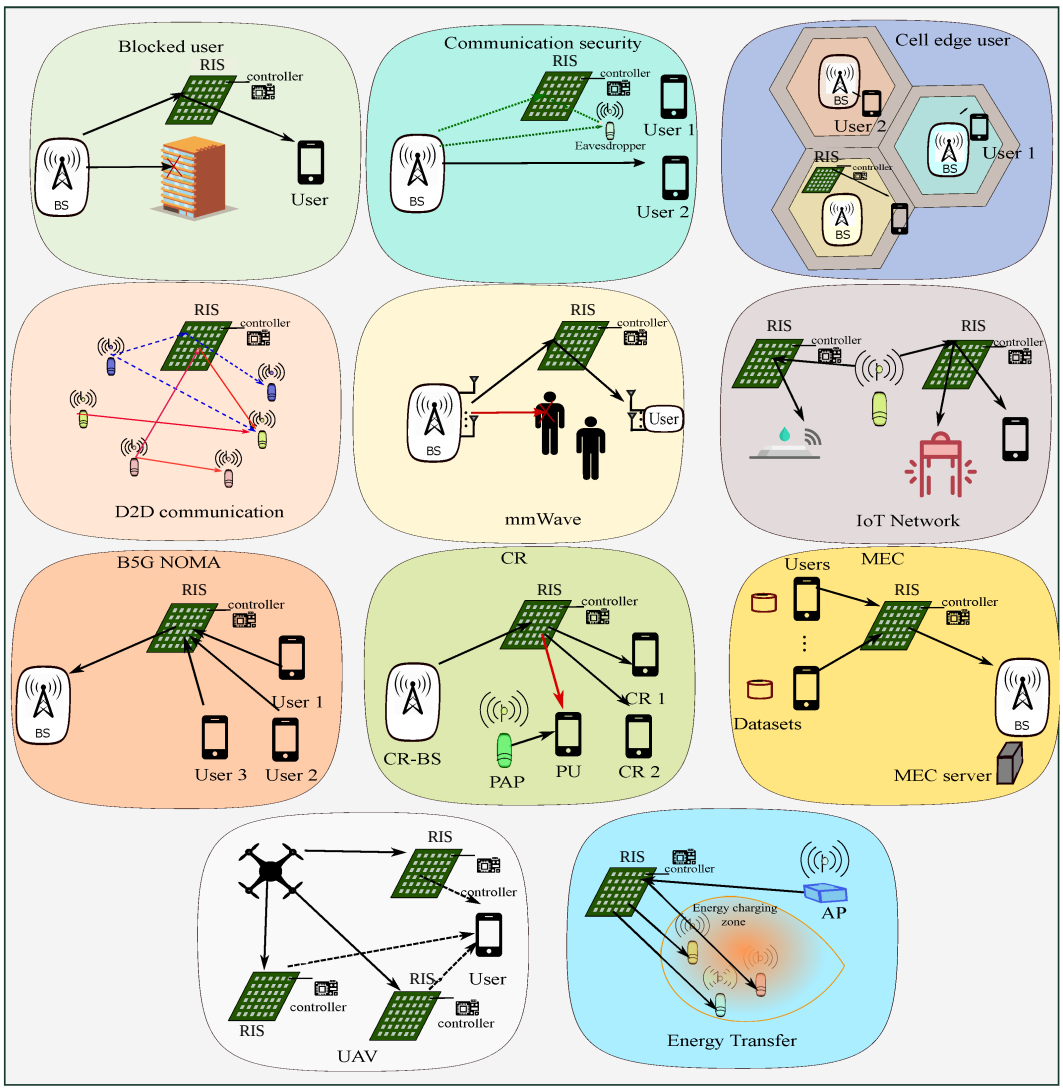

Figure 1.6: RIS application scenarios [5].

[39]. Another interesting application illustrated in Fig. 1.6 is the use of the RIS technology for cognitive radio (CR) networks. Particularly, the RIS can be deployed to improve the communication performance of both primary users (PUs) and secondary users (SUs) via robust RIS beamforming design and spectrum sharing, etc. [40, 41]. The mobile edge computing (MEC) network is an emerging computing paradigm which can guarantee the stringent latency requirements of various applications by offloading the computation-intensive tasks to the network edge cloud platform. By properly deploying RIS in the vicinity of the mobile devices, the service coverage of MEC is largely extended, the SE and EE can be significantly enhanced as well [42]. The application of RIS in unmanned aerial vehicle (UAV) networks is also investigated, where the RISs is used to improve the QoS given the long distance between the UAV and the ground users [43]. The RISs are placed approximately halfway between the UAV and the users (UEs) in the vertical direction. The last application scenario demonstrated

in Fig. 1.6 is to transfer energy with the help of RIS. The authors in [44, 45] proposed RIS as a holistic solution for simultaneous wireless information and power transfer (SWIPT), where the bi-objective of improving both information and power transfer can be satisfied.

1.2 Motivation

RIS has been widely recognized as a promising technology in the 6G networks for realizing a controllable and programmable wireless propagation environment. By intelligently controlling the reflections, RIS can enhance signal strength [46], improve coverage [47], mitigate interference [48], and enable various other functionalities to optimize wireless communication systems. By densely deploying RISs and smartly coordinating them in wireless propagation environments, the reconfigurable and programmable end-to-end wireless channels could be eventually achieved [49].

Nevertheless, while RISs offer advantages, they also introduce complexities to the wireless communication system. This complexity renders conventional techniques such as channel estimation and precoding design potentially inapplicable. In the following, we delineate several hurdles in RIS-assisted systems, which provide the impetus for our research.

- **Channel Estimation**

  Recent research advances have shown the application of RIS in various communication systems, such as RIS-aided NOMA system [50], RIS-aided secure transmission [51], and RIS-aided CR system [52], etc. These works mainly focus on the design and optimization of active and passive beamforming under the assumption that the channel state information (CSI) is perfectly pre-known. To precisely assure system performance of all the above applications, channel estimation is definitely a core issue. However, channel estimation in RIS-assisted communication systems could be hard to achieve due to the passive property of RIS. While some research proposed channel estimation methods in RIS-aided communiaction system, the complexity and cost could be very high, and the estimated CSI can be inaccurate or with high latency.

  Several works have been devoted to this topic. Specifically, a general framework for channel estimation in a RIS-aided system was introduced in [53] by leveraging a combined bilinear spare matrix factorization and matrix completion. This design is enabled by activating elements one by one at each stage of estimation and could therefore lead to poor real-time performance and large estimation variance. Following this work, the authors in [54] designed an optimal channel estimation scheme which is guided by results for the minimum variance unbiased estimation. It is proved that this work ef-

fectively reduces estimation variance. However, the pilot overhead could be extremely high when the size of RIS is large. In addition, the pilot-based estimation method is susceptible to pilot contamination, where the pilot signals from neighbouring cells or users may interfere with the estimation. The compressed sensing (CS)-based estimation was proposed in [55], which leverages the fact that many natural signals are sparse or compressible in some domains and sequentially enables the reconstruction of signals and images from far fewer samples or measurements than traditionally required by the Nyquist-Shannon sampling theorem. Nevertheless, this estimation method requires prior knowledge of the sparsity pattern, which may not always be available. Furthermore, deep learning-based channel estimation for RIS-assisted communication was investigated in [56, 57], which utilizes neural networks to learn the mapping between the received signal and the CSI. However, a large amount of labelled data will be required for training, which might be difficult to obtain, especially for complex scenarios in practical implementation. In conclusion, channel estimation remains a challenging issue that warrants further investigation. In this thesis, the design of broadbeam is proposed to address the complex channel estimation consider its capability to provide robust coverage, which largely reduces the requirements for accurate and real-time CSI acquisition.

- **Operator Collaboration Modes**

  A few studies have been done on resource allocation in RIS-aided systems for their importance in practical deployment. A critical prerequisite generally made is that all BSs agree to collaboratively share resources and configure the RIS. For example, the authors of [58] studied resource allocation in the RIS-aided downlink NOMA system. To maximize the system throughput, a joint optimization problem over the channel assignment, decoding order, power allocation, and reflection coefficients was formulated. However, this work only considered the single-cell scenario with a single BS, while the resource allocation in multi-cell networks investigating the resource management across multiple BSs is more intricate but crucial. A more general RIS-assisted multi-cell mmWave downlink communication network was studied in [59]. A sum-rate maximization problem was proposed by jointly optimizing the RIS beamforming and UE association. Nevertheless, the assumption they made that all BS work under the same frequency is impractical. The authors of [60] investigated power allocation and UE association in the RIS-assisted multi-cell system. Orthogonal frequencies are allocated to adjacents BSs. Note that the UE association is not realistic, as BSs from different operators do not allow connection switching. Furthermore, BSs from multi-

ple operators may not make an agreement on cooperatively using RISs due to cost and security concerns.

To the best of our knowledge, existing literature has not addressed the scenario involving BSs operated by different operators, termed as the BSs' non-cooperative scheme [61]. In practice, BSs belonging to multiple operators may not reach agreements to collaboratively utilize RISs or share resources due to cost and security concerns. Consequently, UE association becomes impractical as BSs from different operators do not allow seamless connection switching. Additionally, BSs from different operators may resist being influenced by RISs with unknown characteristics. Nevertheless, non-cooperative BSs may inevitably direct signals toward RIS, considering the presence of UEs and RIS manipulated by cooperative BSs in the same direction. From a regulatory standpoint, the costs and challenges associated with modifying the configuration and placement of BSs are considerably higher compared to those of RISs. Hence, it is more rational to reconfigure RISs to alleviate the impacts on non-cooperative BSs. In the context of the non-cooperative scheme, traditional resource allocation methodologies are rendered inapplicable. In this thesis, the cooperation mode of BSs is first defined, based on which the resource allocation among cooperative BSs is explored in an RIS-aided system. Particularly, the RISs are designed to assist the communication performance of cooperative BSs while mitigating the effects on reflective links between non-cooperative BSs and their serving users.

- **Computational Complexity and Cost**

  The utilization of RIS across diverse scenarios necessitates optimization tasks such as beamforming, resource allocation, and enhancing EE. These optimization endeavours demand sophisticated algorithms. However, a notable challenge in RIS-assisted systems is the significant computational complexity and cost engendered by these optimization algorithms, particularly for large-scale setups or scenarios with multiple UEs.

  For example, a sum rate maximization problem was formulated in the RIS-assisted single-cell heterogeneous D2D communication scenario in [62]. The D2D user work mode, RIS phase shifts, and power allocation are jointly optimized. Since the signal-to-interference-plus-noise ratio (SINR) and transmission power show continuous properties, the RIS phase shifts and the communication work mode are discrete constraints, the whole problem is a mixed integer non-linear optimization problem, which is hard to solve. Moreover, the authors in [63] evaluated the communication performance of the uplink RIS-assisted cell-free m-MIMO system. On a parallel avenue, the authors in [64] proposed an algorithmic framework for large-scale RIS-assisted wireless systems.

The m-MIMO system and large-scale RIS render extremely high computational complexity due to a large number of variables. A joint transmit and reflective beamforming design in a secure RIS-enabled integrated sensing and communication (ISAC) system was investigated in [65]. The beampattern gain at the target is maximized. The formulated optimization problem is challenging to solve due to its non-convexity and the intricate coupling between the design variables. A high-complex iterative algorithm was developed to solve the proposed problem. In summary, balancing performance objectives with computational resources is crucial for practical implementation.

In addition to the complex optimization algorithms, the computational costs are also associated with various aspects such as signal processing, channel estimation, and real-time control. Addressing these computational challenges is essential for the practical implementation of RIS technology in future wireless communication networks. In this thesis, a low-complexity RIS codebook design leveraging the beam squint effect in the wideband system is proposed, from which a group of RIS weights could be simply looked up from the codebook to generate a beam covering the desired direction.

1.3 Objectives

This thesis is driven by the need to overcome several key challenges that hinder the practical industrial deployment of RIS. The primary objective is to systematically explore and propose innovative solutions that will enable the effective use of RIS in enhancing wireless communication systems.

The first objective of this thesis is to develop the signal power broadbeam generation for robust coverage. One of the major challenges in RIS-assisted systems is the inability of current methods to guarantee real-time, accurate, and low-cost channel estimation. To address this, the thesis introduces a novel approach focused on generating signal power broadbeam. This strategy aims to overcome the difficulties in acquiring precise CSI by enabling blind coverage enhancement. The proposed design ensures that signals with comparable power levels are accessible to UEs across a pre-defined sector area, irrespective of their exact positions, thus reducing the dependency on precise directional information. This design first realize minimized need for real-time CSI. By focusing on broadbeam area coverage instead of targeting specific UEs, the design reduces the need for real-time RIS adjustments in response to UE movements, significantly lowering hardware costs and computational complexity. In addition, the pre-defined area coverage design allows for flexibility in adjusting beam shapes, numbers, and null directions to enhance signal reception within the active UE area, thereby improving the SNR and overall QoS.

The second objective is to develop an advanced resource allocation strategy for RIS-aided communication systems involving both cooperative and non-cooperative BSs. Given the common industrial scenario that BSs from different operators may not make an agreement on jointly utilizing the RISs and sharing the resources, the cooperation modes of BSs should be investigated. This thesis explores the optimization of RIS reflection coefficients, power allocation, sub-channel assignment, and user association to maximize sum rates for UEs served by cooperative BSs while ensuring minimal interference with non-cooperative BSs. We start with a sub-6 GHz system featuring two non-cooperative BSs and a single RIS, which is then extended to multi-RIS and multi-BS networks under mmWave bands, revealing comprehensive resource management and RIS design in various communication environments.

The third objective is to address the computational complexity associated with RIS-assisted systems, particularly in wideband environments. This thesis proposes a low-complexity RIS codebook design that accounts for the often-overlooked beam squint effect — a phenomenon where directional changes across frequencies reduce the average SE. By delivering the RIS codebook design, the UE at an arbitrary direction could always be covered by looking up a group of RIS weight from the codebook, bringing with low computational and hardware cost. The wideband-half-power beamwidt (W-HPBW) by leveraging the concept of HPBW is first defined, which quantifies the signal coverage performance in wideband system considering the beam squint effect. Then, we propose a novel RIS codebook design to enhance signals' spatial coverage in wideband systems. Our design aims to generate multiple beams using different RIS weights, covering the entire spatial domain that the RIS can cover without overlap. The groups of RIS weights formulate the codebook which can largely reduce the hardware and computation complexity.

In summary, this thesis seeks to advance the field of RIS-assisted wireless communication by addressing critical challenges in channel estimation, resource allocation, and system design. Through innovative approaches to broadbeam generation, resource optimization in cooperative and non-cooperative networks, and efficient wideband codebook design, the research aims to lay a solid foundation for the practical deployment of RIS in next-generation communication systems.

1.4 Research Contributions

The aforementioned objectives indicate that the thesis aims to promote further theoretical research and industrial applications of RIS by addressing some practical issues that may exist in its actual deployment for enhancing wireless communication systems. The contributions of this thesis are summarized as follows to achieve these goals:

- We start with a design framework to generate a single broadbeam with a flattened top and maximized average received signal power within a pre-defined sector area. The flat broadbeam ensures the maximum sum rate compared with other beam patterns, which is numerically proved in this thesis. As an important metric to measure QoS, the relationship between the average received power and the phase shifts of RIS is analytically obtained. Specifically, the upper bounds of the average received power given RIS under both uniform rectangular array (URA) and uniform linear array (ULA) configurations are obtained. The difference-of-convex-based semi-definite programming (DC-SDP) algorithm is introduced for the RIS beamforming design to generate a single broadbeam, which effectively transfers the original non-convex problem into a convex form and realizes iterative rank reduction (IRR). We compare the simulation results using the DC-SDP algorithm with other baseline methods; it is worth mentioning that the DC-SDP algorithm could always result in broadbeam with fewer fluctuations. We then extend the generation of a single broadbeam to the multiple wide illumination and null insertion design in an RIS-assisted system. Our aim is to minimize the normalization deviation between the target and optimized pattern via optimizing the passive beamforming at RIS, given constraints of RIS unit modulus weights. A low-complexity alternating direction method of multipliers (ADMM)-based algorithm is proposed, which effectively address the non-convexity.

- Motivated by the fact that operators may not make an agreement on collaboratively using RIS and sharing resources from cost, security, and other concerns, cooperative and non-cooperative BSs are first defined based on whether their belonged operators reach an agreement on jointly controlling RIS and sharing resources such as spectrum, power, etc. A non-cooperation scheme is investigated in which an RIS is solely controlled by one BS, while there is another BS working under an orthogonal frequency band in the adjacent cell that does not need the RIS. On one side, the sub-channel assignment and power allocation are studied as they are important metrics in resource allocation. On the other side, the RIS is designed to further enhance the performance of UEs served by the dedicated BS while alleviating its effect on the links between the adjacent BS and its serving users. Considering the impact of RIS on channels that aim to be either enhanced or unaffected, a sum-rate maximization problem is formulated by jointly optimizing the passive RIS beamforming, sub-channel assignment, and power allocation. Then, a multi-RIS-assisted multi-BS multi-UE mmWave networking system comprising both cooperative and non-cooperative BSs is proposed. We jointly optimize RISs reflection coefficients, active beamforming, power allocation, and UE association to achieve maximal sum rates for UEs served by cooperative BSs, while

adhering to channel gain constraints between non-cooperative BSs and their associated UEs. To solve the formulated non-convex problem with coupled and binary variables, an efficient algorithm exploiting the techniques of block coordinate descent (BCD) is developed.

- To capture the wideband system's HPBW while considering the beam squint effect, the concept of W-HPBW is introduced. Unlike traditional HPBW, W-HPBW accounts for variations in radiation patterns across different frequencies. An innovative design for RIS codebooks is proposed, leveraging beam squint. Here, the RIS beamforming weights are optimized to ensure each spatial coverage aligns with W-HPBW criteria, while collectively covering the entire spatial domain with beams from all RIS weight groups. In scenarios with high mobility, such as vehicular communication, beam broadening techniques is applied to minimize RIS weight switching and reduce pilot overhead in channel estimation.

1.5 Thesis Outline

The rest of this thesis is as follows. In Chapter 2, we introduce the background and discuss the state-of-the-art techniques in beamforming techniques, channel model and estimation, convex optimization, and antennas' radiation pattern. After that, an overview of RIS in the related fields is presented.

Chapter 3 studies the generation of single and multiple flat broadbeams. The single broadbeam investigation involves a numerical analysis on the relationship between the average received power and the phase shifts of RIS, and the RIS beamforming design based on the DC-SDP algorithm. The upper bound of the average received power with respect to the number of elements in RIS is derived. Then, an ADMM-based technique is developed to realize the multiple broadbeams design with null insertion at unwanted directions.

Chapter 4 defines the cooperation modes of BSs based on whether their belonged operators have reached an agreement on the shared use of RIS. We first consider two non-cooepative BSs, where the RIS is designed to enhance the communication performance of its served BS, while mitigating the effects on another one. The sub-channel assignment, power allocation at the RIS-served BS, and RIS passive beamforming are jointly optimized. We then extend to a multi-RIS-assisted multi-BS multi-UE networking system comprising both cooperative and non-cooperative BSs, the power allocation, UE association among cooperative BSs, and the RIS beamforming are jointly designed for sum-rate maximization.

Chapter 5 proposes the codebook design as a possible solution to combat the high com-

putational complexity of RIS beamforming design. Specifically, a RIS codebook based on HPBW concept is designed in wideband system considering the beam squint effect, which shift the beam direction under different frequencies. For an arbitrary direction within the entire coverage range of RIS, a set of RIS configuration can be found in the codebook, enabling the chosen direction to be covered by the beam generated based on this RIS design. To address signal coverage in high-mobility scenarios like vehicular communication, we further employ beam broadening techniques in the codebook to minimize RIS weight switching and pilot overhead in channel estimation.

Finally, conclusions of this thesis and an outlook on possible future work for RIS are given in Chapter 6.

Chapter 2

Background and Literature Review

In this chapter, we first introduce the general background of beamforming techniques. After that, a brief overview of channel model and channel estimation is presented, followed by the introduction of convex optimization. Then, we will discuss the radiation pattern of antenna. Finally, the state-of-the-art schemes concerning beamforming and other metrcis' optimization, channel estimation, and radiation pattern design in RIS-assisted communication systems are investigated.

2.1 Overview of Beamforming Techniques

Beamforming is a radio frequency (RF) technique that allows wireless signals to be targeted toward a specific endpoint or receiving device by using an array of sensors and antennas that optimizes to reduce unintended interference [66]. As opposed to having a wireless signal spread out in all directions with a broadcast antenna, beamforming concentrates the signal at the receiver side. Early experiments with beamforming can be traced back to Guglielmo Marconi, who in 1901 utilized a circular array of four antennas to enhance the gain of trans-Atlantic Morse code transmissions [67], following which the adaptive beamforming emerged in the late 1960s, characterized by the implementation of a processor at the antenna backend that dynamically updates and adjusts the array weights [68]. In the coming 6G systems, beamforming still plays as a critical role in enhancing communication performance. In this section, we introduce several beamforming techniques and their modes of operation.

2.1.1 Narrowband Beamforming

We first classify the beamforming technique in terms of the operating frequency. The vast majority of current wireless communication applications prioritize narrowband beamform-

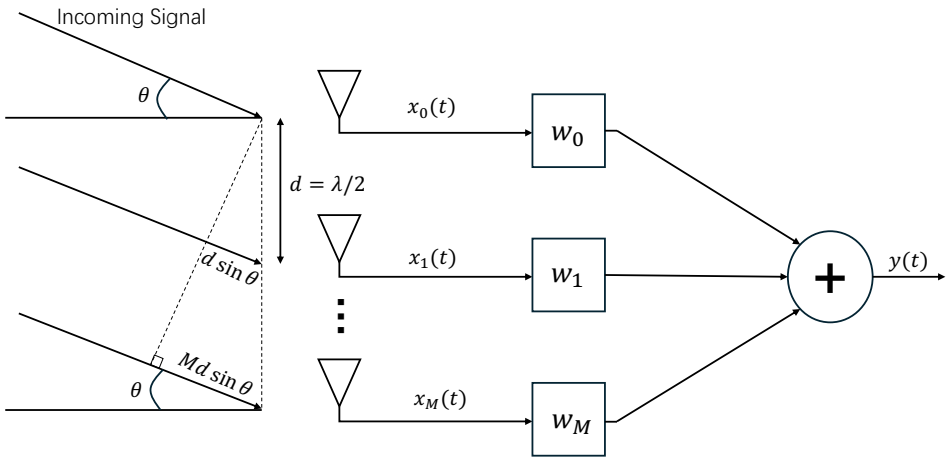

Figure 2.1: Illustration of a narrowband beamformer [6].

ing. For narrowband signals, the required temporal shifts in the mapping matrix are straightforward. This simplicity arises from the fact that altering the phase of a narrowband signal is analogous to a time shift. Consequently, the resulting equations facilitate high-resolution beamforming and accurate determination of the direction-of-arrival (DOA). Fig. 2.1 depicts a conventional narrowband beamformer on an antenna array with M elements. The DOA is indicated by θ, and $x_m(t)$ and w_m denote the impinging signal and the weight at the m-th element, respectively. d is the element spacing of the antenna array, which is equal to half wavelength of the incoming signal frequency f. Then, the output of the narrowband beamformer can be represented as

$$y(t) = \sum_{m=0}^{M} x_m(t) w_m. \tag{2.1}$$

Particularly, the signal received by the m-th element on the antenna array with respect to $x_0(t)$ can be represented by

$$x_m(t) = x_0(t) e^{-j2\pi m \frac{f}{c} d \sin\theta}. \tag{2.2}$$

Consequentially, the output signal at time t can be expressed as

$$y(t) = x_0(t) \sum_{m=0}^{M} e^{-j2\pi m \frac{f}{c} d \sin\theta} w_m. \tag{2.3}$$

2.1.2 Wideband Beamforming

Instantaneous linear combining of the received array signals results in narrowband beamforming. Wideband signals, on the other side, necessitate the use of additional processing dimensions for efficient operation, such as tapped delay lines [6] or the recently suggested

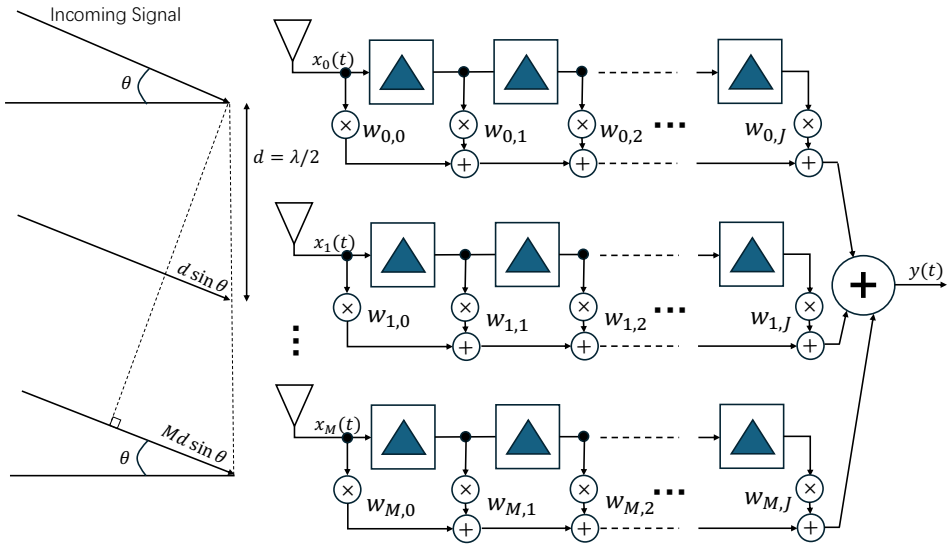

Figure 2.2: Illustration of a wideband beamformer [6].

sensor delay lines [69], which result in a wideband beamforming system. A general structure for wideband beamdorming is demonstrated in Fig. 2.2. The beamformer following this structure samples the propagating wave field in both space and time [70]. Then, the output signal can be expressed as

$$y(t) = \sum_{m=0}^{M} \sum_{i=0}^{J} x_m(t - iT_s) w_{m,i}, \tag{2.4}$$

where M denotes the number of antenna elements, and J is the number of taps associated with each antenna element. T_s represents the delay between adjacent taps. Similar to (2.3), the array output can be further interpreted as

$$y(t) = x_0(t) \sum_{m=0}^{M} \sum_{i=0}^{J} e^{-j2\pi m \frac{f}{c} d \sin\theta} e^{-j2\pi f i T_s} w_{m,i}. \tag{2.5}$$

2.1.3 Analog Beamforming

The implementation of beamforming is of significant interest to the RF industry, given the conflicting requirements of efficiency and flexibility. We first introduce the structure of the analog beamformer. On the Tx side, the baseband signal is generated in the digital domain and converted into an analog signal via a digital-to-analog converter (DAC). This signal is then up-converted to a higher carrier frequency (e.g., 28 GHz) and fed to an analog beamforming network through a splitter. In this network, weights are applied using digitally controlled phase shifters, one per antenna element. Note that only one beam can be generated at a time, the implementation of complex beam patterns in multi-UE environment could be challenging. On the Rx side, the incoming signal is phase-shifted at each antenna element before

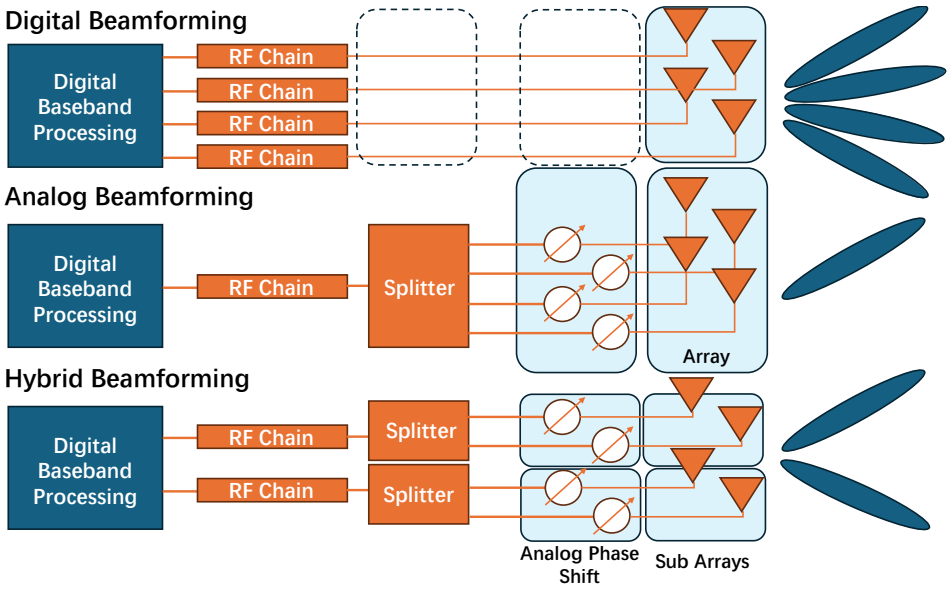

Figure 2.3: Architectures of digital, analog, and hybrid beamforming.

being combined, filtered, and down-converted to baseband or intermediate frequency. The signal is then digitized through an analog-to-digital converter (ADC). Since beamforming has already been performed in the analog domain, the digitized signal represents a superposition of various waves, limiting further manipulation in the digital domain.

The analog beamformer is cost and energy efficient as it is implemented with simpler hardware and avoids extensive digital signal processing. Consequently it has been widely used in radar systems, satellite communications, and some 5^{th} Generation (5G) mmWave systems where lower complexity and cost are advantageous. However, the low-complexity hardware also comes with limited flexibility in beam pattern control due to the fixed phase shifters. Moreover, despite that some wideband analog beamforming solutions exist [71], the analog beamforming is typically designed for narrowband systems [72, 73].

2.1.4 Digital Beamforming

Digital beamforming leverages digital signal processing techniques to manipulate the signals transmitted and received by antenna arrays. In this case, each antenna element has its own dedicated RF chain as well as individual DACs and ADCs, which implies that the gain and phase of each spatial sample is adjusted in an individual manner along with baseband processing before up-conversion at Tx or after down-conversion at Rx. This enables a true implementation of mathematical algorithms with maximum flexibility, most of which treat each antenna output as an accessible sample.

The zero forcing (ZF) beamforming is a typical digital beamforming, which is used in multi-UEs multiple-input-multiple-output (MIMO) systems to effectively nullify interference

between UEs by inversely filtering the channel matrix [74]. Particularly, given a channel matrix $\mathbf{H}^{M\times N}$, where M denotes the number of single-antenna Rx and N denotes the number of Tx antennas, the ZF beamformer weights can be represented as

$$\mathbf{W} = \mathbf{H}^{\dagger} = \mathbf{H}^{*}(\mathbf{H}\mathbf{H}^{*})^{-1}. \tag{2.6}$$

The maximum ratio transmission (MRT) and maximum ratio combining (MRC) beamforming are another two fundamental digital beamforming techniques used in wireless communications to optimize the signal strength and quality. Particularly, MRT is used on the Tx side to maximize the SNR at the Rx. The principle of MRT is to weight the transmitted signal in such a way that the signal aligns constructively at the Rx. On a parallel avenue, MRC is used on the Rx side to combine signals received from multiple antennas in a way that maximizes the SNR. The principle of MRC is to weight each received signal proportional to the complex conjugate of the channel response. To illustrate the MRT, we consider a multi-input-single-output (MISO) system with N_t transmit antennas and a single receive antenna. Let $\mathbf{h} \in \mathbb{C}^{N_t\times 1}$ represent the channel vector from the Tx to Rx. To align with the Rx, the transmitted signal $\mathbf{x}$ combined the MRT beamforming is expressed as

$$\mathbf{x} = \sqrt{P}\frac{\mathbf{h}^{*}}{\|\mathbf{h}\|}s, \tag{2.7}$$

where P denotes the transmit power and s is transmitted symbol. Correspondingly, the received signal at Rx can be represented as

$$y = \mathbf{h}^{T}\mathbf{x} + n = \sqrt{P}\|\mathbf{h}\|s + n, \tag{2.8}$$

where n is the noise.

Then, we consider a single-input-multi-output (SIMO) system with a single transmit antenna at Tx and N_r receive antennas at Rx. Let $\mathbf{h} \in \mathbb{C}^{\mathbf{N_r}\times\mathbf{1}}$, s, and $\mathbf{n} \in \mathbb{C}^{N_r\times 1}$ represent the channel vector from the Tx to the Rx, the transmitted symbol at Tx, and the noise vector, respectively. The received signal vector is given by

$$\mathbf{y} = \mathbf{h}s + \mathbf{n}, \tag{2.9}$$

which is then combined at the Rx as

$$\hat{s} = \mathbf{w}^{H}\mathbf{y}, \tag{2.10}$$

where $\mathbf{w}$ is the combining weight factor. For MRC, the weight factor is designed as

$$\mathbf{w} = \frac{\mathbf{h}}{||\mathbf{h}||}, \tag{2.11}$$

which maximizes the SNR because the signal components are coherently added, while the noise components are combined in a way that minimizes their effect.

While digital beamforming provides advanced capabilities and performance benefits, these advantages come with trade-offs in terms of complexity, cost, power consumption, latency, and scalability. Addressing these challenges is crucial for the successful implementation of digital beamforming in practical wireless communication systems. In balancing cost, size, and complexity, a hybrid solution that combines both of analog and digital beamforming has emerged, which is discussed in the following subsection.

2.1.5 Hybrid Beamforming

The hybrid architecture combining analog and digital beamforming is the preferred choice in current 5G systems and is anticipated to play a crucial role in future wireless communication technologies. Specifically, hybrid beamforming strategically integrates analog and digital components to optimize performance while mitigating the disadvantages inherent in using either beamforming technology alone. Typically, a hybrid beamforming architecture employs a small number of RF chains connected to a large-scaled antenna array through a network of phase shifters and digital processors in analog and digital domains, respectively. A limited performance can be achieved in analog domain by the use of quantized phase shifts, while fine beam adjustments and nulls steering are handled digitally [75].

Unlike conventional microwave architecture, the hybrid beamforming is more suitable for mmWave massive MIMO applications, which benefit from compact RF design [76]. At mmWave frequencies, the multi-path channel experiences higher propagation loss, necessitating compensation through the gain from antenna arrays at the Tx, Rx, or both. These arrays maintain a reasonable physical size due to the short wavelengths, so that fully digital beamforming solutions are infeasible [77]. In hybrid architecture, the beamforming is performed in the analog domain at RF, and multiple sets of beamformers are connected to a small number of ADCs or DACs. To be more specific, hybrid beamforming enables the packaging of mmWave massive MIMO transceivers, allowing them to be deployed in various locations such as lamp posts, power line towers, and building corners. This deployment was previously impractical with digital precoding and beamforming architectures in MIMO systems due to the high cost and power consumption associated with a large number of ADCs and DACs, while can be realized under the hybrid structure.

In conclusion, hybrid beamforming not only reduces the number of required RF chains and ADCs/DACs but also invokes a balance between hardware efficiency and beamforming performance. By leveraging the strengths of both analog and digital beamforming, hybrid beamforming provides a scalable and efficient solution for advanced wireless communication systems, facilitating enhanced signal quality, improved spectral efficiency, and robust multi-UEs support.

2.2 Overview of Channel Model and Estimation

Research on wireless channels is a critical area of focus within the field of wireless communications. It encompasses a wide range of topics aimed at understanding and improving the performance of communication systems across different frequency bands. Here, we focus on the sub-6GHz and mmWave frequency ranges, which are particularly classified in 5G technology. The corresponding channel models and the channel estimation methods are investigated in the following.

2.2.1 Channel Model

Sub-6 GHz is a term used to refer to the frequency range below 6 GHz in the radio spectrum. This frequency range is used to provide wireless services such as 4G, LTE, 5G and WiFi. On the other side, the higher speeds that really set 5G apart from any of the 4G LTE flavors require mmWave high-frequency bands, which has been considered as a promising technology to meet the ever-growing demand for mobile data rate due to its large available bandwidth [84].

Wireless communication channels operating in the sub-6 GHz and mmWave frequency bands exhibit distinct characteristics and behaviors due to their different frequency ranges. Table. 2.1 gives a comprehensive comparison between sub-6 GHz and mmWave channel models. To consider the operating frequency, sub-6 GHz typically refers to the frequencies below 6 GHz. Examples include 700 megahertz (MHz), which is auctioned for commerial use, particularly for long-range and rural coverage, due to its excellent propagation characteristics [85], and 2.4 GHz, which leads to the development of WiFi and bluetooth due to its global availability and low regulation [86]. The mmWave indicates frequencies ranging from 24 to 100 GHz. For example, the 28 GHz band was initially allocated for fixed satellite services and point-to-point links, which was later identified for 5G high-capacity mobile broadband [87]. Moreover, the 60 GHz band, which is originally designed for radar and scientific research, supports Wireless Gigabit Alliance (WiGig) standards for short-range, high-

Table 2.1: A comparison between sub-6 GHz and mmWave channel models.

	Sub-6 GHz	mmWave
References	[78–80]	[81–83]
Frequency Range	Typically refers to frequencies below 6 GHz, which are commonly used in 4^{th} Generation (4G) long term evolution (LTE) and early 5G deployment.	Refers to frequencies ranging from 24 GHz to 100 GHz, which are mostly used in advanced 5G and future wireless technologies.
Antenna and Array Design	The number of antennas that can be practically deployed is limited due to the longer wavelength.	A larger-scaled antenna array due to the shorten wavelength, facilitating advanced beamforming and massive MIMO techniques..
Propagation Characteristics	Less path loss. Rich multipath propagation. Better penetration through obstacles such as walls, buildings, etc.	More severe path loss due to the shorter wavelength. Only a few propagation paths with limited diffraction around obstacles. Poor penetration through obstacles, often requiring line-of-sight (LoS) conditions for performance optimization.
Spectral Efficiency and Bandwidth	High spectral efficiency due to the spatial multiplexing, but limited bandwidth availability.	Low spectral efficiency due to few serving users, servere path loss, and significant noise power, but bandwidth is abundant with channels up to several GHz wide.
Applications in MIMO Systems	Effective spatial multiplexing of tens of users, and the array gain and ability to separate users spatially lead to great capacity and reliability.	Generating highly directional beams due to smaller wavelengths, which greatly improves the link budget.
Deployment Scenario	Macro wide-area cells or indoor environment with support for high user mobility.	Small, high-capacity cells with low user mobility.

throughput applications [88]. Regarding antenna and array design, the number of antennas that can be practically deployed under sub-6 GHz is limited due to the longer wavelength, while a large-scaled antenna array is easier to be realized under mmWave due to the shorten wavelength. The propagation characteristics under different frequency bands can also be different. Particularly, sub-6 GHz channels suffer from less path loss compared to the channels under mmWave frequencies, allowing signals to travel longer distances. In addition, the sub-6 GHz radio wave is less affected by environmental factors such as rain, humidity, and atmospheric absorption, and attains better penetration through obstacles. Therefore, it is more reliable for various propagation conditions. By contrast, mmWave works under more severe path loss due to the shorter wavelength, which limits the propagation range. Furthermore, mmWave signals are highly sensitive to environmental factors, and can be easily blocked by obstacles. The mmWave bands provide significantly larger bandwidths, supporting much higher data rates compared to sub-6 GHz bands. While mmWave bands offer the promise of higher data rates, sub-6 GHz bands generally realize better spectral efficiency in practical deployment scenarios due to their favorable propagation characteristics and efficient spatial multiplexing capabilities. The spatial multiplexing capability of sub-6 GHz promotes its application in MIMO system, as it effectively separate UEs in spatial domain. On the other hand, mmWave bands support highly directional beams using large-scale antenna arrays. This beamforming capability helps compensate for severe path loss by focusing energy towards the intended receiver, improving QoS. Considering the distinctive characteristics of different frequency ranges, the sub-6 GHz is generally deployed in wide-area coverage or indoor environment with support for high user mobility, while mmWave is more suitable for high-capacity, short-range applications, such as dense urban areas, stadiums, and hotspots.

2.2.2 Channel Estimation

Channel estimation is a critical process in wireless communication systems, enabling the adaptation of transmission and reception techniques to current channel conditions. Although the fundamental principles of channel estimation are similar across different frequency bands, the methods and challenges vary significantly between sub-6 GHz and mmWave due to their distinct propagation characteristics and system requirements.

Generally, the sub-6 GHz channel is much richer in multi-path components with more diffuse scattering and more significant diffraction effects, which leads to a denser channel model. On the other side, mmWave channels experience high sparsity due to the directional nature of propagation and limited scattering. This sparsity characteristic is verified by measurements in [89], revealing that mmWave channels typically exhibit only 3-4 scat-

tering clusters in dense-urban non-line-of-sight (NLoS) environments. Consequentially, the traditional training-based channel estimation methods used in sub-6 GHz, such as the least-square estimation in time and frequency domain, seem to be not optimal under these sparse conditions due to the huge channel size [90]. Estimation techniques leveraging CS [91] and sparse recovery algorithms are then developed to exploit the sparse multi-path structure under mmWave frequencies. Specifically, CS tools address the problem of estimating the sparse signal by directly acquiring a compressive signal representation with a lot fewer number of samples than that required by the Shannon-Nyquist theorem, and from which the sparse signal can be recovered through an optimization process [92]. Another main challenge of channel estimation under mmWave bands arises from the hybrid beamforming, where the joint channel estimation for both the RF and baseband components is required. Unlike within the sub-6 GHz system where digital beamforming is mostly used, the hybrid beamforming in mmWave necessitates specialized algorithms that can handle the partitioned signal processing. The Divide-and-conquer approach [93], ping-pong approach [94], etc. were proposed for mmWave channel estimation with hybrid architecture. Moreover, hardware constraints including phase noise, non-linearity, etc., pilot overhead, and beam training scheme are all critical factors differing the channel estimation methods among sub-6 GHz and mmWave systems. On one side, sub-6 GHz systems deal with rich multi-path environments; on the other side, mmWave systems need to deal with sparse channels, directional beams, and more complex hybrid beamforming architectures. Consequently, specialized techniques and optimizations are necessary to effectively obtain CSI in each frequency band.

2.3 Overview of Convex Optimization

Convex optimization is a sub-field of optimization that focuses on problems where the objective function is convex and the feasible set is a convex set. This branch of optimization is particularly important due to its wide applicability and the robustness of its theoretical foundations.

Fig. 2.4 demonstrates the classic graph of a convex function. Particularly, we determine a function f as convex if $\mathbf{dom}\ f$ is a convex set and for all $x, y \in \mathbf{dom} f$, and θ with $0 \leq \theta \leq 1$, we have

$$f(\theta x + (1-\theta)y) \leq \theta f(x) + (1-\theta) f(y). \tag{2.12}$$

Note that a function is convex if and only if it is convex when restricted to any line that intersects its domain. In the following, we introduce convex optimization by reviewing linear and quadratic programming problem, followed by summarizing several technologies used to

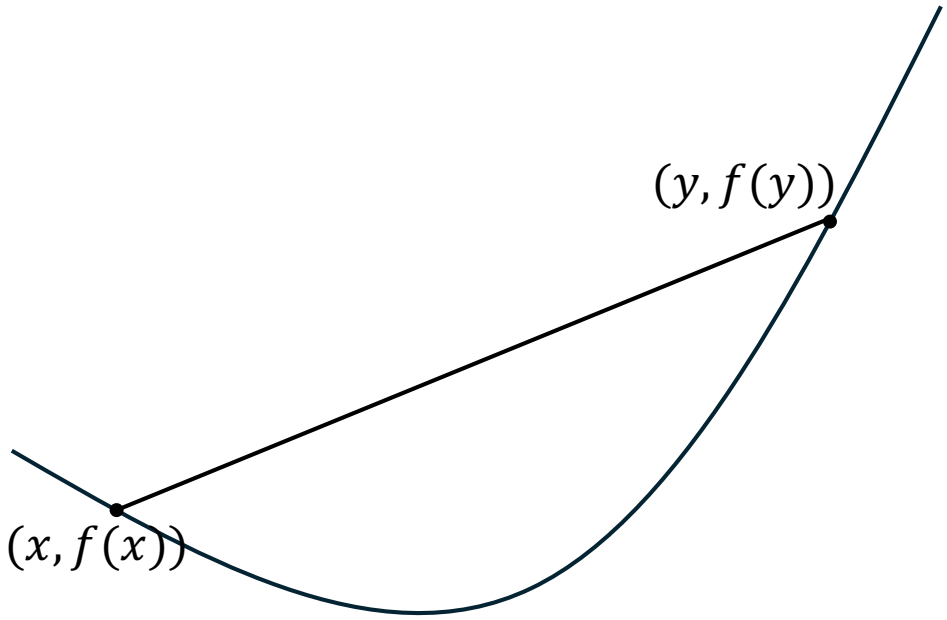

Figure 2.4: Graph of a convex function [7].

transfer the non-convex problem into convex form.

2.3.1 Linear Programming Problem

linear programming (LP) is a method to achieve the best outcome in a mathematical model whose requirements are represented by linear relationships. It is a powerful tool used in various fields such as economics, business, engineering, and military applications to optimize a certain objective, subject to a set of linear constraints.

Typically, a LP problem involves a linear function that needs to be maximized or minimized, several decision variables which determine the output of the objective function, a set of linear inequality or equation constraints that the decision variables must satisfy, and non-negativity restriction. Then, the general LP program can be expressed in the form of

$$\begin{aligned} \min_{\mathbf{x}} \quad & \mathbf{c}^T\mathbf{x} + d \\ \text{s.t.} \quad & \mathbf{A}\mathbf{x} \leq \mathbf{b}, \end{aligned} \tag{2.13}$$

where $\mathbf{x} \in \mathbb{C}^{N\times 1}$ is the vector of decision variables, $\mathbf{c} \in \mathbb{C}^{N\times 1}$ is the vector of coefficients for the objective function, $\mathbf{A} \in \mathbb{C}^{M\times N}$ is a matrix of coefficients for the constraints, $\mathbf{b}$ is a vector of the right-hand side values for the constraints, and d is a constant in the objective function, which can be omitted since it does not affect the optimal (or feasible) set.

Considering the linear property in both the objective function and the constraints, the LP problem can be easily solved by the graphical method, simplex method, interior-point

method, etc. There are some common applications of LP, such as resource allocation, production scheduling, and portfolio optimization. In all, the strength of LP lies in its ability to model real-world problems as linear relationships and solve them efficiently using well-established mathematical methods mentioned above and software tools such as MATLAB, LINGO, etc. Understanding and applying LP can lead to significant improvements in decision-making and resource management across diverse fields.

2.3.2 Quadratic Programming Problem

Quadratic programming (QP) is an optimization technique that extends LP by allowing for a quadratic objective function, which is suitable for applications in economics, finance, engineering, and various scientific fields where the relationships between variables are not strictly linear. The general form of a QP problem can be expressed as

$$\begin{aligned} \min_{\mathbf{x}} \quad & \tfrac{1}{2}\mathbf{x}^T\mathbf{Q}\mathbf{x} + \mathbf{c}^T\mathbf{x} + d \\ \text{s.t.} \quad & \mathbf{A}\mathbf{x} \leq \mathbf{b}, \end{aligned} \tag{2.14}$$

where $\mathbf{Q}$ is a symmetric matrix of coefficients for the quadratic terms. To ensure the convexity, $\mathbf{Q}$ is a positive semidefinite matrix. QP can be considered as a more general form of LP, while quadratically constrained quadratic program (QCQP) further extends QP by allowing both the objective function and the constraints to be quadratic. Particularly, the QCQP problem can be expressed in the form of

$$\begin{aligned} \min_{\mathbf{x}} \quad & \tfrac{1}{2}\mathbf{x}^T\mathbf{Q}_0\mathbf{x} + \mathbf{c}_0^T\mathbf{x} + d \\ \text{s.t.} \quad & \tfrac{1}{2}\mathbf{x}^T\mathbf{Q}_k\mathbf{x} + \mathbf{c}_k^T\mathbf{x} + d_k \leq 0, k = 1, \cdots, K, \end{aligned} \tag{2.15}$$

where $\mathbf{Q}_k$ is positive semidefinite for all $k = 1, \cdots, K$ to ensure the convexity.

Another kind of problem that is closely related to QP is the second-order cone program (SOCP), which can be seen as a generalization of QCQP with the added flexibility of second-order cone constraints. The general form of SOCP is

$$\begin{aligned} \min_{\mathbf{x}} \quad & \mathbf{c}_0^T\mathbf{x} + d_0 \\ \text{s.t.} \quad & \|\mathbf{A}_k\mathbf{x} + \mathbf{b}_k\|_2 \leq \mathbf{c}_k^T\mathbf{x} + d_k, k = 1, \cdots, K \\ & \mathbf{F}\mathbf{x} = \mathbf{g}. \end{aligned} \tag{2.16}$$

Particularly, when $\mathbf{c}_k = \mathbf{0}, \forall k = 1, \cdots, K$, the SOCP is equivalent to QCQP by squaring the constraints. Therefore, SOCP can be considered as the more general form of QCQP, as well as QP and LP.

2.3.3 Transformation from Non-convex to Convex Problem

Non-convex optimization problem represents the optimization problem where the objective function or the feasible region, or both, do not satisfy the convexity property. Examples of non-convex problems include user association [95], traveling salesman problem [96], neural network training [97], etc. Unlike convex problems, non-convex problems can have multiple local optima, making them more challenging to solve. In this section, we introduce several techniques which can effectively address the non-convexity, so that the robust and efficient solution methods available for convex problems can be leveraged.

Convex relaxation is a common technique used to transform the non-convex problem into convex form, which involves approximating a non-convex problem with a convex one by relaxing some constraints or modifying the objective function. A typical example of the relaxation could be transforming an integer program to LP by replacing the integer constraint $x \in \{0, 1\}$ with $0 \leq x \leq 1$. The semidefinite relaxation (SDR) is also an efficient approach to solve the non-convex problem [98]. In many non-convex quadratic optimization problems, we encounter a matrix $\mathbf{X}$ which is intended to be rank-one, i.e., $\mathbf{X} = \mathbf{x}\mathbf{x}^T$. This constraint ensures that $\mathbf{X}$ can be decomposed into the product of a vector and its transpose. However, the rank-one constraint is non-convex because convex combinations of rank-one matrices do not necessarily remain rank-one, due to the non-linearity of the rank function and the typical increase in rank when combining independent matrices. As a consequence, the problem is difficult to be solved directly. To deal with this, the non-convex rank-one constraint $\text{rank}(\mathbf{X}) = 1$ is dropped, allowing $\mathbf{X}$ to be any positive semidefinite matrix. Once the relaxed semidefinite programming (SDP) is solved, the resulting matrix $\bar{\mathbf{X}}$ is typically not rank-one. Eigenvalue decomposition, randomization technique, and other methods are sequentially used to approximate a rank-one solution from $\bar{\mathbf{X}}$.

Convex-concave procedure (CCP) is an iterative method to address the non-convex problem which can be decomposed into the sum of a convex and a concave part. In each iteration, the concave part is linearized around the current solution by applying techniques such as first-order Taylor expansion, leading to a convex sub-problem. For example, given convex functions $f(x)$ and $g(x)$, we formulate an objective function

$$\min_x f(x) - g(x). \tag{2.17}$$

The convexity property of the difference of two convex functions cannot be determined. We therefore iteratively approximate $g(x)$ by its first-order Taylor expansion around the current

solution x^t, which yields

$$\min_x f(x) - (g(x^t) + \nabla g(x^t)^T (x - x^t)). \tag{2.18}$$

Eq. (2.18) refers to the difference between a convex function and a linear function, where the linear function is defined as either a convex or concave function. Therefore, (2.18) is in a convex form. By iteratively updating x^t, the optimal solution can be finally obtained.

In addition to the convex relaxation and CCP, a change of variables or a transformation of the objective and constraint functions can also transform the non-convex into a convex form. geometric programming (GP) is a classic example which can be made convex by means of a change of variables [99]. Specifically, a GP is an optimization problem of the form

$$\begin{aligned} \min_x \quad & f_0(x) \\ \text{s.t.} \quad & f_i(x) \leq 1, i = 1, \cdots, m \\ & g_i(x) = 1, i = 1, \cdots, p. \end{aligned} \tag{2.19}$$

where f_i and g_i are generalized posynomials and monomials, respectively. By using the logarithmic change of variables $y = \log(x)$, the objective function and constraints become linear in the logarithmic variables, resulting in a convex optimization problem [100].

In conclusion, transforming non-convex problems into convex problems leverages various techniques such as convex relaxation, change of variables, and iterative procedures. These transformations enable the application of powerful convex optimization tools to address challenging non-convex issues, leading to more efficient and reliable solutions in practical applications.

2.4 Radiation Pattern of Antenna

The radiation pattern of an antenna is a graphical representation of the relative strength of the radiated electromagnetic field in different directions from the antenna. It describes how the antenna radiates energy into free space and has been widely investigated in radar and communication systems. In this section, we mainly introduce several characteristics which are used to shape the radiation pattern.

Typically, the radiation intensity is represented in either a 2D or three-dimensional (3D) graphical pattern. In 2D plots, the radiation intensity is often shown as a function of azimuth angle across the horizontal plane or elevation angle across the vertical plane. In 3D plots, the radiation intensity is shown as a function of both azimuth and elevation angles, providing a more comprehensive and practical view of the antenna's radiation characteristics. Without

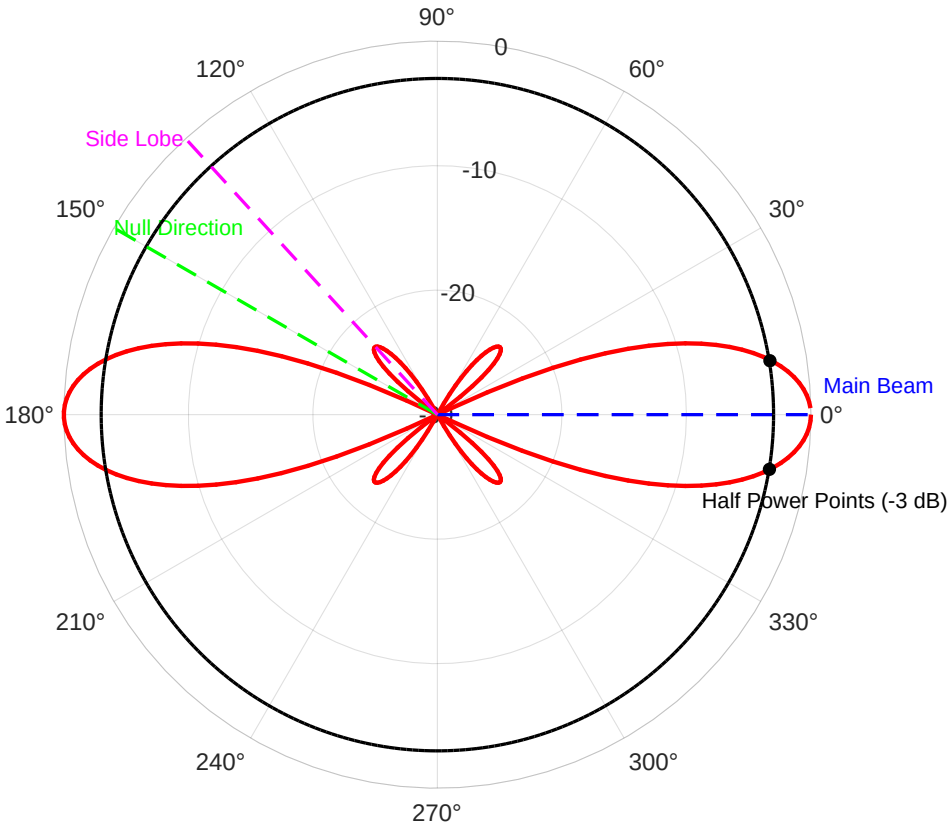

Figure 2.5: An example of the 2D polar radiation pattern.

loss of generality, we focus on the investigation of a 2D radiation pattern, while similar characteristics can be conducted to 3D patterns. Fig. 2.5 demonstrates an example of the 2D polar radiation pattern, which is generated by an array factor for ULA:

$$\mathrm{AF}(\theta) = \left|\frac{\sin(N\pi d \sin\theta)}{\sin(\pi d \sin\theta)}\right|^2, \tag{2.20}$$

where N denotes the number of array elements and d denotes the spacing between elements in wavelengths. The azimuth/elevation angle θ is uniformly distributed between 0 and 2π.

From Fig. 2.5, we can see the directivity, gain, beamwidth, and sidelobes levels jointly characterize the radiation pattern. Specifically, directivity is a fundamental antenna parameter that quantifies the concentration of radiated power in a particular direction compared to an isotropic source. Mathematically, directivity is defined as the ratio of the maximum radiation intensity to the average radiation intensity over all directions, which then generally transfers to dB form. Directivity can vary over several orders of magnitude. For example, a short dipole antenna has a typical directivity of only 1.76 dB [101], while the directivity of a horn antenna can be up to 10-20 dB [102]. The selection of antennas should be tailored to the specific requirements of different applications. For broadcasting, Wi-Fi routers, and other scenarios where transmitting or receiving energy from a wide variety of directions is required, antennas

with low directivity should be chosen. Conversely, remote sensing, satellite communications, and microwave links require a high directivity antenna in order to maximize power transfer and reduce signal from unwanted directions. Another key performance parameter which combines the antenna's directivity and radiation efficiency is gain. To be more specific, the gain is a unitless measure which is the product of the radiation efficiency and directivity, i.e., $G = \eta D$, where η is the radiation efficiency indicating the ratio of the total power radiated by an antenna to the net power accepted by the antenna from the connected transmitter [103], and D refers to the directivity. The gain describes how well the antenna converts between the radio waves and the power in a specific direction. When the direction is not specified, gain generally refers to the peak value of the gain in the direction of the antenna's main beam. The beamwidth of the radiation pattern indicates the angular separation between points where the radiation intensity drops to a certain fraction of the maximum radiation intensity. A narrower beamwidth indicates higher directivity, which is preferred in point-to-point communications. Inspired by the concept of beamwidth, HPBW is a critical metric, which is an angular width (in degrees) measured on the main lobe of an antenna radiation pattern at half-power points, i.e., the points at which the signal power is half that of its peak value. In other words, The HPBW is the angular separation in which the magnitude of the radiation pattern decreases by 50% (or -3 dB) from the peak of the main beam. HPBW concept serves several important purposes in antenna theory and design. One significant purpose is that HPBW helps to characterize the coverage area of the antenna, as it defines the angular range over which the antenna radiates significant power. The characterization of the coverage area is essential for designing and measuring communication systems. Moreover, HPBW provides a quantitative measure of the directivity of an antenna's radiation pattern. By determining the angular range of the main lobe where the radiated power drops from peak to half of the maximum value, HPBW offers insight into how focused or dispersed the antenna's radiation pattern is. In addition to directivity, gain, and beamwidth, the radiation pattern is also characterized by the sidelobes. The sidelobes are smaller beams that are away from the main beam. They are usually radiated in undesired directions which cannot be completely eliminated but can lead to several challenges and limitations. Specifically, the sidelobes incur severe interference with neighbouring communication systems, reduced signal strength in the desired direction, and security issues by unintentionally leaking or receiving signals in unintended directions. To mitigate the negative effects of sidelobes, various design methods, such as beamforming and adjusting the antenna aperture and element spacing, are used.

Overall, the directivity, gain, beamwidth, and sidelobes jointly build the antenna's radiation pattern. The study of the radiation pattern lays the foundation for designing more secure and efficient wireless communication systems.

2.5 State-of-the-Art in RIS

As a recent-developed promising technology in the coming 6G network, tremendous efforts is necessary for completing the detailed design of RIS. In this section, a literature review covering state-of-the-art investigations on the aforementioned topics in RIS-assisted systems is presented.

Beamforming is crucial to the operation of RIS-aided systems as it enhances signal quality, system capacity, energy efficiency, and more. Unlike traditional communication systems, the active beamforming at BSs and the passive beamforming at RISs should be jointly considered in a RIS-aided system. Beamforming in narrowband [104, 105] and wideband [106, 107] RIS-aided systems were both widely investigated. In [108], a hybrid beamforming architectures was studied in both RIS-aided narrowband and OFDM mmWave MIMO systems. Moreover, the authors in [109] aims at the secrecy capacity maximization via jointly optimizing the hybrid beamforming at BS and passive beamforming at RIS. In addition to the above works, research of beamforming in RIS-aided systems also focus on the practical RIS design. Particularly, a total achievable rate maximization problem was proposed in [110] by optimizing discrete RIS phase shift, which is more challenging compared with perfect continuous phase shift design due to the presence of discrete variables. While most works on RIS focused on the ideal phase shift model assuming full signal reflection, the authors in [111] proposed a practical phase shift model that captures the phase-dependent amplitude variation in the element-wise reflection design. Based on the proposed model a transmit power minimization problem was formulated by optimizing the active and passive beamforming. Additionally, the authors in [112] utilized the extended error vector magnitude (EEVM) model to characterize the impact of RF impairments at the BS and considered phase noise at the RIS. It is proved that the hardware impairments and phase noise affect beamforming design and could degrade spectral efficiency.

Acquiring CSI is the foundation for the design of various communication and radar systems for its importance in shaping the propagation environment. However, channel estimation in RIS-aided systems presents several challenges due to the unique nature of these systems and their operational environment, such as the intensive computational complexity caused by the large number of reflecting elements and the passive transmission and receiving capabilities. The machine learning (ML)-based approaches [56], CS [55], and iterative algorithms [113] were developed to improve the accuracy and efficiency of channel estimation in RIS-aided systems. Nevertheless, most state-of-the-art works have not been verified in practical deployment, where the wireless channels can be highly dynamic due to user mobility, environmental changes, and other factors. Furthermore, practical implementation of RIS comes

with hardware imperfections, such as phase noise, quantization errors, and non-linearities. These imperfections need to be accounted for in the channel estimation process as well. To address the aformentioned issues, recent research has investigated RIS-aided systems with incomplete CSI [114]. For example, the authors in [115] proposed a RIS phase shift design based on the statistical CSI and the formulated upper bound of the ergodic spectral efficiency. Additionally, a MISO system deploying distributed RISs was investigated in [116], where the achievable rate of the network was analyzed considering the CSI estimation error. Furthermore, a RIS-assisted anti-jamming communication scenario was proposed in [117]. Specifically, a robust RIS beamforming design was formulated to enhance the security performance with or without imperfect jammer's CSI.

Another trending topic in studying RIS is optimization. Optimization in RIS-aided systems is crucial for maximizing the performance and efficiency of wireless communication networks, while it also involves addressing complex problems. One of the main difficulties in optimizing the performance of RIS-aided systems is the coupling of multiple variables. For example, the authors in [118] proposed a joint optimization of sensing duration, passive beamforming, and 3D location in a cognitive UAV networks. As the variables are coupled, the overall achievable throughput maximization problem was divided into three subproblems, and an efficient alternating optimization algorithm was developed to obtain a high-quality suboptimal solution. In [119], the time delays was applied to RIS to address the beam squint problem in THz communication systems. A weighted sum rate maximization problem was sequentially formulated via joint optimization of the BS beamforming as well as RIS reflection coefficients and time delays. An alternate optimization algorithm was developed to divide the original optimization problem into three subproblems and solve them iteratively until convergence. In addition to the coupling issue, the non-convexity is another challenging factor in solving optimization problems in RIS-aided systems. The authors in [120] investigate a RIS-aided MISO system with SWIPT. For the purpose of maximizing the EE of the system, the transmit beamforming, the RIS reflective beamforming, and the power splitting ratios were jointly optimized, while considering the maximum transmit power budget, the RIS reflection constraints and the QoS requirements. To address the non-convex fractional objective function, the authors first applied the Dinkelbach method to convert it into a subtractive form. The successive convex approximation (SCA) as well as the SDR techniques were also developed to address the non-convexity. Moreover, the authors in [121] formulated a network SE maximization problem by jointly optimizing active beamforming at the BSs, passive beamforming at the RISs, and UE-BS association. This problem is challenging due to its intractable mixed-integer non-convex property. To solve this problem, a fractional programming technique is first used to optimize active and passive beamforming,

and a penalization method combined with SCA is then applied for the binary UE association optimization.

In RIS-aided systems, the radiation pattern is shaped by the intelligent control of the reflective elements on the RIS. Two critical metrics, the sidelobes and beamwidth, have been widely investigated in RIS-aided systems. The authors in [122] addressed the challenge of introducing RIS in secure directional modulation is that an additional beam, other than the user-specific beam, is required to align to the RIS, while the interaction between the two beams can cause high sidelobe. A novel cross-entropy iterative method was developed to achieve low-sidelobe hybrid beamforming for secure directional modulation in RIS-aided networks. Moreover, a multi-user coverage infill scenario was considered in [123], where the direct beam pattern synthesis method with superposition can result in undesirable sidelobe levels. Motivated by this fact, deep reinforcement learning was proposed to optimize the far-field pattern. Simulation results verified that a 4 dB reduction in the unwanted sidelobe levels can be realized, which sequentially leads to improved EE and decreased co-channel interference levels. Instead of generating directional beams as discussed in most works, a codebook of beams with variable width for the near field using a technique that maps the RIS elements to a tunable spherical surface was proposed in [124]. By properly tuning the size and center of the RIS, variable width beams and illuminated areas can be achieved. The authors in [125] illustrated that the maximization size of a RIS provides the adequate signal at a given location, while inevitably reducing the beamwidth and bandwidth of the radar cross section pattern. To address this issue, a shaped reflector profiled as a truncated ellipse that can give a widened “equi-ripple” beam was proposed. It is shown that by careful designing the phase profile, the beamwidth can be expanded by a factor of 3.5 with a corresponding increase in the useable bandwidth.

Chapter 3

On the Design of Broadbeam on RIS

Motivated by the fact that channel estimation is challenging in RIS-aided communication system, especially when the UE is with high mobility, in this chapter, we study the broad beamwidth design of RIS. We first investigate the generation of a single broadbeam with maximum and equal power gain within a pre-defined angular region given constraints of the unit modulus weights of RIS. We propose the DC-SDP algorithm to design the RIS passive beamforming. In addition, as important guidance of signal coverage for arbitrary angular regions, we mathematically derive the relationship between the angular range of the spatial sector and the maximum average received power. The upper bounds of the average received power with different RIS configurations are also obtained, where ULA and URA are considered. Then, we focus on the generation of multiple broadbeams, which can be applied in cellular networks, broadcasting, and radar systems, enabling multiple wide null and illumination at arbitrary directions. We minimize the deviation between the target pattern and the practical power pattern by designing the passive beamforming at RIS. The low-complexity ADMM algorithm is proposed.

3.1 Introduction

Since the acquired CSI in an RIS-aided system is often inaccurate and entails complex estimation algorithms, current research has been devoted to the study of robust beamforming [126, 127]. Robust beamforming techniques hold promise for handling the uncertainties typically encountered in channel estimation. The broadbeam can be seen as a form of “implicit robustness", sacrificing some beamforming gain to ensure broader coverage, which mitigates the impact of CSI errors. Specifically, as a low-cost and passive device, it is more realistic to use RIS to generate broadbeam, which could cover an angular region instead of locating UEs with real-time beam tracking or CSI, largely reducing computational complexity. In

addition, broadbeam design is also rewarding and beneficial for coverage enhancement. Furthermore, the design and implementation of the broadbeam can be simpler compared to the narrow-beam antenna system, as there is no need to steer the beam towards a specific direction precisely. This can lead to reduced complexity and much lower cost and henceforth, is more suitable to be deployed in practice. Specifically, in broadbeam design, the average received power and variance are generally considered as two critical metrics to measure the designed system. On one side, the average received power reflects the average QoS of all UEs in a specific area; the variance of the beam pattern, on the other side, validates the communication stability for UEs in movements. Therefore, this thesis focuses on the generation of broadbeam, where the average received power and the variance of the beam pattern are numerically analyzed.

To the best of our knowledge, there are only a few works investigating broadbeam design via RIS so far. For example, the authors in [128] proposed a RIS-aided downlink transmission where the reflection link is used to illuminate the area centred around the mobile UE. However, they only focused on the cover area but not the flatness of the generated beam pattern, which may lead to unstable data transmission. Motivated by this fact, the authors in [129] proposed a novel 3D beam broadening and flattening technique on an aerial intelligent reflecting surface (AIRS), where the AIRS is divided into several sub-arrays. By synthesizing the beams generated by each sub-array, a broad and flat beam could be achieved. However, the beamwidth could be restricted, especially when a small RIS is applied. In [130], a design framework to synthesize the power pattern reflected by the RIS was proposed, which meets the customized requirements of broad coverage and considers the flatness of the generated beams. An arbitrarily defined beamwidth at the RIS could be realized. However, the flat broadbeam is realized by minimizing the difference between the target pattern and the optimized pattern, where the average received power and variance of the beam pattern were not investigated.

To address the aforementioned issues, we propose the blind coverage enhancement design, where signals with comparable received power are received by UEs at arbitrary places in pre-defined sector areas without knowing their precise directions. We illustrate the utility and superiority of our design for the following several reasons. Firstly, in this broadbeam-enhanced area coverage way, where a flat broadbeam is generated to cover a whole range instead of one specific UE, the issue caused by the UE's position changes can be solved well. Besides, RIS with the flat broadbeam design is not required to respond in real-time to UEs' movements, which could largely reduce the hardware cost as well as computational complexity. Furthermore, the possible active area of UEs is generally pre-known; the increase in SNR and the improvement in QoS could be enhanced by proposing the pre-defined area

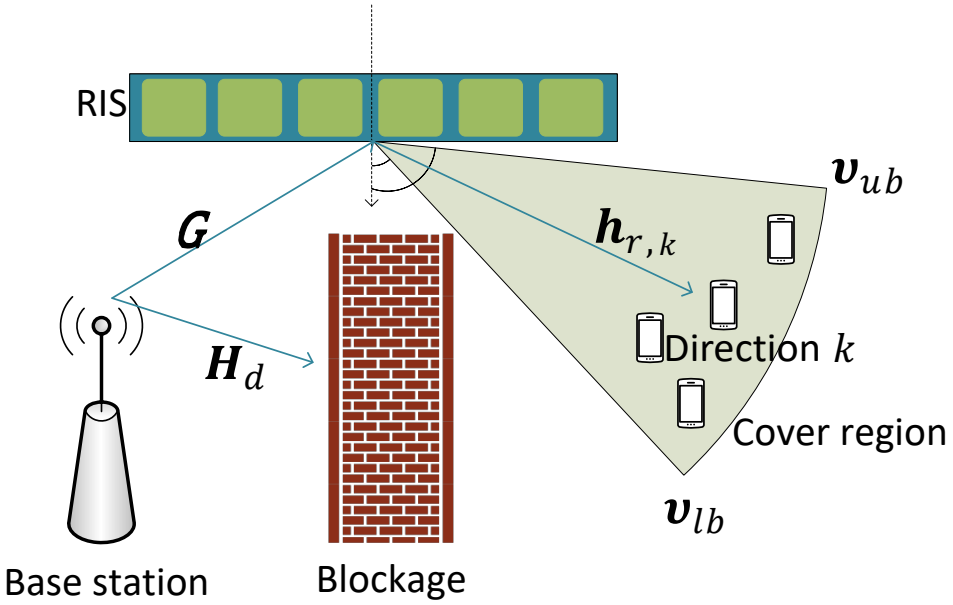

Figure 3.1: System model of RIS-aided flat broadbeam design for K random directions.

coverage enhancement design. Additionally, the SNR is further improved by maximizing the signals' received power within the pre-defined area or suppressing signals towards unwanted directions.

In summary, the flat broadbeam design is well-suited for various applications, such as cellular communication, satellite broadcasting, and Wi-Fi networks, where wide coverage and robust performance are essential. Besides, the role of this design in establishing connections between RIS and UEs can be regarded as an initial step for other channel estimation algorithms.

3.2 Generation of a Single Broadbeam

We first investigate the generation of a single broadbeam with a flattened top and maximized average power within an arbitrary angular region. As an important metric to measure QoS, the relationship between the average received power and the phase shifts of RIS is analytically obtained. Specifically, we obtain the upper bound of the average received power given RIS under both URA and ULA configurations. To derive the flat broadbeam, the DC-SDP algorithm is introduced for RIS passive beamforming optimization.

3.2.1 System Model

We model a RIS-aided downlink system[1] as illustrated in Fig. 3.1. For a single user, K random directions in the set $\mathcal{K}$ are chosen within the pre-defined area, which is constrained by $\varphi_{\{lb,ub\}}$ and $\theta_{\{lb,ub\}}$. Specifically, $\varphi_{\{lb,ub\}}$ and $\theta_{\{lb,ub\}}$ refer to horizontal and vertical lower and upper boundary angles of the cover region. We sequentially integrate $\upsilon_{lb} = [\varphi_{lb}, \theta_{lb}]$ and $\upsilon_{ub} = [\varphi_{ub}, \theta_{ub}]$. The BS is implemented with N antennas. And the proposed RIS contains M reflecting elements. In addition, UEs with a single antenna are assumed. Reflective links $\mathbf{h}_{r,k} \in \mathbb{C}^{M\times 1}, \forall k \in \mathcal{K}$ are built to assist the BS in transmitting signals to multiple UEs within a sector area. Moreover, the BS-RIS and BS-UE channels are denoted as $\mathbf{G} \in \mathbb{C}^{M\times N}$ and $\mathbf{H}_d = [\mathbf{h}_{d,1}, \cdots, \mathbf{h}_{d,k}, \cdots, \mathbf{h}_{d,K}] \in \mathbb{C}^{N\times K}$, respectively. We assume that the system works on the sub-6 GHz frequency band. The direct link $\mathbf{h}_{d,k}$ follows Rayleigh fading, while RIS-aided channels $\mathbf{h}_{r,k}$ and $\mathbf{G}$ follow Rician fading. Then, these channels are modelled as

$$\mathbf{h}_{d,k} = \mathrm{PL}_{\mathrm{NLoS}}\overline{\mathbf{h}}_{d,k}, \tag{3.1}$$

$$\mathbf{h}_{r,k} = \mathrm{PL}_{\mathrm{LoS},k}\left(\sqrt{\frac{\varepsilon}{\varepsilon+1}}\boldsymbol{a}(\boldsymbol{\zeta}_{RO,k}) + \sqrt{\frac{1}{\varepsilon+1}}\overline{\mathbf{h}}_{r,k}\right), \tag{3.2}$$

$$\mathbf{G} = \mathrm{PL}_{\mathrm{LoS},0}\left(\sqrt{\frac{\varepsilon}{\varepsilon+1}}\boldsymbol{a}(\boldsymbol{\zeta}_{RI})\boldsymbol{a}^H(\boldsymbol{\zeta}_{BS}) + \sqrt{\frac{1}{\varepsilon+1}}\overline{\mathbf{G}}\right). \tag{3.3}$$

Specifically, $\mathrm{PL}_{\mathrm{NLoS}}$, $\mathrm{PL}_{\mathrm{LoS},k}$ and $\mathrm{PL}_{\mathrm{LoS},0}$ denote the corresponding path-loss. ε is the Rician factor. $\overline{\mathbf{h}}_{d,k}$, $\overline{\mathbf{h}}_{r,k}$, and $\overline{\mathbf{G}}$ denote the NLoS components of channels, each element of which follows $\mathcal{CN}(0,1)$. In addition, $\boldsymbol{a}(\boldsymbol{\zeta})$ denotes the steering vector as a function of the spatial information $\boldsymbol{\zeta}$ [131], which is represented as

$$\boldsymbol{a}(\boldsymbol{\zeta}) = e^{j\frac{2\pi d}{\lambda}\boldsymbol{\zeta}}. \tag{3.4}$$

Note that $\boldsymbol{\zeta}$ can follow either ULA or URA configuration. Moreover, $\boldsymbol{\zeta}_{RO,k}$, $\boldsymbol{\zeta}_{RI}$, and $\boldsymbol{\zeta}_{BS}$ are the functions of the angle of departure (AOD) towards the UE at the k-th direction, angle of arrival (AOA) at RIS and AOD at BS towards RIS, respectively. Specifically, we consider the URA configuration for both BS and RIS in our proposed system, then $\boldsymbol{\zeta}_{RO,k}$, $\boldsymbol{\zeta}_{RI}$, and $\boldsymbol{\zeta}_{BS}$ can be generalized as $\boldsymbol{\zeta} = f(\varphi, \theta)$, where φ and θ refer to the azimuth and elevation angle, respectively. Fig. 3.2 shows the RIS model under URA configuration. Assume that there are M_y elements along the Y-axis and M_z elements along the Z-axis, then we have $M = M_y M_z$. In addition, we denote the azimuth angle $\varphi_{i,m}$ and elevation angle $\theta_{i,m}$ as the incident angles

[1]The system model is presented in 2D for simplicity, which can be easily extended to the general 3D model.

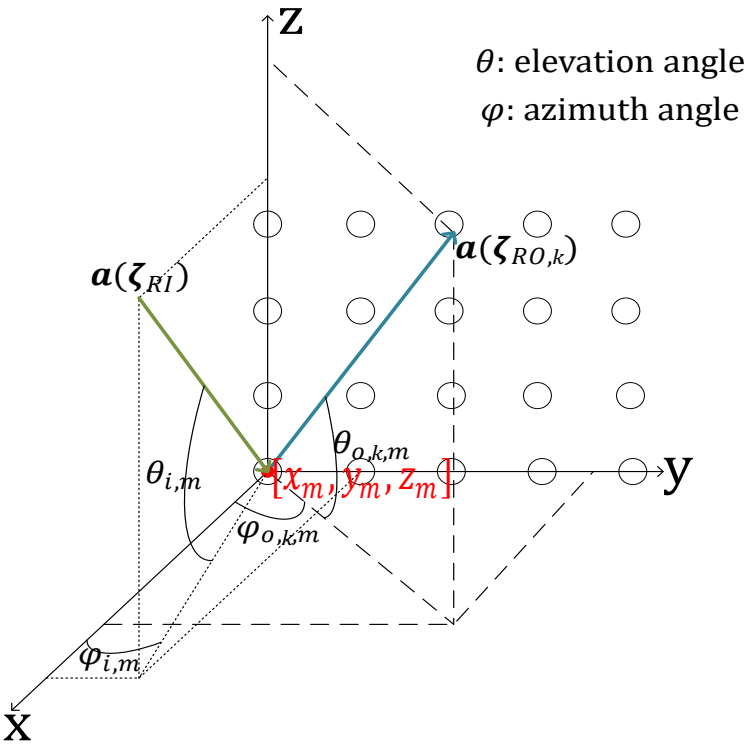

Figure 3.2: 2D RIS under URA configuration in 3D geometry axis.

at the m-th element, and $\varphi_{o,k,m}$ and $\theta_{o,k,m}$ as the azimuth and elevation reflection angles at the m-th element in RIS. Note that m has a relationship with m_y and m_z as $m = (m_y - 1)M_z + m_z$, where $m_y \in \{1, \cdots, M_y\}$, $m_z \in \{1, \cdots, M_z\}$. The angle information $\zeta_{RI,m}$ and $\zeta_{RO,k,m}$ at the m-th element could be sequentially represented as

$$\zeta_{RI,m} = (m_y - 1)\cos\theta_{i,m}\sin\varphi_{i,m} + (m_z - 1)\sin\theta_{i,m}, \tag{3.5}$$

$$\zeta_{RO,k,m} = (m_y - 1)\cos\theta_{o,k,m}\sin\varphi_{o,k,m} + (m_z - 1)\sin\theta_{o,k,m}. \tag{3.6}$$

Similarly, the BS is modelled under the URA configuration on the x-y plane. We assume N_x elements along the X-axis and N_y elements along the Y-axis, where $N = N_x N_y$. φ_n and θ_n denote the azimuth and elevation angles from the n-th element of BS, respectively. The angle spatial information $\zeta_{BS,n}$ at the n-th element can be expressed as

$$\zeta_{BS,n} = (n_x - 1)\cos\theta_n\cos\varphi_n + (n_y - 1)\cos\theta_n\sin\varphi_n, \tag{3.7}$$

where $n = (n_x - 1)N_y + n_y$, $n_x \in \{1, \cdots, N_x\}$, $n_y \in \{1, \cdots, N_y\}$.

Let $\boldsymbol{w} = [w_1, w_2, ..., w_M]^H$ denotes the weight vector of the RIS and each element $w_m, m = 1, 2, ..., M$ could be expressed as $w_m = \beta_m e^{j\alpha_m}$. For maximum reflecting efficiency, we let $\beta_m = 1$ and $\alpha_m \in [0, 2\pi]$. And the transmit beamforming vector at BS is $\mathbf{b} \in \mathbb{C}^{N\times 1}$. Then, the

received signal at the k-th direction could be expressed as

$$y_k = (\mathbf{h}_{d,k}^H + \mathbf{h}_{r,k}^H \boldsymbol{W}\mathbf{G})\mathbf{b}\sqrt{p_t}s + n_k,\ \forall k \in \mathcal{K}, \tag{3.8}$$

where $\boldsymbol{W} = \text{diag}(\boldsymbol{w}^T) \in \mathbb{C}^{M\times M}$ and n_k is the additive white Gaussian noise (AWGN) with zero mean and variance σ_n^2, i.e., $n_k \sim \mathcal{CN}(0, \sigma_n^2)$. Additionally, p_t denotes the transmit power at the BS. Therefore, the received power at the k-th direction could be expressed as

$$p_k = |(\mathbf{h}_{d,k}^H + \mathbf{h}_{r,k}^H \boldsymbol{W}\mathbf{G})\mathbf{b}|^2 p_t + \sigma_n^2,\ \forall k \in \mathcal{K}. \tag{3.9}$$

Based on the expression of the received power at the k-th direction, we formulate the optimization problem in the following subsection.

We propose the novel design of a perfect flat broadbeam with equal received power at all directions within the pre-defined cover region, which could be interpreted as

$$\begin{aligned} \text{(P3-1):}\quad \max_{\boldsymbol{w},\mathbf{b}}\quad & \Xi \\ \text{s.t.}\quad & p_k = \Xi,\ \forall k \in \mathcal{K} \\ & |w_m| = 1,\ m = 1, \cdots, M, \end{aligned} \tag{3.10}$$

where Ξ is defined as the average received power within the cover region. By solving (P3-1), a broadbeam with a flattened top and maximized average received power could be realized given the RIS unit modulus weights constraints.

By proposing the flat broadbeam design, UEs' received power can always be guaranteed without knowing their precise directions, and beam tracking is not required. Additionally, the investigation of flat broadbeam is crucial to realize the maximum sum rate, which enables the same received power along all directions. Specifically, based on the expression of the received power, the SNR for the UE at the k-th direction could be expressed as

$$\text{SNR}_k = \frac{|(\mathbf{h}_{d,k}^H + \mathbf{h}_{r,k}^H \boldsymbol{W}\mathbf{G})\mathbf{b}|^2 p_t}{\sigma_n^2},\ \forall k \in \mathcal{K}. \tag{3.11}$$

Sequentially, we represent the sum-rate of the chosen K directions between the cover range υ_{lb} and υ_{ub} as

$$R_{total} = \sum_{k=1}^{K} \log_2(1 + \text{SNR}_k). \tag{3.12}$$

Moreover, we assume that the total received power of all directions within the cover region

$[\upsilon_{lb}, \upsilon_{ub}]$ is denoted as P_{total}, which could be represented as

$$P_{total} = \sum_{k=1}^{K} (|(\mathbf{h}_{d,k}^H + \mathbf{h}_{r,k}^H \boldsymbol{\Psi} \mathbf{G})\mathbf{b}|^2 p_t + \sigma_n^2). \tag{3.13}$$

Note that K should be sufficiently large to approximate that the received power at an arbitrary direction within the cover region $[\upsilon_{lb}, \upsilon_{ub}]$ equals the average received power. We further rewrite (3.12) as

$$R_{total} = \log_2(\prod_{k=1}^{K}(1 + \mathrm{SNR}_k)). \tag{3.14}$$

According to the Cauchy–Schwarz inequality [132], the following lemma can be derived.

Lemma 1: *For several variables denoted as $x_1, \cdots, x_N$ with fixed sum value, i.e., $x = x_1 + \cdots + x_N$, the maximum multiplication result can be achieved when and only when $x_1 = \cdots = x_N$.*

Based on **Lemma 1**, we can safely draw the conclusion that the maximum sum rate could be realized when

$$p_k = \Xi, \ \forall k \in \mathcal{K}. \tag{3.15}$$

In detail, the maximum sum rate can be realized when signals with the same received power are received by all directions within the pre-defined cover region.

3.2.2 Analysis on Average Received Power

In order to evaluate the average received power within a pre-defined angular region, which is considered as an important metric to measure the performance of communications, some characteristics of the maximum average power based on the cover area are proposed in this section. Besides, an upper bound of the maximum average received power is derived for an arbitrary cover region.

We consider BS applying MRT for maximal power transmission towards RIS, as the direct link suffers from serious channel fading and comprises only NLoS paths. Then we have $\mathbf{b} = \boldsymbol{a}^*(\boldsymbol{\zeta}_{BS})$. Moreover, the unit transmit power is assumed at the BS. Sequentially, the received power at the k-th direction [2] can be approximated as

$$p_k \approx |\boldsymbol{a}^H(\boldsymbol{\zeta}_{RO,k}) \boldsymbol{\Psi} \boldsymbol{a}(\boldsymbol{\zeta}_{RI})|^2, \ \forall k \in \mathcal{K}. \tag{3.16}$$

By applying the change of variables $\boldsymbol{\gamma}_k = \boldsymbol{a}(\boldsymbol{\zeta}_{RO,k}) \odot \boldsymbol{a}(\boldsymbol{\zeta}_{RI}) \in \mathbb{C}^{M \times 1}$, we reformulate (3.16)

[2] To be noted that in the subsequent derivation, we omit the noise in the expression of the received power, as the noise power is usually very low and will not affect the flatness of the generate beam over time scale.

as

$$p_k = |\boldsymbol{w}^H \boldsymbol{\gamma}_k|^2, \ \forall k \in \mathcal{K}. \tag{3.17}$$

We further define $\boldsymbol{Q}_k = \boldsymbol{\gamma}_k \boldsymbol{\gamma}_k^H \in \mathbb{C}^{M \times M}$, then (3.17) is equivalent to

$$p_k = \boldsymbol{w}^H \boldsymbol{Q}_k \boldsymbol{w}, \tag{3.18}$$

which can be transformed as $\boldsymbol{w}^H \boldsymbol{Q}_k \boldsymbol{w} = \mathrm{Tr}(\boldsymbol{Q}_k \boldsymbol{w}\boldsymbol{w}^H), \forall k \in \mathcal{K}$. The matrix lifting technique [133] is used to lift the original vector $\boldsymbol{w}$ as a positive positive semi-definite (PSD) matrix $\mathbf{X}$, which equals the multiplication of $\boldsymbol{w}$ and its corresponding conjugate transpose, i.e., $\mathbf{X} = \boldsymbol{w}\boldsymbol{w}^H$, where $\mathrm{rank}(\mathbf{X}) = 1$ and $\mathbf{X} \succeq 0$. Given $|w_m| = 1, m = 1, 2, ..., M$, $\mathbf{X}$ has to additionally satisfy $\mathrm{Diag}(\mathbf{X}) = \mathbf{1}_M$. Then, the expression for p_k can be equivalently reformulated as

$$p_k = \mathrm{Tr}(\boldsymbol{Q}_k \mathbf{X}), \ \forall k \in \mathcal{K}. \tag{3.19}$$

In terms of (3.19), the average received power in all directions could be expressed as

$$\Xi = \mathbb{E}\{\mathrm{Tr}(\boldsymbol{Q}_k \mathbf{X})\}, \ \forall k \in \mathcal{K}, \tag{3.20}$$

where $\mathbf{X}$ is the PSD matrix of RIS phase shifts, which is independent of received direction and can be fixed once RIS phase shifts are all determined. Then, (3.20) can be equivalently written as

$$\Xi = \mathrm{Tr}(\mathbb{E}\{\boldsymbol{Q}_k\}\mathbf{X}), \ \forall k \in \mathcal{K}. \tag{3.21}$$

We expand the expression of $\boldsymbol{\gamma}_k$ as

$$\boldsymbol{\gamma}_k = [\gamma_{k,11}, \cdots, \gamma_{k,1M_z}, \cdots, \gamma_{k,p_y p_z}, \cdots, \gamma_{k,M_y M_z}], \tag{3.22}$$

where $p_y = 1, \cdots, M_y$ and $p_z = 1, \cdots, M_z$. Similarly, we have $q_y = 1, \cdots, M_y$ and $q_z = 1, \cdots, M_z$. Then $\boldsymbol{Q}_k$ can be expressed as (3.23), which is shown on the top of next page.

We denote $\mathbb{E}\{\boldsymbol{Q}_k\}$ as $\boldsymbol{\Upsilon} \in \mathbb{C}^{M \times M}$, then the average received power could be expressed as

$$\begin{aligned} \Xi = \ & \underbrace{\boldsymbol{\Upsilon}(1,1)\mathbf{X}(1,1) + \cdots, + \boldsymbol{\Upsilon}(1,M)\mathbf{X}(M,1)}_{M} + \underbrace{\cdots}_{M(M-2)} \\ & + \underbrace{\boldsymbol{\Upsilon}(M,1)\mathbf{X}(1,M) + \cdots, \boldsymbol{\Upsilon}(M,M)\mathbf{X}(M,M)}_{M}. \end{aligned} \tag{3.24}$$

$$\boldsymbol{Q}_k = \begin{bmatrix} \gamma_{k,11}\gamma_{k,11}^H & \cdots & \gamma_{k,11}\gamma_{k,1M_z}^H & \cdots & \gamma_{k,11}\gamma_{k,q_yq_z}^H & \cdots & \gamma_{k,11}\gamma_{k,M_y1}^H & \cdots & \gamma_{k,11}\gamma_{k,M_yM_z}^H \\ \vdots & \ddots & & & & & & & \vdots \\ \gamma_{k,1M_z}\gamma_{k,11}^H & \cdots & \gamma_{k,1M_z}\gamma_{k,1M_z}^H & \cdots & \gamma_{k,1M_z}\gamma_{k,q_yq_z}^H & \cdots & \gamma_{k,1M_z}\gamma_{k,M_y1}^H & \cdots & \gamma_{k,1M_z}\gamma_{k,M_yM_z}^H \\ \vdots & & & \ddots & & & & & \vdots \\ \gamma_{k,p_yp_z}\gamma_{k,11}^H & \cdots & \gamma_{k,p_yp_z}\gamma_{k,1M_z}^H & \cdots & \gamma_{k,p_yp_z}\gamma_{k,q_yq_z}^H & \cdots & \gamma_{k,p_yp_z}\gamma_{k,M_y1}^H & \cdots & \gamma_{k,p_yp_z}\gamma_{k,M_yM_z}^H \\ \vdots & & & & & \ddots & & & \vdots \\ \gamma_{k,M_y1}\gamma_{k,11}^H & \cdots & \gamma_{k,M_y1}\gamma_{k,1M_z}^H & \cdots & \gamma_{k,M_y1}\gamma_{k,q_yq_z}^H & \cdots & \gamma_{k,M_y1}\gamma_{k,M_y1}^H & \cdots & \gamma_{k,M_y1}\gamma_{k,M_yM_z}^H \\ \vdots & & & & & & & \ddots & \vdots \\ \gamma_{k,M_yM_z}\gamma_{k,11}^H & \cdots & \gamma_{k,M_yM_z}\gamma_{k,1M_z}^H & \cdots & \gamma_{k,M_yM_z}\gamma_{k,q_yq_z}^H & \cdots & \gamma_{k,M_yM_z}\gamma_{k,M_y1}^H & \cdots & \gamma_{k,M_yM_z}\gamma_{k,M_yM_z}^H \end{bmatrix} \tag{3.23}$$

Both $\boldsymbol{\Upsilon}$ and $\mathbf{X}$ are Hermitian matrices, we can henceforth derive that

$$\boldsymbol{\Upsilon}(p,q)\mathbf{X}(q,p) + \boldsymbol{\Upsilon}(q,p)\mathbf{X}(p,q) = 2\mathscr{R}e\{\boldsymbol{\Upsilon}(p,q)\mathbf{X}(q,p)\}, \tag{3.25}$$

where both p and $q = 1, \cdots, M$. Note that p_y/q_y and p_z/q_z contain the placement information of the p/q-th elements in RIS. The average received power could be reformulated as

$$\Xi = 2\sum_{p=1}^{M}\sum_{q=p+1}^{M}\mathscr{R}e\{\boldsymbol{\Upsilon}(p,q)\mathbf{X}(q,p)\} + \sum_{q=1}^{M}\mathscr{R}e\{\boldsymbol{\Upsilon}(q,q)\mathbf{X}(q,q)\}. \tag{3.26}$$

Because the positions of BS and RIS are generally fixed, the transmission paths between BS and RIS are pre-known. As a consequence, the steering vector $\boldsymbol{a}(\boldsymbol{\zeta}_{RI})$ is fixed. In addition, we assume that the distance between BS and RIS is much longer than the element spacing in RIS, based on which we have $\theta_i = \theta_{i,m}, \varphi_i = \varphi_{i,m}, \forall m \in M$. Then, we define

$$\psi_y = \cos\theta_i \sin\varphi_i, \tag{3.27}$$

$$\psi_z = \sin\theta_i. \tag{3.28}$$

The spatial information incident at the m-th element of RIS can be sequentially expressed as

$$\boldsymbol{\zeta}_{RI,m} = (m_y - 1)\psi_y + (m_z - 1)\psi_z. \tag{3.29}$$

Additionally, we assume that the element spacing equals half wavelength, i.e., $d = \lambda/2$. Then, for the URA case, $\boldsymbol{\Upsilon}(p,q)$ as the function of θ_{lb}, θ_{ub}, φ_{lb}, and φ_{ub} can be expressed as

$$\boldsymbol{\Upsilon}(p,q) = \frac{\int_{\theta_{lb}}^{\theta_{ub}}\int_{\varphi_{lb}}^{\varphi_{ub}} e^{j\pi\iota} d\varphi d\theta}{(\theta_{ub} - \theta_{lb})(\varphi_{ub} - \varphi_{lb})}, \tag{3.30}$$

where $\iota = [(p_y - q_y)(\cos\theta\sin\varphi + \psi_y) + (p_z - q_z)(\sin\theta + \psi_z)]$.

Note that the direct integral of the angle ranges will be challenging, especially when both θ and φ are variables. We then discuss the average received power Ξ in the following three special cases:

A. When $\theta_{o,k,m}$ is a fixed value, $\varphi_{o,k,m} \in (-90°, 90°)$, $m = 1, \cdots, M$:

Assume that the elevation angle $\theta_{o,k,m}$ is fixed to be a constant angle $\overline{\theta}$, then (3.6) can be rewritten as

$$\zeta_{RO,k,m} = (m_y - 1)\cos\overline{\theta}\sin(\varphi_{o,k,m}) + (m_z - 1)\sin\overline{\theta}. \tag{3.31}$$

As the direct integral over the angle $\varphi_{o,k,m}$ can be challenging, we map $\tau_{lb} = \sin(\varphi_{lb})$ and $\tau_{ub} = \sin(\varphi_{ub})$, and the variable τ follows uniform distribution over the pre-defined cover region in terms of $[\tau_{lb}, \tau_{ub}]$. Then, the certain element $\Upsilon(p, q)$ can be approximated as [134]

$$\Upsilon(p,q) = \frac{\int_{\tau_{lb}}^{\tau_{ub}} A_p A_q^H \, d\tau}{\tau_{ub} - \tau_{lb}}, \tag{3.32}$$

where $A_{\{i=p,q\}} = e^{j\pi(\zeta_{RI,i} + \zeta_{RO,i})}$.

Moreover, $\zeta_{RO,i}$ originated from (3.31), k is eliminated as the continuous integral is considered over the cover region $[\tau_{lb}, \tau_{ub}]$ in (3.32). We expand the integral term, and (3.32) can be further expressed as

$$\Upsilon(p,q) = \begin{cases} \xi, & p_y = q_y, \\ \frac{e^{j\pi(p_y - q_y)\cos\overline{\theta}\tau_{ub}} - e^{j\pi(p_y - q_y)\cos\overline{\theta}\tau_{lb}}}{j\pi(p_y - q_y)(\tau_{ub} - \tau_{lb})\cos\overline{\theta}}\xi, & p_y \neq q_y, \end{cases} \tag{3.33}$$

where $\xi = e^{j\pi[(p_y - q_y)\psi_y + (p_z - q_z)(\sin\overline{\theta} + \psi_z)]}$.

When the full cover of the azimuth angle from $-90°$ to $90°$ is considered, i.e., $\tau_{lb} = -1$ and $\tau_{ub} = 1$, it should be noticed that

$$\Upsilon(p,q) = \frac{\sin(\pi(p_y - q_y)\cos\overline{\theta})}{\pi(p_y - q_y)\cos\overline{\theta}} \cdot \xi, \tag{3.34}$$

when $p_y \neq q_y$. Particularly, when the elevation angle $\overline{\theta} = 0$, we have

$$\Upsilon(p,q) = \begin{cases} e^{j\pi(p_z - q_z)\psi_z}, & p_y = q_y, \\ 0, & p_y \neq q_y. \end{cases} \tag{3.35}$$

Then, the average received power Ξ could be expressed as

$$\Xi = \sum_{p_y=q_y} \Upsilon(p,q)\mathbf{X}(q,p). \tag{3.36}$$

From (3.23), we can get that M_z elements in each row of $\boldsymbol{Q}_k \in \mathbb{C}^{M_y M_z \times M_y M_z}$ meet the condition $p_y = q_y$. Therefore, there are $M_y M_z^2$ elements in $\Upsilon = \mathbb{E}\{\boldsymbol{Q}_k\}$ satisfying $\Upsilon(p,q) \neq 0$. The following corollary can be sequentially obtained.

Corollary 1: *The upper bound of the average received power is reached when* $w_{m_y,m_z} = e^{j\pi m_z \psi_z}$. *The upper bound across the azimuth domain denoted as* $\hat{\Xi}_\varphi$ *can be obtained as*

$$\hat{\Xi}_\varphi = M_y M_z^2. \tag{3.37}$$

To be noted, the integral is taken over the mapped sin function τ of the directions, as the direct integral over $\varphi_{o,k,m}$ can be challenging. The variable chosen criterion is to find sufficient random directions which are non-overlapping and could well represent the predefined cover region. Indeed, integrals taken over the mapped sin function τ and the direction φ by applying the Riemann sum approximation method [135] result in the same average received power. See proof in APPENDIX A.1.

B. When $\varphi_{o,k,m}$ is fixed, $\theta_{o,k,m} \in (-90°, 90°)$, $m = 1, \cdots, M$:

Assume that $\varphi_{o,k,m}$ is fixed as $\varphi_{o,k,m} = \overline{\varphi}$, then (3.6) can be rewritten as

$$\zeta_{RO,k,m} = (m_y - 1)\cos(\theta_{o,k,m})\sin\overline{\varphi} + (m_z - 1)\sin(\theta_{o,k,m}). \tag{3.38}$$

We define $\nu_{ub} = \sin(\theta_{o,ub})$ and $\nu_{lb} = \sin(\theta_{o,lb})$, which contains the phase information of the boundary of the cover region. Similar to (3.32), we can get the expression for a certain element in $\Upsilon(p,q)$ as

$$\Upsilon(p,q) = \frac{\int_{\nu_{lb}}^{\nu_{ub}} Z_p \cdot Z_q \, d\nu}{\nu_{ub} - \nu_{lb}}, \tag{3.39}$$

where $Z_{\{i=p,q\}} = e^{j\pi((p_y-1)(\pm\sqrt{1-\nu^2}\sin\overline{\varphi}+\psi_y)+(p_z-1)(\nu+\psi_z))}$.

As the integral can be challenging to solve analytically, we assume $\overline{\varphi} = 0$. Then Υ is further discussed considering the relationship between p_z and q_z. We firstly have

$$\Upsilon(p,q) = \begin{cases} \varrho, & p_z = q_z, \\ \frac{e^{j\pi(p_z-q_z)\nu_{ub}} - e^{j\pi(p_z-q_z)\nu_{lb}}}{j\pi(p_z-q_z)(\nu_{ub}-\nu_{lb})}\varrho, & p_z \neq q_z, \end{cases} \tag{3.40}$$

where $\varrho = e^{j\pi((p_y-q_y)\psi_y+(p_z-q_z)\psi_z)}$.

By introducing the full cover of the elevation angle from -90° to 90°, i.e., $\nu_{lb} = -1$ and $\nu_{ub} = 1$, $\Upsilon(p,q)$ can be rewritten as

$$\Upsilon(p,q) = \begin{cases} e^{j\pi((p_y-q_y)\psi_y+(p_z-q_z)\psi_z)}, & p_z = q_z, \\ 0, & p_z \neq q_z. \end{cases} \tag{3.41}$$

Furthermore, from (3.23), we observe that in each column of $\boldsymbol{Q}_k$, there are M_y elements satisfying $p_z = q_z$. In total, there should be $M_y^2 M_z$ elements meeting the $p_z = q_z$ condition in $\Upsilon = \mathbb{E}\{\boldsymbol{Q}_k\}$. With fixed azimuth angle $\overline{\varphi} = 0$, the average received power Ξ with $\theta_{o,m} \in (-90^\circ, 90^\circ)$ can be expressed as

$$\Xi = \sum_{p_z=q_z} \Upsilon(p,q)\mathbf{X}(q,p). \tag{3.42}$$

Based on the derivation, we get a corollary, as shown below.

Corollary 2: *The upper bound of the average power across the elevation domain $\hat{\Xi}_\theta$ as*

$$\hat{\Xi}_\theta = M_y^2 M_z, \tag{3.43}$$

which is achieved when $w_{m_y,m_z} = e^{j\pi(m_y\psi_y+m_z\psi_z)}$.

C. When $M_x = 1$ or $M_y = 1$:

The designed URA configuration is transferred in the ULA model with either $M_x = 1$ or $M_y = 1$. In the case of ULA, we give the following analysis and derivation regarding the average received power.

When ULA configuration is applied, (3.6) can be rewritten as

$$\zeta_{RO,k,m} = (m-1)\sin(\phi_{o,k,m}), \tag{3.44}$$

where $\phi_{o,k,m}$ denotes the steering angle towards the k-th direction in the ULA model, and $m = 1, \cdots, M$. And we further define $\psi_{\text{ULA}} = \sin\theta_i$. Regarding to (3.32) and (3.39), $\Upsilon(p,q)$ can be expressed as

$$\Upsilon(p,q) = \frac{\int_{\mu_{lb}}^{\mu_{ub}} e^{j\pi(p-1)(\mu+\psi_{\text{ULA}})} e^{-j\pi(q-1)(\mu+\psi_{\text{ULA}})}\, d\mu}{\mu_{ub} - \mu_{lb}}, \tag{3.45}$$

which could be further rewritten as

$$\Upsilon(p,q) = \begin{cases} 1, & p = q, \\ \frac{e^{j\pi(p-q)\mu_{ub}} - e^{j\pi(p-q)\mu_{lb}}}{j\pi(p-q)(\mu_{ub}-\mu_{lb})} e^{j\pi(p-q)\psi_{\text{ULA}}}, & p \neq q. \end{cases} \tag{3.46}$$

Note that $\mu = sin(\phi_{o,k,m})$. μ_{ub} and μ_{lb} contain the phase information of boundaries of the cover region. Since both Υ and $\mathbf{X}$ are Hermitian matrices, we can easily get that

$$\sum_{q=1}^{M} \mathscr{R}e\{\Upsilon(q,q)\mathbf{X}(q,q)\} = M, \tag{3.47}$$

based on which we rewrite (3.26) as

$$\Xi = 2\sum_{p=1}^{M}\sum_{q=p+1}^{M} \mathscr{R}e\{\Upsilon(p,q)\mathbf{X}(q,p)\} + M. \tag{3.48}$$

According to (3.89) and (3.48), we can derive the following corollary.

Corollary 3: *The average received power within a specific range from μ_{lb} to μ_{ub} could be expressed as*

$$\Xi = M + 2\sum_{p=1}^{M-1}\sum_{q=p+1}^{M} \mathscr{R}e\{w_q w_p^* \frac{e^{j\pi(p-q)\mu_{ub}} - e^{j\pi(p-q)\mu_{lb}}}{j\pi(p-q)(\mu_{ub}-\mu_{lb})} e^{j\pi(p-q)\psi_{\text{ULA}}}\}, \tag{3.49}$$

where the average received power is a function of the cover region boundaries μ_{lb} and μ_{ub}, the incident angle information ψ_{ULA}, and the RIS phase shifts $\boldsymbol{w}$.

Specially, when full cover from $\phi = -90°$ to $90°$ is considered, i.e., $\mu_{lb} = -1$ and $\mu_{ub} = 1$, we have

$$\frac{e^{j\pi(p-q)\mu_{ub}} - e^{j\pi(p-q)\mu_{lb}}}{j\pi(p-q)(\mu_{ub}-\mu_{lb})} = 0, \tag{3.50}$$

when $p \neq q$. By taking (3.50) into (3.49), we can henceforth get the theorem as shown below.

Theorem 1: *When full cover from RIS is considered, the average received power $\Xi_{ULA} = M$ can be realized regardless of the phase shifts configuration of RIS.*

When other sizes of cover area are considered, the maximum average received power, and its corresponding RIS phase shifts cannot be mathematically derived. We, therefore, aim to find an upper bound of the average received power that an arbitrary cover region could realise.

Based on **Theorem 1**, we can get the sum power receiving from RIS as

$$\Xi_{total} = \int_{-1}^{1} \Xi_{ULA} d\mu = 2M. \tag{3.51}$$

It is noted that the sum power is calculated based on dimensionless values of trigonometric functions and henceforth is with no unit. Since the average received power within a pre-defined target region is aimed to be maximized, we take the value $\hat{\Xi}_{ULA}$ obtained when the beams are all within this range as the upper bound of the average power, i.e., there are no side lobes in other areas. Note that no side lobes might be impractical in the real application; however, the side lobes could be significantly suppressed by some beamforming designs such as MRT and the beam broadening technique addressed in [129]. Then the upper bound of the average received power $\hat{\Xi}_{ULA}$ as a function of the angular range can be interpreted as

$$\hat{\Xi}_{ULA} = \frac{2M}{\mu_{ub} - \mu_{lb}}, \quad \mu_{ub} - \mu_{lb} \in (0, 2]. \tag{3.52}$$

The derived upper bound of the received power can be effectively used as the benchmark to evaluate the amount of the power reflecting to the pre-defined angular region. Following this, we get a corollary shown below.

Corollary 4: *The range of the upper bound for an arbitrary pre-defined cover region could be derived as*

$$\hat{\Xi}_{ULA} \in [M, M^2]. \tag{3.53}$$

To be noted, when the length of the range tends to zero, the upper bound average received power is not obtained by (3.52). In detail, the derivation can be seen in APPENDIX A.2.

We further assume that there is a specific cover range $[\phi_a, \phi_b]$, whose corresponding determined sinusoidal range is $[\mu_a, \mu_b]$, where $\mu_a = \sin\phi_a$ and $\mu_b = \sin\phi_b$. Its maximum average received power Ξ_{ab} is realized when RIS's phase shift is $\alpha^* \in \mathbb{C}^{M\times 1}$, which can not be mathematically derived in close-form but can be obtained by some optimization algorithms such as interior method [136], etc. Specifically, the m-th phase shift in RIS is α_m^*. Another cover region which has the same sinusoidal range as $[\mu_a, \mu_b]$ is denoted as $[\phi'_a, \phi'_b]$, where its corresponding sinusoidal range is set as $[\mu_a + \Delta, \mu_b + \Delta]$. Δ is defined as the sinusoidal difference between ϕ_a/ϕ_b and ϕ'_a/ϕ'_b, which should be within the range $\Delta \in [-1-\mu_a, 1-\mu_b]$. Furthermore, we define the same difference of these sinusoidal ranges as $\overline{\zeta}$, where $\overline{\zeta} = \mu_b - \mu_a$. The following theorem can be derived.

Theorem 2: *The same maximum average received power can always be realized by RIS phase shift regardless of the orientation of the cover region as long as the sinusoidal difference $\overline{\zeta}$ is equal. However, when the cover region is shifted to be near the cover boundaries, the power pattern will degrade compared with the pattern which points to the centre angle by using only the phase information of the weight.*

The proof can be seen in APPENDIX A.3.

As an important metric that characterises the generated broadbeam's performance, we de-

rive the maximum average received power within a specific sector area on the communication system. These numerical results can serve as a baseline for evaluating the concentration of signals' power within the specific cover region.

3.2.3 The DC-SDP Algorithm

In this section, we investigate the solutions for the RIS-aided flat broad beamwidth design proposed in Section 3.2.1 based on the maximum average received power derived in Section 3.2.2. The DC-SDP algorithm, which effectively addresses the non-convexity issue while keeping the unit modulus characteristic of RIS weights, is introduced.

In (P3-1), we aim to maximize the average received power within an arbitrary pre-defined angular region while all UEs in that region could receive signals with the same power. To proceed, we choose a set of uniformly distributed directions $\{1, 2, \cdots, K\} \in [\upsilon_{lb}, \upsilon_{ub}]$ under both ULA and URA configurations. The BS is implemented with MRT beamforming design.

Additionally, it is proved that for an arbitrary ULA, when only one element is with unit power while others are zero, the perfect flat broadbeam can be realized [137]. It can also be easily verified in the case of URA configuration. This perfect broadbeam design with only one active element obviously violates the unit modulus principle regarding RIS weights. To achieve a flat beam design, we henceforth introduce δ to characterize the fluctuation of the generated broadbeam. Then, our optimization problem could be re-interpreted as

$$\begin{aligned} \text{(P3-1.1):} \quad \max_{\boldsymbol{w}} \quad & \Xi \\ \text{s.t.} \quad & p_k = \Xi + \delta, \quad k = 1, 2, \cdots, K \\ & |\delta| \leq \delta_{max}, \\ & |w_m| = 1, \quad m = 1, \cdots, M. \end{aligned} \tag{3.54}$$

where a small fluctuation $0 < |\delta| \ll 1$ is tolerable and is designed to be smaller than δ_{max}.

Furthermore, we assume that the UEs are in the vicinity of the RIS while far from the BS. Therefore, we rewrite $\mathbf{h}_{d,k} = \mathbf{h}_d, k = 1, \cdots, K$, and sequentially, we have $\mathbf{h}_d^H \mathbf{b}\sqrt{p_t} = \hat{h_d}$ and $\mathbf{G}\mathbf{b}\sqrt{p_t} = \hat{\mathbf{g}} \in \mathbb{C}^{M\times 1}$. Then, the received power at the k-th direction can be expressed as

$$p_k \approx |\hat{h_d} + \mathbf{h}_{r,k}^H \boldsymbol{W} \hat{\mathbf{g}}|^2 + \sigma_n^2. \tag{3.55}$$

We define $\boldsymbol{\eta}_k = \text{diag}(\mathbf{h}_{r,k}^H)\hat{\mathbf{g}} \in \mathbb{C}^{M\times 1}$, then (3.55) is transformed as

$$p_k = \boldsymbol{w}^H \mathbf{C}_k \boldsymbol{w} + 2\mathscr{R}e\{\boldsymbol{w}^H \mathbf{u}_k\} + |\hat{h_d}|^2 + \sigma_n^2, \tag{3.56}$$

where $\mathbf{C}_k = \boldsymbol{\eta}_k \boldsymbol{\eta}_k^H \in \mathbb{C}^{M\times M}$, and $\mathbf{u}_k = \boldsymbol{\eta}_k^H \hat{h_d} \in \mathbb{C}^{M\times 1}$. We further let $\mathbf{R}_k = \begin{bmatrix} \mathbf{C}_k & \mathbf{u}_k \\ \mathbf{u}_k^H & 0 \end{bmatrix}$ and $\overline{\boldsymbol{w}} = \begin{bmatrix} \boldsymbol{w} \\ 1 \end{bmatrix}$, then the received power at the k-th direction can be rewritten as

$$p_k = (\overline{\boldsymbol{w}}^H \mathbf{R}_k \overline{\boldsymbol{w}}) + |\hat{h_d}|^2 + \sigma_n^2 \tag{3.57}$$

By introducing $\overline{\boldsymbol{w}}^H \mathbf{R}_k \overline{\boldsymbol{w}} = \mathrm{Tr}(\mathbf{R}_k \overline{\boldsymbol{W}})$, where $\overline{\boldsymbol{W}} = \overline{\boldsymbol{w}}\overline{\boldsymbol{w}}^H$, the problem (P3-1.1) can be henceforth reformulated as a standard SDP problem [138] without loss of generality:

$$\begin{aligned} \text{(P3-1.2):} \quad \max_{\overline{\boldsymbol{W}}} \quad & \Xi \\ \text{s.t.} \quad & \mathrm{Tr}(\mathbf{R}_k \overline{\boldsymbol{W}}) + |\hat{h_d}|^2 + \sigma_n^2 = \Xi + \delta, k = 1, \cdots, K \\ & |\delta| \le \delta_{max}, \\ & \overline{\boldsymbol{W}}_{m,m} = 1, \quad m = 1, \cdots, M+1, \\ & \mathrm{rank}(\overline{\boldsymbol{W}}) = 1, \\ & \overline{\boldsymbol{W}} \succeq 0, \end{aligned} \tag{3.58}$$

Note that problem (P3-1.2) is a non-convex optimization problem due to the rank-one constraint. Instead of simply dropping the rank-one condition or relaxing the strict unit modulus weights constraint, we rewrite the rank-one constraint into an equivalent form:

$$\mathrm{rank}(\overline{\boldsymbol{W}}) = 1 \Longleftrightarrow \mathrm{Tr}(\overline{\boldsymbol{W}}) - \|\overline{\boldsymbol{W}}\|_2 = 0, \tag{3.59}$$

which can be considered as the difference between the two convex functions. Specifically, $\mathrm{Tr}(\overline{\boldsymbol{W}}) = \sum_{i=1}^{M+1} \sigma_i(\overline{\boldsymbol{W}})$ and $\|\overline{\boldsymbol{W}}\|_2 = \sigma_1(\overline{\boldsymbol{W}})$, where $\sigma_i(\overline{\boldsymbol{W}})$ denotes the i-th largest singular value of matrix $\overline{\boldsymbol{W}}$. From $\mathrm{Tr}(\overline{\boldsymbol{W}}) = \|\overline{\boldsymbol{W}}\|_2$, we can easily indicate that all singular values equal 0 except the largest one, equivalently, the rank-one constraint can be met.

Unfortunately, problem (P3-1.2) is still non-convex in terms of $\overline{\boldsymbol{W}}$ when substituting the rank-one constraint by (3.59), given the fact that $-\|\overline{\boldsymbol{W}}\|_2$ is a concave term. In order to solve the non-convexity issue, a penalty-based method is firstly invoked by adding the penalty component into the objective function in problem (P3-1), yielding

$$\begin{aligned} \text{(P3-1.3):} \quad \min_{\overline{\boldsymbol{W}}} \quad & -\Xi + \rho(\mathrm{Tr}(\overline{\boldsymbol{W}}) - \|\overline{\boldsymbol{W}}\|_2) \\ \text{s.t.} \quad & \mathrm{Tr}(\boldsymbol{Q}_k \overline{\boldsymbol{W}}) + |\hat{h_d}|^2 + \sigma_n^2 = \Xi + \delta, k = 1, \cdots, K \\ & |\delta| \le \delta_{max}, \\ & \overline{\boldsymbol{W}} \succeq 0, \\ & \overline{\boldsymbol{W}}_{m,m} = 1, \quad m = 1, \cdots, M+1, \end{aligned} \tag{3.60}$$

Algorithm 1 DC algorithm for IRR

Input: $\mathbf{Y}^0$.
Output: $\mathbf{Y}^T$.
1: **for** $t = 0 : T-1$ **do**
2: $\quad \mathbf{Z}^t = \partial h_{\mathbf{Y}^t}(\mathbf{Y})$;
3: $\quad \mathbf{Y}^{t+1} \in \operatorname{arginf}\left\{g(\mathbf{Y}) - h\left(\mathbf{Y}^t\right) - \left\langle \mathbf{Y} - \mathbf{Y}^t, \mathbf{Z}^t \right\rangle\right\}$;
4: **end for**

where ρ is the penalty factor and should satisfy $\rho > 0$.

Note that the non-convexity issue is not fully addressed since the concave term $-\rho\|\overline{\boldsymbol{W}}\|_2$ still exists. However, our objective function is now in a standard difference-of-convex (DC) form. We, therefore, use the DC algorithm, where the SCA approach can be developed to construct a convex function at the specific point in each iteration based on the original non-convex objective function. Then the proposed problem can be iterative-optimized, where a convex problem is formulated in each iteration. Specifically, we formulate an objective function in the form of a standard DC programming, which is generally expressed as

$$\min \quad f(\mathbf{Y}) = g(\mathbf{Y}) - h(\mathbf{Y}) \tag{3.61}$$

$$\text{s.t.} \quad \mathbf{Y} \in \mathcal{Y}, \tag{3.62}$$

where both $g(\mathbf{Y})$ and $h(\mathbf{Y})$ are convex and differentiable, $\mathcal{Y}$ is a bounded and convex set. A conceptual method to solve the problem is to apply Taylor's theorem [139] to approximate the lower bound of the objective function. Specifically, the variable $\mathbf{Y}$ is iteratively updated by

$$\mathbf{Y}^{t+1} = \arg\min_{\mathbf{Y}\in}\{g(\mathbf{Y}) - h(\mathbf{Y}^t) - \langle \nabla h(\mathbf{Y}^t), \mathbf{Y} - \mathbf{Y}^t\rangle\}. \tag{3.63}$$

Sequentially, the objective function can be addressed by the generic DC programming approach through Algorithm 1 without considering the constraint functions in problem (P3-1.3). The algorithm reveals the standard procedure of iteratively linearizing the concave part and solving the resulting convex subproblem.

Furthermore, we take the DC form into the objective function in (P3-1.3) and define

$$g(\overline{\boldsymbol{W}}) = \operatorname{Tr}(\overline{\boldsymbol{W}}), \tag{3.64}$$

$$h(\overline{\boldsymbol{W}}) = \|\overline{\boldsymbol{W}}\|_2. \tag{3.65}$$

It can be seen that an affine majorization is applied to the concave part $-h(\overline{\boldsymbol{W}})$. The subgradient of the function $h(\overline{\boldsymbol{W}})$ at $\overline{\boldsymbol{W}}^t$ can be obtained via $\partial\|\overline{\boldsymbol{W}}\|_2 = v_1 v_1^H$, where v_1 is the leading eigenvector of matrix $\overline{\boldsymbol{W}}$. Then, we use singular value decomposition (SVD) tech-

nique [140] to decompose matrix $\overline{\boldsymbol{W}}$ into $\overline{\boldsymbol{W}} = \mathbf{U}\mathbf{S}\mathbf{V}^H$, where the singular values in $\mathbf{S}$ are in decreasing order. Therefore, the most leading eigenvector is $\mathbf{U}(:,1)$, i.e., $v_1 = \mathbf{U}(:,1)$.

Based on Algorithm 1, the DC part can be equivalently rewritten as

$$F = \mathrm{Tr}(\overline{\boldsymbol{W}}) - \langle \overline{\boldsymbol{W}} - \overline{\boldsymbol{W}}^{t-1}, \partial_{\overline{\boldsymbol{W}}^{t-1}} \|\overline{\boldsymbol{W}}\|_2 \rangle, \tag{3.66}$$

in the t^{th} iteration, where $\|\overline{\boldsymbol{W}}^{t-1}\|_2$ is ignored since it is a fixed value. To be noted, (3.66) is a convex function. We can, therefore, formulate problem (P3-1.3) into the following convex programming:

$$\begin{aligned} \text{(P3-1.4):} \quad \min_{\overline{\boldsymbol{W}}} \quad & -\Xi + \rho \cdot F \\ \text{s.t.} \quad & \mathrm{Tr}(\mathbf{R}_k \overline{\boldsymbol{W}}) + |\hat{h_d}|^2 + \sigma_n^2 = \Xi + \delta, k = 1, \cdots, K \\ & |\delta| \leq \delta_{max}, \\ & \overline{\boldsymbol{W}} \succeq 0, \\ & \overline{\boldsymbol{W}}_{m,m} = 1, \quad m = 1, \cdots, M+1. \end{aligned} \tag{3.67}$$

In each iteration, the original SDP problem is transformed into a standard convex optimization problem, which can be efficiently solved by CVX toolbox [141]. After T^{th} iteration, we obtain the optimized $\overline{\boldsymbol{W}}$ corresponding to the objective function with minimized value. The iteration can also be interrupted if the convergence reaches, which could be expressed as

$$\mathcal{C} = \Xi^{t-1} - \Xi^t + \rho \cdot (F^t - F^{t-1}) \leq \varsigma. \tag{3.68}$$

Note that ς is the threshold that indicates when the optimization reaches convergence and is then interrupted. After iterative optimization, however, $\mathrm{Tr}(\overline{\boldsymbol{W}}) - \|\overline{\boldsymbol{W}}\|_2$ might be infinitely close to zero, denoting a quasi-rank one matrix $\overline{\boldsymbol{W}}$. Therefore SVD technique is adopted to decompose the PSD matrix $\overline{\boldsymbol{W}}$ into $\overline{\boldsymbol{W}} = \mathbf{U}\mathbf{S}\mathbf{V}^H$, where $\mathbf{V}^H$ is the Hermitian transpose of $\mathbf{U}$. By remaining the largest non-zero eigenvalue e_1 in $\mathbf{S}$, which could be much larger than all other eigenvalues, and forcing others as zero, a new approximated eigenvalue matrix $\overline{\mathbf{S}}$ is formed, which can be expressed as $\overline{\mathbf{S}} = [e_1, 0, \cdots, 0]^T \in \mathbb{C}^{(M+1)\times 1}$. We define

$$\overline{\mathbf{U}} = [\mathbf{U}(:,r)]_{r=1,\cdots,R}, \tag{3.69}$$

where r depends on the number of non-zero elements in $\overline{\mathbf{S}}$. It can be easily derived that $R = 1$. Finally, we could get the expression of $\overline{\boldsymbol{w}}$ as

$$\overline{\boldsymbol{w}} = e^{j\angle(\sqrt{\overline{\mathbf{U}}e_1})} / \overline{w}_{M+1}, \tag{3.70}$$

Algorithm 2 Proposed DC-SDP algorithm for RIS-aided broadbeam generation

Input: $\mathbf{R}_k \in \mathbb{C}^{(M+1)\times(M+1)}, k = 1, \cdots, K$, $\overline{\boldsymbol{W}}^0 \in \mathbb{C}^{(M+1)\times(M+1)}$, $\hat{h_d}$.
Output: $\boldsymbol{w} \in \mathbb{C}^{M\times 1}$, p_k, $k = 1, 2, \ldots, K$.
for $t = 1 : T$ **do**
Obtain $\overline{\boldsymbol{W}}^t$ and $-\Xi^t + \rho \cdot F^t$ by solving problem (P3-1.4) using CVX toolbox;
$[\mathbf{U}, \mathbf{S}, \mathbf{V}] = \text{svd}(\overline{\boldsymbol{W}}^{\text{t}})$;
$\partial_{\overline{\boldsymbol{W}}^t} \|\overline{\boldsymbol{W}}\|_2 = \mathbf{U}(:, 1)\mathbf{U}(:, 1)^{'}$;
Identify the convergence status by (3.68);
if $\mathcal{C} \leq \varsigma$ **then**
BREAK
end if
end for
$[\mathbf{U}, \mathbf{S}, \mathbf{V}] = \text{svd}(\overline{\boldsymbol{W}}^t)$.
$\mathbf{S} \longrightarrow \overline{\mathbf{S}}$ and get e_1.
Obtain $\overline{\mathbf{U}}$ by (3.69).
Obtain $\overline{\boldsymbol{w}}$ by (3.70), and obtain $\boldsymbol{w}$ by $\boldsymbol{w} = \overline{w}_{1:M}$.
Obtain p_k by (3.9), where $k = 1, 2, \ldots, K$.

where $\sqrt{\overline{\mathbf{U}} e_1} \in \mathbb{C}^{(M+1)\times 1}$ and $\overline{\boldsymbol{w}} \in \mathbb{C}^{(M+1)\times 1}$ correspondingly. $\overline{w}_{M+1}$ denotes the $(M+1)$-th element of $\overline{\boldsymbol{w}}$. The RIS phase shifts $\boldsymbol{w}$ can be obtained by extracting the first M elements from $\overline{\boldsymbol{w}}$, i.e., $\boldsymbol{w} = \overline{w}_{1:M}$.

The entire algorithm is summarized in Algorithm 2. Specifically, $\overline{\boldsymbol{W}}^0$ represents the initialized PSD matrix. The proposed problem (P3-1.4) is a standard convex programming, which gradually and monotonously converges through iterative optimization and eventually becomes stable. We henceforth get RIS phase shifts $\boldsymbol{w}$, which enable flat broadbeam in a pre-defined cover area.

3.2.4 Simulation Results

Numerical results are provided to evaluate the performance of our proposed algorithm. We first clarify the simulation parameters, followed by a numerical analysis of the sum rate under different beamforming designs. Then, simulations are demonstrated to verify our derivation in Section 3.2.2. As important indicators of iterative algorithms, the complexity and convergence of our proposed algorithm are analyzed. Furthermore, the power patterns under the practical channel model are simulated under both ULA and URA configurations.

A. Simulation Scenario

We assume a scenario placed in an x-y-z Cartesian coordinate system, where a 2×2 antennas BS located at $(0, 0)$m, with a height of 10 m, and a single RIS is implemented in the vicinity of

Table 3.1: Simulation Parameters.

Parameters	Values
BS location (in meters)	(0, 0, 10)
RIS location (in meters)	(1000, 0, 10)
Path-loss for $\mathbf{G}$ and $\mathbf{h}_{r,k}$ (in dB)	$35.6+22.0lg(d)$
Path-loss for $\mathbf{h}_{d,k}$ (in dB)	$32.6+36.7lg(d)$
Transmit power	30 dBm
Noise power	-117 dBm

UEs to provide high-quality reflective links between the BS and UEs. Specifically, the RIS's location is at $(1000, 0, 10)$m, with a distance of 1000 m to the BS. Moreover, considering the orientation of BS and RIS, we let $\varphi_n = 30°$, $\theta_n = -60°$, $n = 1, \cdots, N$, and $\varphi_{i,m} = -30°$, and $\theta_{i,m} = 60°, m = 1, \cdots, M$ under URA configuration. The cover range at the reflecting side of RIS with a radius of 10 m is studied. The K chosen directions are uniform-distributed in both elevation and azimuth domains. Under ULA configuration, we assume the distance between BS and RIS is 1000 m as well. The AOD at BS is set as 60°, and the AOA at RIS is $-60°$. As the direct links are severely blocked and only NLoS paths exist, we consider MRT beamforming at BS towards the RIS for maximal power transmission. The detailed simulation parameters refer to [142] and are given in Table 3.1. Specifically, we assume the carrier frequency is 2.4 GHz, and the path-loss of channels is set according to the the 3rd Generation Partnership Project (3GPP) propagation environment. Furthermore, we set the element spacing distance at the BS and the RIS as $d = \lambda/2$. The noise power has a spectral density of -170 dBm/Hz. We assume the transmission bandwidth is 200 kHz; therefore, the noise power is about $\sigma_n^2 = -117$ dBm. Additionally, unless stated otherwise, we assume $K = M$, and the Rician factor has been set to $\varepsilon = 10$. All the simulation results are averaged over 1000 independent realizations of channel small-scale fading. The tolerated fluctuation of the power pattern, i.e., the variance, is set to be $\delta = 0.01$ dB. The penalty component ρ is set as 100. The iteration interruption threshold is set as $\varsigma = 10^{-4}$. We initialize $\overline{\boldsymbol{w}}^0 \in \mathbb{C}^{(M+1)\times 1}$ a randomly generated unit-modulus complex vector, then $\overline{\boldsymbol{W}}^0 = \overline{\boldsymbol{w}}^0(\overline{\boldsymbol{w}}^0)^H$. Furthermore, we denote the maximum number of iterations as $T = 100$.

B. The sum rate analysis

To illustrate the maximum sum rate property of the flat broadbeam, we compare the sum rate of the flat broadbeam with other generated beams under the same system model. The sum rate is calculated across the uniform-distributed K directions. Particularly, the MRT beamforming is applied to maximize the receiver signal power at the center direction of the

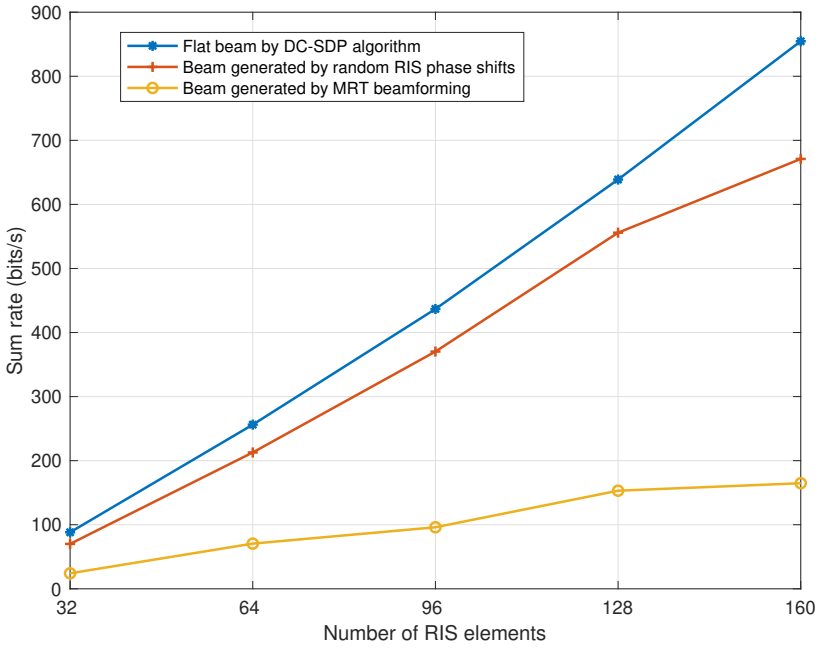

Figure 3.3: Investigation of sum rate for different generated beams.

pre-defined cover region. Specifically, the sum rates of the full cover case are compared under different sizes of RIS. The simulation results are shown in Fig. 3.3. It can be seen that the flat broadbeam design could always realize the highest sum rate compared with the beam generated by other RIS beamforming designs. For example, when the number of RIS elements is $M = 160$, the sum rate realized by the flat broadbeam, the beam generated by random RIS phase shifts, and the beam generated by MRT directional beamforming is 854.69, 670.96, and 164.79 bits/s, respectively, which is consistent with the **Lemma 2** proposed in Section 3.2.1.

C. Proof of the derivation under ULA and URA configuration

According to **Corollary 1** and **Corollary 2**, where the upper bounds of the average received power are obtained when $\overline{\theta} = 0$ and $\overline{\varphi} = 0$, respectively. In order to highlight the differences between these two cases, we consider a RIS in URA configuration where $M_x \neq M_y$. Specifically, we have $M_x = 8$ and $M_y = 12$. We consider the full cover case, where the cover region is uniformly divided into $K = 90$ sub-areas in either azimuth or elevation domain, and the angle of each sub-area is 2°. The flat broadbeam design is then investigated. Fig. 3.4 shows the derived upper bounds and the simulation results at $\overline{\theta} = 0$ and $\overline{\varphi} = 0$. Flat beam patterns with subtle fluctuation are obtained. Additionally, it can be seen that there is not much difference between the simulation results and the theoretical upper limit. Specifically, there is approxi-

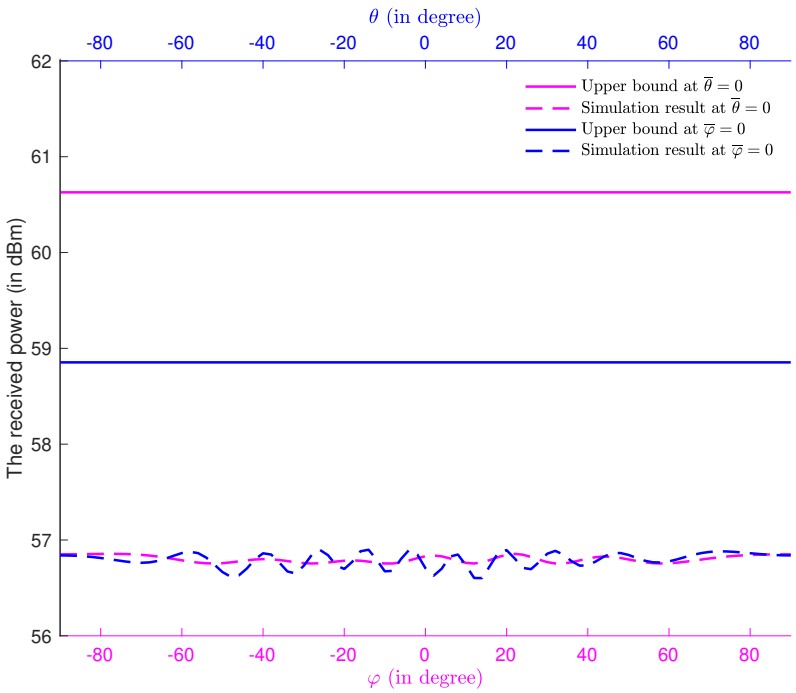

Figure 3.4: Comparison between the derived upper bound and the simulation results with flat broadbeam design.

mately a 4 dB difference when $\overline{\theta} = 0$ and a 2 dB difference when $\overline{\varphi} = 0$, which indicates that the proposed flat broadbeam design is with high energy efficiency.

Based on **Corollary 3**, we have mathematically verified that when $\lambda/2$-spaced RIS is used, the average gain improvement in all directions is dependent on RIS's size, i.e., $\Xi = M$. We also derive the upper bound of the average received power within an arbitrary angular region, which is dependent on both the size of RIS and the size of the cover region.

In Fig. 3.5, we compare the simulated maximum average received power versus the upper bound $\hat{\Xi}_{ULA}$ when different angular regions are set. RIS with 16, 32 and 64 elements are used, and the sinusoidal difference $\overline{\zeta} = \mu_{ub} - \mu_{lb}$ is set to be $\{1/8, 1/4, \cdots, 15/8, 2\}$, corresponding to different pre-defined angular regions. It can be seen that our optimal solutions, considering both the flatness and average received power of the broadbeam, are always close to the upper bound regardless of the size of the RIS, revealing that the side lobe power is limited. Particularly, when the full cover is considered, our optimal solution reaches the same as the upper bound, which is in accordance with **Theorem 1**.

D. Analysis of the DC-SDP algorithm

In this part, we first give an analysis of the complexity and convergence of our proposed algorithm. Then, we compare the DC-SDP algorithm with other state-of-the-art.

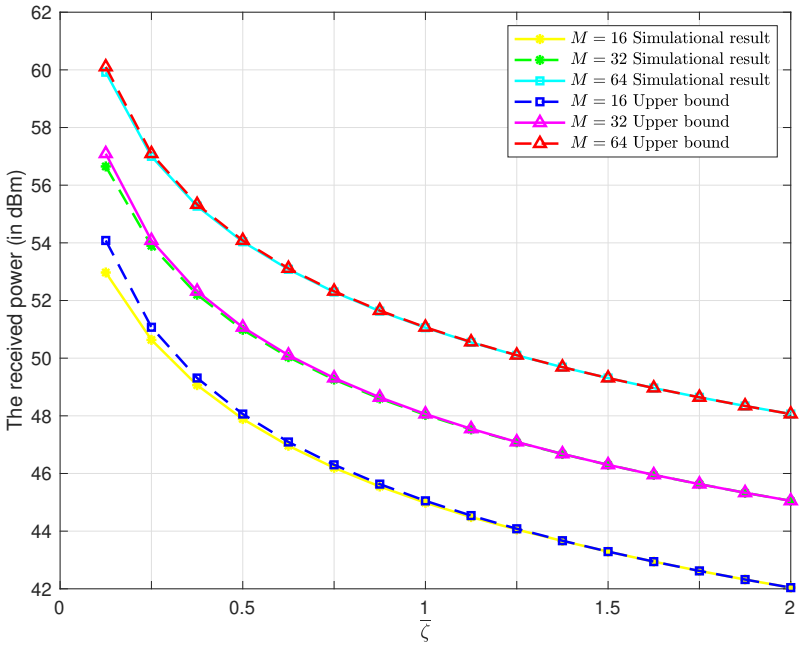

Figure 3.5: Comparison of the simulated and theoretical average received power.

Firstly, the complexity of initializing $\mathbf{R}_k$, $k = 1, \cdots, K$ is $\mathcal{O}(K(M^2+M))$. According to [143], the complexity of an SDP problem to optimize an $n \times n$ PSD matrix with m SDP constraints in each iteration is given by $\mathcal{O}(\sqrt{n}log(1/\epsilon)(mn^3+m^2n^2+m^3))$, where $\epsilon > 0$ is the solution accuracy. Therefore, the complexity of the iterative optimization is approximately $\mathcal{O}(log(1/\epsilon)\min\{T, t_{BREAK}\}(K+2)((M+1)^3+K(M+1)^{2.5}))$, where T denotes the maximum number of iterations and t_{BREAK} denotes the number of iterations when convergence reaches. The singular value decomposition of the obatined semi-definite matrix $\overline{\boldsymbol{W}}^t$ has the complexity of $\mathcal{O}((M+1)^3)$. In conclusion, our proposed algorithm has the complexity of $\mathcal{O}(K(M^2+M)+log(1/\epsilon)\min\{T, t_{BREAK}\}(K+2)((M+1)^3+K(M+1)^{2.5})+(M+1)^3)$.

On the other side, since both the objective function and the constraints are convex, the value of the objective function is non-increasing after each iteration by applying the DC-SDP algorithm. Furthermore, the objective function possesses a finite lower bound due to the principle of energy conservation, which restricts the received power from exceeding its limit. Fig. 3.6 verifies the convergence of our proposed algorithm numerically, from which we can see that the objective function converges rapidly within the limited number of iterations.

In addition, we compare our broadbeam design with the matching method proposed in [128], the ADMM algorithm proposed in [144], and also with the cases when either no RIS is implemented or when the RIS is randomly designed. Both the average received power and the variance are presented. Particularly, for the ULA model, we optimize the average received power and the variance over the full cover range from $\phi = -90°$ to $90°$ with RIS

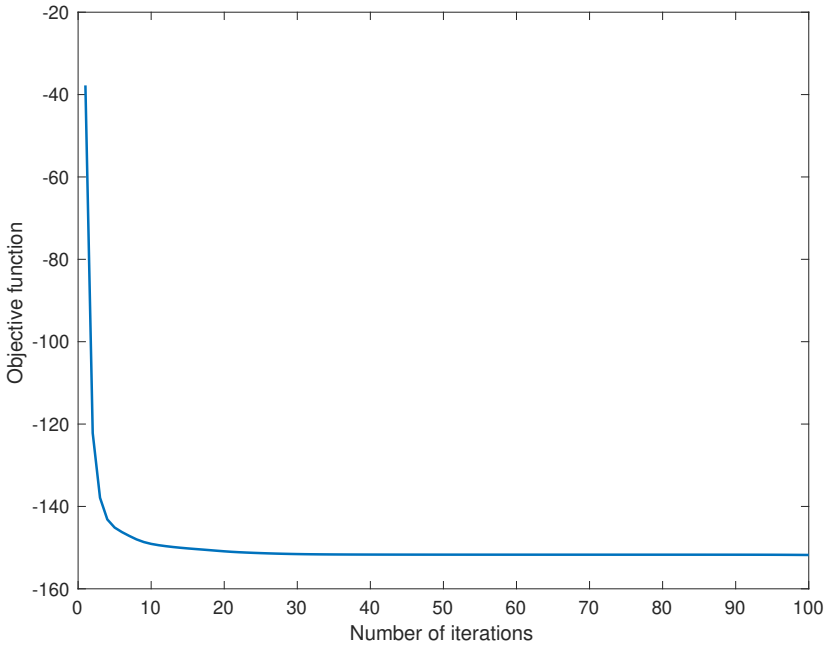

Figure 3.6: Proof of convergence of the proposed algorithm.

composed of $M = 32,\ 64,\ 96,\ 128$, and 160 elements. It can be seen from Fig. 3.7 that a higher average received power could always be realized with the help of RIS. As the full cover is considered, the RIS beamforming design mainly influences the variance of the beam pattern, while the average received power could be similar. In detail, our proposed algorithm results in a variance lower than 10^{-2} dB, while all other beamforming designs lead to higher variance and more severe fluctuation of the generated broadbeam. For the URA configuration model, the RIS with 2×16, 4×16, 6×16, 8×16, and 10×16 elements are implemented, respectively. We set the target region with the azimuth angle $\varphi \in [-90°, 90°]$ and the elevation angle $\theta \in [-30°, 30°]$. By proposing our developed DC-SDP algorithm, the highest received power could be realized within the pre-defined angular region. On the other side, the variance is minimized to be less than 10^{-2} dB, revealing a perfect flat broadbeam within the cover region.

E. The performance of the proposed algorithm with practical channel model

In this subsection, the power pattern is simulated under both ULA and URA configurations. In detail, the power pattern with different sizes of RIS and different sizes of pre-defined angular regions are investigated. Furthermore, we consider the full cover over the spatial domain, and symmetrical and unsymmetrical pre-defined angular regions are also considered when the region of interest is not the whole spatial domain.

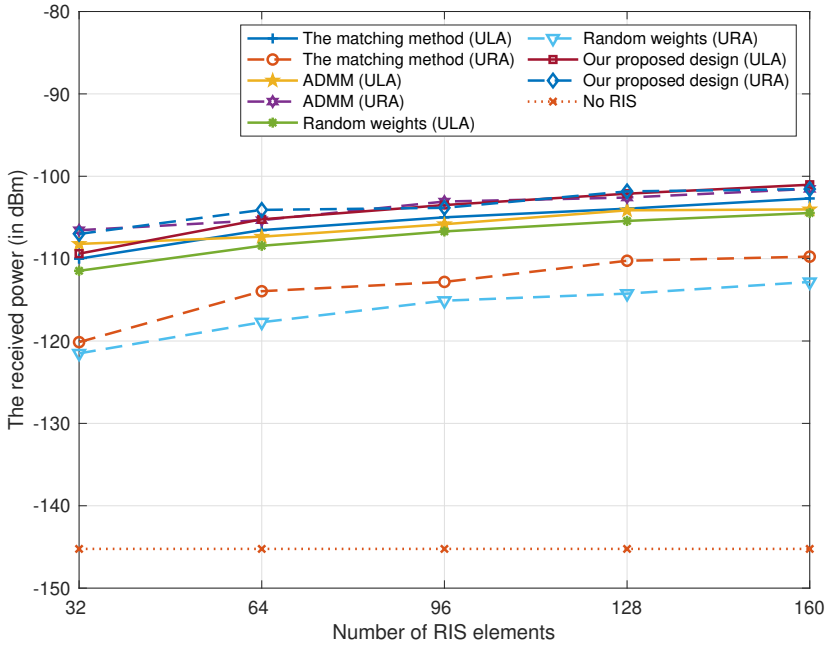

(a) The comparison of the average received power.

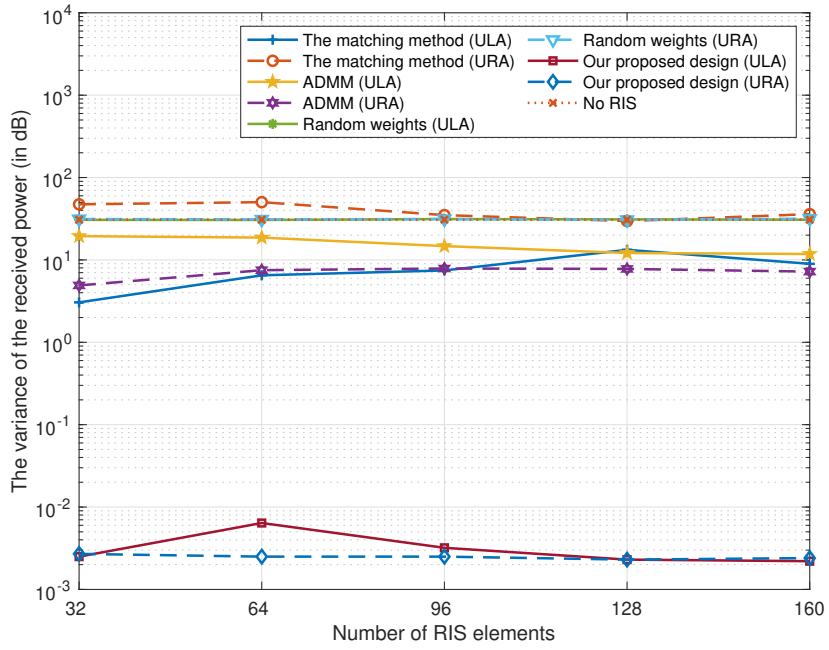

(b) The comparison of the variance of the power pattern.

Figure 3.7: The comparison under both ULA and URA configurations.

a. The power pattern under ULA configuration

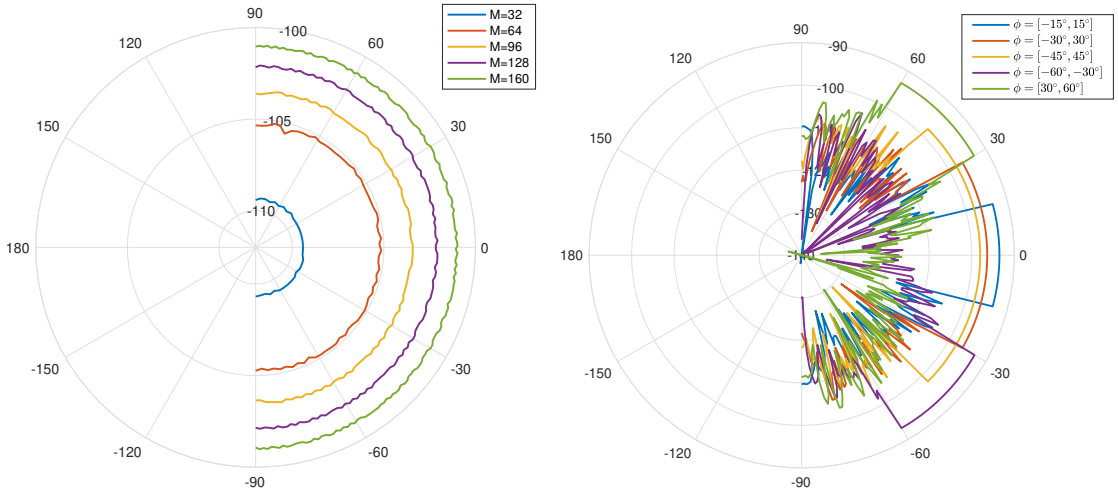

(a) The power pattern with different numbers of RIS elements.

(b) The power pattern with different pre-defined angular regions.

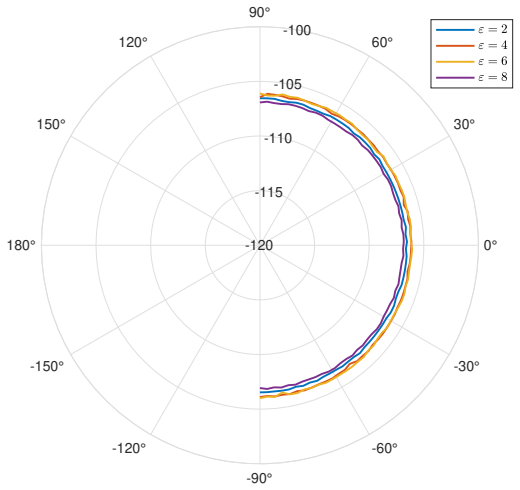

(c) The power pattern with different Rician factor ε.

Figure 3.8: The power pattern under practical channel model when ULA configuration is applied.

Fig. 3.8(a) demonstrates the power pattern under different numbers of RIS elements. We use the RIS composed of $M = 32,\ 64,\ 96,\ 128$, and 160 elements, respectively. The full cover $\phi \in [-90°, 90°]$ is considered. Specifically, the average received power under different sizes of RIS is -109.37, -105.23, -103.49, -102.12, and -101.03 dBm, while the corresponding variance of each power pattern is 0.0025, 0.0064, 0.0032, 0.0023, and 0.0022 dB, respectively. The variance results are lower than the threshold $\delta = 0.01$ dB, revealing the good flatness of the generated power pattern.

Fig. 3.8(b) shows the power pattern when different sizes of the pre-defined angular region are considered. A RIS with 180 elements is applied. It is worth mentioning that the side

lobes are given in the simulation. Specifically, when the cover region is $\phi = [-45°, 45°]$, the average power of the side lobes is -113.39 dBm, while the average received power of directions within the pre-defined angular region is -98.04 dBm, which is 15.35 dB higher than the average power within the side lobes area. Moreover, when $\phi = [-30°, 30°]$, the average received power within the region of interest is -96.38 dBm, which is 17.52 dB higher than the average power outside the target region. In addition, when the cover region is set to be $\phi = [-15°, 15°]$, the average received power within and outside the target region is -93.51 dBm and -115.86 dBm, respectively. It is found that there is 22.35 dB higher average received power within $\phi \in [-15°, 15°]$ compared with the power within the sidelobe. At the same time, the beam within the region of interest is significantly flattened, with power variance lower than the threshold. In addition, the power patterns when the cover region is not symmetrical are also presented, as it could be a common and practical scenario that needs to be considered. When the target cover region is $\phi \in [-60°, -30°]$, the average received power within and outside the target region is -93.23 and -114.10 dBm, respectively. When the target cover region is $\phi \in [30°, 60°]$, the average received power within and outside the target region is -93.08 and -115.92 dBm, respectively. The variances of the regions of interest are also lower than the threshold, revealing good flatness. It can be seen that our proposed algorithm is robust regardless the shift of the cover range.

Fig. 3.8(c) shows the power pattern under different Rician factors when a RIS with $M = 64$ elements is applied. The full cover within $\phi = [-90°, 90°]$ is considered. Specifically, when the Rician factor is $\varepsilon = \{2, 4, 6, 8\}$, the corresponding average received power are -106.59, -106.18, -106.13, -106.89 dBm, and the variances of the power pattern are 0.0024, 0.0041, 0.0058, and 0.0023 dB, respectively. Note that this simulation is generated with instantaneous CSI, as the average over channel fading could weaken the effects of the Rician factor. The generated broadbeams reveal that our proposed DC-SDP algorithm is robust against various channel environments.

b. The power pattern under URA configuration

Specifically, a RIS with 16×16 elements is applied to generate the flat broadbeam to cover the pre-defined angular region. Fig. 3.9(a) presents the power pattern when the pre-defined angular region is across $\theta \in [-30°, 30°]$ and $\varphi \in [-30°, 30°]$. In detail, the average received power within the target region is -96.97 dBm and the power pattern is flattened with a variance of only 0.0024 dB. On the other side, the average received power towards other angles is only -121.95 dBm, which is about 25 dB lower than the average power received in the target region. Furthermore, Fig. 3.9(b) shows the unsymmetrical power pattern when the pre-defined angular region is across $\theta \in [-90°, -30°]$ and $\varphi \in [-30°, 30°]$. The average received power and the variance within the specific range are -95.53 dBm and 0.0025 dB,

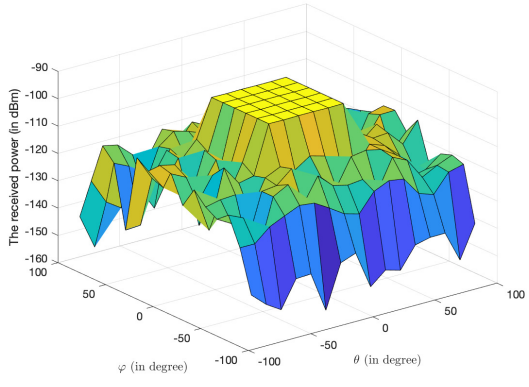

(a) The symmetrical power pattern with $\theta \in [-30°, 30°], \varphi \in [-30°, 30°]$.

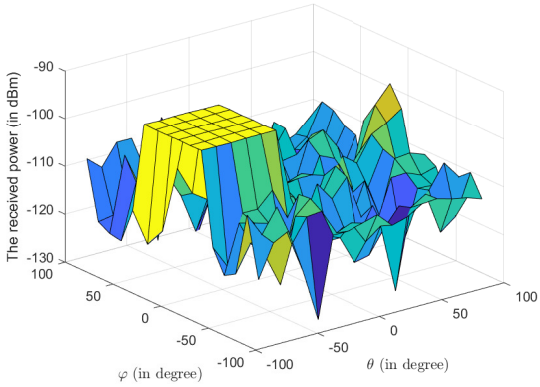

(b) The unsymmetrical power pattern with $\theta \in [-90°, -30°], \varphi \in [-30°, 30°]$.

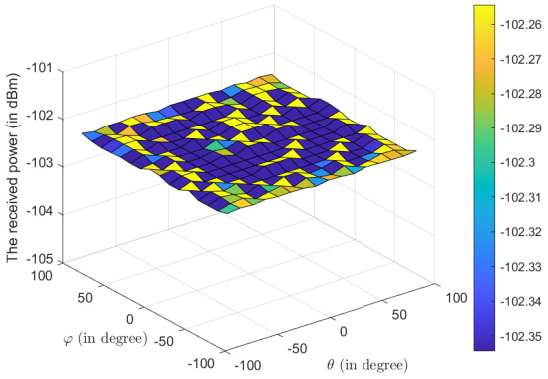

(c) The full cover power pattern.

Figure 3.9: The 3D power pattern under URA configuration.

respectively. At the same time, the average received power at other angles is -113.34 dBm. It is worth mentioning that our proposed DC-SDP algorithm can optimize the flat beam towards arbitrary angular regions in the 3D space. Fig. 3.9(c) shows the full cover in both the elevation and azimuth domain. In detail, the average received power among all directions is -102.31 dBm with a variance of only 0.0021 dB. To be noted, when the RIS with the same number of elements is applied, URA configuration will result in a higher sidelobe level compared with ULA model, as directions in both azimuth and elevation domains need to be considered. In order to realize the sidelobe suppression under URA configuration without sacrificing the resolution, a larger RIS or multi-RISs need to be applied.

3.3 Generation of Multiple Broadbeams

Motivated by the design of a single broadbeam within an arbitrary region, we propose a multiple wide illumination and null insertion design in RIS-assisted system via optimizing the

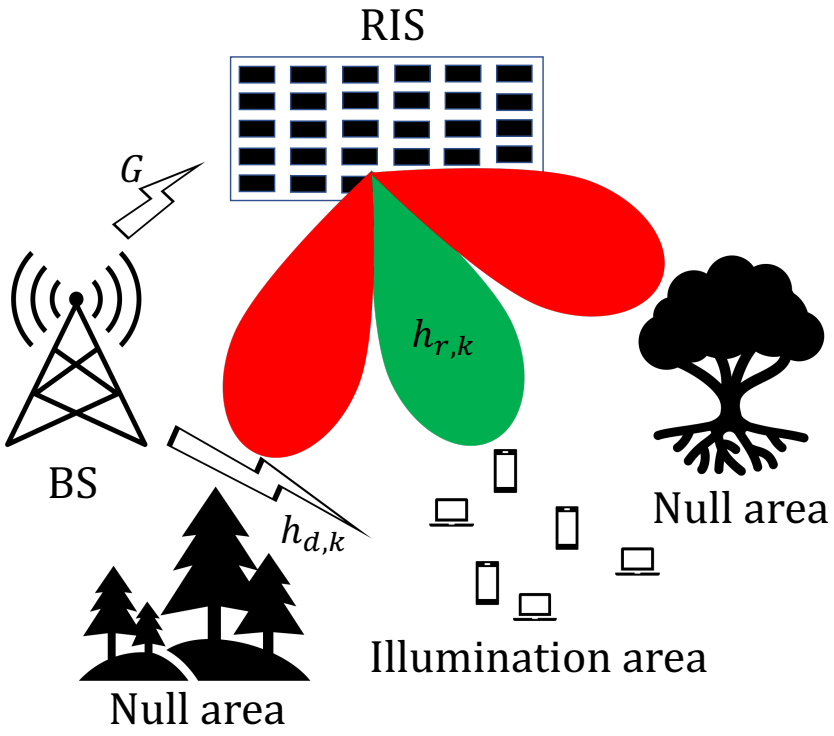

Figure 3.10: System model of RIS-assisted joint wide illumination and null insertion design.

passive beamforming at RIS, given constraints of RIS unit modulus weights. On one side, the wide illumination ensures reliable signal transmission without the accurate CSI of UEs; on the other side, the extended-null insertion are essential for suppressing signals towards unwanted directions. Instead of using classical SDR based method [145], which lifts the problem dimension from N to N^2 and significantly increases the computational complexity [146], a low-complexity ADMM-based algorithm is proposed, which effectively address the non-convexity by introducing auxiliary variables. Via alternatively updating RIS phase shifts and the auxiliary variables, a minimized normalization deviation between the target and optimized pattern can be obtained.

3.3.1 System Model

We model a RIS-aided wide illumination and null insertion design as in Fig. 3.10. Specifically, we assume that there are R null areas, where nulls are needed to either combat interference or suppress signals towards blockages and unwanted directions. In addition, there are Q illumination areas, where UEs with a single antenna are located. Let $\boldsymbol{w} = [w_1, w_2, ..., w_M]^H$ denote the RIS phase shift matrix and each element $w_m, m = 1, \cdots, M$ in $\boldsymbol{w}$ could be expressed as $w_m = \beta_m e^{j\alpha_m}$. For maximum reflection efficiency, we let $\beta_m = 1$ and $\alpha_m \in [0, 2\pi]$. Besides, the BS has N elements.

Assume that there are K look-directions across the whole cover domain. Specifically, K_R

and K_Q refer to the directions within the null and illumination areas, respectively. We denote $\mathbf{h}_{d,k} \in \mathbb{C}^{N\times 1}$, $\mathbf{G} \in \mathbb{C}^{M\times N}$, and $\mathbf{h}_{r,k} \in \mathbb{C}^{M\times 1}$ as the channel expressions of BS-k-th direction, BS-RIS, and RIS-k-th direction, respectively, where $\forall k \in \mathcal{K}$. We further define $\mathbf{b} \in \mathbb{C}^{N\times 1}$ as the precoding vector at BS, and s is the transmit signal with $\mathbb{E}\{ss^*\} = 1$. Then the received signal at the direction k could be expressed as

$$y_k = (\mathbf{h}_{d,k}^H + \mathbf{h}_{r,k}^H \boldsymbol{W}\mathbf{G})\mathbf{b}s + n_k, \forall k \in \mathcal{K}, \tag{3.71}$$

where $\boldsymbol{W} = \mathrm{diag}(\boldsymbol{w}^T) \in \mathbb{C}^{M\times M}$ and n_k is the AWGN with zero mean and variance σ_n^2, i.e., $n_k \sim \mathcal{CN}(0, \sigma_n^2)$.

We apply the ULA configuration to channel vectors, which is generally expressed as

$$\boldsymbol{a}_{\mathrm{ULA}}(\boldsymbol{\zeta}) = e^{j\frac{2\pi f}{c}d\boldsymbol{\zeta}}, \tag{3.72}$$

where $\boldsymbol{\zeta} = [1, \cdots, (N_s - 1)\cos\theta] \in \mathbb{C}^{1\times N_s}$. θ refers to either AOA or AOD. We assume that the direct link $\mathbf{h}_{d,k}$ follows Rayleigh fading, while RIS-aided channels $\mathbf{h}_{r,k}$ and $\mathbf{G}$ follow Rician fading. Then $\mathbf{h}_{d,k}$, $\mathbf{h}_{r,k}$, and $\mathbf{G}$ are modeled as

$$\mathbf{h}_{d,k} = \mathrm{PL}_{\mathrm{NLoS}}\overline{\mathbf{h}}_d, \tag{3.73}$$

$$\mathbf{h}_{r,k} = \mathrm{PL}_{\mathrm{LoS},k}\left(\sqrt{\frac{\varepsilon}{\varepsilon+1}}\boldsymbol{a}(\boldsymbol{\zeta}_{R,k}) + \sqrt{\frac{1}{\varepsilon+1}}\overline{\mathbf{h}}_r\right), \tag{3.74}$$

$$\mathbf{G} = \mathrm{PL}_{\mathrm{LoS},0}\left(\sqrt{\frac{\varepsilon}{\varepsilon+1}}\boldsymbol{a}(\boldsymbol{\zeta}_{R,0})\boldsymbol{a}^T(\boldsymbol{\zeta}_B) + \sqrt{\frac{1}{\varepsilon+1}}\overline{\mathbf{G}}\right). \tag{3.75}$$

Specifically, $\mathrm{PL}_{\mathrm{NLoS}}$, $\mathrm{PL}_{\mathrm{LoS},k}$ and $\mathrm{PL}_{\mathrm{LoS},0}$ denote the corresponding path-loss. ε is the Rician factor. $\boldsymbol{\zeta}_{R,k}$, $\boldsymbol{\zeta}_{R,0}$, and $\boldsymbol{\zeta}_B$ denote the departing angle towards the direction k, incident angle at RIS and departing angle at BS towards RIS, respectively. $\overline{\mathbf{h}}_d$, $\overline{\mathbf{h}}_r$, and $\overline{\mathbf{G}}$ denote the NLoS components of channels, each element of which follows $\mathcal{CN}(0, 1)$.

Additionally, as the direct links are severely blocked and only NLoS paths exist, the channel gain is generally lower than that of the reflective links. We therefore initialize the active beamforming at BS with MRT for maximal power transmission towards RIS, which can be expressed as $\mathbf{b} = \boldsymbol{a}^*(\boldsymbol{\zeta}_B)$. With fixed active beamforming $\mathbf{b}$, we rewrite $\hat{h_{d,k}} = \mathbf{h}_{d,k}^H\mathbf{b}$ and $\hat{\mathbf{g}} = \mathbf{G}\mathbf{b} \in \mathbb{C}^{M\times 1}$, then the beam pattern at the k-th direction in the far field can be expressed as

$$p_k = |\hat{h_{d,k}} + \mathbf{h}_{r,k}^H \boldsymbol{W}\hat{\mathbf{g}}|. \tag{3.76}$$

Note that the noise is ignored here as its power is much lower than that of the signal, especially over the time scale.

We further introduce the target pattern $\mathbf{t} \in \mathbb{C}^{K\times 1}$ and the weighting factor $\boldsymbol{\kappa} \in \mathbb{C}^{K\times 1}$, which can be designed to assign different weights for different angular regions. Then our proposed design can be interpreted as the following matching problem:

$$\text{(P3-2)} \ : \min_{\boldsymbol{w}} \quad \|\boldsymbol{\kappa} \cdot (\mathbf{t} - \mathbf{p})\|_2^2. \tag{3.77a}$$

$$\text{s.t.} \quad |w_m| = 1, m = 1, \cdots, M, \tag{3.77b}$$

where $\mathbf{p} = [p_1, \cdots, p_K]^T$. In the following, we develop the ADMM algorithm to solve the problem (P3-2).

3.3.2 ADMM Algorithm

We firstly combine the RIS-assisted reflective links as $\boldsymbol{\eta}_k = \text{diag}(\mathbf{h}_{r,k}^H)\hat{\mathbf{g}} \in \mathbb{C}^{M\times 1}$, then the objective function (3.77a) can be reinterpreted as

$$\min_{\boldsymbol{w}} \quad \|\mathbf{v} - |\mathbf{u} + \boldsymbol{\Lambda}^H \boldsymbol{w}|\|_2^2, \tag{3.78}$$

where $\mathbf{u} = [\kappa_1 \hat{h_{d,1}}, \cdots, \kappa_K \hat{h_{d,K}}]^T \in \mathbb{C}^{K\times 1}$, $\boldsymbol{\Lambda} = [\kappa_1 \boldsymbol{\eta}_1, \cdots, \kappa_K \boldsymbol{\eta}_K] \in \mathbb{C}^{M\times K}$, and $\mathbf{v} = \boldsymbol{\kappa} \odot \mathbf{t} \in \mathbb{C}^{K\times 1}$.

Then we introduce an auxiliary variable $\boldsymbol{\tau} \in \mathbb{C}^{K\times 1}$, which is a unit-modulus vector containing the phase information of the target beam pattern. The problem (P3-2) can be sequentially reformulated as

$$\text{(P3-2.1)} \ : \min_{\boldsymbol{w},\boldsymbol{\tau}} \quad \|\mathbf{V}\boldsymbol{\tau} - \mathbf{u} - \boldsymbol{\Lambda}^H \boldsymbol{w}\|_2^2. \tag{3.79a}$$

$$\text{s.t.} \quad |w_m| = 1, m = 1, \cdots, M, \tag{3.79b}$$

$$|\tau_k| = 1, k = 1, \cdots, K, \tag{3.79c}$$

where $\mathbf{V} = \text{diag}(\mathbf{v})$.

In order to realize the normalization minimization, the two variables $\boldsymbol{w}$ and $\boldsymbol{\tau}$ are optimized iteratively until convergence. Firstly, with fixed RIS passive beamforming $\boldsymbol{w}$, $\boldsymbol{\tau}$ can be obtained by $\boldsymbol{\tau}^* = e^{j\angle(\mathbf{u}+\boldsymbol{\Lambda}^H\boldsymbol{w})}$ (see proof in [144]). Then, with fixed $\boldsymbol{\tau}$, we rewrite $\overline{\mathbf{v}} = \begin{bmatrix} \mathcal{R}e\{\mathbf{V}\boldsymbol{\tau} - \mathbf{u}\} \\ \mathcal{I}m\{\mathbf{V}\boldsymbol{\tau} - \mathbf{u}\} \end{bmatrix}$, $\overline{\boldsymbol{\Lambda}} = \begin{bmatrix} \mathcal{R}e\{\boldsymbol{\Lambda}\} & -\mathcal{I}m\{\boldsymbol{\Lambda}\} \\ \mathcal{I}m\{\boldsymbol{\Lambda}\} & \mathcal{R}e\{\boldsymbol{\Lambda}\} \end{bmatrix}$, and $\overline{\boldsymbol{w}} = \begin{bmatrix} \mathcal{R}e\{\boldsymbol{w}\} \\ \mathcal{I}m\{\boldsymbol{w}\} \end{bmatrix}$. The RIS unit modulus weights constraint (3.79b) can be therefore rewritten as

$$\overline{w}_m^2 + \overline{w}_{m+M}^2 = 1, \quad m = 1, \cdots, M. \tag{3.80}$$

Furthermore, we introduce a new auxiliary variable $\boldsymbol{\eta}$, and then the original problem can be

transformed into the following form:

$$\text{(P3-2.2)} \ : \min_{\overline{\mathbf{w}}} \quad \|\overline{\mathbf{v}} - \overline{\mathbf{\Lambda}}^H \overline{\mathbf{w}}\|_2^2. \tag{3.81a}$$

$$\text{s.t.} \quad \boldsymbol{\eta} = \overline{\mathbf{w}}. \tag{3.81b}$$

$$\eta_m^2 + \eta_{m+M}^2 = 1, \quad m = 1, \cdots, M. \tag{3.81c}$$

The raised optimization problem can be effectively solved by the ADMM algorithm [147]. Specifically, by introducing a Lagrangian multiplier $\boldsymbol{\lambda} \in \mathbb{C}^{2M\times 1}$, problem (P3-2.2) can be rephrased as

$$\min \quad \mathscr{L}_\rho(\overline{\mathbf{w}}, \boldsymbol{\eta}, \boldsymbol{\lambda}) = \|\overline{\mathbf{v}} - \overline{\mathbf{\Lambda}}^H \overline{\mathbf{w}}\|_2^2 + \frac{\rho}{2}\|\boldsymbol{\eta} - \overline{\mathbf{w}}\|_2^2 + \lambda^T(\boldsymbol{\eta} - \overline{\mathbf{w}}), \tag{3.82}$$

where $\overline{\mathbf{w}}$, $\boldsymbol{\eta}$, and $\boldsymbol{\lambda}$ are updated alternatively. Particularly, in the t-th iteration, $\boldsymbol{\eta}$, $\overline{\mathbf{w}}$, and $\boldsymbol{\lambda}$ are updated as

$$\boldsymbol{\eta}^{(t)} = \arg \min_{(3.81c)} \mathscr{L}_\rho(\overline{\mathbf{w}}^{(t-1)}, \boldsymbol{\eta}, \boldsymbol{\lambda}^{(t-1)}), \tag{3.83}$$

$$\overline{\mathbf{w}}^{(t)} = \arg\min \mathscr{L}_\rho(\overline{\mathbf{w}}, \boldsymbol{\eta}^{(t)}, \boldsymbol{\lambda}^{(t-1)}), \tag{3.84}$$

$$\boldsymbol{\lambda}^{(t)} = \boldsymbol{\lambda}^{(t-1)} + \rho(\boldsymbol{\eta}^{(t)} - \overline{\mathbf{w}}^{(t)}). \tag{3.85}$$

Note that the optimization of $\boldsymbol{\eta}$ is constrained by (3.81c). By solving (3.83) and (3.84), we can get

$$\eta_{i=\{m,m+M\}}^{(t)} = \frac{\overline{w}_i^{(t-1)} + (1/\rho)\lambda_i^{(t-1)}}{\sqrt{(\overline{w}_m^{(t-1)} + (1/\rho)\lambda_m^{(t-1)})^2 + (\overline{w}_{m+M}^{(t-1)} + (1/\rho)\lambda_{m+M}^{(t-1)})^2}}, \tag{3.86}$$

$$\overline{\mathbf{w}}^{(t)} = (\overline{\mathbf{\Lambda}\mathbf{\Lambda}}^T + \rho\mathbf{I})^{-1}(\overline{\mathbf{\Lambda}}\overline{\mathbf{v}} + \rho\boldsymbol{\eta}^{(t)} - \boldsymbol{\lambda}^{(t-1)}). \tag{3.87}$$

With updated $\overline{\mathbf{w}}$, $\boldsymbol{w}$ can be recovered, and the phase of the desired pattern can be sequentially obtained by

$$\boldsymbol{\tau}^{(t)} = e^{j\angle(\mathbf{u} + \mathbf{\Lambda}^H \boldsymbol{w}^{(t)})}. \tag{3.88}$$

The iterative optimization stops either when the maximum number of iterations or the convergence reaches. In particular, the convergence criterion is [147]

$$\mathscr{C} : \begin{cases} \|\boldsymbol{\eta}^{(t)} - \overline{\mathbf{w}}^{(t)}\|_2^2 \le \epsilon_1 \\ \|\rho(\overline{\mathbf{w}}^{(t)} - \overline{\mathbf{w}}^{(t-1)})\|_2^2 \le \epsilon_2 \end{cases}. \tag{3.89}$$

The entire algorithm is summarized in Algorithm 3.

Algorithm 3 Proposed passive beamforming $\boldsymbol{w}$ optimization algorithm for pattern synthesis

Input: $\mathbf{V}$, $\mathbf{u}$, $\boldsymbol{\Lambda}$, $\boldsymbol{w}^0$, and $\boldsymbol{\lambda}^0$.
Output: $\boldsymbol{w}$, $p_k, k = 1, \cdots, K$.
for $t = 1 : T$ **do**
Obtain $\boldsymbol{\tau}$ by (3.88);
Update $\overline{\mathbf{v}}$, $\overline{\boldsymbol{\Lambda}}$, and $\overline{\mathbf{w}}$;
With fixed $\boldsymbol{w}^{(t-1)}$ and $\boldsymbol{\lambda}^{(t-1)}$, update $\boldsymbol{\eta}^{(t)}$ by (3.86);
With fixed $\boldsymbol{\eta}^{(t)}$ and $\boldsymbol{\lambda}^{(t-1)}$, update $\overline{\mathbf{w}}^{(t)}$ by (3.87);
With fixed $\boldsymbol{\eta}^{(t)}$ and $\overline{\mathbf{w}}^{(t)}$, update $\boldsymbol{\lambda}^{(t)}$ by (3.85).
if $\mathscr{C}$ satisfies **then**
BREAK
end if
end for
Obtain $\boldsymbol{w}$ by $w_m = \overline{w}_m + j\overline{w}_{m+M}, m = 1, \cdots, M$.
Obtain p_k by (3.76), where $k = 1, 2, \ldots, K$.

3.3.3 Simulation Results

We consider a BS equipped with a 32-antenna array located at coordinates $(0,0)$m. A single RIS is employed to establish high-quality reflective connections between the BS and UEs. The angular parameters are set as follows: $\varphi_n = 30°$, $\theta_n = -60°$ for $n = 1, \cdots, N$, and $\varphi_{i,m} = -30°$, $\theta_{i,m} = 60°$ for $m = 1, \cdots, M$. We select K directions in the vicinity of the RIS, covering a radius of 10 m. The specific simulation parameters are outlined in Table 3.1. Notably, the channel path-loss adheres to the 3GPP propagation environment guidelines [142]. The noise power has a spectral density of -170 dBm/Hz. We assume the transmission bandwidth is 200 kHz, and therefore the noise power is about $\sigma_n^2 = -117$ dBm. Furthermore, the Rician factor is set as $\varepsilon = 10$.

Fig. 3.11 demonstrates the convergence of our proposed algorithm under the different number of RIS elements. It can be seen that the objective function decreases rapidly at initial, and converges to a stable value within limited iterations, revealing good convergence behaviour of the proposed ADMM algorithm. Additionally, it can be discovered that the RIS comprising more elements results in a smaller objective function value, representing a better match between the optimized and target beam pattern.

In Fig. 3.12, we study the comparison between the target and optimized power pattern by our proposed algorithm under different numbers of illumination and null areas. A RIS with 180 elements is applied. In detail, we set $Q = \{1, 2\}$ and $R = \{1, 2\}$. In order to illustrate the suppression within the null spaces, the weighting factor within the null areas is set as $\kappa_l = 1000$, while the weighting factor at other directions is set as 1. To evaluate the matching between the actual and target pattern at the null and illumination areas, we introduce the mea-

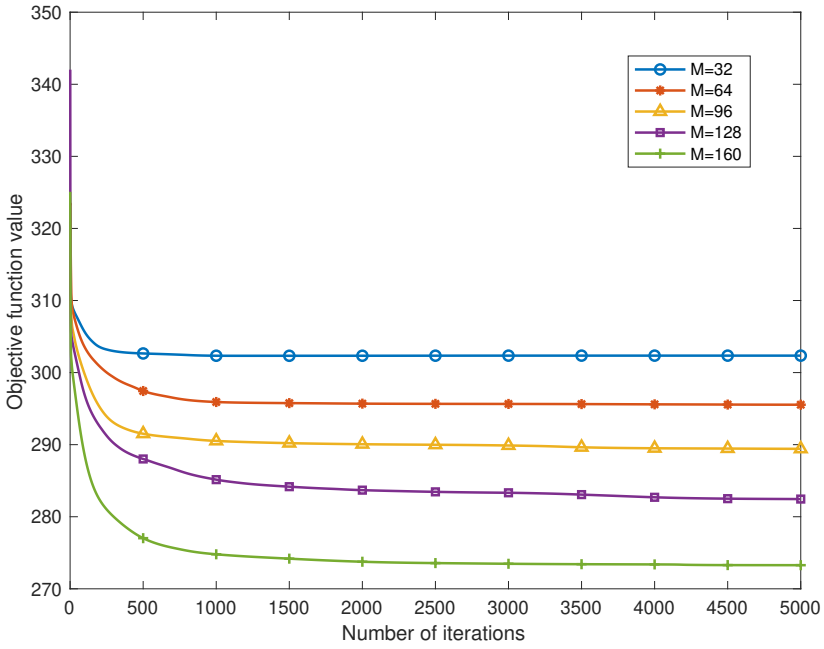

Figure 3.11: The convergence behaviour of the proposed algorithm.

surement indicator ι, which is defined as $\iota = \|\hat{\boldsymbol{t}} - \hat{\boldsymbol{p}}\|_2$, where $\hat{\boldsymbol{t}} = \boldsymbol{t}(K_Q, K_R)$, $\hat{\boldsymbol{p}} = \boldsymbol{p}(K_Q, K_R)$. Then, ι for the four cases are 16.06, 10.50, 16.85, and 14.88 dB, respectively. It can be seen that the optimized power pattern always matches well with the target pattern with the minimized deviation. Our proposed algorithm is robust against different numbers and sizes of both illumination and null areas.

3.4 Summary

In this chapter, we investigate a RIS-assisted multi-user (MU) communication system, where a RIS is deployed to generate a flat broadbeam for robust coverage without known accurate CSI or feedback mechanism. This design holds promise for practical deployment as channel estimation is always a challenging issue in RIS-assisted systems due to its high complexity, high latency, and low accuracy. We first investigate the generation of single broadbeam. We mathematically derive the maximum average radiated power that could be achieved in a cover area with an arbitrary size, and propose a broad beam-width design where the average radiated power is maximized and a minimal fluctuation is allowed in the beampattern by optimizing RIS phase shifts. In order to address this non-convex problem, DC-SDP algorithm is applied. Compared with other state-of-the-art algorithms, we have well-transformed the non-convex constraint into convex form and the unit modulus characteristic of RIS weights

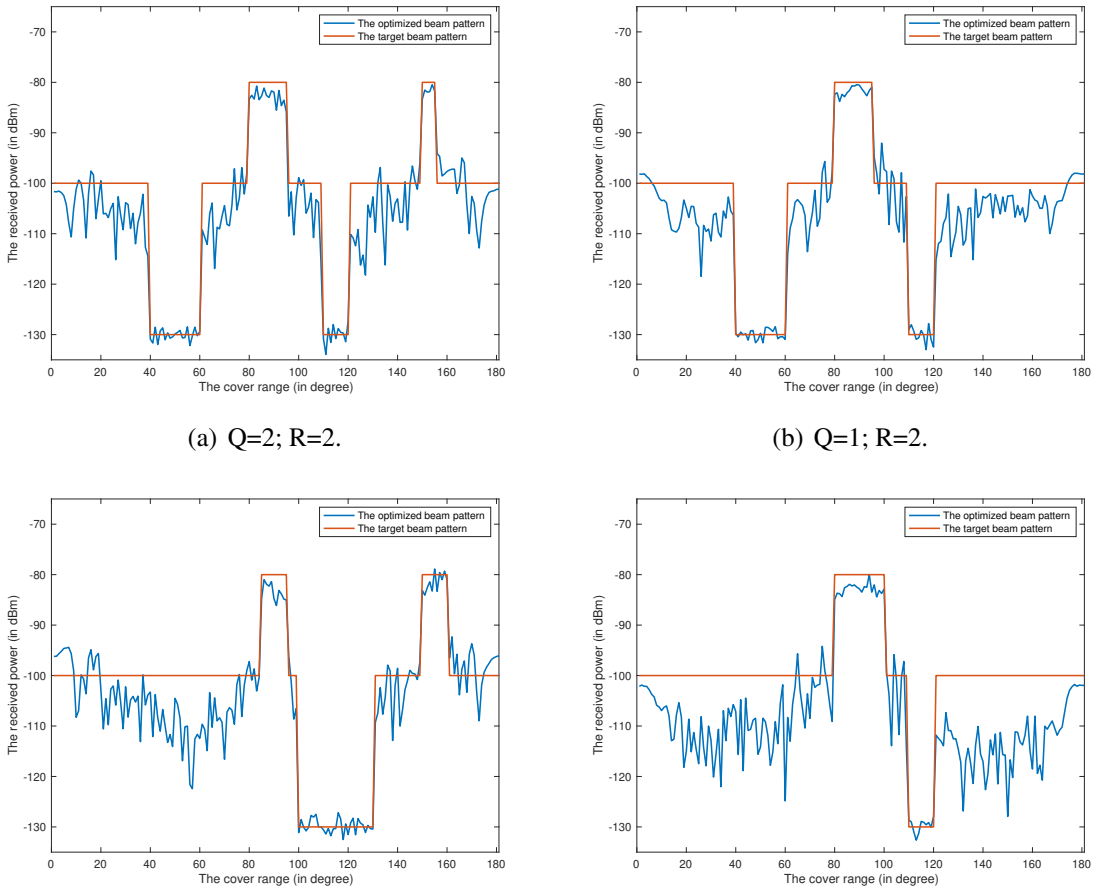

(a) Q=2; R=2.

(b) Q=1; R=2.

(c) Q=2; R=1.

(d) Q=1; R=1.

Figure 3.12: The comparison between the target and optimized power pattern.

is retained. Simulation results verify our proposed corollaries and indicate that broadbeam with good flatness could be generated by our proposed approaches. Then, we study the generation of multiple broadbeams. The accurate CSI is not required as the robust coverage can be realized by the broadbeam, and at the same time signals are suppressed towards unwanted regions. Specifically, we propose an optimization problem to minimize the deviation between the desired and actual power patterns. To address the non-convexity, an ADMM-based algorithm is proposed, which formulates a Lagrangian function enabling the optimized RIS phase shifts within finite update iterations. Simulation results prove the convergence of our proposed algorithm and demonstrate the good match between the target and optimized power pattern. Overall, this work can be viewed as a foundation for the practical implementation of RIS on wireless communication enhancement and can also be seen as an initial step towards achieving channel estimation.

Chapter 4

Resource Allocation in RIS-Aided Non-Cooperative BS Networks

A broadbeam design on RIS has been given in the previous chapter, with in-depth analysis on the achievable average received power under both ULA and URA configurations. In this chapter, we focus on RIS-aided resource allocation under BSs' non-cooperation scheme. Due to cost and privacy concerns, different operators may not make an agreement on cooperatively utilizing RISs and sharing resources. In the presence of non-cooperative BSs from different operators, conventional resource allocation and RIS design are rendered inapplicable. Motivated by this fact, we explore the resource allocation scheme for RIS-assisted with cooperative and non-cooperative BSs. We start with the resource allocation investigation in a system comprising two non-cooperative BSs and one RIS, which is further generalized to a multi-RISs-multi-BSs network.

4.1 Introduction

In real-world settings, BSs operated by multiple companies may not collaborate on using RIS or sharing resources due to concerns about costs and security. This lack of cooperation makes UE association challenging, as BSs from different operators do not support seamless connection transitions. Furthermore, BSs from different operators might resist the influence of RISs with unverified properties. However, BSs under non-cooperation mode might still direct signals towards RISs due to the presence of UEs and RISs managed by cooperative BSs in the same vicinity. Regulatory constraints make adjusting BS configurations and placements significantly more expensive and difficult compared to configuring RISs, especially considering their low-cost and flexible properties. Therefore, it is more feasible to reconfigure RISs to minimize their impact on non-cooperative BSs. In this non-cooperative context, resource

allocation merits further investigation.

Motivated by this fact, we studied the resource allocation scheme for a RIS-aided communication system with cooperative and non-cooperative BSs. On one side, multiple BSs operate in cooperation mode, jointly leveraging RISs to enhance the performance of UEs associated with the respective BSs. The resource allocation among them is also studied. On the other side, the RISs are engineered to mitigate their impact on the links between non-cooperative BSs and the corresponding UEs they serve. We start with a sub-6 GHz communication system with only two non-cooperative BSs and a single RIS. Specifically, we formulate the joint optimization problem of the reflection coefficients of RISs, power allocation, and sub-channel assignment at RIS-aided BS. The objective is to maximize the sum rates for UEs served by the RIS-aided BS while ensuring the channel gain constraints between another BS and its associated UEs so as to mitigate the effects of RISs on the communication of the non-cooperative BS. We then generalize the two BSs ans a single RIS scenario to multi-RISs-multi-BSs network, where the active beamforming at cooperative BSs, the reflection coefficients of RISs, power allocation, and UE association are jointly optimized for the sum rate maximization. We model the general scenario under mmWave band to facilitate a more comprehensive investigation on the resource allocation for RIS-aided communication system with cooperative and non-cooperative BSs.

4.2 Resource Allocation for Single c-BS - n-BS - RIS System

4.2.1 System Model under Sub-6GHz Frequency Band

Under BSs' non-cooperation scheme, we model a RIS-aided MU downlink communication system as in Fig.4.1. We assume that c-BS controls the RIS with M passive antennas, while the communication of n-BS should not be affected by the RIS. In detail, n-BS from another operator works under an orthogonal frequency band of c-BS and does not need the RIS. Let $\mathbf{w} = [w_1, w_2, ..., w_M]^H$ denote the RIS weight vector and each element $w_m, m = 1, \cdots, M$ in $\mathbf{w}$ could be expressed as $w_m = \beta_m e^{j\alpha_m}$. For maximum reflection efficiency, we let $\beta_m = 1$ and $\alpha_m \in [0, 2\pi]$. The number of UEs served by c-BS and n-BS are $K_{\mathcal{C}}$ and $K_{\mathcal{N}}$, respectively. Then, the sets of UEs served by c-BS and n-BS are represented as $\mathcal{K}_{\mathcal{C}} = \{1, \cdots, K_{\mathcal{C}}\}$ and $\mathcal{K}_{\mathcal{N}} = \{1, \cdots, K_{\mathcal{N}}\}$. Moreover, $j = \{0, 1\}$ is used to distinguish the BSs. Particularly, $j = 0$ refers to c-BS, while $j = 1$ refers to n-BS. All UEs are with a single antenna. Besides, both c-BS and n-BS have N elements. Specifically, we assume that the transmit beamforming vector for a specific UE k is $\mathbf{b}_k \in \mathbb{C}^{N\times 1}$.

We denote $\mathbf{h}_{\mathbf{d}_{j,k}} \in \mathbb{C}^{N\times 1}$, $\mathbf{G}_j \in \mathbb{C}^{M\times N}$, and $\mathbf{h}_{\mathbf{r}_{j,k}} \in \mathbb{C}^{M\times 1}$ as the channel expressions of BS-

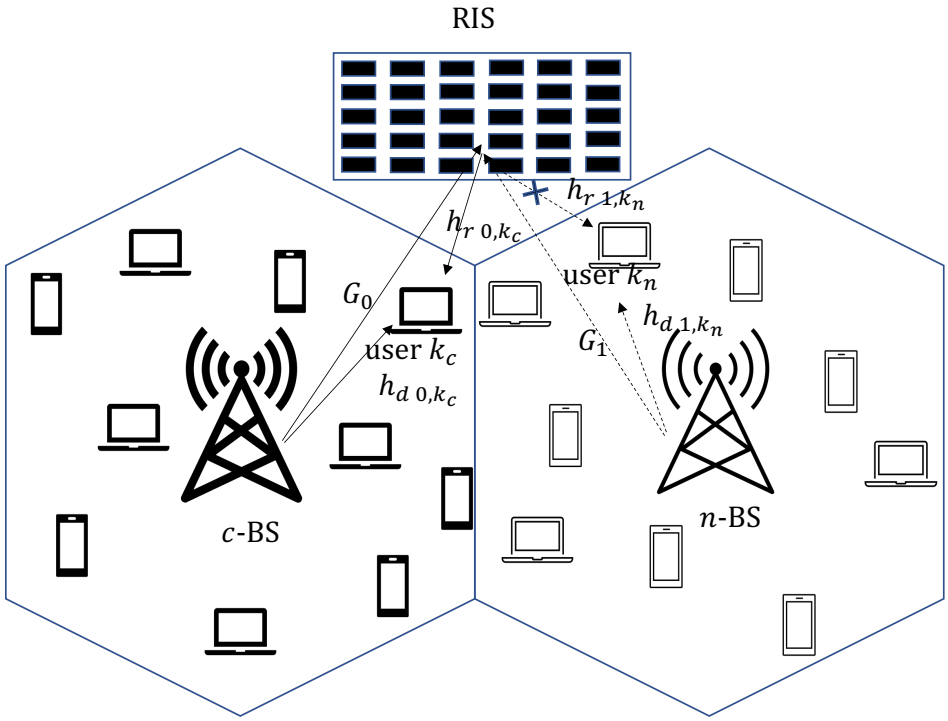

Figure 4.1: System model of BSs' non-cooperation scheme.

UE k, BS-RIS, and RIS-UE k, respectively, where $k \in \{\mathcal{K}_\mathcal{C}, \mathcal{K}_\mathcal{N}\}$, $j = \{0,1\}$. Specifically, k_c and k_n denotes the UE belonging to the set of $\mathcal{K}_\mathcal{C}$ and $\mathcal{K}_\mathcal{N}$, respectively. In addition, the power allocation vector of c-BS is denoted as $\mathbf{p} \in \mathbb{C}^{1\times K_\mathcal{C}}$. And $\sum_{u=1}^{K_\mathcal{C}} p_u \leq P_{\max}$ satisfies. Then, the received signal at UE k_c served by c-BS could be expressed as

$$y_{k_c} = (\mathbf{h}_{\mathbf{d}0,k_c}^H + \mathbf{h}_{\mathbf{r}0,k_c}^H \mathbf{W}\mathbf{G}_0) \sum_{u=1}^{K_\mathcal{C}} \mathbf{b}_u s_u p_u + n_{k_c}, \forall k_c \in \mathcal{K}_\mathcal{C}, \tag{4.1}$$

where $\mathbf{W} = \text{diag}(\mathbf{w}^T) \in \mathbb{C}^{M\times M}$ and n_{k_c} is the AWGN with zero mean and variance σ_n^2, i.e., $n_{k_c} \sim \mathcal{CN}(0, \sigma_n^2)$. Assume that there are L sub-channels in total, K_l represents the number of UE within the same l-th sub-channel of the UE k, where $K_l \leq K_{th}, \forall l \in L$. K_{th} denotes the maximum number of UE that one sub-channel can carry. We use matrix $\mathbf{B} \in \mathbb{C}^{K_\mathcal{C}\times L}$ to quantify the sub-channel assignment. Specifically, $\mathbf{B}(k,l) = 1$ denotes that the UE k is allocated to the l-th sub-channel; otherwise $\mathbf{B}(k,l) = 0$. Assume that each UE can only be allocated to one sub-channel, then we have

$$\sum_{l=1}^{L} \mathbf{B}(k_c, l) = 1, \forall k_c \in \mathcal{K}_\mathcal{C}. \tag{4.2}$$

We apply the ULA configuration to channel vectors, which is generally expressed as

$$\mathbf{a}_{\mathrm{ULA}}(\theta, f) = [1, e^{j\frac{2\pi f}{c}d\cos\theta}, \cdots, e^{j\frac{2\pi f}{c}d(N-1)\cos\theta}]^T. \tag{4.3}$$

We assume that the direct link $\mathbf{h_d}_{j,k}$ follows Rayleigh fading, while RIS-aided channels $\mathbf{h_r}_{j,k}$ and $\mathbf{G}_j$ follow Rician fading. Then $\mathbf{h_d}_{j,k}$, $\mathbf{h_r}_{j,k}$, and $\mathbf{G}_j$ are modeled as

$$\mathbf{h_d}_{j,k} = \mathrm{PL}_{\mathrm{NLOS}}\overline{\mathbf{h}}_{\mathbf{d}}, \tag{4.4}$$

$$\mathbf{h_r}_{j,k} = \mathrm{PL}_{\mathrm{LOS},k}(\sqrt{\frac{\varepsilon}{\varepsilon+1}}\mathbf{a}(\theta_{R,k}, f_l) + \sqrt{\frac{1}{\varepsilon+1}}\overline{\mathbf{h}}_{\mathbf{r}}{}_{j,k}), \tag{4.5}$$

$$\mathbf{G}_j = \mathrm{PL}_{\mathrm{LOS},0}(\sqrt{\frac{\varepsilon}{\varepsilon+1}}\mathbf{a}(\theta_{R,0}, f_l)\mathbf{a}^T(\theta_B, f_l) + \sqrt{\frac{1}{\varepsilon+1}}\overline{\mathbf{G}}). \tag{4.6}$$

Note that f_l denotes the operating frequency on the l-th sub-channel. $\mathrm{PL}_{\mathrm{NLOS}}$, $\mathrm{PL}_{\mathrm{LOS},k}$ and $\mathrm{PL}_{\mathrm{LOS},0}$ denote the corresponding path-loss. ε is the Rician factor. $\theta_{R,k}$, $\theta_{R,0}$, and θ_B denote the departing angle towards UE k, incident angle at RIS and departing angle at BS towards RIS, respectively. $\overline{\mathbf{h}}_{\mathbf{d}}{}_{j,k}$, $\overline{\mathbf{h}}_{\mathbf{r}}{}_{j,k}$, and $\overline{\mathbf{G}}$ denote the NLoS components of channels, each element of which follows $\mathcal{CN}(0,1)$.

Consider c-BS applying MRT for maximal power transmission, we approximate

$$\mathbf{b}_{k_c} = \mathbf{a}^*(\theta_B, f_l),\ \forall k_c \in K_{\mathcal{C}}. \tag{4.7}$$

For simplicity, we let $\mathbf{b} = \mathbf{b}_{k_c}, \forall k_c \in K_{\mathcal{C}}$. Then, we denote

$$h_{d0,k} = \mathbf{h}_{\mathbf{d}0,k}^H\mathbf{b}, \tag{4.8}$$

$$\mathbf{f}(\theta_{R,0}, f_l) = \mathbf{G}_0\mathbf{b}. \tag{4.9}$$

The received signal y_{k_c} in (4.1) can be transformed to

$$y_{k_c} = (h_{d0,k_c} + \mathbf{h}_{\mathbf{r}0,k_c}^H\mathbf{W}\mathbf{f}(\theta_{R,0}, f_l))\sum_{u=1}^{K_l} s_u p_u + n_{k_c}. \tag{4.10}$$

We abbreviate $\mathbf{f}(\theta_{R,0}, f_l)$ to $\mathbf{f}$ throughout the chapter. Then, the SINR for the UE k_c could be represented as

$$\mathrm{SINR}_{k_c} = \frac{|(h_{d0,k_c} + \mathbf{h}_{\mathbf{r}0,k_c}^H\mathbf{W}\mathbf{f})|^2 p_{k_c}}{|(h_{d0,k_c} + \mathbf{h}_{\mathbf{r}0,k_c}^H\mathbf{W}\mathbf{f})|^2 \sum_{u\neq k_c}^{K_l} p_u + \sigma_n^2}, \tag{4.11}$$

where $\mathrm{SINR}_{k_c} \geq \mathrm{SINR}_{th}, \forall k_c \in \mathcal{K}_{\mathcal{C}}$. Based on (4.11), we could get the expression of the

sum-rate of UE served by c-BS as

$$R = \sum_{u=1}^{K_{\mathcal{C}}} \log_2(1 + \mathrm{SINR}_u). \tag{4.12}$$

In addition, the signal received by the UE k_n within the adjacent cell and served by n-BS could be expressed as

$$y_{k_n} = (\mathbf{h}_{\mathbf{d}}^H{}_{1,k_n} + \mathbf{h}_{\mathbf{r}}^H{}_{1,k_n} \mathbf{W}\mathbf{G}_1) \sum_{r=1}^{K_\eta} \mathbf{b}_r s_r p_r + n_{k_n}, \forall k_n \in \mathcal{K}\eta. \tag{4.13}$$

Consider the non-cooperation scheme, i.e., to mitigate the effect of RIS on n-BS-UE k_n links, the UE $k_n, \forall k_n \in \mathcal{K}\eta$ would receive comparable signals when only direct link exists as when the RIS-aided reflective links also exist. Then, we have

$$y_{k_n} \approx \mathbf{h}_{\mathbf{d}}^H{}_{1,k_n} \sum_{r=1}^{K_\eta} \mathbf{b}_r s_r p_r + n_{k_n}. \tag{4.14}$$

By combining (4.13) and (4.14), we get

$$\|\mathbf{h}_{\mathbf{r}}^H{}_{1,k_n} \mathbf{W}\mathbf{G}_1\| \leq \delta, \ \forall k_n \in \mathcal{K}\eta, \tag{4.15}$$

where δ denotes the threshold for the channel gain of the reflective link n-BS-RIS-UE k_n, which should satisfy $0 < \delta \ll 1$ to guarantee the largely mitigated impact of RIS.

By jointly considering the power allocation $\mathbf{p}$, sub-channel assignment $\mathbf{B}$ at c-BS, and the RIS passive beamforming $\mathbf{w}$, we formulate the following optimization problem:

$$\begin{aligned}
\text{(P4-1)} \ : \max_{\mathbf{p},\mathbf{B},\mathbf{w}} \quad & R && \text{(4.16a)}\\
\text{s.t.} \quad & \mathrm{SINR}_{k_c} \geq \mathrm{SINR}_{th}, \forall k_c \in \mathcal{K}_{\mathcal{C}}, && \text{(4.16b)}\\
& \|\mathbf{h}_{\mathbf{r}}^H{}_{1,k_n} \mathbf{W}\mathbf{G}_1\| \leq \delta, \forall k_n \in \mathcal{K}\eta, && \text{(4.16c)}\\
& K_l \leq K_{th}, \forall l \in L, && \text{(4.16d)}\\
& \sum_{u=1}^{K_{\mathcal{C}}} p_u \leq P_{\max}, && \text{(4.16e)}\\
& \sum_{l=1}^{L} \mathbf{B}(k,l) = 1, \forall k_c \in \mathcal{K}_{\mathcal{C}}, && \text{(4.16f)}\\
& |w_m| = 1, m = 1, \cdots, M. && \text{(4.16g)}
\end{aligned}$$

Algorithm 4 Sub-channel assignment optimization based on two-sided Matching (TSM) algorithm — Matching Sets Initialization

Input: $\mathbf{Z} = \mathbf{0} \in \mathbb{C}^{K_{\mathcal{C}} \times L}$,$\mathbf{r} = \emptyset$, $\mathbf{s_0} = \mathbf{0} \in \mathbb{C}^{1 \times K_{\mathcal{C}}}$, $\mathbf{v} = \mathbf{0} \in \mathbb{C}^{1 \times K_{\mathcal{C}}}$.
while $\mathcal{K}_{\mathcal{C}} \neq \emptyset$ **do**
  for $k = 1 : K_{\mathcal{C}}$ **do**
    for $l = 1 : L$ **do**
      if $\mathbf{Z}(\mathcal{K}_{\mathcal{C}}(k), l) == 0$ **then**
        $\mathbf{g}(l) = |(h_{d0,k_c} + \mathbf{h}_{\mathbf{r}0,k_c}^H \mathbf{W}\mathbf{f})|^2$;
      else
        $\mathbf{g}(l) = 0$;
      end if
    end for
    $[\mathbf{v}(\mathcal{K}_{\mathcal{C}}(k)), \mathbf{s_0}(\mathcal{K}_{\mathcal{C}}(k))] = \max(\mathbf{g})$;
  end for
  for $l = 1 : L$ **do**
    $\mathbf{x} = \text{find}(\mathbf{s_0} == l)$;
    if $\mathcal{L}(\mathbf{x}) \leq K_{th}$ **then**
      $\mathbf{Z}(\mathbf{x}, l) = 1$;
    else
      get $\widetilde{\mathbf{x}}$ as the sorted $\mathbf{x}$ corresponding to $\mathbf{v}(\widetilde{\mathbf{x}})$ in a descend manner;
      update $\mathbf{Z}(\widetilde{\mathbf{x}}(1 : K_{\mathcal{C}}), l) = 1$, and $\mathbf{Z}(\widetilde{\mathbf{x}}(K_{\mathcal{C}} + 1 : \mathcal{L}(\mathbf{x})), l) = 2$;
    end if
  end for
  $[\mathbf{r}, \mathbf{c}] = \text{find}(\mathbf{Z} == 1)$, $\mathcal{K}_{\mathcal{C}} = \mathcal{K}_{\mathcal{C}} \setminus \mathbf{r}$;
end while
Output: $\mathbf{s_0}$.

Note that this problem is challenging due to the non-convexity of the objective function and multiple constraints. And there is no standard method to get a global-optimal solution. In the following, we develop the BCD algorithm to solve the problem (P4-1).

4.2.2 Sub-channel Assignment Design

We firstly initialize $\mathbf{p}$ as $p_{k_c} = P_{max}/K_{\mathcal{C}}, \forall k_c \in \mathcal{K}_{\mathcal{C}}$. And $\mathbf{w}$ is initialized as $w_m = \angle\widetilde{h_{d0,k_c}} - \angle\widetilde{[\mathbf{g}_{k_c}]_m}$ as in [58], where $\mathbf{g}_{k_c} = \mathbf{h}_{\mathbf{r}0,k_c}^H \text{diag}(\mathbf{f})$, and $[\widetilde{h_{d0,k_c}}, \widetilde{g_{k_c}}] = \arg\min_{k_c \in \mathcal{K}_{\mathcal{C}}} |h_{d0,k_c}|$. With fixed $\mathbf{p}$ and $\mathbf{w}$, the formulated problem can be transformed as

$$(\text{P4-1.1}): \quad \max_{\mathbf{B}} \quad R \tag{4.17}$$

$$\text{s.t.} \quad (4.16\text{b}), (4.16\text{d}), (4.16\text{f}). \tag{4.18}$$

In order to solve this discrete optimization problem, the TSM algorithm [148] is applied. Specifically, the algorithm can be decomposed into two processes.

Algorithm 5 Sub-channel assignment optimization based on TSM algorithm — Matching Stability Verification

Input: $\mathbf{s_0}$.
for $k = 1 : K_{\mathcal{C}}$ **do**
  $\mathbf{sv} = \mathbf{0} \in \mathbb{C}^{1\times K_{\mathcal{C}}}$;
  $\mathbf{f} = \text{find}(\mathbf{s_0} == \mathbf{s_0}(k))$;
  Find the set of UE allocated to different sub-channels to the k-th UE by $\mathbf{d} = \mathcal{K}_{\mathcal{C}} \setminus \mathbf{f}$;
  for $j = 1 : \mathcal{L}(\mathbf{d})$ **do**
    $\tilde{l} = \mathbf{s_0}(j)$;
    calculate R_1 and R_2;
    swap the k-th and $\mathbf{d}(j)$-th UE to each other's sub-channel; calculate $\widetilde{R_1}$ and $\widetilde{R_2}$;
    if $|\widetilde{R_1} + \widetilde{R_2}| \geq |R_1 + R_2|$ & $\text{SINR}_u \geq \text{SINR}_{th}$, $\text{SINR}_u \in \{\mathbf{SINR}_l, \mathbf{SINR}_{\tilde{l}}\}$ **then**
      $\mathbf{sv}(\mathbf{d}(j)) = |\widetilde{R_1} + \widetilde{R_2} - R_1 - R_2|$;
    end if
    Find the maximum value in $\mathbf{sv}$ and the corresponding $\widetilde{\mathbf{d}(j)}$-th UE;
    $\mathbf{s_0}(k) \leftrightarrow \mathbf{s_0}(\widetilde{\mathbf{d}(j)})$;
    update $\hat{\mathbf{s_0}} = \mathbf{s_0}$;
  end for
end for
Output: $\hat{\mathbf{s_0}}$.

- **Matching sets initialization:** We firstly initialize $\mathbf{Z} = \mathbf{0} \in \mathbb{C}^{K_{\mathcal{C}}\times L}$, which records the matching states between UE and sub-channels. Specifically, '0', '1', and '2' denote 'Unallocated', 'Accepted', and 'Rejected', respectively. In each iteration, we calculate the channel gain $|(h_{d0,k_c} + \mathbf{h}_{\mathbf{r}0,k_c}^H \mathbf{W}\mathbf{f})|^2$ for all UEs that have not been accepted. The channel gains vary on different sub-channels. Then, UEs are assigned to channels that can achieve the highest gains and have not been rejected by that channel before. After that, the sub-channel chooses UE with the highest channel gain and rejects the others. The iteration ends when all UE are accepted by one specific sub-channel. The procedure is shown as **Algorithm 4**.

- **Matching stability verification:** An unstable matching pair is defined as a pair of elements that prefer each other over the state they have already matched. A UE will be paired with others that are allocated to different sub-channels in each iteration. Assume that the UE is on the l-th sub-channel and the potential switching UE is on the $\tilde{l}$-th sub-channel. The sum-rate on the l-th sub-channel before and after switching is defined as R_1 and $\widetilde{R_1}$, respectively. Similarly, the sum-rate on the $\tilde{l}$-th sub-channel before and after switching is R_2 and $\widetilde{R_2}$, respectively. Then the switching pair is determined by (a) $\max|\widetilde{R_1} + \widetilde{R_2} - R_1 - R_2|$; (b) $\text{SINR}_u \geq \text{SINR}_{th}$, $\text{SINR}_u \in \{\mathbf{SINR}_l, \mathbf{SINR}_{\tilde{l}}\}$, where $\{\mathbf{SINR}_l, \mathbf{SINR}_{\tilde{l}}\}$ denotes the SINR sets of UE on l-th and $\tilde{l}$-th sub-channels. This procedure is summarized as in **Algorithm 5**.

The output $\hat{\mathbf{s_0}}$ can be easily transformed to the matrix $\mathbf{B}_{\text{opt}}$ by $\mathbf{B}_{\text{opt}}(k, \hat{\mathbf{s_0}}(k)) = 1, \forall k_c \in \mathcal{K}_{\mathcal{C}}$, while other elements in $\mathbf{B}_{\text{opt}}$ are fixed to be 0.

4.2.3 Power Allocation Design

Given $\mathbf{B}$ and $\mathbf{w}$, the problem (P4-1) can be simplified as

$$\text{(P4-1.2)}: \max_{\mathbf{p}} \quad R \tag{4.19}$$

$$\text{s.t.} \quad \text{(4.16b), (4.16e).} \tag{4.20}$$

To address the non-convexity of the objective function, we introduce a new variable set $\chi = \{\chi_1, \cdots, \chi_{K_{\mathcal{C}}}\}$. Then we let

$$\frac{|(h_{d0,k_c} + \mathbf{h}_{\mathbf{r}0,k_c}^H \mathbf{W}\mathbf{f})|^2 p_{k_c}}{|(h_{d0,k_c} + \mathbf{h}_{\mathbf{r}0,k_c}^H \mathbf{W}\mathbf{f})|^2 \sum_{u \neq k_c}^{K_l} p_u + \sigma_n^2} \geq \chi_{k_c}, \forall k_c \in \mathcal{K}_{\mathcal{C}}, \tag{4.21}$$

which could be further represented as

$$p_{k_c} \geq \chi_{k_c} (\sum_{u \neq k_c}^{K_l} p_u + \mu_{k_c}), \forall k_c \in \mathcal{K}_{\mathcal{C}}, \tag{4.22}$$

where $\mu_{k_c} = \frac{\sigma_n^2}{|(h_{d0,k_c} + \mathbf{h}_{\mathbf{r}0,k_c}^H \mathbf{W}\mathbf{f})|^2}$. The optimization problem (P4-1.2) can be then rewritten as

$$\text{(P4-1.2.1)}: \max_{\mathbf{p}, \boldsymbol{\chi}} \quad \sum_{u=1}^{K_{\mathcal{C}}} \log_2(1 + \chi_u) \tag{4.23}$$

$$\text{s.t.} \quad \chi_{k_c} \geq \text{SINR}_{th}, \forall k_c \in \mathcal{K}_{\mathcal{C}} \tag{4.24}$$

$$\text{(4.16e), (4.22).} \tag{4.25}$$

However, (4.22) is still non-convex. In order to address this issue, we apply the convex upper bound approximation [149].

Lemma 2: *Given $g(x, y) = xy$ and $f(x, y) = \frac{\alpha}{2}x^2 + \frac{1}{2\alpha}y^2 (\alpha > 0)$, $f(x, y) \geq g(x, y)$ always holds. Specifically, when $\alpha = \frac{y}{x}$, there are $f(x, y) = g(x, y)$. Note that $f(x, y)$ is convex.*

Based on **Lemma 2**, we rewrite the non-convex term $\chi_k \sum_{u \neq k}^{K_l} p_u$ in (4.22) as

$$\chi_{k_c} \sum_{u \neq k_c}^{K_l} p_u \leq \frac{\alpha_{k_c}}{2} \chi_{k_c}^2 + \frac{1}{2\alpha_{k_c}} (\sum_{u \neq k_c}^{K_l} p_u)^2. \tag{4.26}$$

Algorithm 6 Proposed power allocation algorithm based on convex upper bound approximation

Input: $\mathbf{p}^0 \in \mathbb{C}^{1\times K_{\mathcal{C}}}$, $\boldsymbol{\chi}^0 \in \mathbb{C}^{1\times K_{\mathcal{C}}}$, $t_1 = 1$.
repeat
Obtain $\alpha_{k_c}^{t_1}, \forall k_c \in \mathcal{K}_{\mathcal{C}}$ by (4.27);
Solve (P4-1.2.2) by CVX toolbox, and get $\mathbf{p}^{t_1}$, $\boldsymbol{\chi}^{t_1}$;
$t_1 = t_1 + 1$;
until convergence reaches
Output: $\mathbf{p}^{t_1}$, $\boldsymbol{\chi}^{t_1}$.

When $\alpha_{k_c} = \frac{\sum_{u\neq k_c}^{K_l} p_u}{\chi_{k_c}}$, the equality holds. Then successive convex approximation algorithm is applied to solve (P4-1.2.1). Specifically, the $\alpha_{k_c}^{t_1}$ in the t_1-th iteration is obtained by $(\sum_{u\neq k_c}^{K_l} p_u)^{t_1-1}$ and $\chi_{k_c}^{t_1-1}$, which is expressed as

$$\alpha_{k_c}^{t_1} = \frac{(\sum_{u\neq k_c}^{K_l} p_u)^{t_1-1}}{\chi_{k_c}^{t_1-1}}. \tag{4.27}$$

And (4.22) can be consequently rewritten in the convex form as

$$p_{k_c} \geq \frac{\alpha_{k_c}^{t_1}}{2}\chi_{k_c}^2 + \frac{1}{2\alpha_{k_c}^{t_1}}(\sum_{u\neq k_c}^{K_l} p_u)^2 + \chi_{k_c}\mu_{k_c}, \forall k_c \in \mathcal{K}_{\mathcal{C}}. \tag{4.28}$$

The optimization of (P4-1.2) can be therefore transformed into iteratively solving the problem (P4-1.2.2), which is expressed as

$$\text{(P4-1.2.2)} \quad \max_{\mathbf{p},\boldsymbol{\chi}} \quad \sum_{u=1}^{K_{\mathcal{C}}} \log_2(1+\chi_u) \tag{4.29}$$

$$\text{s.t.} \quad \text{(4.16e)}, \text{(4.24)}, \text{(4.28)}. \tag{4.30}$$

Note that the problem (P4-1.2.2) is convex and can be easily solved by CVX toolbox. The iteration ends until it converges. The algorithm is summarized as **Algorithm 6**. Finally, we get the optimized power allocation vector $\hat{\mathbf{p}} = \mathbf{p}^{t_1}$.

4.2.4 RIS Passive Beamforming Design

We fix the variables $\mathbf{p}$ and $\mathbf{B}$ and optimize $\mathbf{w}$, then the problem (P4-1) can be simplified as

$$\text{(P4-1.3)} \quad \max_{\mathbf{w}} \quad O(\mathbf{w}) = R \tag{4.31}$$

$$\text{s.t.} \quad \text{(4.16b)}, \text{(4.16c)}, \text{(4.16g)}. \tag{4.32}$$

Inspired by [150], the objective function in (P4-1.3) is a standard multi-ratio fractional programming (FP) problem. The quadratic transformation method is applied, which efficiently transforms the fractional form into a quadratic function. Specifically, we introduce a new variable set $\boldsymbol{\lambda} = [\lambda_1, \cdots, \lambda_{K_\mathcal{C}}]^T$, and we further define $\mathbf{g}_{k_c} = \text{diag}(\mathbf{h}_{\mathbf{r}0,k_c}^H)\mathbf{f}$. Then the objective function is rewritten as

$$O(\boldsymbol{\lambda}, \mathbf{w}) = \sum_{k_c \in \mathcal{K}_\mathcal{C}} \log_2(1+2\lambda_{k_c}\sqrt{p_{k_c}}\mathcal{R}e\{h_{d0,k_c}+\mathbf{w}^H\mathbf{g}_{k_c}\}-\lambda_{k_c}^2(\sum_{u\neq k_c}^{K_I} p_u|h_{d0,k_c}+\mathbf{w}^H\mathbf{g}_{k_c}|^2+\sigma_n^2)), \tag{4.33}$$

which can be maximized by iteratively optimizing $\boldsymbol{\lambda}$ and $\mathbf{w}$. Particularly, with the optimized $\mathbf{w}^{t_2-1}$ in the (t_2-1)-th iteration, the $\lambda_{k_c}^{t_2}$ can be obtained as

$$\lambda_{k_c}^{t_2} = \frac{\sqrt{p_{k_c}}\mathcal{R}e\{h_{d0,k_c}+(\mathbf{w}^{t_2-1})^H\mathbf{g}_{k_c}\}}{\ln(2)(\sum_{u\neq k_c}^{K_I} p_u|h_{d0,k_c}+(\mathbf{w}^{t_2-1})^H\mathbf{g}_{k_c}|^2+\sigma_n^2)}. \tag{4.34}$$

With given $\lambda_{k_c}^{t_2}$, the SINR_{k_c} part with respect to $\mathbf{w}$ is denoted as

$$\text{SINR}_{k_c} = -\mathbf{w}^H\boldsymbol{\Lambda}_{k_c}\mathbf{w}+2\mathcal{R}e\{\mathbf{w}^H\mathbf{v}_{k_c}\}+\varphi_{k_c}, \tag{4.35}$$

where $\boldsymbol{\Lambda}_{k_c}$,$\mathbf{v}_{k_c}$, and φ_{k_c} are defined as

$$\boldsymbol{\Lambda}_{k_c} = (\lambda_{k_c}^{t_2})^2\sum_{u\neq k_c}^{K_I} p_u(h_{d0,k_c}+\mathbf{g}_{k_c}\mathbf{g}_{k_c}^H), \tag{4.36}$$

$$\mathbf{v}_{k_c} = 2\lambda_{k_c}^{t_2}\sqrt{p_{k_c}}\mathbf{g}_{k_c} - (\lambda_{k_c}^{t_2})^2\sum_{u\neq k_c}^{K_I} p_u h_{d0,k_c}^*\mathbf{g}_{k_c}, \tag{4.37}$$

$$\varphi_{k_c} = 2\lambda_{k_c}^{t_2}\sqrt{p_{k_c}}\mathcal{R}e\{h_{d0,k_c}\} - (\lambda_{k_c}^{t_2})^2(\sum_{u\neq k_c}^{K_I} p_u|h_{d0,k_c}|^2+\sigma_n^2). \tag{4.38}$$

Then by taking (4.35) into the objective function, the optimization of $\mathbf{w}$ in the t_2-th iteration could be summarized as

$$\text{(P4-1.3.1)} \quad \max_{\mathbf{w}} \quad \sum_{u=1}^{K_\mathcal{C}} \log_2(1+\text{SINR}_u) \tag{4.39}$$

$$\text{s.t.} \quad \text{(4.16b)}, \text{(4.16c)}, \text{(4.16g)}. \tag{4.40}$$

We notice that (P4-1.3.1) is still non-convex due to the non-convex constraint (4.16b) and (4.16g). To address the non-convexity of (4.16g), the penalty method is firstly applied, which

rewrite (4.16g) into the objective function by multiplying a positive penalty factor τ. Then the objective function could be consequently expressed as

$$O'(\mathbf{w}) = \sum_{u=1}^{K_{\mathcal{C}}} \log_2(1+\mathrm{SINR}_u) + \tau \sum_{m=1}^{M} (|\theta_m|^2 - 1). \tag{4.41}$$

Sequentially, (P4-1.3.1) can be rewritten as

$$\text{(P4-1.3.2)} \quad \max_{\mathbf{w}} \quad O'(\mathbf{w}) \tag{4.42}$$

$$\text{s.t.} \quad (4.16\text{b}), (4.16\text{c}) \tag{4.43}$$

$$|w_m| \leq 1, \quad m = 1, \cdots, M. \tag{4.44}$$

Then, we deal with the non-convexity of the non-convex term in $O'(\mathbf{w})$ and (4.16b) by SCA. We represent the first-order Taylor series approximation of the objective function as

$$O''(\mathbf{w}) = \sum_{u=1}^{K_{\mathcal{C}}} \log_2(1+\mathrm{SINR}_u) + \tau \sum_{m=1}^{M} w_m^{t_2}(w_m - w_m^{t_2}). \tag{4.45}$$

We further define

$$\imath_{k_c} = \mathscr{R}e\{h_{d0,k_c} + \mathbf{w}^H \mathbf{g}_{k_c}\}, \tag{4.46}$$

$$i_{k_c} = \mathscr{I}m\{h_{d0,k_c} + \mathbf{w}^H \mathbf{g}_{k_c}\}. \tag{4.47}$$

Similarly, by applying the first-order Taylor series expansion, (4.16b) can be rewritten as

$$(\imath_{k_c}^{t_2-1})^2 + (i_{k_c}^{t_2-1})^2 + 2\imath_{k_c}^{t_2-1}(\imath_{k_c} - \imath_{k_c}^{t_2-1}) + 2i_{k_c}^{t_2-1}(i_{k_c} - i_{k_c}^{t_2-1}) \geq (\imath_{k_c}^2 + i_{k_c}^2)\epsilon + \xi, \forall k_c \in \mathcal{K}_{\mathcal{C}}, \tag{4.48}$$

where

$$\epsilon = \frac{\mathrm{SINR}_{th} \sum_{u \neq k_c}^{K_l} p_u}{p_k}, \tag{4.49}$$

$$\xi = \frac{\mathrm{SINR}_{th} \sigma_n^2}{p_{k_c}}. \tag{4.50}$$

Finally, the corresponding convex optimization problem with respect to $\mathbf{w}$ can be formulated as

$$\text{(P4-1.3.3)} \quad \max_{\mathbf{w}} \quad O''(\mathbf{w}) \tag{4.51}$$

$$\text{s.t.} \quad (4.16\text{c}), (4.44), (4.48). \tag{4.52}$$

The SCA is used to iteratively optimize $\mathbf{w}$, while in each iteration, the problem (P4-1.3.3) is

Algorithm 7 Proposed RIS beamforming optimization based on SCA

Input: $\mathbf{w}^0 \in \mathbb{C}^{M\times 1}$, $t_2 = 1$.
repeat
Obtain $\tau_{k_c}^{t_2-1}$ and $\iota_{k_c}^{t_2-1}$ by (4.46) and (4.47);
Obtain $\boldsymbol{\lambda}^{t_2} \in \mathbb{C}^{K_C\times 1}$ by (4.34);
Solve (P4-1.3.3) by CVX toolbox, and get $\mathbf{w}^{t_2}$;
$t_2 = t_2 + 1$;
until convergence reaches
Output: $\mathbf{w}^{t_2}$.

Algorithm 8 The overall BCD algorithm

Input: $\mathbf{w}^0 \in \mathbb{C}^{M\times 1}$, $\mathbf{p}^0 \in \mathbb{C}^{M\times 1}$, $t = 1$.
Obtain $\mathbf{s_0}$ by **Algorithm 4**;
Obtain $\hat{\mathbf{s_0}}$ by **Algorithm 5**;
Obtain $\mathbf{B}_{\text{opt}}$ based on $\hat{\mathbf{s_0}}$.
repeat
Given $\mathbf{B}_{\text{opt}}$ and $\mathbf{w}^{t-1}$, obtain $\mathbf{p}^t$ by **Algorithm 6**;
Given $\mathbf{B}_{\text{opt}}$ and $\mathbf{p}^t$, obtain $\mathbf{w}^t$ by **Algorithm 7**;
$t = t + 1$;
until convergence reaches
$\mathbf{p}_{\text{opt}} = \mathbf{p}^t$, and $\mathbf{w}_{\text{opt}} = \mathbf{w}^t$;
Output: $\mathbf{B}_{\text{opt}}$, $\mathbf{p}_{\text{opt}}$, and $\mathbf{w}_{\text{opt}}$.

a standard convex optimization problem and can be solved by CVX toolbox. The algorithm is summarized as **Algorithm 7**.

4.2.5 The Overall Solution

The overall algorithm for sum-rate maximization via jointly optimizing sub-channel assignment $\mathbf{B}$, power allocation $\mathbf{p}$, and passive RIS beamforming $\mathbf{w}$ is summarized as **Algorithm 8**.

4.2.6 Simulation Results

In this section, numerical examples are demonstrated to verify the effectiveness of our system model and algorithms. We place c-BS, n-BS, and RIS at $(200, 30)$m, $(220, 30)$m, and $(200, 0)$m, respectively. The radius of both cells is set to be 10 m. Assume that there are 20 UEs served by c-BS and 20 UEs served by n-BS. The center frequency of c-BS's working band is 2.5 GHz. The frequency band is divided into $L = 10$ sub-channels, where the bandwidth of each sub-channel is 20 kHz and can tolerant up to 2 UEs, i.e., $K_{th} = 2$. The Rician factor of RIS-aided channels is set to be 10. The path-loss in dB as a function of distance d is defined as $\text{PL}_{\text{LoS}} = 112.6 + 22.0\lg(d)$ and $\text{PL}_{\text{NLoS}} = 109.6 + 36.7.0\lg(d)$ for LoS and NLoS

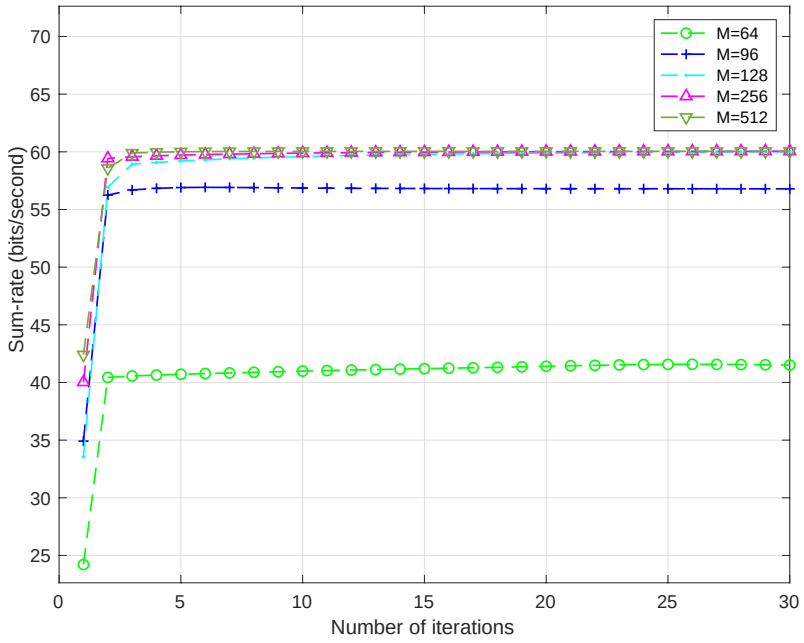

Figure 4.2: Convergence of the proposed algorithm.

paths, respectively. The SINR constraint for UEs served by c-BS is set as $\text{SINR}_{th} = 0.01$, and the constraint for the channel gain of n-BS-RIS-UEs served by n-BS is set as $\delta = 0.001$.

Fig. 4.2 demonstrates the convergence of our proposed algorithm. The transmit power at c-BS is set as $P_{\max} = 35$ dBm. And we verify the convergence under different RIS elements. It can be seen that the sum rate of UEs served by c-BS increases rapidly at initial, and converges to a stable value within limited iterations.

In Fig. 4.3, we study the effects of RIS reflecting elements and the total transmit power. Our proposed design is compared with the cases that (a) equal power allocation at c-BS; (b) no RIS is deployed. And we relax the SNR constraint (4.16b) under no RIS case as it can not be realized without the RIS-aided channels. Fig. 4.3 depicts that when only direct links exist, the sum rate could be extremely low. By introducing RIS and proposing the passive beamforming design, the sum rate increases significantly. Compared with the RIS-aided system where the transmit power is equally allocated, the achievable sum rate can be further improved by optimizing the power allocation.

Fig. 4.4 investigates the effects of RIS on n-BS - UEs served by n-BS channels. The random RIS weights design and optimization without constraint on the n-BS-RIS-UEs served by n-BS links, i.e., (4.16c), are used for comparison. It can be seen that both designs for comparison result in high average channel gains of n-BS-RIS-UEs served by n-BS links, revealing severe effects taken by RIS to the QoS in the cell worked by n-BS. In contrast, our proposed design enables low average channel gain of the reflective links, satisfying

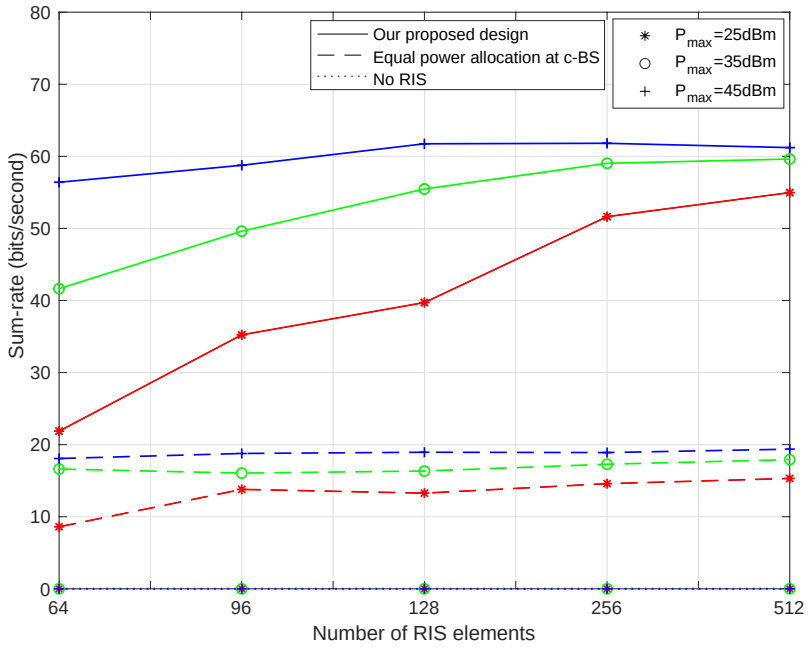

Figure 4.3: The Sum-rate for $M = \{64, 96, 128, 256, 512\}$, and $P_{\max} = \{25, 35, 45\}$ dBm.

$\|\mathbf{h}_{\mathbf{r}1,k_n}^H \mathbf{W}\mathbf{G}_1\| \leq \delta, \forall k_n \in \mathcal{K}_\eta$. It can be concluded that our proposed design alleviates the impacts of RIS on n-BS-served cells to large extents.

4.3 Resource Allocation for Multiple c-BSs - n-BSs - RISs Network

4.3.1 System Model under mmWave Frequency Band

As shown in Fig. 4.5, the system consists of J BSs, among which there are $J_\mathcal{C}$ BSs under the cooperation scheme, named c-BSs, jointly controlling the UE association and sharing the RISs. In addition, there are J_η BSs under the non-cooperation scheme, named n-BSs, which refused to be affected by the RISs and do not participate in the resource sharing and allocation. The sets of cooperative and non-cooperative BSs are denoted by $\mathcal{J}_\mathcal{C} = \{1, \cdots, J_\mathcal{C}\}$, $\mathcal{J}_\eta = \{1, \cdots, J_\eta\}$, respectively. Each BS is implemented with N antennas. The c-UE and n-UE are used to distinguish the UEs served by either cooperative or non-cooperative BSs. The number of c-UE and n-UE are $K_\mathcal{C}$ and K_η, respectively. All UEs have a single antenna. Similarly, we denote the sets of UE served by cooperative and non-cooperative BSs as $\mathcal{K}_\mathcal{C} = \{1, \cdots, K_\mathcal{C}\}$, $\mathcal{K}_\eta = \{1, \cdots, K_\eta\}$, respectively. Specifically, we assume that the transmit beamforming vector at the j-th BS for a specific UE k

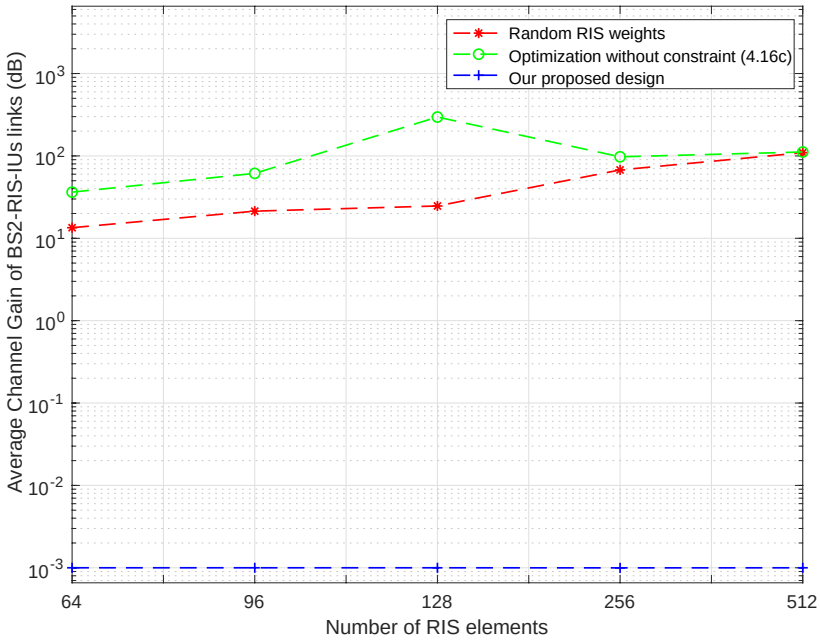

Figure 4.4: The effects of RIS on n-BS - UEs served by n-BS links.

is $\mathbf{b}_{j,k} \in \mathbb{C}^{N\times 1}, \forall j \in \mathcal{J}_{\mathcal{C}}, k \in \mathcal{K}_{\mathcal{C}}$. Note that $\|\mathbf{b}_{j,k}\|_2 = 1$. Then, the active beamfomer at BS j can be denoted as $\mathbf{A}_j = [\mathbf{b}_{j,1}, \cdots, \mathbf{b}_{j,K_j}] \in \mathbb{C}^{N\times K_j}$, where K_j refers to the number of UE served by BS j. For the BS j, we define the set of served UE as $\mathcal{K}_j = \{1, \cdots, K_j\}$. Furthermore, we assume that there are Q RISs, denoted by $\mathcal{Q} = \{1, \cdots, Q\}$. Each RIS has the same number of elements, denoted as M, and the q-th RIS phase shift vector can be represented as $\mathbf{w}_q = [w_{q,1}, w_{q,2}, ..., w_{q,M}]^H \in \mathbb{C}^{M\times 1}$, $\forall q \in \mathcal{Q}$. Each element $w_{q,m}, m = 1, \cdots, M$ in $\mathbf{w}_q$ could be expressed as $w_{q,m} = \beta_{q,m} e^{j\alpha_{q,m}}$. For maximum reflection efficiency, we let $\beta_{q,m} = 1$ and $\alpha_{q,m} \in [0, 2\pi]$. The overall RIS matrix can be represented by $\overline{\mathbf{W}} = [\mathbf{w}_1, \cdots, \mathbf{w}_Q] \in \mathbb{C}^{M\times Q}$.

We denote $\mathbf{h_d}_{j,k} \in \mathbb{C}^{N\times 1}$, $\mathbf{G}_{j,q} \in \mathbb{C}^{M\times N}$, and $\mathbf{h_r}_{q,k} \in \mathbb{C}^{M\times 1}$ as the channel expressions of j-th BS-k-th UE, j-th BS-q-th RIS, and q-th RIS-k-th UE, $\forall j \in \{\mathcal{J}_{\mathcal{C}}, \mathcal{J}_{\mathcal{N}}\}, k \in \{\mathcal{K}_{\mathcal{C}}, \mathcal{K}_{\mathcal{N}}\}, q \in \mathcal{Q}$, respectively. Following by this, the overall channel between the j-th BS and the k-th UE could be expressed as

$$\mathbf{h}_{j,k} = \mathbf{h_d}_{j,k}^H + \sum_{q=1}^{Q} \mathbf{h_r}_{q,k}^H \mathbf{W}_q \mathbf{G}_{j,q}, \tag{4.53}$$

where $\mathbf{W}_q = \text{diag}(\mathbf{w}_q^T) \in \mathbb{C}^{M\times M}$. We apply the mmWave channel model. Specifically, the BS-UE direct link $\mathbf{h_d}_{j,k}^H$, the reflective links $\mathbf{h_r}_{q,k}^H$ and $\mathbf{G}_{j,q}$ are all modeled according to 3D Saleh-Valenzuela (S-V) channel model [151, 152], which are expressed as

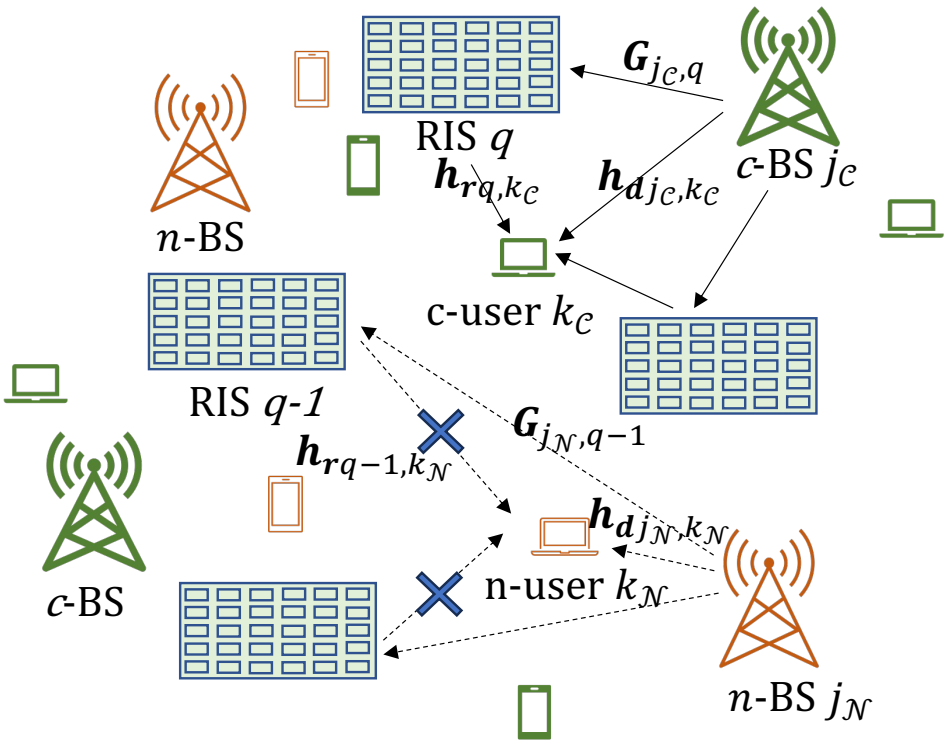

Figure 4.5: System model of RIS-aided mmWave System with Cooperative and Non-cooperative Networks.

$$\mathbf{h}_{\mathbf{d}j,k} = \alpha_0^{j,k}\zeta_t\zeta_r\mathbf{a}\left(\varphi_{j,k,0}^{\mathrm{AoD}},\theta_{j,k,0}^{\mathrm{AoD}}\right) + \sqrt{\frac{1}{L_{j,k}}}\sum_{l=1}^{L_{j,k}}\alpha_l^{j,k}\zeta_t\zeta_r\mathbf{a}\left(\varphi_{j,k,l}^{\mathrm{AoD}},\theta_{j,k,l}^{\mathrm{AoD}}\right), \tag{4.54}$$

$$\mathbf{h}_{\mathbf{r}q,k} = \alpha_0^{q,k}\mathbf{a}\left(\varphi_{q,k,0}^{\mathrm{AoD}},\theta_{q,k,0}^{\mathrm{AoD}}\right) + \sqrt{\frac{1}{L_{q,k}}}\sum_{l=1}^{L_{q,k}}\alpha_l^{q,k}\mathbf{a}\left(\varphi_{q,k,l}^{\mathrm{AoD}}\theta_{q,k,l}^{\mathrm{AoD}}\right), \tag{4.55}$$

$$\begin{aligned}\mathbf{G}_{j,q} = {} & \alpha_0^{j,q}\zeta_t\zeta_r\mathbf{a}\left(\varphi_{j,q,0}^{\mathrm{AoA}},\theta_{j,q,0}^{\mathrm{AoA}}\right)\mathbf{a}\left(\varphi_{j,q,0}^{\mathrm{AoD}},\theta_{j,q,0}^{\mathrm{AoD}}\right)^{\mathrm{H}} \\ & + \sqrt{\frac{1}{L_{j,q}}}\sum_{l=1}^{L_{j,q}}\alpha_l^{j,q}\zeta_t\zeta_r\mathbf{a}\left(\varphi_{j,q,l}^{\mathrm{AoA}},\theta_{j,q,l}^{\mathrm{AoA}}\right)\mathbf{a}\left(\varphi_{j,q,l}^{\mathrm{AoD}},\theta_{j,q,l}^{\mathrm{AoD}}\right)^{\mathrm{H}}.\end{aligned} \tag{4.56}$$

For simplicity, we generalize $z = \{(j,k),(q,k),(j,q)\}$, then (L_z+1) denotes the total number of paths, among which there are L_z NLoS paths and one LoS path. α_l^z indicates the complex gain of the corresponding l-th path. ζ_t and ζ_r represent the transmit and receive antenna gains, respectively. In addition, we consider BSs and RISs under URA configuration, then $\mathbf{a}(\cdot)$ denotes the steering vector as a function of the spatial information with respect to the azimuth and elevation domain [131]. Specifically, $\mathbf{a}\left(\varphi_{z,l}^{\mathrm{AoA}},\theta_{z,l}^{\mathrm{AoA}}\right)$ can be represented as

$$\mathbf{a}\left(\varphi_{z,l}^{\mathrm{AoA}},\theta_{z,l}^{\mathrm{AoA}}\right) = e^{j\frac{2\pi f d}{c}\boldsymbol{\psi}\left(\varphi_{z,l}^{\mathrm{AoA}},\theta_{z,l}^{\mathrm{AoA}}\right)}, \tag{4.57}$$

where f denotes the operating carrier frequency, and d represents the distance measured from the centre of adjacent elements on the surface. $\mathbf{a}\left(\varphi_{z,l}^{\mathrm{AoD}}, \theta_{z,l}^{\mathrm{AoD}}\right)$ can be similarly derived. Generally, the element spacing is set as half-wavelength, i.e., $d = \lambda/2$, which is, in fact, a function of the centre frequency f_c. As RISs are utilized collaboratively by multiple c-BSs working under different bands, the element spacing d must be meticulously designed to accommodate the requirements of all c-BSs. Therefore, we introduce a weighted centre frequency design for the c-BSs. Specifically, we assume each c-BS has a centre frequency of f_j and a bandwidth of B_j. Then, the weighted centre frequency will be

$$f_c = \frac{\sum_{j=1}^{J_{\mathcal{C}}} f_j B_j}{\sum_{j=1}^{J_{\mathcal{C}}} B_j}, \tag{4.58}$$

based on which the element spacing of RISs will be designed. Additionally, the particular r-th element in $\boldsymbol{\psi}\left(\varphi_{z,l}^{\mathrm{AoA}}, \theta_{z,l}^{\mathrm{AoA}}\right)$ can be interpreted as

$$\psi_{r=\{m,n\}}(\varphi, \theta) = (r_x - 1)\sin\varphi\cos\theta + (r_y - 1)\sin\theta, \tag{4.59}$$

where r has a relationship with r_x and r_y as $r = (r_x - 1)R_y + r_y$, $r_x \in \{1, \cdots, R_x\}$, $r_y \in \{1, \cdots, R_y\}$. Note that $R = \{M, N\}$ indicate the number of elements on RIS and BS, respectively. Particularly, R_x and R_y denote the number of elements on the x/y-axis of a planar surface.

In addition, we suppose that each BS can serve multiple UEs with a maximum number of serving UE K_{BS}. Then, the power allocation vector of the BS j is denoted as $\mathbf{P}_j \in \mathbb{C}^{1\times K_{\mathrm{BS}}}$, where $\sum_{u=1}^{K_{\mathrm{BS}}} p_{j,u} \leq p_{\max}$ satisfies. To be noted, as there are only K_j UE served by BS j, the rest $(K_{\mathrm{BS}} - K_j)$ elements in $\mathbf{p}_j$ are given with 0, $\forall j \in \mathcal{J}_{\mathcal{C}}$. We further define the power allocation matrix $\mathbf{P} = [\mathbf{p}_1^T, \cdots, \mathbf{p}_{J_{\mathcal{C}}}^T]^T \in \mathbb{C}^{J_{\mathcal{C}}\times K_{\mathrm{BS}}}$. Then, the received signal at the k-th UE associated with BS j considering the intra-cell interference can be represented as

$$y_{j,k} = \mathbf{h}_{j,k}\mathbf{w}_{j,k}\sqrt{p_{j,k}}s_p + \mathbf{h}_{j,k}\sum_{u\neq k}^{K_j}\mathbf{w}_{j,u}\sqrt{p_{j,u}}s_u + \sum_{i\neq j}^{J_{\mathcal{C}}}\sum_{u=1}^{K_i}\mathbf{h}_{i,u}\mathbf{w}_{i,u}\sqrt{p_{i,u}}s_u + n, \forall k \in \mathcal{K}_{\mathcal{C}}, \tag{4.60}$$

where n is the noise with zero mean and variance σ_n^2, i.e., $n_k \sim \mathcal{CN}(0, \sigma_n^2)$.

Furthermore, we use matrix $\mathbf{U} \in \mathbb{C}^{J_{\mathcal{C}}\times K_{\mathcal{C}}}$ to measure the UE association. Then, the binary association variable $u_{j,k} \in \mathbf{U}$ can be represented as

$$u_{j,k} = \begin{cases} 1, & \text{UE } k \text{ is associated with BS } j, \\ 0, & \text{otherwise.} \end{cases} \tag{4.61}$$

Note that each UE can only associate with one BS, while each BS can serve multiple UE with a maximum number of serving UE K_{BS}, which can be interpreted as

$$\sum_{k=1}^{K_{\mathcal{C}}} u_{j,k} \leq K_{\mathrm{BS}}, \forall j \in \mathcal{J}_{\mathcal{C}}. \tag{4.62}$$

$$\sum_{j=1}^{\mathcal{J}_{\mathcal{C}}} u_{j,k} = 1, \forall k \in \mathcal{K}_{\mathcal{C}}. \tag{4.63}$$

We suppose that neighbouring BSs are allocated frequency bands that are either orthogonal or implemented with advanced techniques for inter-cell interference coordination [60]. In addition, for c-BSs, frequency division multiple access (FDMA) and code division multiple access (CDMA) can be applied for intra-cell interference mitigation. Then, the SNR for the UE k could be approximated as

$$\mathrm{SNR}_k = \frac{|\sum_{j=1}^{J_{\mathcal{C}}} u_{j,k} \mathbf{h}_{j,k} \mathbf{w}_{j,k}|^2 p_{j,k}}{\sigma_n^2}, \forall k \in \mathcal{K}_{\mathcal{C}}. \tag{4.64}$$

Based on (4.64), we get the expression of the sum rate of UE served by all c-BSs as

$$R = \sum_{u=1}^{K_{\mathcal{C}}} \log_2(1 + \mathrm{SNR}_u). \tag{4.65}$$

In addition, we consider the BSs under non-cooperation scheme, whose communications with serving UE refuse to be affected by the RISs. As the UE association strategy of non-cooperative BSs are not known, we assume that UE $\hat{k} \in \mathcal{K}_{\mathcal{N}}$ is served by the nearest BS $\hat{j} \in \mathcal{J}_{\mathcal{N}}$. Then, for a particular communication pair $\langle \hat{j}, \hat{k} \rangle, \forall \hat{j} \in \mathcal{J}_{\mathcal{N}}, \hat{k} \in \mathcal{K}_{\mathcal{N}}$, the BS $\hat{j}$-UE $\hat{k}$, BS $\hat{j}$-RIS q, and RIS q-UE $\hat{k}$ channels are defined as $\mathbf{h}_{\mathbf{d}_{\hat{j},\hat{k}}} \in \mathbb{C}^{N \times 1}$, $\mathbf{G}_{\hat{j},q} \in \mathbb{C}^{M \times N}$, and $\mathbf{h}_{\mathbf{r}_{q,\hat{k}}} \in \mathbb{C}^{M \times 1}$, respectively. The signal received by the UE $\hat{k} \in \mathcal{K}_{\mathcal{N}}$ is expressed as

$$y_{\hat{k}} = (\mathbf{h}_{\mathbf{d}_{\hat{j},\hat{k}}}^H + \sum_{q=1}^{Q} \mathbf{h}_{\mathbf{r}_{q,\hat{k}}}^H \mathbf{W}_q \mathbf{G}_{\hat{j},q}) \sum_{r=1}^{K_{\hat{j}}} \mathbf{w}_{\hat{j},r} \sqrt{p_{\hat{j},r}} s_r + n, \forall \hat{k} \in \mathcal{K}_{\mathcal{N}}, \tag{4.66}$$

where $K_{\hat{j}}$ denotes the number of UE served by BS $\hat{j}, \forall \hat{j} \in \mathcal{J}_{\mathcal{N}}$.

In order to mitigate the effect of RISs on all BS $\hat{j}$-UE $\hat{k}$ links, the UE $\hat{k}, \forall \hat{k} \in \mathcal{K}_{\mathcal{N}}$ would receive comparable signals when only direct link exists as when the RIS-aided reflective links

also exist. Then, we have

$$y_{\hat{k}} \approx \mathbf{h_d}_{\hat{j},\hat{k}}^{H} \sum_{r=1}^{K_{\hat{j}}} \mathbf{w}_{\hat{j},r} \sqrt{p_{\hat{j},r}} s_r + n_{\hat{k}}, \forall \hat{k} \in \mathcal{K}_{\mathcal{H}}, \tag{4.67}$$

By combining (4.66) and (4.67), we get

$$\| \sum_{q=1}^{Q} \mathbf{h_r}_{q,\hat{k}}^{H} \mathbf{W}_q \mathbf{G}_{\hat{j},q} \| \leq \delta, \ \forall \hat{k} \in \mathcal{K}_{\mathcal{H}}, \tag{4.68}$$

where δ denotes the threshold for the channel gain of the reflective links BS $\hat{j}$-RISs-UE $\hat{k}$ for all non-cooperative BSs and their serving UE' pair, which should satisfy $0 < \delta \ll 1$ to guarantee the largely mitigated impact of RISs.

By jointly considering the UE association $\mathbf{U}$, power allocation $\mathbf{P}$, active beamforming at cooperative BSs $\mathbf{W}_j, \forall j \in \mathcal{J}_{\mathcal{C}}$, and the RISs passive beamforming $\overline{\mathbf{W}}$, we formulate the following optimization problem:

$$\begin{aligned}
\text{(P4-2)} : \max_{\mathbf{W}_{j,\forall j \in \mathcal{J}_{\mathcal{C}}}, \overline{\mathbf{W}}, \mathbf{U}, \mathbf{P}} \quad & R && \text{(4.69a)} \\
\text{s.t.} \quad & \mathrm{SNR}_k \geq \mathrm{SNR}_{th}, \forall k_c \in \mathcal{K}_{\mathcal{C}}, && \text{(4.69b)} \\
& \| \sum_{q=1}^{Q} \mathbf{h_r}_{q,\hat{k}}^{H} \mathbf{W}_q \mathbf{G}_{\hat{j},q} \| \leq \delta, \ \forall \hat{k} \in \mathcal{K}_{\mathcal{H}}, && \text{(4.69c)} \\
& \|\mathbf{w}_{j,k}\|_2 = 1, \forall k \in \mathcal{K}_j, j \in \mathcal{J}_{\mathcal{C}} && \text{(4.69d)} \\
& \sum_{u=1}^{K_j} p_{j,u} \leq p_{\max}, \forall j \in \mathcal{J}_{\mathcal{C}} && \text{(4.69e)} \\
& \sum_{k=1}^{K_{\mathcal{C}}} u_{j,k} \leq K_{\mathrm{BS}}, \forall j \in \mathcal{J}_{\mathcal{C}}, && \text{(4.69f)} \\
& \sum_{j=1}^{J_{\mathcal{C}}} u_{j,k} = 1, \forall k_c \in \mathcal{K}_{\mathcal{C}}, && \text{(4.69g)} \\
& u_{j,k} = \{0,1\}, \forall j \in \mathcal{J}_{\mathcal{C}}, k_c \in \mathcal{K}_{\mathcal{C}}, && \text{(4.69h)} \\
& \left| w_{q,m} \right| = 1, \forall q \in \mathcal{Q}, m = 1, \cdots, M. && \text{(4.69i)}
\end{aligned}$$

Specifically, constraint (4.69b) ensures that the SNR of all UEs served by cooperative BSs can be higher than the pre-defined threshold SNR_{th}. (4.69c) indicates that the gains of the reflective links between non-cooperative BSs and their serving UE are kept below δ. Furthermore, (4.69f), (4.69g), and (4.69h) jointly regulate the UE association rule. (4.69i) accounts

for the fact that the RISs elements are all unit-modulus constrained.

The challenging nature of this problem arises from the multiple cross-term variables and the presence of multiple constraints. In addition, the optimization dilemma takes into account discrete binary variables, and the issue persists as non-convex after relaxing. Therefore, it is difficult to obtain a globally optimal solution using standard methods. In the subsequent sections, we propose a BCD algorithm to address problem (P4-2).

Regarding the optimization of the active beamforming $\mathbf{A}_j, \forall j \in \mathcal{J}_{\mathcal{C}}$, as low-complexity linear processing techniques are near-optimal [153], we consider cooperative BSs applying MRT. Particularly, $\mathbf{b}_{j,k}$ is set as $\mathbf{b}_{j,k} = \frac{\mathbf{h}_{j,k}^H}{\|\mathbf{h}_{j,k}\|_2}, \forall k \in \mathcal{K}_j, j \in \mathcal{J}_{\mathcal{C}}$, which satisfies the active beamforming constraint (4.69d).

4.3.2 Power Allocation Design

Given $\mathbf{U}$, $\mathbf{A}_j, \forall j \in \mathcal{J}_{\mathcal{C}}$ and $\overline{\mathbf{W}}$, we rewrite the problem (P4-2) with respect to $\mathbf{P}$ as

$$
\begin{aligned}
(\text{P4-2.1}): \max_{\mathbf{P}} \quad & R && \text{(4.70a)}\\
\text{s.t.} \quad & \text{SNR}_k \geq \text{SNR}_{th}, \forall k_c \in \mathcal{K}_{\mathcal{C}}, && \text{(4.70b)}\\
& \sum_{u=1}^{K_j} p_{j,u} \leq p_{\max}, \forall j \in \mathcal{J}_{\mathcal{C}}. && \text{(4.70c)}
\end{aligned}
$$

It is easy to find that the problem in optimizing the power allocation variable $\mathbf{P}$ is convex and can be solved by the water-filling algorithm [154]. In the following, we give a numerical analysis of the optimized solution and prove its global optimality.

Specifically, we divide the power for each UE $k \in \mathcal{K}_{\mathcal{C}}$ into two parts, which can be expressed as

$$p_{j,k} = p_{j,k,1} + p_{j,k,2}, \forall j \in \mathcal{J}_{\mathcal{C}}, k \in \mathcal{K}_{\mathcal{C}}. \tag{4.71}$$

Firstly, in order to satisfy the SNR constraint (4.70b) [1], we let

$$p_{j,k,1} = \frac{\text{SNR}_{th}\sigma_n^2}{|\sum_{j=1}^{J_{\mathcal{C}}} u_{j,k}\mathbf{h}_{j,k}\mathbf{w}_{j,k}|^2}. \tag{4.72}$$

Furthermore, to maximize the sum rate, all power needs to be allocated to UEs, revealing that

[1] We suppose that a $p_{\max}$ is given, which enables all UEs' SNRs to exceed the threshold.

equality holds in (4.70c). Then, (P4-2.1) can be reinterpreted as

$$\begin{aligned}
&(\text{P4-2.1.1}):\\
&\max_{\mathbf{P}} \sum_{j=1}^{J_{\mathcal{C}}} \sum_{k=1}^{K_j} \log_2(1+\text{SNR}_{th}+\frac{|\sum_{j=1}^{J_{\mathcal{C}}} u_{j,k}\mathbf{h}_{j,k}\mathbf{w}_{j,k}|^2 p_{j,k,2}}{\sigma_n^2}) &(4.73a)\\
&\sum_{u=1}^{K_j} p_{j,u,2} = p_{\max} - \sum_{u=1}^{K_j} p_{j,u,1}, \forall j \in \mathcal{J}_{\mathcal{C}}. &(4.73b)
\end{aligned}$$

For simplicity, we abbreviate $\hat{p}_{\max} = p_{\max} - \sum_{u=1}^{K_j} p_{j,u,1}$ in the sequel. A Lagrangian multiplier vector $\boldsymbol{\tau}_1 \in \mathbb{C}^{1\times J_{\mathcal{C}}}$ associated with (4.73b) is sequentially introduced, resulting in a formed objective function:

$$O(\mathbf{P},\boldsymbol{\tau}_1) = \sum_{j=1}^{J_{\mathcal{C}}}\Big(\sum_{k=1}^{K_j}\log_2(\pi_{th}+\varpi_{j,k}p_{j,k,2}) - \tau_{1,j}(\sum_{u=1}^{K_j} p_{j,u,2} - \hat{p}_{\max})\Big), \tag{4.74}$$

where $\pi_{th} = 1+\text{SNR}_{th}$ and $\varpi_{j,k} = \frac{|\sum_{j=1}^{J_{\mathcal{C}}} u_{j,k}\mathbf{h}_{j,k}\mathbf{w}_{j,k}|^2}{\sigma_n^2}$. For $\tau_{1,j} \gg 0, \forall j \in \mathcal{J}_{\mathcal{C}}$, the results of the relaxed problem will be equivalent to the problem shown as $\mathbb{P}2.1$.

As the power allocation of each BS is independent, we consider it for BS j in the following, while the allocation optimization for all other BSs can be similarly derived. Particularly, for the BS j, we have the objective function given as

$$O_j(\mathbf{p}_j,\boldsymbol{\tau}_{1,j}) = \sum_{k=1}^{K_j}\log_2(\pi_{th}+\varpi_{j,k}p_{j,k,2}) - \tau_{1,j}(\sum_{u=1}^{K_j} p_{j,u,2} - \hat{p}_{\max}). \tag{4.75}$$

Then, we take the derivative of $O_j(\mathbf{p}_j,\tau_{1,j})$ in $\mathbf{p}_j$ and $\tau_{1,j}$, respectively, leading to the following power allocation relationship to maximize the sum rate:

$$\begin{cases} \frac{\pi_{th}}{\varpi_{j,k}} + p_{j,k,2} = \bar{c}, \forall k \in \mathcal{K}_j, \\ \sum_{u=1}^{K_j} p_{j,u,2} = \hat{p}_{\max}, \end{cases} \tag{4.76}$$

where $\bar{c}$ denotes a constant value. As the optimized power allocation scheme in (4.76) may not satisfy due to the total power limit, we therefore find the solution to minimize the difference between $\frac{\pi_{th}}{\varpi_{j,k}} + p_{j,k,2}, \forall k \in \mathcal{K}_j$ to reach the actual maximum sum rate, which is derived as the following proposition.

Proposition 1: The maximum sum rate in optimizing power allocation can be realized

when

$$\begin{cases} p_{j,k,2} = 0, & k \in \hat{\mathcal{K}}_j, \\ p_{j,k,2} = \frac{\hat{p}_{\max} + \sum_{u \notin \hat{\mathcal{K}}_j} \frac{\pi_{th}}{\varpi_{j,u}}}{K_j - n(\hat{\mathcal{K}}_j)} - \frac{\pi_{th}}{\varpi_{j,k}}, & k \notin \hat{\mathcal{K}}_j, \end{cases} \tag{4.77}$$

where $\hat{\mathcal{K}}_j = \{k | k \leq \hat{k}, K_j - \frac{\varpi_{j,\hat{k}+1} \Upsilon_{\hat{k}+1}}{\pi_{th}} \leq \hat{k} \leq K_j + 1 - \frac{\varpi_{j,\hat{k}} \Upsilon_{\hat{k}}}{\pi_{th}}\}$, and $\Upsilon_k = \hat{p}_{\max} + \sum_{u=k}^{K_j} \frac{\pi_{th}}{\varpi_{j,u}}$.

Proof: See Appendix A.4.

Based on (4.71), (4.72), and **Proposition 1**, we can get the general expression of the optimized power allocation for an arbitrary BS $j, \forall j \in \mathcal{J}_{\mathcal{C}}$ as the sum of the two divided power parts, which can be closed-form interpreted as

$$\begin{cases} p_{j,k} = \frac{\pi_{th} - 1}{\varpi_{j,k}}, & k \in \hat{\mathcal{K}}_j, \\ p_{j,k} = \frac{\hat{p}_{\max} + \sum_{u \notin \hat{\mathcal{K}}_j} \frac{\pi_{th}}{\varpi_{j,u}}}{K_j - n(\hat{\mathcal{K}}_j)} - \frac{1}{\varpi_{j,k}}, & k \notin \hat{\mathcal{K}}_j. \end{cases} \tag{4.78}$$

4.3.3 UE Association Design

For given $\mathbf{A}_j, \forall j \in \mathcal{J}_{\mathcal{C}}$, $\mathbf{P}$ and $\overline{\mathbf{W}}$, the UE association sub-problem is reformulated as

$$(\text{P4-2.2}): \max_{\mathbf{U}} \quad R \tag{4.79a}$$

$$\text{s.t.} \quad \text{SNR}_k \geq \text{SNR}_{th}, \forall k_c \in \mathcal{K}_{\mathcal{C}}, \tag{4.79b}$$

$$\sum_{k=1}^{K_{\mathcal{C}}} u_{j,k} \leq K_{\text{BS}}, \forall j \in \mathcal{J}_{\mathcal{C}}, \tag{4.79c}$$

$$\sum_{j=1}^{J_{\mathcal{C}}} u_{j,k} = 1, \forall k_c \in \mathcal{K}_{\mathcal{C}}, \tag{4.79d}$$

$$u_{j,k} = \{0, 1\}, \forall j \in \mathcal{J}_{\mathcal{C}}, k_c \in \mathcal{K}_{\mathcal{C}}. \tag{4.79e}$$

As the main difficulty of (P4-2.2) lies in the discrete binary constraint (4.79e), we further equivalently interpret (4.79e) as

$$u_{j,k} = u_{j,k}^2, u_{j,k} \in [0, 1]. \tag{4.80}$$

Then, by applying the penalty method, we rewrite (4.79e) into the objective function by multiplying a positive penalty factor τ_u. The problem (P4-2.2) could be consequently expressed

as

$$(\text{P4-2.2.1}): \max_{\mathbf{U}} \quad O(\mathbf{U}) = R + \tau_u \sum_{j=1}^{J_{\mathcal{C}}} \sum_{k=1}^{K_j} (u_{j,k}^2 - u_{j,k}) \tag{4.81a}$$

$$\text{s.t.} \quad (4.79\text{b}), (4.79\text{c}), (4.79\text{d}), \tag{4.81b}$$

$$u_{j,k} \in [0,1], \forall j \in \mathcal{J}_{\mathcal{C}}, k_c \in \mathcal{K}_{\mathcal{C}}. \tag{4.81c}$$

Note that $\tau_u \gg 0$ should be satisfied so that the objective function (4.79a) is equivalent to (4.81a) [155].

Specifically, by introducing the new-formed SNR, we rephrase the expression of the sum rate R as

$$R = \sum_{j=1}^{J_{\mathcal{C}}} \sum_{k=1}^{K_j} u_{j,k} \log_2(1 + \frac{u_{j,k} p_{j,k} |\mathbf{h}_{j,k} \mathbf{w}_{j,k}|^2}{\sigma_n^2}). \tag{4.82}$$

We take the second derivative of R with respect to $\mathbf{U}$, which can be expressed as

$$\begin{aligned} \frac{dR}{d\mathbf{U}^2} &= \sum_{j=1}^{J_{\mathcal{C}}} \sum_{k=1}^{K_j} \frac{d}{du_{j,k}} \left(\log_2(1 + u_{j,k}\chi_{j,k}) + \frac{u_{j,k}\chi_{j,k}}{\ln(2)(1 + u_{j,k}\chi_{j,k})} \right) \\ &= \sum_{j=1}^{J_{\mathcal{C}}} \sum_{k=1}^{K_j} \frac{\chi_{j,k}}{\ln(2)(1 + u_{j,k}\chi_{j,k})^2}, \end{aligned} \tag{4.83}$$

where we abbreviate $\chi_{j,k} = \frac{p_{j,k}|\mathbf{h}_{j,k}\mathbf{w}_{j,k}|^2}{\sigma_n^2}$, which is always positive. Consequently, the second derivative in $\mathbf{U}$ is always positive, and the sum rate R is concave in $\mathbf{U}$. At the same time, it is easy to verify that $\tau_u \sum_{j=1}^{J_{\mathcal{C}}} \sum_{k=1}^{K_j} (u_{j,k}^2 - u_{j,k})$ is convex in $\mathbf{U}$. The objective function is therefore a standard DC programming as illustrated in the previous chapter, which is expressed as $g(\mathbf{U}) - h(\mathbf{U})$ with $g(\mathbf{U}) = -R$ and $h(\mathbf{U}) = -\tau_u \sum_{j=1}^{J_{\mathcal{C}}} \sum_{k=1}^{K_j} (u_{j,k}^2 - u_{j,k})$. The SCA is then applied to iteratively update the variable $\mathbf{U}$ until convergence. We formulate the first-order Taylor polynomial, i.e., $O^1(\mathbf{U})$, of the objective function $O(\mathbf{U})$, which is represented as

$$O^1(\mathbf{U}) = \sum_{j=1}^{J_{\mathcal{C}}} \sum_{k=1}^{K_j} u_{j,k} \log_2(1 + u_{j,k}\chi_{j,k}) + \tau_u((u_{j,k}^{t_1})^2 - u_{j,k}^{t_1}) + \tau_u(2u_{j,k}^{t_1} - 1)(u_{j,k} - u_{j,k}^{t_1}) \tag{4.84}$$

Note that $u_{j,k}^{t_1}$ denotes the updated UE association factor in the t_1-th iteration.

Proposition 2: The approximation of $O^1(\mathbf{U})$ gives a tight lower bound for the objective function $O(\mathbf{U})$.

Proof: We define the approximation of $h(\mathbf{U})$ at the point of $\mathbf{U}^{t-1}$ as $\hat{h}(\mathbf{U}, \mathbf{U}^{t-1})$. Then, we

have

$$\hat{O}^1(\mathbf{U}, \mathbf{U}^{t-1}) = -\hat{h}(\mathbf{U}, \mathbf{U}^{t-1}) - g(\mathbf{U}). \tag{4.85}$$

The function $\hat{h}(\mathbf{U}, \mathbf{U}^{t-1})$ satisfies the following conditions:

- $\hat{h}(\mathbf{U}^{t-1}, \mathbf{U}^{t-1}) = h(\mathbf{U}^{t-1}), \forall \mathbf{U}^{t-1} \in \mathcal{X}$.
- $\hat{h}(\mathbf{U}, \mathbf{U}^{t-1}) \geq h(\mathbf{U}^{t-1}), \forall \mathbf{U} \in \mathcal{X}$.

Consequentially, the equality $\hat{O}^1(\mathbf{U}, \mathbf{U}^{t-1}) = \hat{O}^1(\mathbf{U}^{t-1}, \mathbf{U}^{t-1})$ holds at $\mathbf{U} = \mathbf{U}^{t-1}$, indicating the tightness of the approximation function.

By replacing the objective function in (P4-2.2.1) with its corresponding locally tight lower bound expression, we have

$$(\text{P4-2.2.2}): \max_{\mathbf{U}^{t_1}} \quad O^1(\mathbf{U}) \tag{4.86a}$$

$$\text{s.t.} \quad (4.81\text{b}), (4.81\text{c}). \tag{4.86b}$$

Problem (P4-2.2.2) is a standard convex optimization problem in each iteration and can be solved by the CVX toolbox.

4.3.4 RIS Passive Beamforming Design

We fix the variables $\mathbf{A}_j, \forall j \in \mathcal{J}_{\mathcal{C}}$, $\mathbf{U}$ and $\mathbf{P}$ and optimize $\overline{\mathbf{W}}$, then the problem (P4-2) can be simplified as

$$(\text{P4-2.3}): \max_{\overline{\mathbf{W}}} \quad R \tag{4.87a}$$

$$\text{s.t.} \quad \text{SNR}_k \geq \text{SNR}_{th}, \forall k_c \in \mathcal{K}_{\mathcal{C}}, \tag{4.87b}$$

$$\| \sum_{q=1}^{Q} \mathbf{h}_{\mathbf{r}_{q,\hat{k}}}^H \mathbf{W}_q \mathbf{G}_{\hat{j},q} \| \leq \delta, \ \forall \hat{k} \in \mathcal{K}_{\mathcal{H}}, \tag{4.87c}$$

$$\left| w_{q,m} \right| = 1, \forall q \in \mathcal{Q}, m = 1, \cdots, M. \tag{4.87d}$$

We first derive an analysis of the objective function. Particularly, the objective function can be expanded as

$$O(\overline{\mathbf{W}}) = \sum_{j=1}^{J_{\mathcal{C}}} \sum_{k=1}^{K_j} \log_2 (1 + \frac{|(\mathbf{h}_{\mathbf{d}_{j,k}}^H + \sum_{q=1}^{Q} \mathbf{h}_{\mathbf{r}_{q,k}}^H \mathbf{W}_q \mathbf{G}_{j,q}) \mathbf{w}_{j,k}|^2 p_{j,k}}{\sigma_n^2}). \tag{4.88}$$

We define $\overline{\mathbf{g_q}}_{j,k} = \text{diag}(\mathbf{h_r}_{q,k}^H)\mathbf{G}_{j,q}\mathbf{w}_{j,k}$, $\overline{h_d}_{j,k} = \mathbf{h_d}_{j,k}^H\mathbf{w}_{j,k}$, then the objective function can be simplified as

$$O(\overline{\mathbf{W}}) = \sum_{j=1}^{J_C}\sum_{k=1}^{K_j}\log_2(1+\frac{|\overline{h_d}_{j,k}+\sum_{q=1}^{Q}\mathbf{w}_q^H\overline{\mathbf{g_q}}_{j,k}|^2 p_{j,k}}{\sigma_n^2}) \tag{4.89}$$

In order to deal with the logarithmic and fractional objective function, the Lagrangian dual and quadratic transformation method is applied [150]. Specifically, we introduce auxiliary variables $\eta_{j,k}, \forall j \in \mathcal{J}_C, k \in \mathcal{K}_j$, and a new variable set $\boldsymbol{\lambda} = [\lambda_1, \cdots, \lambda_{j,k}]^T$. Then, the objective function is rewritten as

$$\begin{aligned} O(\boldsymbol{\lambda}, \overline{\mathbf{W}}) = \sum_{j=1}^{J_C}\sum_{k=1}^{K_j} & 2\sqrt{p_{j,k}\eta_{j,k}}\mathcal{R}e\{\lambda_{j,k}^*\overline{h_d}_{j,k}+ \\ & \lambda_{j,k}^*\sum_{q=1}^{Q}\mathbf{w}_q^H\overline{\mathbf{g_q}}_{j,k}\} - |\lambda_{j,k}|^2(\sigma_n^2 + p_{j,k}|\overline{h_d}_{j,k} + \sum_{q=1}^{Q}\mathbf{w}_q^H\overline{\mathbf{g_q}}_{j,k}|^2), \end{aligned} \tag{4.90}$$

which can be maximized by iteratively optimizing $\boldsymbol{\lambda}$ and $\overline{\mathbf{W}}$. Particularly, for each iteration t_2, $\eta_{j,k}^{t_2} = \frac{|\overline{h_d}_{j,k}+\sum_{q=1}^{Q}(\mathbf{w}_q^{t_2-1})^H\overline{\mathbf{g_q}}_{j,k}|^2 p_{j,k}^{t_2-1}}{\sigma_n^2}$. With the optimized $\overline{\mathbf{W}}^{t_2-1}$ in the (t_2-1)-th iteration, the $\lambda_{j,k}^{t_2}$ can be obtained as

$$\lambda_{j,k}^{t_2} = \frac{\sqrt{p_{j,k}\eta_{j,k}}\mathcal{R}e\{\overline{h_d}_{j,k}+\sum_{q=1}^{Q}(\mathbf{w}_q^{t_2-1})^H\overline{\mathbf{g_q}}_{j,k}\}}{\sigma_n^2 + p_{j,k}|\overline{h_d}_{j,k}+\sum_{q=1}^{Q}(\mathbf{w}_q^{t_2-1})^H\overline{\mathbf{g_q}}_{j,k}|^2}. \tag{4.91}$$

With given $\lambda_{j,k}^{t_2}$, $\mathbf{w}_q, \forall q \in \mathcal{Q}$ can be updated iteratively. Specifically, we let $\overline{f}_s = \overline{h_d}_{j,k} + \sum_{q\neq s}^{Q}(\mathbf{w}_q^{t_2-1})^H\overline{\mathbf{g_q}}_{j,k}, \forall s \in \mathcal{Q}$, then the objective function with respect to $\mathbf{w}_s$ can be written as

$$\begin{aligned} O(\boldsymbol{\lambda}, \mathbf{w}_s) = \sum_{j=1}^{J_C}\sum_{k=1}^{K_j} & 2\sqrt{p_{j,k}\eta_{j,k}}\mathcal{R}e\{\lambda_{j,k}^*\overline{f}_s + \lambda_{j,k}^*\mathbf{w}_s^H\overline{\mathbf{g}_k}_{j,k}\} \\ & - |\lambda_{j,k}|^2(\sigma_n^2 + p_{j,k}|\overline{f}_s + \mathbf{w}_s^H\overline{\mathbf{g}_k}_{j,k}|^2), \end{aligned} \tag{4.92}$$

which can be rephrased in the form of

$$O(\boldsymbol{\lambda}, \mathbf{w}_s) = -\mathbf{w}_s^H\Lambda_s\mathbf{w}_s + 2\mathcal{R}e\{\mathbf{w}_s^H\boldsymbol{\nu}_s\} + \varepsilon_s, \tag{4.93}$$

with

$$\Lambda_s = \sum_{j=1}^{J_C}\sum_{k=1}^{K_j}|\lambda_{j,k}|^2\overline{\mathbf{g}_k}_{j,k}\overline{\mathbf{g}_k}_{j,k}^H, \tag{4.94}$$

$$\boldsymbol{\nu}_s = \sum_{j=1}^{J_{\mathcal{C}}} \sum_{k=1}^{K_j} (\sqrt{p_{j,k}\eta_{j,k}} \lambda_{j,k}^* \overline{\mathbf{g}_{k\,j,k}} - |\lambda_{j,k}|^2 p_{j,k} \overline{f}_s \overline{\mathbf{g}_{k\,j,k}}), \tag{4.95}$$

$$\varepsilon_s = \sum_{j=1}^{J_{\mathcal{C}}} \sum_{k=1}^{K_j} \Big(2\sqrt{p_{j,k}\eta_{j,k}} \mathcal{R}e\{\lambda_{j,k}^* \overline{f}_s\} - |\lambda_{j,k}|^2 (\sigma_n^2 + p_{j,k} |\overline{f}_s|^2) \Big). \tag{4.96}$$

The optimization of the reflection coefficients of RISs thus constitutes a standard QCQP problem. However, it is still non-convex due to the non-convex constraint (4.87d). To address the non-convexity in (4.87d), the penalty method is firstly applied, which rewrites (4.87d) into the objective function by multiplying a positive penalty factor τ_θ. Then the objective function could be consequently expressed as

$$O'(\overline{\mathbf{W}}) = O(\boldsymbol{\lambda}^{t_2}, \overline{\mathbf{W}}) + \tau_\theta \sum_{q=1}^{Q} \sum_{m=1}^{M} (|w_{q,m}|^2 - 1). \tag{4.97}$$

Sequentially, $\mathbb{P}4$ can be rewritten as

$$\begin{aligned} (\text{P4-2.3.1}) \quad \max_{\overline{\mathbf{W}}^{t_2}} \quad & O'(\overline{\mathbf{W}}) && (4.98) \\ \text{s.t.} \quad & (4.87\text{b}), (4.87\text{c}), && (4.99) \\ & \left|w_{q,m}\right| \leq 1, q = 1, \cdots, Q, m = 1, \cdots, M. && (4.100) \end{aligned}$$

Then, we deal with the non-convexity of the non-convex term in $O'(\overline{\mathbf{W}})$ by SCA. As the variable $\overline{\mathbf{W}}$ is complex, the approximation of the objective function in which could be hard to derive. We therefore convert the complex variables into real versions and represent the first-order Taylor series approximation of the objective function as

$$\begin{aligned} O''(\overline{\mathbf{W}}) = O(\boldsymbol{\lambda}^{t_2}, \overline{\mathbf{W}}) + \tau_\theta \sum_{q=1}^{Q} \sum_{m=1}^{M} \Big(& (w_{r_{q,m}}^{t_2})^2 + (w_{i_{q,m}}^{t_2})^2 \\ & + 2w_{r_{q,m}}^{t_2} (w_{r_{q,m}} - w_{r_{q,m}}^{t_2}) + 2w_{i_{q,m}}^{t_2} (w_{i_{q,m}} - w_{i_{q,m}}^{t_2}) \Big), \end{aligned} \tag{4.101}$$

where w_r and w_i denote the real and imaginary parts of w, respectively. The constraint (4.100) is correspondingly rewritten as

$$(w_{r_{q,m}})^2 + (w_{i_{q,m}})^2 \leq 1, \{w_{r_{q,m}}, w_{i_{q,m}}\} \in [-1, 1]. \tag{4.102}$$

Finally, the corresponding convex optimization problem with respect to $\mathbf{w}$ can be formu-

Algorithm 9 The overall BCD algorithm

Input: Initialize $\overline{\mathbf{W}}^0 \in \mathbb{C}^{M\times Q}$, $\mathbf{P}^0 \in \mathbb{C}^{J_{\mathcal{C}}\times K_{\mathrm{BS}}}$, $\mathbf{U}^0 \in \mathbb{C}^{J_{\mathcal{C}}\times K_{\mathcal{C}}}$, $t = 1$.
repeat
Obtain channel realizations $\mathbf{h}_{\mathbf{d}\,j,k}$, $\mathbf{h}_{\mathbf{r}q,k}$, $\mathbf{G}_{j,q}$, $\mathbf{h}_{\mathbf{d}\,\hat{j},\hat{k}}$, $\mathbf{G}_{\hat{j},q}$, and $\mathbf{h}_{\mathbf{r}_{q,\hat{k}}}$ for all k.
Given $\overline{\mathbf{W}}^{t-1}$, $\mathbf{P}^{t-1}$, and $\mathbf{U}^{t-1}$, update $\mathbf{A}_j^t, \forall j \in \mathcal{J}_{\mathcal{C}}$;
Given $\mathbf{A}_j^t, \forall j \in \mathcal{J}_{\mathcal{C}}$, $\overline{\mathbf{W}}^{t-1}$, and $\mathbf{P}^t$, form the Taylor series approximated objective function by (4.84);
Update $\mathbf{U}^t$ by solving (P4-2.2.2) with SCA algorithm;
Given $\mathbf{A}_j^t, \forall j \in \mathcal{J}_{\mathcal{C}}$, $\overline{\mathbf{W}}^{t-1}$, and $\mathbf{U}^{t-1}$, update $\mathbf{P}^t$ by (4.78);
Given $\mathbf{A}_j^t, \forall j \in \mathcal{J}_{\mathcal{C}}$, $\mathbf{U}^t$, and $\mathbf{P}^t$, form objective function by (4.90);
Alternatively update $\boldsymbol{\lambda}$ by (4.91) and $\overline{\mathbf{W}}$ by solving (P4-2.3.1) with CVX toolbox until convergence;
$t = t + 1$;
until convergence reaches
Output: $\mathbf{A}_j^t, \forall j \in \mathcal{J}_{\mathcal{C}}$, $\mathbf{P}^t$, and $\mathbf{U}^t$, $\overline{\mathbf{W}}^t$.

lated as

$$\text{(P4-2.3.1)} \quad \max_{\overline{\mathbf{W}}^{t_2}} \quad O''(\overline{\mathbf{W}}) \tag{4.103}$$

$$\text{s.t.} \quad \text{(4.87c), (4.87b), (4.102).} \tag{4.104}$$

The SCA algorithm is used to iteratively optimize $\overline{\mathbf{W}}$, while in each iteration, the problem (P4-2.3.1) is a standard convex optimization problem and can be solved by CVX toolbox.

4.3.5 The Overall Solution

The overall algorithm for sum-rate maximization via jointly optimizing active beamforming $\mathbf{A}_j, \forall j \in \mathcal{J}_{\mathcal{C}}$, power allocation $\mathbf{P}$, UE association $\mathbf{U}$, and passive RIS beamforming $\overline{\mathbf{W}}$ is summarized as **Algorithm 9**. For the initialization, we randomly set $\overline{\mathbf{W}}^0$ to satisfy $\left|w_{q,m}\right| = 1, \forall q \in \mathcal{Q}, m = 1, \cdots, M$. The sum power is equally allocated to all UEs, i.e., $p_{j,k}^0 = \frac{\sum_{j=1}^{J_{\mathcal{C}}} \mathbf{p}_j}{K_{\mathcal{C}}}$. Furthermore, as the penalty factor $\tau_u \gg 0$, the imposition of constraints on the initial setup of $\mathbf{U}^0$ may trap the objective function and impede the identification of the optimal solution. Sequentially, we set $\mathbf{U}^0 = \mathbf{0}$.

We now analyze the computational complexity and convergence behaviour of **Algorithm 9**. The complexity to update $\mathbf{A}_j, \forall j \in \mathcal{J}_{\mathcal{C}}$ and $\mathbf{P}$ are $\mathcal{O}(K_{\mathcal{C}} M^2)$ and $\mathcal{O}(K_{\mathcal{C}} J_{\mathcal{C}})$, respectively. For the UE association, the computational complexity of solving (P4-2.2) is polynomial in the number of variables and constraints. (P4-2.2) is an optimization problem with a linear objective associated with $(K_{\mathcal{C}} J_{\mathcal{C}})$ variables, and $(K_{\mathcal{C}} + 2J_{\mathcal{C}} + K_{\mathcal{C}} J_{\mathcal{C}})$ linear constraints. By referring that the complexity of solving an iterative-optimized problem with a variables and

b linear constraints is $\mathcal{O}((1+a+b)a^2\sqrt{b+1})$ [156], the complexity required to solve (P4-2.2) is approximated as $\mathcal{O}((K_{\mathcal{C}}+2J_{\mathcal{C}}+2K_{\mathcal{C}}J_{\mathcal{C}})^{3/2}(K_{\mathcal{C}}J_{\mathcal{C}})^2)$. In the sequel, the complexity of updating $\overline{\mathbf{W}}$ can be obtained as $\mathcal{O}((K_{\eta}Q+2J_{\mathcal{C}}K_{\mathcal{C}}+2QM)^{3/2}Q^2M^2)$. Denote by T the number of iterations. The overall computational complexity can be approximately summarized as $\mathcal{O}\{T((K_{\mathcal{C}}J_{\mathcal{C}})^{7/2}+K_{\eta}Q^3M^2+K_{\mathcal{C}}J_{\mathcal{C}}Q^2M^2+(QM)^{7/2})\}$. The proof of convergence can be found in Appendix A.5.

4.3.6 Simulation Results

In this section, numerical examples are demonstrated to verify the effectiveness of our system model and algorithms. We assume that there are two c-BSs located at $(10\sqrt{2},10\sqrt{2})$m, $(-10\sqrt{2},-10\sqrt{2})$m, and two n-BSs located at $(10\sqrt{2},-10\sqrt{2})$m, $(-10\sqrt{2},10\sqrt{2})$m. Each of them is equipped with $N=16$ antennas. In addition, 4 RISs, each comprising $M=64$ passive elements, are uniform-placed along the line connecting two c-BSs, with the coordinate $(-6\sqrt{2},-6\sqrt{2})$m, $(-2\sqrt{2},-2\sqrt{2})$m, $(2\sqrt{2},2\sqrt{2})$m, $(6\sqrt{2},6\sqrt{2})$m, respectively. $K_{\mathcal{C}}=K_{\eta}=16$ single-antenna UEs are randomly distributed in a circular area with a center of $(0,0)$m and a radius of 20 m. The weighted centre frequency is set as $f_c=28$ GHz, where c-BSs have the same bandwidth. We refer to [151] to set the channel parameters. $L_z=3, z=\{(j,k),(q,k),(j,q)\}$. The complex gain $\alpha_l^z, \forall l\in L_z$ is generated according to the complex Gaussian distribution $\alpha_l^z\sim\mathcal{CN}(0,10^{-0.1\kappa})$. The free space path loss κ can be generally expressed as $\kappa=\kappa_a+10\kappa_b\log_{10}(d)+\kappa_c$, where d represents the distance in meters. For LoS and NLoS path, κ_a, κ_b, and κ_c are set as $\kappa_{a,\text{LoS}}=61.4$, $\kappa_{b,\text{LoS}}=2$, $\kappa_{c,\text{LoS}}\sim\mathcal{N}(0,\sigma^2_{\text{LoS}})$,$\kappa_{a,\text{NLoS}}=72.0$, $\kappa_{b,\text{NLoS}}=2.92$, $\kappa_{c,\text{NLoS}}\sim\mathcal{N}(0,\sigma^2_{\text{NLoS}})$, where $\sigma_{\text{LoS}}=5.8$ dB, $\sigma_{\text{NLoS}}=8.7$ dB. In addition, we have $\zeta_t=9.82$ dBi, $\zeta_r=0$, $K_{\text{BS}}=8$, $p_{\max}=30$ dBm, $\sigma_n^2=-85$ dBm. The SNR constraint for c-UEs is set as $\text{SNR}_{th}=10^{-4}$, and the constraint for the reflective channel gain of n-BSs to the associated UEs is set as $\delta=10^{-15}$.

Fig. 4.6 shows the convergence behaviour of the proposed algorithm in terms of the sum rate with different numbers of UEs and RIS elements. It can be seen that the sum rate of UEs served by cooperative BSs increases rapidly at initial and converges to a stable value within limited iterations, ensuring the feasibility of our proposed algorithm. It can also be seen that with the increase in the number of serving UEs and RIS elements, the sum rate has been improved.

Fig. 4.7 demonstrates the sum rate under different numbers of RIS elements. Specifically, we set the number of RIS elements as $M=\{32,64,96,128,160,192\}$. Each RIS has the same size. We define several baselines: (a) RPBF (random passive beamforming): optimize $\mathbf{A}_j, \forall j\in\mathcal{J}_{\mathcal{C}}$, $\mathbf{P}$, and $\mathbf{U}$ with randomly generated RIS weights, (b) FUA (fixed UE

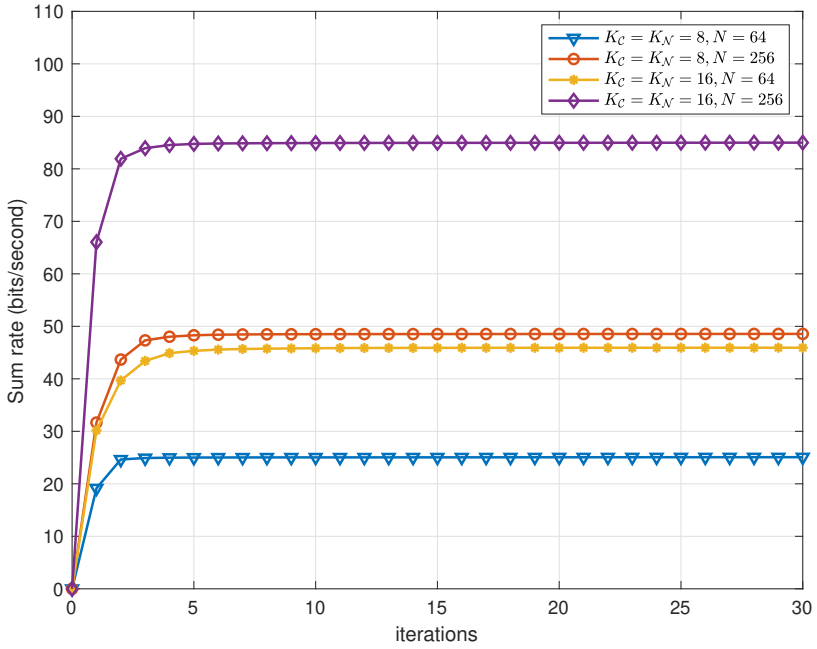

Figure 4.6: Convergence behaviour of the proposed algorithm.

association): optimize $\mathbf{A}_j, \forall j \in \mathcal{J}_{\mathcal{C}}$, $\mathbf{P}$, and $\overline{\mathbf{W}}$ with randomly UE association, (c) FPA (fixed power allocation): optimize $\mathbf{A}_j, \forall j \in \mathcal{J}_{\mathcal{C}}$, $\mathbf{U}$, and $\overline{\mathbf{W}}$ with equal power allocation, and (d) No RIS: optimize $\mathbf{A}_j, \forall j \in \mathcal{J}_{\mathcal{C}}$, $\mathbf{U}$, and $\mathbf{P}$ when no RISs exist, to compare with our proposed design. It can be seen that the sum rate increases with an increase number of RIS elements, regardless of the RIS weights, power allocation, and UE association. However, our proposed design could always realize the maximum sum rate compared with the baselines, indicating the significance of designing RISs and optimizing resource allocation for enhancing sum rate performance.

Fig. 4.8 shows the impact of the transmit power on the achievable sum rate. Specifically, we set the transmit power as $p_{\max} = \{15, 20, 25, 30, 35, 40\}$dBm for both c-BSs. Our proposed design is compared with the baselines introduced above. We can first observe that the sum rate monotonically increases as more transmit power is given. It can be seen that the achievable sum rate with 40 dBm transmit power is up to 94 bits/second by our proposed resource allocation design, while the sum rate with 15 dBm is only about 11 bits/second. On the other hand, we observe that the significance of the power allocation scheme is accentuated particularly in scenarios with limited total transmit power. This is because in scenarios characterized by low total power, a substantial portion of the available power is necessitated to satisfy the SNR requirements. However, in instances of abundant total power, in accordance with the AM-GM inequality theorem [157], there is a positive correlation between the sum rate and the fairness of allocation. Consequently, the outcome of optimization closely approximates

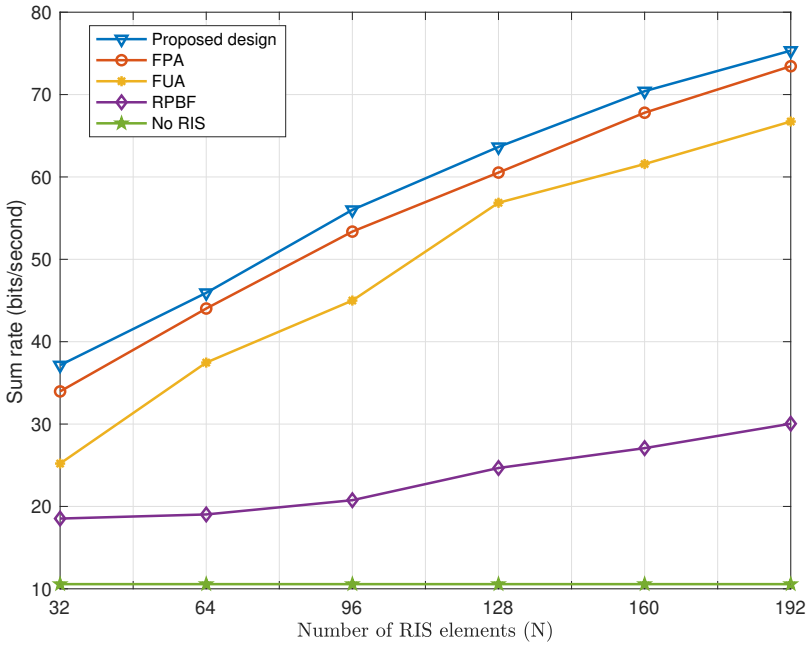

Figure 4.7: Sum rate under different numbers of RIS elements.

that of fixed equal power allocation when the total power is high. The power allocation at a high sum power may not be needed. Particularly, when $p_{\max} = 40$ dBm, the maximized sum rate of our proposed algorithm is only as high as 0.34% of the rate achieved by FPA, while the improvement can be 25.6% when the total transmit power is $p_{\max} = 15$ dBm. In addition, the configuration design of RISs and the UE association are vital, which largely affect the sum rate performance.

Fig. 4.9 shows the UE association and power allocation scheme for $K_{\mathcal{C}} = K_{\mathcal{H}} = 16$ UEs with randomly generated locations in a circular area with the radius of 20 m. The number of elements on each RIS is set as $M = 64$. Specifically, UEs are optimized to associate with the two cooperative BSs, satisfying $K_j \leq K_{\text{BS}}, \forall j \in \mathcal{J}_{\mathcal{C}}$. Different colors are used to indicate the association between BSs and UEs. On the other hand, The height of each bar represents the allocated power. It can be seen that for each BS, the power is not equally allocated to the serving UEs for the maximal sum rate, revealing the necessity to optimize the power allocation. In addition, the achievable SNR of each UE served by cooperative BSs is presented by the solid line, while a dashed line is used to indicate the SNR threshold. We can observe that the SNRs of all UEs are higher than the given threshold with a maximum sum rate.

Fig. 4.10 investigates the effects of RISs on n-BSs' reflective channels. The RPBF design and optimization without channel gain constraint on the reflective links, i.e., (4.69c), are used for comparison. It can be seen that both designs for comparison result in high average

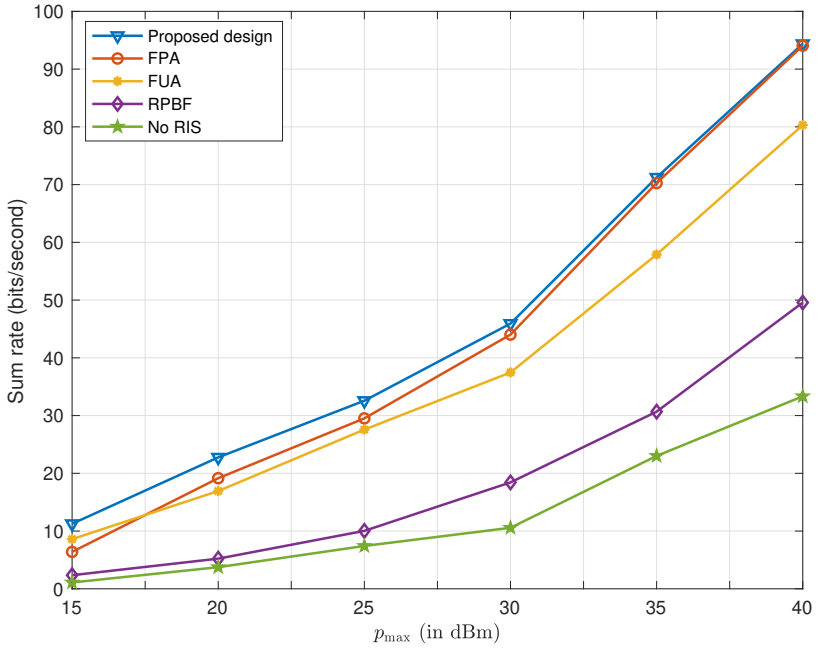

Figure 4.8: Sum rate under different transmit power.

channel gains of n-BSs-RISs-n-UEs links, revealing severe effects taken by RISs to the UEs served by n-BSs. Additionally, with the increase in the number of elements of each RIS, the average channel gain increases correspondingly, resulting in more significant influences. In contrast, our proposed design enables a much lower average channel gain of the reflective links, realizing more than 100 times suppression compared with the baselines. The pre-defined channel gain constraint $\delta = 10^{-15}$ can be satisfied. It can be concluded that our proposed design alleviates the impacts of RISs on the links between n-BSs and their serving UEs to a large extent.

4.4 Summary

In this chapter, we propose resource allocation under a RIS-aided hybrid BS cooperative and non-cooperative network. We first propose the idea of BSs' cooperation and non-cooperation scheme based on their agreement on whether to jointly utilize the RISs and share resources. Our study is crucial since BSs from different operators may not always agree to cooperatively use the same RIS or share spectrum, power, and other resources for security and cost concerns. Specifically, we consider that the RISs are designed to improve the communication performance of cooperative BSs and cannot affect the communication of other non-cooperative BSs. We start with a simple scenario where two non-cooperative BSs exist. The sub-channel assignment, power allocation, and RIS beamforming are jointly optimized

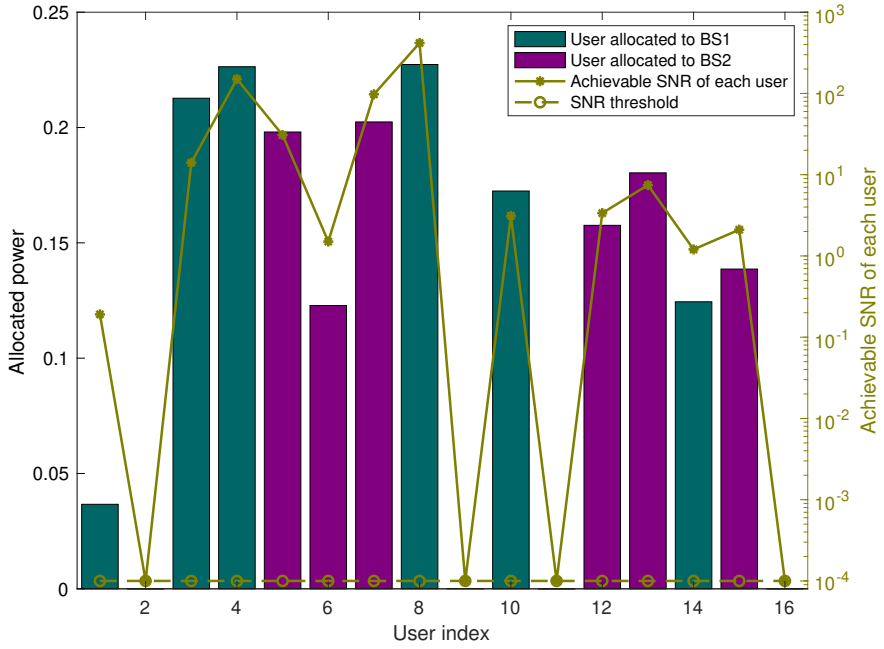

Figure 4.9: Power allocation, user association, and the achievable SNR of each UE. (The color and height of each bar corresponds to the user association and allocated power level; the solid and dashed line corresponds the achieved and the threshold SNR.)

to maximize the sum rate of UEs served by RIS-aided BS. At the same time, the channel gain of the reflective link between another BS and its corresponding UEs through the RIS is constrained. Then, we generalize to the investigation of resource allocation for multiple c-BSs - n-BSs - RISs network. For UEs served by the RIS-aided BSs, the sum rate is maximized by jointly optimizing UE association, power allocation, active beamforming, and passive RIS beamforming. On a parallel avenue, the RIS is designed to alleviate its effect on the links between the non-cooperative BSs and their corresponding UEs. An efficient algorithm leveraging the BCD technology is applied to solve the non-convex optimization problem under both scenarios. Simulation results reveal the feasibility of our proposed algorithm in realizing the maximum sum rate with constrained channel gain between non-cooperative BSs and their serving UEs.

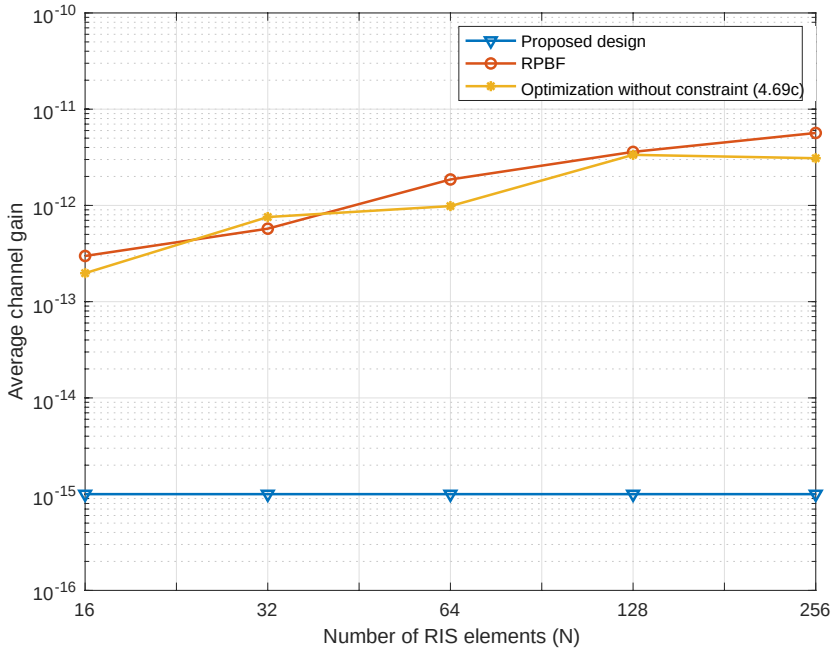

Figure 4.10: The effects of RISs on n-BSs-RISs-n-UEs links under different numbers of RIS elements.

Chapter 5

A Codebook Design of RIS Leveraging Beam Squint

In the previous two Chapters, the generation of broadbeam on RIS and the cooperation relationship between BSs in RIS-assisted network are designed and analyzed. However, the RIS-assisted wideband system is less focused. This chapter presents further analysis of RIS in wideband system with beam squint effect. In particular, we propose a novel RIS codebook design by leveraging beam squint with the help of HPBW concept. We aim to design the RIS phase shifts such that the beams with squint generated by different RIS weights could tile over the entire spatial domain of the RIS without overlapping. To quantify the spatial coverage performance in wideband systems, a new term — W-HPBW, is introduced based on the definition of HPBW. This design could largely reduce computational complexity and the requirements for channel estimation.

5.1 Introduction

Many investigations have been involved in the design and implementation of RIS, while most of them are restricted to the narrowband system [158–160]. It is worth mentioning that when considering more general wideband channels, both channel estimation and beamforming optimization could be quite different and even more difficult to be addressed [161]. Several works considered the wideband channels in RIS-aided systems. For example, a novel twin-RIS structure consisting of two RIS planes with a relative spatial rotation was proposed for channel estimation and UE localization in RIS-assisted MIMO-OFDM systems in [162]. The resource allocation issue in a RIS-aided OFDM system was investigated in [163]. Specifically, the authors proposed the system sum-rate maximization framework, where sub-carrier allocation, BS transmit beamforming, and RIS phase shift were jointly optimized.

However, the work mentioned above did not consider the beam squint effect, which could result in a tremendous loss in the average SE [164]. Since RIS phase shifts are restricted to be the same, beam squint incurs the array response's direction change of RIS under different frequencies. Only a few works [165, 166] investigated the beam squint effect of RIS-aided wideband systems. Specifically, some RIS phase shift design schemes for mitigating beam squint effect for the LoS and NLoS scenarios were investigated in [165]. Moreover, the authors in [166] proposed a twin-stage orthogonal matching pursuit (TS-OMP) algorithm to reduce the influence of false angles on channel estimation taking the beam squint effect. These works considered the beam squint effect in SE improvement and channel estimation, making the applied algorithms and theoretical findings more adequate for practical systems.

Nevertheless, the key issue — signal coverage is less focused. It is undoubted that signal coverage is a crucial indicator to be investigated in RIS-aided systems, as the coverage quality highly impacts the system performance and UE experience [167]. To quantify the signal coverage performance, the HPBW is one of the most important metrics [168]. HPBW is conventionally defined as the beamwidth within which the signals' normalized radiated power is higher than -3 dB in a narrowband system. The investigation of HPBW is crucial since it ensures the SNR of transceivers. In addition, a high SNR is a prerequisite for accurate channel estimation and data transmission.

In this chapter, with the help of HPBW concept, we propose a novel RIS codebook design for signals' spatial coverage enhancement in wideband systems considering beam squint effect. The main idea of this design is to generate multiple beams by different RIS weights which could cover the whole spatial domain of the RIS without overlap. The contributions are summarized as follows:

- To characterize the HPBW in wideband systems taking beam squint effect, we generalize HPBW to W-HPBW. The W-HPBW indicates the HPBW decided by the radiated patterns under different frequencies.

- A novel RIS codebook design is proposed by leveraging beam squint. In this case, we design the RIS beamforming weights such that each spatial coverage satisfies the W-HPBW criteria and the beams generated by all groups of RIS weights complete the coverage of spatial domain.

- For signal coverage in high mobility scenarios, such as vehicular communication, we apply the beam broadening technique to further reduce RIS weights switching and pilot overhead in channel estimation.

5.2 System Model

For simplicity, we consider a single antenna-implemented-BS and a RIS in ULA configuration with M elements. We define $w_m = \beta_m e^{j\alpha_m}$ as the weight of the m-th element in the RIS, where $\beta_m = 1$, $\alpha_m \in [0, 2\pi], m = 1, \cdots, M$. Then we denote $\mathbf{a}(\Omega_{in}) \in \mathbb{C}^{M\times 1}$ as the channel vector from the BS to RIS. With the ULA configuration, the BS-RIS channel vector can be expressed as

$$\mathbf{a}(\Omega_{in}, f) = [1, e^{j\frac{2\pi f}{c}d\cos\theta_{in}}, \cdots, e^{j\frac{2\pi f}{c}d(M-1)\cos\theta_{in}}]^T. \tag{5.1}$$

Note that f is the frequency within the bandwidth and d is the element spacing. We define Ω_k as the term containing the spatial information with respect to θ_k, i.e., $\Omega_k = \cos\theta_k$. Therefore, we have $\Omega_{in} = \cos\theta_{in}$. Similarly, the steering vector from RIS to the direction θ_{out} could be given by

$$\mathbf{a}(\Omega_{out}, f) = [1, e^{j\frac{2\pi f}{c}d\cos\theta_{out}}, \cdots, e^{j\frac{2\pi f}{c}d(M-1)\cos\theta_{out}}]^T. \tag{5.2}$$

Combining $\mathbf{a}(\Omega_{out}, f)$ and $\mathbf{a}(\Omega_{in}, f)$, we can get the channel vector of the RIS-aided system as

$$\mathbf{a}_C(\Omega_{in}, \Omega_{out}, f) = \mathbf{a}(\Omega_{in}, f) \odot \mathbf{a}(\Omega_{out}, f) \in \mathbb{C}^{M\times 1}. \tag{5.3}$$

For simplicity, we first assume the locations of the RIS and BS are fixed. The array factor could then be represented as a function of Ω_{out} and f, which is given by

$$AF(\Omega_{out}, f) = \mathbf{a}_C(\Omega_{in}, \Omega_{out}, f)^T \cdot \mathbf{w}. \tag{5.4}$$

We further define

$$A = \cos\theta_{out} + \cos\theta_{in}, \tag{5.5}$$

then the expression in (5.4) can be transformed into

$$AF(\Omega_{out}, f) = \frac{1}{M}|\sum_{m=1}^{M} w_m e^{j\frac{2\pi f}{c}dA(m-1)}|. \tag{5.6}$$

It can be seen that $AF(\Omega_{out}, f)$ varies with regard to the frequency. The beam squint phenomenon incurs due to the fact that the weights are fixed for all different sub-carriers of the wideband system.

5.2.1 Beam Squint Effect

To illustrate the beam squint effect and the definition of W-HPBW, we assume a system with B bandwidth at f_c carrier frequency. In Fig. 5.1, we use a 16-element RIS by applying

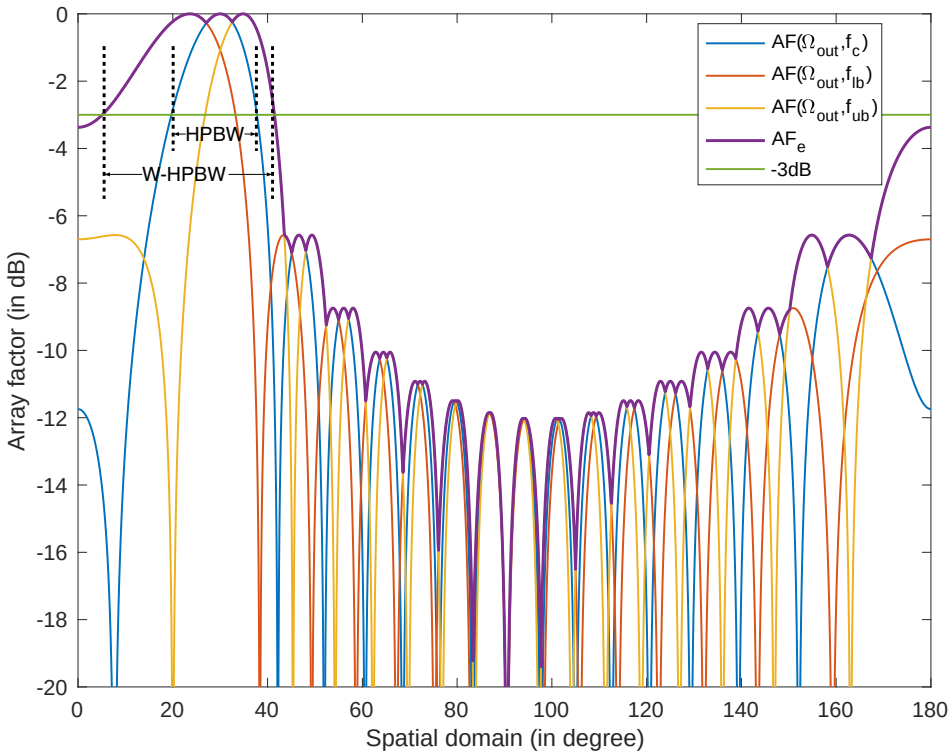

Figure 5.1: Beam squint effect with $\theta_{in} = 90°$ and $\theta_{out} = 30°$.

the MRT beamforming towards $\theta_{out} = 30°$. We also consider an incident angle $\theta_{in} = 90°$, and the carrier frequency is set to be $f_c = 73$ GHz with $B = 8$ GHz bandwidth. Note that the bandwidth is chosen to be quite large for purposes of illustration. The minimum and maximum frequency is $f_{lb} = 69$ GHz and $f_{ub} = 77$ GHz, respectively.

As can be seen from Fig. 5.1, beam squint is the change in the beam direction as a function of operating frequency [169]. This change could result in severe degradation in SE considering the beam misalignment of the wideband system. Specifically, we define $\hbar$ as the function of the operating frequency f as

$$\hbar(f) = \frac{2\pi f}{c}. \tag{5.7}$$

We denote a term $f^{\dagger}$ as either f_{lb} or f_{ub}, where $f_{lb} = f_c - \frac{B}{2}$ and $f_{ub} = f_c + \frac{B}{2}$. Then the absolute value of the difference between $\hbar(f_c)$ and $\hbar(f^{\dagger})$ could be expressed as

$$\Delta\hbar = \frac{\pi B}{c}. \tag{5.8}$$

Based on (5.8), the array factor under frequency $f^{\dagger}$ could then be given by

$$\begin{aligned} AF(\Omega_{out}, f^{\dagger}) &= \frac{1}{M}|\sum_{m=1}^{M} w_m e^{j\hbar(f^{\dagger})A(m-1)}| \\ &= \frac{1}{M}|\sum_{m=1}^{M} w_m e^{j(\hbar(f_c)\pm\Delta\hbar)A(m-1)}|. \end{aligned} \tag{5.9}$$

It can be seen that there is a phase shift $\Delta\phi = \pm\Delta\hbar A(m-1), m = 1, \cdots, M$ when the operating frequency is either f_{lb} or f_{ub}, resulting in the change in the beam direction. To explicitly analyze the change in the beam direction under different frequencies, we firstly define a reflected direction under f_c as $\theta_{out,c}$, then we have

$$A_c = \cos\theta_{out,c} + \cos\theta_{in}. \tag{5.10}$$

Compared with other frequencies within the bandwidth, it is not hard to find that the most heavy squints are generated under f_{lb} and f_{ub}. We further define $\theta_{out,lb}$ and $\theta_{out,ub}$ as the radiated direction under f_{lb} and f_{ub}, respectively, which are generated regarding $\theta_{out,c}$ due to the beam squint effect. Then, by solving

$$AF(\Omega_{out,c}, f_c) = \begin{cases} AF(\Omega_{out,lb}, f_{lb}) \\ AF(\Omega_{out,ub}, f_{ub}) \end{cases}, \tag{5.11}$$

we can derive that when

$$\theta_{out,lb} = \arccos(\frac{\hbar(f_c)A_c}{\hbar(f_c) - \Delta\hbar} - \cos\theta_{in}), \tag{5.12}$$

and

$$\theta_{out,ub} = \arccos(\frac{\hbar(f_c)A_c}{\hbar(f_c) + \Delta\hbar} - \cos\theta_{in}), \tag{5.13}$$

the array responses under f_{lb}/f_{ub} reach the same level as the array response under f_c, while a change in the beam direction could be observed. Here, $\frac{k(f_c)A_c}{k(f_c)\pm\Delta\hbar} - \cos\theta_{in}$ might be beyond the range $[-1, 1]$, meaning that even though there is still a change in the beam direction, the array response of the squint beam will not be the same as that under the carrier frequency f_c, which can be observed in Fig. 5.1.

Specifically, when $\theta_{out,c} = 180^{\circ} - \theta_{in}$, i.e., $A_c = 0$, we have

$$AF(\Omega_{out}, f^{\dagger}) = \frac{1}{M}|\sum_{m=1}^{M} w_m|, \tag{5.14}$$

which means that at this specific radiation direction, we have $\theta_{out,c} = \theta_{out,lb} = \theta_{out,ub}$. The array factor is always the same regardless of the frequency and RIS weights. When $A_c > 0$, i.e., $\theta_{out,c} \in [0, 180° - \theta_{in}]$, a $\theta_{out,lb}$ satisfying $\theta_{out,lb} < \theta_{out,c}$ will be obtained by (5.12), and a $\theta_{out,ub}$ satisfying $\theta_{out,ub} > \theta_{out,c}$ will be obtained by (5.13). Therefore, a left/right-towards change in the beam direction under f_{lb}/f_{ub} will be produced, respectively. Likewise, when $A_c < 0$, i.e., $\theta_{out,c} \in [180° - \theta_{in}, 180°]$, a right/left-towards change in the beam direction under f_{lb}/f_{ub} will be inversely produced, respectively.

5.2.2 The Definition of W-HPBW

We mainly leverage the beam squint effect caused by the frequency of beam broadening to support spatial coverage from a RIS. In detail, we define a new term — W-HPBW, which is generalized by HPBW. Specifically, W-HPBW indicates a spatial domain that an array can receive/transmit more than half of its maximum beamforming power from/to possible transceivers in the wideband system. An example of W-HPBW is indicated in Fig. 5.1, which is defined by the envelope generated by multiple array factors under different frequencies within the bandwidth. The array response of the envelope is represented as

$$AF_e(\Omega_{out}) = \max\{AF(\Omega_{out}, f)\},\ f \in [f_{lb}, f_{ub}]. \tag{5.15}$$

And the W-HPBW is constrained by the beamwidth which satisfies

$$AF_e(\overline{\Omega}) \geq -3\text{dB},\ \overline{\Omega} \in [\Omega_L, \Omega_R]. \tag{5.16}$$

Note that, for W-HPBW, Ω_L and Ω_R contain the spatial information of the left-hand side and right-hand side, respectively. Since the most heavily squinted beams are generated at the maximum and minimum frequencies, as can be observed in Fig. 5.1, Ω_L and Ω_R are obtained by the beams generated under either f_{lb} or f_{ub}.

5.3 The RIS Codebook Design

In order to achieve spatial coverage, as shown in Fig. 5.2, we propose a RIS codebook design to divide the whole spatial domain from 0 to 180° into Q sub-areas. Specifically, each sub-area is defined to be the same size as W-HPBW under different groups of RIS weights. For the signal coverage of the q-th sub-area, a group of RIS weights denoted as $\mathbf{w}_q$ will be given. These sub-areas can cover the entire spatial domain without overlapping with each other.

The proposed codebook design can be considered as finding the boundaries of each sub-

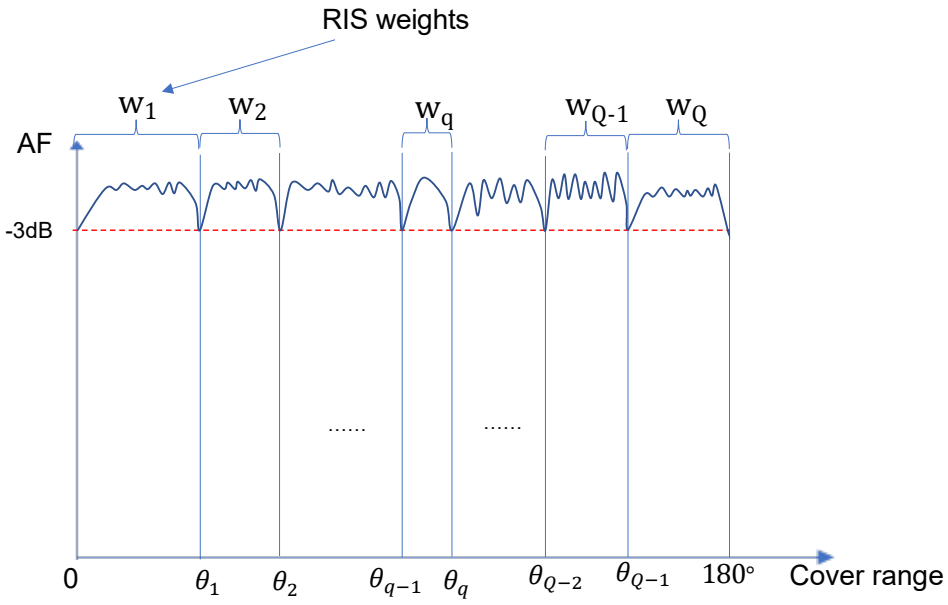

Figure 5.2: Spatial domain covered by beams generated by Q group of RIS weights. Each group of RIS weights leverages the beam squint for signal coverage.

area $\mathbf{\Theta} = \{\theta_1, \cdots, \theta_{Q-1}\}$ and the corresponding codebook $\mathcal{W} = \{\mathbf{w}_1, \cdots, \mathbf{w}_Q\}$ for all sub-areas. As a consequence, the UE at an arbitrary location could therefore receive signals with power exceeding the level of 3 dB below the array's maximum power gain.

5.3.1 Codebook Design with MRT Beamforming

For each sub-area, we design RIS beamforming weights by applying MRT beamforming as did in [168]. In detail, the RIS weights $\mathbf{w}_q \in \mathbb{C}^{M\times 1}$ for the q-th sub-area is expressed as the function of a reference angle θ_q^*, which is defined as a specific direction within the sub-area $[\theta_{q-1}, \theta_q]$. For the specific m-th element in $\mathbf{w}_q$, we have

$$w_{q,m} = e^{-j\frac{2\pi f_c}{c}d(m-1)(\cos\theta_{in}+\cos\theta_q^*)}. \tag{5.17}$$

Since $\mathbf{w}_q$ can be expressed as the function of θ_q^*, the RIS codebook design is equivalent to finding the boundaries of each sub-area $\mathbf{\Theta} = \{\theta_1, \cdots, \theta_{Q-1}\}$ and the reference angle $\mathbf{\Theta}^* = \{\theta_1^*, \cdots, \theta_Q^*\}$ within each sub-area. As a consequence, the codebook $\mathcal{W} = \{\mathbf{w}_1, \cdots, \mathbf{w}_Q\}$ could be further obtained.

With given θ_{in}, we first let $\theta_q^* = 180^\circ - \theta_{in}$, which is the reference angle of the q-th sub-area. Therefore, the codebook design is now equivalent to finding the boundaries of the q-th sub-area, i.e., θ_{q-1} and θ_q, and also the reference angles of the adjacent $(q-1)$-th and $(q+1)$-th sub-area, i.e., θ_{q-1}^*, and θ_{q+1}^*. Then, angles $\{\theta_1, \cdots, \theta_{q-2}, \theta_{q+1}, \cdots, \theta_{Q-1}\}$ and $\{\theta_1^*, \cdots, \theta_{q-2}^*, \theta_{q+2}^*, \cdots, \theta_Q^*\}$ are iteratively and similarly obtained. For each iteration, the

procedure can be divided into the following two steps:

A. Find the q-th sub-area domain $[\theta_{q-1}, \theta_q]$ with known reference angle θ_q^*

As illustrated in Section 5.2, the two sides of the W-HPBW, i.e., the boundaries of the sub-area, are obtained by the beams under $f^\dagger$. To get the expression of the array factor AF under $f^\dagger$, by following (5.5), we firstly define

$$A_1 = \cos\theta_{in} + \cos\theta_q^*, \tag{5.18}$$

and

$$A_2 = \cos\theta_{in} + \cos\theta_b, \tag{5.19}$$

where θ_b is denoted as the boundary of the sub-area, and is either θ_{q-1} or θ_q. Then the array factor AF under $f^\dagger$ could be represented as

$$\begin{aligned} AF(\Omega_b, f^\dagger) &= \tfrac{1}{M}\left|\textstyle\sum_{m=1}^{M} w_n e^{j(m-1)d\hbar(f^\dagger)A_2}\right| \\ &= \tfrac{1}{M}\left|\textstyle\sum_{m=1}^{M} e^{j(m-1)d(\hbar(f^\dagger)A_2 - \hbar(f_c)A_1)}\right| \\ &= \tfrac{1}{M}\left[\tfrac{\sin(\frac{Md}{2}(\hbar(f^\dagger)A_2 - k(f_c)A_1))}{\sin(\frac{d}{2}(\hbar(f^\dagger)A_2 - \hbar(f_c)A_1))}\right] \\ &\approx \tfrac{\sin(\frac{Md}{2}(\hbar(f^\dagger)A_2 - \hbar(f_c)A_1))}{\frac{Md}{2}(\hbar(f^\dagger)A_2 - \hbar(f_c)A_1)}. \end{aligned} \tag{5.20}$$

Note that $AF(\Omega_b, f^\dagger)$ is in the form of $\sin(\chi)/\chi$ with $\chi = \frac{Md}{2}(\hbar(f^\dagger)A_2 - \hbar(f_c)A_1)$. Assume the power threshold is set as δ, which is generally -3 dB, we therefore have

$$AF(\Omega_b, f^\dagger) = \frac{\sin(\chi)}{\chi} = 10^{\frac{\delta}{20}}, \tag{5.21}$$

which enables the interaction of Ω_b at -3 dB level. It is not hard to find that there are two solutions regarding χ, which are denoted as $\pm\xi$. Then, by solving (5.21) we get

$$\chi = \frac{Md}{2}(\hbar(f^\dagger)A_2 - \hbar(f_c)A_1) = \pm\xi. \tag{5.22}$$

By taking (5.18) and (5.19) into (5.22), with $f^\dagger$ is either f_{lb} or f_{ub}, the θ_b is given by

$$\begin{cases} \theta_{b1} = \arccos\left(\frac{\frac{\pm 2\xi}{Md} + \hbar(f_c)A_1}{\hbar(f_{lb})} - \cos\theta_{in}\right), \\ \theta_{b2} = \arccos\left(\frac{\frac{\pm 2\xi}{Md} + \hbar(f_c)A_1}{\hbar(f_{ub})} - \cos\theta_{in}\right). \end{cases} \tag{5.23}$$

Note that both θ_{b1} and θ_{b2} have two solutions, indicating that there are four possible values of θ_{q-1} and θ_q, respectively.

According to the characteristics of beam squint proposed in section 5.2.1, we know that the change in the beam direction depends on the relationship between the reflected direction

and the incident direction. The solutions to θ_{q-1} and θ_q based on θ_q^* can be henceforth represented as

$$\begin{cases} \theta_{q-1} = \min\{\theta_{b1}\}, \ \theta_q^* \le 180^\circ - \theta_{in} \\ \theta_{q-1} = \min\{\theta_{b2}\}, \ \theta_q^* > 180^\circ - \theta_{in} \\ \theta_q = \max\{\theta_{b1}\}, \quad \theta_q^* \ge 180^\circ - \theta_{in} \\ \theta_q = \max\{\theta_{b2}\}, \quad \theta_q^* < 180^\circ - \theta_{in}. \end{cases} \tag{5.24}$$

Specially, we let $\theta_{q-1} = 0$ if $\theta_{q-1} < 0$ is obtained; and $\theta_q = 180^\circ$ if $\theta_q > 180^\circ$. The W-HPBW of the q-th sub-area when $\theta_{q-1} < 0$ or $\theta_q > 180^\circ$ could be $[0, \theta_q]$ or $[\theta_{q-1}, 180^\circ]$. So far the spatial domain of the q-th sub-area is obtained.

B. Find the reference angles θ_{q-1}^* and θ_{q+1}^* within the adjacent sub-areas

With given θ_{q-1}, which acts not only the left-side boundary of q-th sub-area, but also the right-side boundary of the $(q-1)$-th sub-area, we aim to obtain θ_{q-1}^*. In detail, A_2 is now fixed with known θ_{q-1}, while A_1 is a variable with unknown θ_{q-1}^*. Therefore, by taking θ_{q-1} into the term A_2 in (5.22), we get

$$\begin{cases} \chi(\hbar(f_{lb}), \theta_{q-1}) = \pm\xi \\ \chi(\hbar(f_{ub}), \theta_{q-1}) = \pm\xi. \end{cases} \tag{5.25}$$

By solving (5.25), we get $\theta_{q-1}^* \in \{\theta_{r1}, \theta_{r2}\}$, which is given by

$$\begin{cases} \theta_{r1} = \arccos\left(\frac{\frac{\pm 2\xi}{Md} + \hbar(f_{lb})(\cos\theta_{in} + \cos\theta_{q-1})}{\hbar(f_c)} - \cos\theta_{in}\right) \\ \theta_{r2} = \arccos\left(\frac{\frac{\pm 2\xi}{Md} + \hbar(f_{ub})(\cos\theta_{in} + \cos\theta_{q-1})}{\hbar(f_c)} - \cos\theta_{in}\right). \end{cases} \tag{5.26}$$

Note that θ_{q-1}^* has four possible solutions since both θ_{r1} and θ_{r2} have two values.

Then, θ_{q+1}^* can be similarly obtained with given θ_q, as θ_q acting as the left-side boundary of the $(q+1)$-th sub-area. Specifically, by taking θ_q into the term A_2 in (5.22), we get

$$\begin{cases} \chi(\hbar(f_{lb}), \theta_q) = \pm\xi \\ \chi(\hbar(f_{ub}), \theta_q) = \pm\xi. \end{cases} \tag{5.27}$$

Similarly, there are four possible values of $\theta_{q+1}^* \in \{\theta_{r3}, \theta_{r4}\}$. The expressions of θ_{r3} and θ_{r4} are represented as

$$\begin{cases} \theta_{r3} = \arccos\left(\frac{\frac{\pm 2\xi}{Md} + \hbar(f_{lb})(\cos\theta_{in} + \cos\theta_q)}{\hbar(f_c)} - \cos\theta_{in}\right) \\ \theta_{r4} = \arccos\left(\frac{\frac{\pm 2\xi}{Md} + \hbar(f_{ub})(\cos\theta_{in} + \cos\theta_q)}{\hbar(f_c)} - \cos\theta_{in}\right). \end{cases} \tag{5.28}$$

As a consequence, the solutions for θ^*_{q-1} and θ^*_{q+1} are obtained based on the beam direction regarding the frequency and incident angle:

$$\begin{cases} \theta^*_{q-1} = \min\{\theta_{r1}\},\ \theta^*_q > 180° - \theta_{in} \\ \theta^*_{q-1} = \min\{\theta_{r2}\},\ \theta^*_q \leq 180° - \theta_{in} \\ \theta^*_{q+1} = \max\{\theta_{r3}\},\ \theta^*_q < 180° - \theta_{in} \\ \theta^*_{q+1} = \max\{\theta_{r4}\},\ \theta^*_q \geq 180° - \theta_{in}. \end{cases} \tag{5.29}$$

The iteration ends when $\theta^*_{q-1} \leq 0$ and $\theta^*_{q+1} \geq 180°$, indicating that the first and Q-th subareas are obtained.

5.3.2 Codebook Design with Beam Broadening Technique

In order to further enlarge W-HPBW and reduce RIS weights switching, we apply the beam broadening technique by using a larger phased array RIS with multiple sub-arrays in the wideband system [170]. Each sub-array has the same size as the phased array used in the preceding case. Specifically, we consider a RIS with $M_s = MN_s$ elements, where N_s denotes the number of sub-arrays and M denotes the number of elements in each sub-array. The aforementioned codebook design is equivalent to considering the case when a single sub-array, i.e., $N_s = 1$, is applied. We define $w_{m,n} = \beta_{m,n} e^{j\alpha_{m,n}}$ as the weight of the m-th element in the n-th sub-array in the RIS, where $\beta_{m,n} = 1$ for maximum reflection efficiency, and $\alpha_{m,n} \in [0, 2\pi], m = 1, \cdots, M, n = 1, \cdots, N_s$.

Similarly, we firstly define a reference angle $\theta^\dagger_q \in [\theta_{q-1}, \theta_q]$. The RIS weights $\mathbf{w}_q \in \mathbb{C}^{MN_s \times 1}$ can then be expressed as a function of $\theta^\dagger_q$. Specifically, drawing parallels from OFDM systems, where the subcarriers are placed at minimas; we place the beams at

$$\Omega^\dagger_{q,n} = \Omega^\dagger_q + \frac{-N_s + 2n - 1}{M},\ n = 1, \cdots, N_s, \tag{5.30}$$

where $\Omega^\dagger_{q,n} = \cos\theta^\dagger_{q,n}$, containing the spatial information of the target direction for the n-th sub-array. Note that $\Omega^\dagger_q \in [-1 + \frac{N_s-1}{M}, 1 - \frac{N_s-1}{M}]$. All $\theta^\dagger_{q,n},\ n = 1, \cdots, N_s$ will be within the range $[\theta_{q-1}, \theta_q]$. Then the m-th element in the n-th sub-array $w_{m,n}$ could be expressed as

$$w_{m,n} = e^{-j\frac{2\pi f_c}{c} d((n-1)M + m - 1)(\Omega^\dagger_{q,n} + \cos\theta_{in})}. \tag{5.31}$$

The codebook design in finding $\mathbf{\Theta} = \{\theta_1, \cdots, \theta_{Q-1}\}$ and the RIS weights $\mathcal{W} = \{\mathbf{w}_1, \cdots, \mathbf{w}_Q\}$ is therefore equivalent to finding $\mathbf{\Theta} = \{\theta_1, \cdots, \theta_{Q-1}\}$ and $\mathbf{\Theta}^\dagger = \{\theta^\dagger_1, \cdots, \theta^\dagger_Q\}$.

Based on the reference angle $\theta^\dagger_q$, the target directions of all sub-arrays, i.e., $\theta^\dagger_{q,n},\ n \in$

$\{1, \cdots, N_s\}$, are obtained by (5.30). The broadened beam is synthesized by the N_s array factors, which are denoted as AF_n, $n = 1, \cdots, N_s$. Then, the array factor with beam broadening could be represented as

$$AF(\Omega_{out}, f) = \frac{1}{M} |\sum_{n=1}^{N_s} \sum_{m=1}^{M} w_{m,n} e^{j\frac{2\pi f}{c} dA((n-1)M+m-1)}|. \tag{5.32}$$

Note that the normalizing factor is set to be $\frac{1}{M}$ as in (5.20), where a single sub-array is applied. Based on the beam placement criterion shown in (5.30), the comparable radiated power could be achieved by this beam broadening technique for single and multiple sub-arrays cases.

Furthermore, since all beams are placed at minimas with regard to the adjacent beams, it is not hard to find that the edges of the main lobe are primarily defined by AF_1 and AF_N, which are generated by the first and N_s-th sub-array, respectively. Other array factors $AF_n, n \neq \{1, N_s\}$ contribute negligible power along these specific directions. Particularly, the n-th sub-array response can be expressed as

$$AF_n(\Omega_{out}, f) = \sum_{m=1}^{M} w_{m,n} e^{j\hbar(f)Ad((n-1)M+m-1)}. \tag{5.33}$$

We then use the method similar to that used in the case with a single sub-array to get the codebook based on the expression of $AF_n(\Omega_{out}, f)$. In detail, we firstly obtain θ_{q-1} and θ_q with given $\theta_q^\dagger$. The expressions of θ_{q-1} and θ_q are given by

$$\begin{cases} \theta_{q-1} = \min\{\theta_{q-1} \Big| \frac{1}{M} |AF_N(\Omega_q^\dagger, f^\dagger)| = 10^{\frac{\delta}{20}}\}, \\ \theta_q = \max\{\theta_q \Big| \frac{1}{M} |AF_1(\Omega_q^\dagger, f^\dagger)| = 10^{\frac{\delta}{20}}\}. \end{cases} \tag{5.34}$$

Following (5.34), the reference angles of adjacent areas, i.e., $\theta_{q\pm1}^\dagger$, are obtained, which are denoted as

$$\begin{cases} \theta_{q-1}^\dagger = \min\{\theta_{q-1}^\dagger \Big| \frac{1}{M} |AF_1(\Omega_{q-1}, f^\dagger)| = 10^{\frac{\delta}{20}}\}, \\ \theta_{q+1}^\dagger = \max\{\theta_{q+1}^\dagger \Big| \frac{1}{M} |AF_N(\Omega_q, f^\dagger)| = 10^{\frac{\delta}{20}}\}. \end{cases} \tag{5.35}$$

After several iterations until $\theta_{q-1} = 0$ or $\theta_q = 180°$, we get the complete RIS codebook for the entire spatial domain.

5.4 Simulation Results

We design the RIS codebook in the wideband system based on our derivations. In detail, we set $\theta_{in} = 90°$. The iteration therefore starts with $\theta_q^* = 90°$ for $N_s = 1$, and $\theta_q^\dagger = 90°$ for $N_s > 1$.

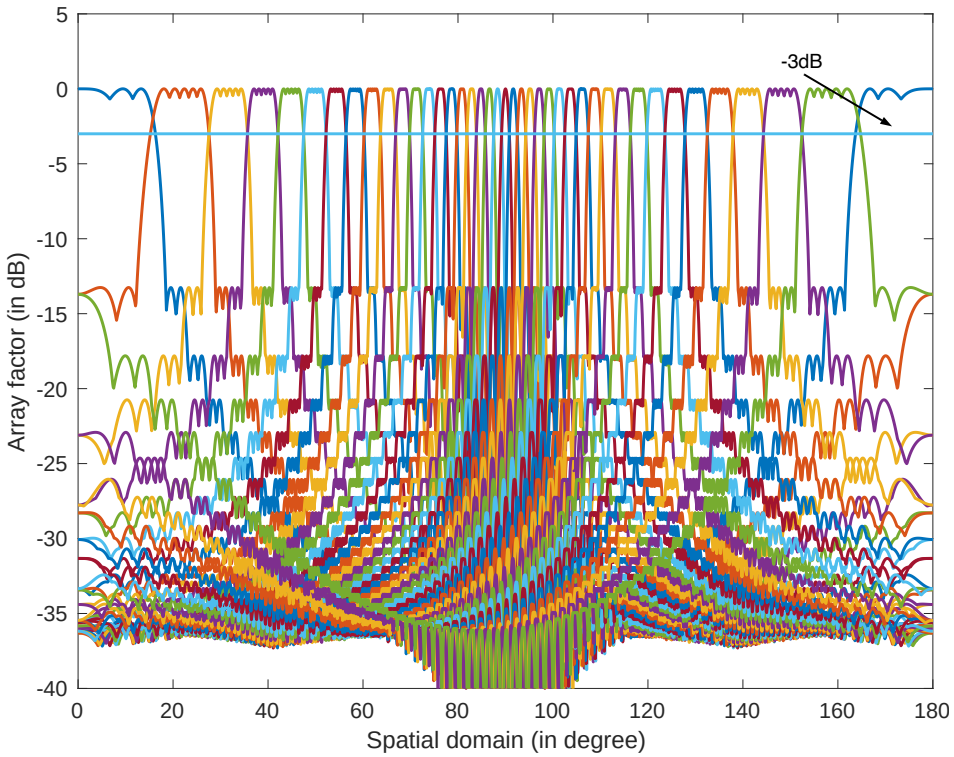

Figure 5.3: RIS codebook design with $N_s = 1$.

The carrier frequency is set to be 73 GHz. The lower and upper bound of the available frequency band is set to be $f_{lb} = 71$ GHz and $f_{ub} = 75$ GHz, respectively. Additionally, the power threshold is set as $\delta = -3$ dB.

In Fig. 5.3, we demonstrate the simulation results when a single sub-array RIS, i.e., $N_s = 1$, with $M = 64$ elements is applied. The beam patterns are generated as the envelope of multiple array factors, i.e., AF_e. For simplicity, we sample the bandwidth $[f_{lb}, f_{ub}]$ at 1 GHz intervals, and AF_e for each sub-area is obtained by applying (5.15). The plots are obtained under different RIS weights as the function of the reference angle θ_q^* proposed by (5.17). Note that UEs at all directions could receive signals with power higher than -3 dB. In addition, we can find that the adjacent generated beams always interact at the -3 dB line, which means that the proposed RIS codebook design can satisfy the condition of the reduced times of RIS phase shift adjustment under the W-HPBW criterion compared with real-time beam tracking.

Fig. 5.4 shows the array factors under different RIS weights when a RIS with 512 elements is applied. Specifically, we have $N_s = 8$ and $M = 64$. Similar to Fig. 5.3, the beam pattern under each group of RIS weights is generated as the envelope of multiple array responses, i.e., AF_e. Compared with the codebook design for a single sub-array, 32 fewer groups of RIS weights are used with the same incident direction $\theta_{in} = 90°$. Besides, the adjacent beam patterns also show a satisfied connection at the -3 dB level. It is worth noting that the W-HPBWs at the first and Q-th sub-areas are truncated by the boundary of the entire

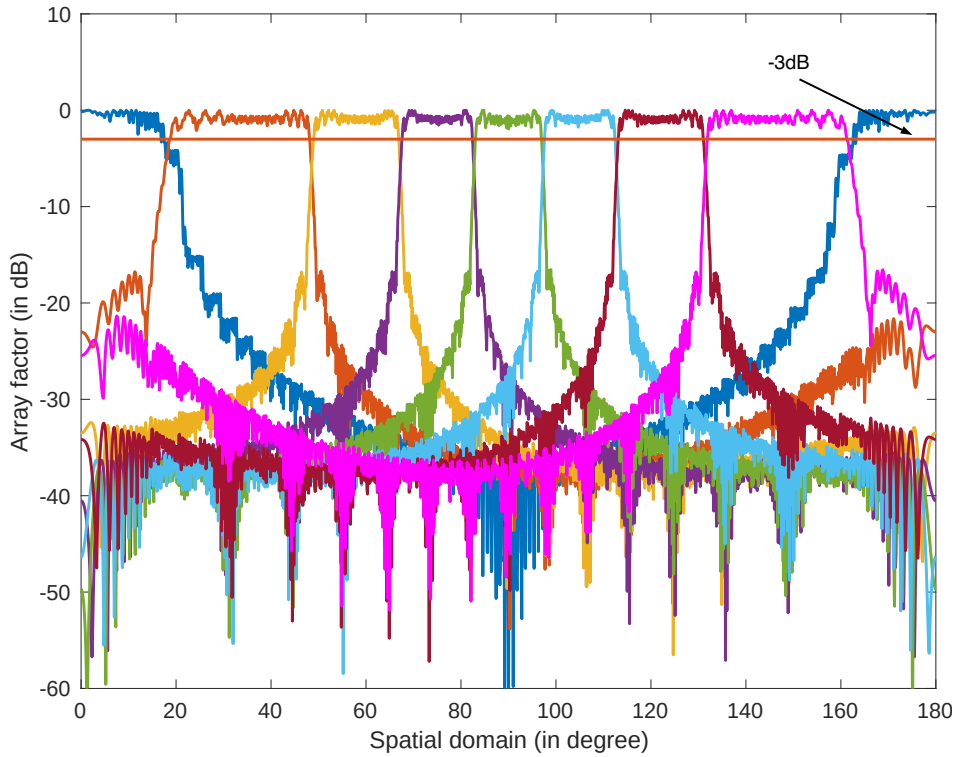

Figure 5.4: RIS codebook design with $N_s = 8$.

spatial domain, i.e., 0 and 180°.

Fig. 5.5 demonstrates the number of groups of RIS weights and the W-HPBW of each sub-area with different numbers of sub-arrays in a RIS. We fix the number of elements in each sub-array to be $M = 64$. It can be seen that a larger N_s, i.e., a larger RIS phased array, results in less RIS weights switching and wider W-HPBW. As the sub-area is near the boundary of the whole spatial domain, the W-HPBW is wider. However, an abrupt change in the beamwidth could be observed in the edge sub-areas as illustrated in Fig. 5.4, so that the beamwidth is shortened [168].

5.5 Summary

This chapter investigates the novel RIS codebook design by leveraging beam squint. We define W-HPBW to characterize the region that could receive signals with more than half of the maximum array power's gain. We aim to design the RIS phase shifts such that the generated W-HPBWs could tile over the entire spatial domain of the RIS with reduced RIS weights switching. To further enlarge the size of W-HPBW under each group of RIS weights, we apply a beam broadening technique. The simulation results prove the effectiveness of our proposed RIS codebook design to realize spatial coverage with W-HPBW. This design could be a cornerstone for real-time and accurate channel estimation.

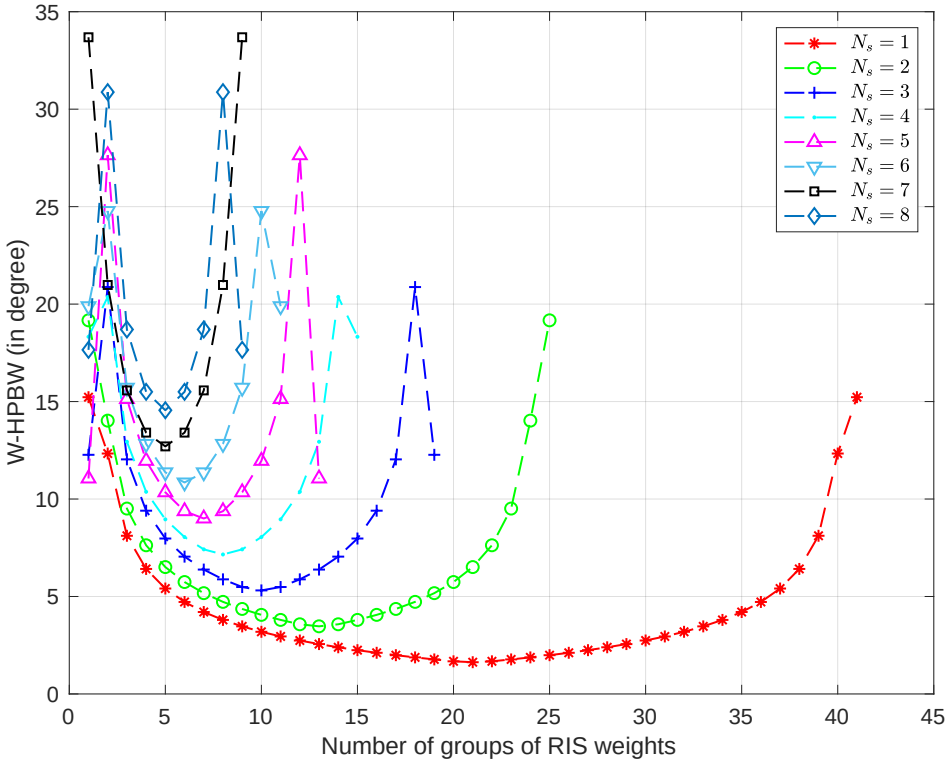

Figure 5.5: The W-HPBW of each sub-area regarding different size of RIS.

Chapter 6

Conclusion and Future Work

The RIS has gained significant attention due to its potential to revolutionize wireless communication systems, which represents a new paradigm in wireless communications by introducing the concept of actively controlling the propagation of electromagnetic waves in the environment. As a pivotal and promising technology in shaping the future of wireless communications, RIS has attracted lots of interests across various sectors, including 5G and beyond wireless networks, indoor localization, IoT connectivity, and more. This thesis comprehensively studied the limitations of current theoretical research in RISs' practical implementation. Potential solutions with analytical derivation and simulation were proposed accordingly. This chapter concludes the main work and contributions presented in this thesis, together with a brief discussion on future works about the RIS.

6.1 Conclusion

In Chapter 1, an overview of RIS, including its detailed hardware realization, modelling, basic EM functionalities, and application scenarios, is presented. We then summarize several limitations of state-of-the-art literature investigating RIS, which motivate our research interests.

Overviews of beamforming techniques, channel models, convex optimization, radiation pattern of antenna are provided in Chapter 2. Meanwhile, a literature review of RIS in the related fields is presented.

In Chapter 3, we explore the application of a RIS-assisted MU communication system, employing a RIS to create a flat broadbeam without relying on known CSI or feedback mechanisms. Initially, we investigate the generation of a single broadbeam. We analytically determine the maximum average radiated power achievable within a coverage area of arbitrary size and propose a broad beam-width design aimed at maximizing average radiated power

while minimizing fluctuations in the beam pattern through optimization of RIS phase shifts. To address the non-convex nature of this problem, we employ the DC-SDP algorithm. Simulation results verify the efficacy of our proposed methods in generating broadbeam with desirable flatness. Subsequently, we explore the generation of multiple broadbeams, where accurate CSI is not required to cover the target region while simultaneously suppressing signals towards unwanted regions. We formulate an optimization problem to minimize deviation between desired and actual power patterns. To handle the non-convexity inherent in this problem, we introduce an ADMM-based algorithm, formulating a Lagrangian function to enable optimized RIS phase shifts within a finite number of update iterations. Simulation results demonstrate the convergence of our proposed algorithm and the alignment between target and optimized power patterns. Overall, this study lays a groundwork for the practical implementation of RIS in coverage enhancement and represents an initial step towards achieving accurate channel estimation.

Towards the communication networks involving multiple BSs and RISs, the non-cooperative BSs scheme is studied in Chapter 4. In this chapter, we first delineate cooperation modes of BSs based on the consensus reached among operators regarding shared RIS usage. Initially focusing on scenarios with only two non-cooperative BSs, the chapter details RIS optimization to enhance communication for the serving BS while mitigating the effects towards others. Subsequently, it expands to encompass a multi-RIS-assisted multi-BS multi-UE networking system, where joint optimization of power allocation, UE association among cooperative BSs, and RIS beamforming aims to maximize sum-rate. An efficient BCD algorithm is studied to address the non-convex problem with discrete binary and coupled variables. The simulation outcomes demonstrate the viability of our proposed algorithm in achieving the maximum sum rate while ensuring limited channel gain between non-cooperative BSs and the respective served UEs.

Involving the beam squint effect, a RIS codebook design based on the HPBW is studied in Chapter 5. We introduce the concept of W-HPBW to delineate the region capable of receiving signals with more than half of the maximum array power's gain. Our objective is to engineer the RIS phase shifts in such a way that the resulting W-HPBW effectively cover the entire spatial domain of the RIS with limited RIS weight switching. To enhance the size of W-HPBW under each set of RIS weights, we implement a beam broadening technique. Simulation results validate the efficacy of our proposed RIS codebook design in achieving spatial coverage with W-HPBW. This design holds potential as a foundational element for facilitating real-time and accurate channel estimation.

6.2 Future Work

6.2.1 Extension of this work

Although the work in this thesis proposed solutions to challenges encountered in RIS-assisted systems, there are a couple of following works that remain to be discussed and solved in the future.

- Even though RIS can be applied across different frequency bands [142, 171, 172], deploying RISs at higher carrier frequencies, such as the mmWave frequency band, is more rewarding, as severe signal attenuation is a fatal weakness of mmWave communication. Additionally, signals carried on high-frequency bands are more susceptible to blockages due to the short wavelength and high directivity. By smartly designing RIS configurations, several virtual LoS links can be built to compensate for the blocked channel by obstacles. Following the RIS-assisted broadbeam design under sub-6 GHz band proposed in Chapter 3, the design under mmWave band is worthy of investigation as well.

- In most of the theoretical works [173, 174], including the work in Chapter 3 in this thesis, the implementation of single RIS is studied. Nevertheless, deploying multiple RISs is a more prevailing strategy aimed at enhancing communication performance, particularly considering that the power gain from a single RIS may be modest, especially in scenarios requiring broadbeam generation. Moreover, to mitigate higher side lobes, the element spacing between unit cells is typically set as half-wavelength, thereby constraining the size of the RIS, particularly in applications operating below 6 GHz. Concurrently, the introduction of multiple RISs may introduce multi-order reflection effects and other complexities [175]. Consequently, the investigation of broadbeam generation in multi-RIS-assisted systems presents both promising opportunities and formidable challenges.

- The 6G networks are required to have intelligence and autonomy attributes [176]. The concepts of intelligent transportation [177], smart home [178], and intelligent health monitoring [179] have to be put forward consequentially. The integration of intelligence into wireless communication systems offers several notable advantages that significantly enhance the performance, efficiency, and capabilities of these systems. Apart from the aforementioned scenarios, ML and artificial intelligence (AI) can also be leveraged in the work in Chapter 4 to improve the optimization process and realize a more adaptive resource allocation scheme. Predictive models can be implemented

to anticipate network conditions and optimize RIS configurations and resource allocations. The resources including spectrum, power, and association scheme can be dynamically allocated based on usage patterns and demand.

- In Chapter 4, some approximations and relaxations are proposed in order to solve non-convex problem, which may lead to performance degradation. For example, **Lemma 2** is proposed to give an approximation of the multiplication of two variables. However, the approximation cannot ensure the optimality of the result. The GP is potentially result in a better performance, which is particularly designed to optimize the function in a monomial/posynomial form. In conclusion, further investigation should be devoted into constructing more efficient and reliable algorithms.

- Chapter 5 proposed a novel RIS codebook design based on the HPBW concept involving the beam squint effect, which is conducted under perfect assumption with no path-loss and multi-path effect. A practical codebook design under the complex propagation environment should be investigated based on current work. Prototypes and experimental validations of the proposed design and configurations should be developed and conducted as well. The testbeds are needed to measure the real-world performance of RIS-assisted systems and refine the theoretical models based on empirical data.

6.2.2 Promising Future Direction

The future directions of RIS technology are poised to revolutionize various aspects of wireless communication and beyond. As we move towards the deployment of 6G networks, the integration of RIS technology presents a significant opportunity for enhancing spectrum efficiency, reliability, and energy efficiency. Based on the knowledge of the author, following directions should be of great importance to exploit more features and value about RIS-assisted wireless cellular systems.

- Beyond traditional communication enhancements, RIS compasses new possibilities in the realms of sensing and localization, which are critical for various applications. For example, RIS can be used to assist in accurate localization and positioning. High-precision localization is crucial for applications such as autonomous vehicles, drones, and augmented reality. RIS can enhance localization accuracy by creating controllable reflections that provide additional signal paths, improving the accuracy of time-of-arrival (TOA) and AOA measurements. Additionally, RIS can be used for sensing and imaging by manipulating and analyzing the reflected signals. This application has

significant potential in security, surveillance, and healthcare. The application of RIS in ISAC system is also worth of further investigation.

- RIS technology can play a pivotal role in enabling smart environments and enhancing IoT communications, given expected billions of connected devices in the near future. In smart buildings, RIS can enhance connectivity for a multitude of IoT devices, ensuring robust and efficient communication without the need for extensive cabling or multiple access points. In industrial settings, reliable and low-latency communication is critical for applications such as real-time monitoring, automation, and remote control. RIS can be designed to provide stable and high-quality communication links in challenging environments like factories and warehouses, where metal structures and machinery often cause severe signal interference and attenuation.

- The near-field area is usually less focused when studying RIS-assisted systems. Unlike the conventional far-field assumptions, where signals interact with RIS elements from a distance, the near-field domain deals with scenarios where the RIS is placed in close proximity to the signal sources and receivers. This proximity necessitates a more detailed analysis of near-field effects to optimize performance, as the effective area of RIS elements and the corresponding power gain depend on the precise positions of transceivers. By leveraging the near-field effects, researchers and engineers can unlock new dimensions of wireless system performance and pave the way for more efficient, reliable, and versatile communication infrastructures.

Appendix A

Derivation of Theorems

A.1 Integral approximation by Riemann sum method

Consider the fixed elevation angle $\overline{\theta}$, the (p,q)-th element $\Upsilon(p,q)$ in terms of the variable φ can be expressed as

$$\Upsilon(p,q) = \frac{\int_{\varphi_{lb}}^{\varphi_{ub}} A_p A_q^H \, d\varphi}{\varphi_{ub} - \varphi_{lb}}. \tag{A.1}$$

As it is challenging to integral over φ directly, we apply the Riemann sum. The main idea of the Riemann sum is to obtain an approximation of a region's area by adding up the areas of multiple simplified slices of the region. Specifically, we divide the azimuth range from φ_{lb} to φ_{ub} into n_a sub-intervals, where each sub-interval has a range of $\Delta\varphi = \frac{\varphi_{ub}-\varphi_{lb}}{n_a}$. A larger number of sub-intervals n_a is desired for a more accurate approximation result. Then (A.1) can be approximated as

$$\Upsilon(p,q) = \frac{e^{j\pi((p_y-q_y)\psi_y+(p_z-q_z)\psi_z)}}{\varphi_{ub}-\varphi_{lb}} \cdot \sum_{t_1=1}^{n_a} e^{j\pi((p_y-q_y)\cos\overline{\theta}\sin(\varphi_{lb}+\frac{2t_1-1}{2}\Delta\varphi)+(p_z-q_z)\sin\overline{\theta})}\Delta\varphi. \tag{A.2}$$

Particularly, when the elevation angle $\overline{\theta} = 0$, and the full cover from $\varphi_{lb} = -90^\circ$ to $\varphi_{ub} = 90^\circ$ is considered, (A.2) can be rewritten as $\Upsilon(p,q) = \frac{e^{j\pi((p_y-q_y)\psi_y+(p_z-q_z)\psi_z)}}{n_a} \sum_{t_1=1}^{n_a} e^{j\pi(p_y-q_y)\sin(-\frac{\pi}{2}+\frac{2t_1-1}{2n_a}\pi)}$. By considering $p_y = q_y$ and $p_y \neq q_y$ cases, Υ can be explained as

$$\Upsilon(p,q) = \begin{cases} e^{j\pi(p_z-q_z)\psi_z}, & p_y = q_y, \\ 0, & p_y \neq q_y. \end{cases} \tag{A.3}$$

The result is consistent with (3.35). Sequentially, **Corollary 1** can be obtained, verifying the feasibility of deriving the average received power by taking integral over the mapped sin function. **Corollary 2** and **Corollary 3** can be similarly derived by taking integral over the

$$
\begin{aligned}
\Xi &= M+2\sum_{p=1}^{M-1}\sum_{q=p+1}^{M}\frac{Re\{(\cos(\alpha_q-\alpha_p)+j\sin(\alpha_q-\alpha_p))e^{j\pi(p-q)(\frac{\mu_{ub}+\mu_{lb}}{2}+\psi_{\mathrm{ULA}})}(e^{j\pi(p-q)\frac{\mu_{ub}-\mu_{lb}}{2}}-e^{-j\pi(p-q)\frac{\mu_{ub}-\mu_{lb}}{2}})\}}{j\pi(p-q)(\mu_{ub}-\mu_{lb})}\\
&= M+4\sum_{p=1}^{M-1}\sum_{q=p+1}^{M}\frac{Re\{(j\cos(\alpha_q-\alpha_p)-\sin(\alpha_q-\alpha_p))e^{j\pi(p-q)(\frac{\mu_{ub}+\mu_{lb}}{2}+\psi_{\mathrm{ULA}})}\sin(\pi(p-q)\frac{\mu_{ub}-\mu_{lb}}{2})\}}{j\pi(p-q)(\mu_{ub}-\mu_{lb})}\\
&= M+4\sum_{p=1}^{M-1}\sum_{q=p+1}^{M}\frac{Re\{(\cos(\alpha_q-\alpha_p)+j\sin(\alpha_q-\alpha_p))e^{j\pi(p-q)(\frac{\mu_{ub}+\mu_{lb}}{2}+\psi_{\mathrm{ULA}})}\sin(\pi(q-p)\frac{\mu_{ub}-\mu_{lb}}{2})\}}{\pi(q-p)(\mu_{ub}-\mu_{lb})}\\
&= M+4\sum_{p=1}^{M-1}\sum_{q=p+1}^{M}\frac{(\cos(\alpha_q-\alpha_p)\cos(\pi(p-q)(\frac{\mu_{ub}+\mu_{lb}}{2}+\psi_{\mathrm{ULA}}))-\sin(\alpha_q-\alpha_p)\sin(\pi(p-q)(\frac{\mu_{ub}+\mu_{lb}}{2}+\psi_{\mathrm{ULA}}))sin(\pi(q-p)\frac{\mu_{ub}-\mu_{lb}}{2})}{\pi(q-p)(\mu_{ub}-\mu_{lb})}\\
&= M+4\sum_{p=1}^{M-1}\sum_{q=p+1}^{M}\frac{\cos(\alpha_q-\alpha_p+\pi(p-q)(\frac{\mu_{ub}+\mu_{lb}}{2}+\psi_{\mathrm{ULA}}))\sin(\pi(q-p)\frac{\mu_{ub}-\mu_{lb}}{2})}{\pi(q-p)(\mu_{ub}-\mu_{lb})}.
\end{aligned}
\tag{A.4}
$$

angles with the Riemann sum approximation method, which are omitted here due to the page limitation.

A.2 Proof of Corollary 4

From (3.52), it can be seen that $\hat{\Xi}_{ULA}$ is inversely proportional to the difference of the sinusoidal function of the area angle range, i.e., $\mu_{ub}-\mu_{lb}$. However, the received power can not be infinitely large when $\mu_{ub}-\mu_{lb}\rightarrow 0$ considering the limited transmitted power at BS as well as the limited size of RIS. We henceforth further investigate the maximum average received power that could be realized in a cover area and rewrite the expression for the average received power as (A.4). To be noted, $\alpha_m, m=1,\cdots,M$ is the phase shift of RIS's elements.

From (A.4) we can indicate that

$$
\Xi = M+2\sum_{p=1}^{M-1}\sum_{q=p+1}^{M}\cos(\alpha_q-\alpha_p+\pi(p-q)(\frac{\mu_{ub}+\mu_{lb}}{2}+\psi_{\mathrm{ULA}})), \tag{A.5}
$$

when $\mu_{ub}-\mu_{lb}\rightarrow 0$, given the fact that $\sin(x)/x=1$ when $x\rightarrow 0$. For an extremely small cover area, i.e., $\mu_{ub}-\mu_{lb}\rightarrow 0$, $\hat{\Xi}_{max}=M^2$ can be realized through careful designing of RIS phase shifts as

$$
\alpha_m = \pi m(\frac{\mu_{ub}+\mu_{lb}}{2}+\psi_{\mathrm{ULA}}), m=1,2,\cdots,M. \tag{A.6}
$$

Therefore, **Corollary 4** can be obtained.

A.3 Proof of Theorem 2

Given that the optimal RIS phase shifts is $\boldsymbol{\alpha}^*\in\mathbb{C}^{M\times 1}$ when the sinusoidal range of the cover area is $[\mu_a,\mu_b]$, the average received power for the range $[\mu_a+\Delta,\mu_b+\Delta]$ can be then ex-

pressed as

$$\Xi' = M + 4\sum_{p=1}^{M-1}\sum_{q=p+1}^{M} \cos(\alpha_q{}' - \alpha_p{}' + \pi(p-q)(\frac{\mu_b+\mu_a+2\Delta}{2} + \psi_{\mathrm{ULA}}))\chi, \tag{A.7}$$

where

$$\chi = \frac{\sin(\pi(p-q)\frac{\overline{\zeta}}{2})}{\pi(q-p)\overline{\zeta}}. \tag{A.8}$$

Note that α'_p and α'_q denote the p and q-th phase shift in RIS when the cover range is $[\mu_a + \Delta, \mu_b + \Delta]$. It can be seen that χ keeps the same when $\overline{\zeta}$ is unchanged. Therefore we mainly focus on the term $\cos(\alpha_q{}' - \alpha_p{}' + \pi(p-q)(\frac{\mu_{ub}+\Delta+\mu_{lb}+\Delta}{2} + \psi_{\mathrm{ULA}}))$. When

$$\alpha_q{}' = \alpha_q{}^* + \pi q\Delta, \tag{A.9}$$

and

$$\alpha_p{}' = \alpha_p{}^* + \pi p\Delta, \tag{A.10}$$

the maximum average received power $\Xi_{ab}{}' = \Xi_{ab}$ is realized. We can get the general expression of the RIS phase shift as

$$\alpha'_m = \alpha^*_m + \pi m\Delta, m = 1, \cdots, M. \tag{A.11}$$

As a consequence, there will always exist a group of RIS phase shifts $\boldsymbol{\alpha}'$ satisfying (A.11), such that the maximum average received power for the range $[\mu_a + \Delta, \mu_b + \Delta]$ is the same as that for the range $[\mu_a, \mu_b]$. However, consider that the shape of the broad beam will be hard to be optimized when the target cover region is at the boundary of the area where the RIS can cover, such as cover regions centred at $\pm 80°$, and the side lobes will be hard to be suppressed, the same maximum power is therefore hard to achieve. **Theorem 2** is obtained.

A.4 Proof of Proposition 1

To prove *proposition 1*, we first define our proposed solution as $\mathbf{p}^* = [p^*_{j,1,2}, \cdots, p^*_{j,K,2}] \in \mathbb{C}^{1\times K_{\mathcal{C}}}$. Then, we sort $\varpi_{j,k}$ in ascending order, so that $\varpi_{j,k} \leq \varpi_{j,k+1}, \forall k = 1, \cdots, K_{\mathcal{C}} - 1$. A critical point $\hat{k}$ is introduced to assist the power allocation analysis, where we have $\hat{\mathcal{R}}_j =$

$\{k|k \leq \hat{k}\}$. Then the optimized $\mathbf{p}^*$ can be represented as

$$\mathbf{p}^* : \begin{cases} p_{j,k,2} = 0, & \forall k \leq \hat{k}, \\ p_{j,k,2} = \frac{\hat{p}_{\max} + \sum_{u=\hat{k}+1}^{K} \frac{\pi_{th}}{\varpi_{j,u}}}{K_j - \hat{k}} - \frac{\pi_{th}}{\varpi_{j,k}}, & \forall k > \hat{k}, \end{cases} \tag{A.12}$$

where the critical point $\hat{k}$ should satisfy

$$\begin{cases} \frac{\pi_{th}}{\varpi_{j,\hat{k}}} \geq \frac{\hat{p}_{\max} + \sum_{u=\hat{k}}^{K_j} \frac{\pi_{th}}{\varpi_{j,u}}}{K_j - \hat{k}+1}, \\ \frac{\pi_{th}}{\varpi_{j,\hat{k}+1}} \leq \frac{\hat{p}_{\max} + \sum_{u=\hat{k}+1}^{K_j} \frac{\pi_{th}}{\varpi_{j,u}}}{K_j - \hat{k}}. \end{cases} \tag{A.13}$$

Eq. (A.13) can be further interpreted as

$$\sum_{\hat{k}+1}^{K} \left(\frac{\pi_{th}}{\varpi_{j,\hat{k}+1}} - \frac{\pi_{th}}{\varpi_{j,k}}\right) \leq \hat{p}_{\max} \leq \sum_{\hat{k}}^{K} \left(\frac{\pi_{th}}{\varpi_{j,\hat{k}}} - \frac{\pi_{th}}{\varpi_{j,k}}\right). \tag{A.14}$$

Moreover, we rewrite the objective function in the form of

$$\max_{\mathbf{p}_j} \quad \mathcal{O}_j(\mathbf{p}_j) = \sum_{k=1}^{K_j} \log_2\left(\frac{\pi_{th}}{\varpi_{j,k}} + p_{j,k,2}\right) + \sum_{k=1}^{K_j} \log_2 \varpi_{j,k}. \tag{A.15}$$

As the $\sum_{k=1}^{K_j} \log_2 \varpi_{j,k}$ is a fixed term, we henceforth focus on the investigation of the first term. We define an arbitrary solution $\overline{\mathbf{p}}$, which is different from $\mathbf{p}^*$. In the following, we verify the optimality of $\mathbf{p}^*$ by comparing with $\overline{\mathbf{p}}$ under two situations.

Situation 1: We assume $\overline{p}_{j,k,2} = 0, \forall k \leq \hat{k}$, then we focus on the optimization of the sum part when $k > \hat{k}$ by designing $\overline{p}_{j,k,2}, \forall k > \hat{k}$. According to the AM-GM inequality theorem [157], the maximized objective function is realized when

$$\frac{\pi_{th}}{\varpi_{j,\hat{k}+1}} + p_{j,\hat{k}+1,2} = \cdots = \frac{\pi_{th}}{\varpi_{j,k}} + p_{j,k,2}, \forall k > \hat{k}, \tag{A.16}$$

where $\sum_{u=\hat{k}+1}^{K} p_{j,u,2} = \hat{p}_{\max}$. By solving (A.16) we can obtain that

$$\overline{p}_{j,k,2} = \frac{\hat{p}_{\max} + \sum_{u=\hat{k}+1}^{K} \frac{\pi_{th}}{\varpi_{j,u}}}{K_j - \hat{k}} - \frac{\pi_{th}}{\varpi_{j,k}}, \ \forall k > \hat{k}, \tag{A.17}$$

which is consistent with the result in (A.12).

Situation 2: We assume $\overline{p}_k \neq 0, \forall k \leq \hat{k}$, and the total power allocated to users $k \leq \hat{k}$ is Δp, which satisfying $\sum_{u=1}^{\hat{k}} (\overline{p}_{j,u,2} - p^*_{j,u,2}) = \sum_{u=\hat{k}+1}^{K} (p^*_{j,u,2} - \overline{p}_{j,u,2}) = \Delta p$. We further take the

derivative of $\mathcal{O}_j$ with respect to $p_{j,u,2}$, resulting

$$\mathcal{O}'_j(p_{j,u,2}) = \frac{1}{\ln(2)(\frac{\pi_{th}}{\varpi_{j,u}} + p_{j,u,2})} \geq 0. \tag{A.18}$$

As we know that $\frac{\pi_{th}}{\varpi_{j,k}} + p_{j,k,2} \geq \frac{\pi_{th}}{\varpi_{j,k+1}} + p_{j,k+1,2}, \forall k \in \mathcal{K}_j$, we can derive that

$$\mathcal{O}'_j(p_{j,1,2}) \leq \cdots \mathcal{O}'_j(p_{j,\hat{k},2}) \leq \cdots \leq \mathcal{O}'_j(p_{j,K,2}). \tag{A.19}$$

When Δp power is allocated to users $k \leq \hat{k}$, we have

$$\sum_{u=1}^{\hat{k}} \Big(\mathcal{O}_j(\overline{p}_{j,u,2}) - \mathcal{O}_j(p^*_{j,u,2}) \Big) \leq \mathcal{O}'_j(p_{j,\hat{k},2})\Delta p \leq \sum_{u=\hat{k}+1}^{K} \Big(\mathcal{O}_j(p^*_{j,u,2}) - \mathcal{O}_j(\overline{p}_{j,u,2}) \Big), \tag{A.20}$$

which can be further interpreted as

$$\sum_{u=1}^{K} \mathcal{O}_j(\overline{p}_{j,u,2}) \leq \sum_{u=1}^{K} \mathcal{O}_j(p^*_{j,u,2}). \tag{A.21}$$

We summarize the result under situations 1 and 2 and verify that $\mathbf{p}^*$ is the globally optimized solution of the original problem.

A.5 Proof of the convergence behaviour

Let f^t denote the optimized objective function in the t-th iteration. The closed-form solutions of $\mathbf{A}_{j,\forall j \in \mathcal{G}_\mathcal{C}}, \mathbf{P}$ are given, and the optimization of the binary variable $\mathbf{U}$ is transformed into the continuous and differentiable form, where a tight and convex lower bound is given for successive approximation. An approximated convex form of the original problem in $\overline{\mathbf{W}}$ is also deducted by applying the first-order Taylor expansion. The sub-problems are all convex. Then, we have

$$f^t(\mathbf{A}_{j,\forall j \in \mathcal{G}_\mathcal{C}}) = f(\mathbf{A}^*_{j,\forall j \in \mathcal{G}_\mathcal{C}} | \mathbf{U}_{t-1}, \mathbf{P}_{t-1}, \overline{\mathbf{W}}_{t-1}) \geq f^{t-1}, \tag{A.22}$$

$$f^t(\mathbf{U}) = f(\mathbf{U}^* | \mathbf{W}^*_{j,\forall j \in \mathcal{G}_\mathcal{C}}, \mathbf{P}_{t-1}, \overline{\mathbf{W}}_{t-1}) \geq f^t(\mathbf{A}_{j,\forall j \in \mathcal{G}_\mathcal{C}}), \tag{A.23}$$

$$f^t(\mathbf{P}) = f(\mathbf{P}^* | \mathbf{A}^*_{j,\forall j \in \mathcal{G}_\mathcal{C}}, \mathbf{U}^*, \overline{\mathbf{W}}_{t-1}) \geq f^t(\mathbf{U}), \tag{A.24}$$

$$f^t(\overline{\mathbf{W}}) = f(\overline{\mathbf{W}}^* | \mathbf{A}^*_{j,\forall j \in \mathcal{G}_\mathcal{C}}, \mathbf{U}^*, \mathbf{P}^*) \geq f^t(\mathbf{P}), \tag{A.25}$$

Thus, the sequence of f^t is monotonically increasing. In addition, the objective function is upper-bounded due to the limited transmit power and number of RIS elements. Consequen-

tially, there exists a $f_{\max}$ such that

$$f^t(\mathbf{A}_{j,\forall j\in\mathcal{G}_c}, \overline{\mathbf{W}}, \mathbf{U}, \mathbf{P}) \leq f^{t+1}(\mathbf{A}_{j,\forall j\in\mathcal{G}_c}, \overline{\mathbf{W}}, \mathbf{U}, \mathbf{P}) \leq f_{\max}, \tag{A.26}$$

where $f_{\max} > 0$ is a constant. After a limited number of iterations T, $|f^T - f^{T-1}| \leq \epsilon$ should be satisfied, revealing the convergence of our proposed algorithm.

Bibliography

[1] J. Rains, J. ur Rehman Kazim, A. Tukmanov, L. Zhang, Q. H. Abbasi, M. A. Imran, Practical Design Considerations for Reconfigurable Intelligent Surfaces, 2023, pp. 99–122.

[2] X. Wan, M. Q. Qi, T. Chen, T. Cui, Field-programmable Beam Reconfiguring based on Digitally-controlled Coding Metasurface, Scientific Reports 6 (2016) 20663.

[3] A. Araghi, M. Khalily, M. Safaei, A. Bagheri, V. Singh, F. Wang, R. Tafazolli, Reconfigurable Intelligent Surface (RIS) in the Sub-6 GHz Band: Design, Implementation, and Real-World Demonstration, IEEE Access 10 (2022) 2646–2655.

[4] M. Di Renzo, A. Zappone, M. Debbah, M.-S. Alouini, C. Yuen, J. De Rosny, S. Tretyakov, Smart Radio Environments Empowered by Reconfigurable Intelligent Surfaces: How It Works, State of Research, and the Road Ahead, IEEE journal on selected areas in communications 38 (11) (2020) 2450–2525.

[5] D. Pérez-Adán, Fresnedo, J. P. González-Coma, L. Castedo, Intelligent Reflective Surfaces for Wireless Networks: An overview of Applications, Approached Issues, and Open Problems, Electronics 10 (19) (2021).

[6] J. Rodrigues, L. Lonappan, D. Menon, L. J. Gudino, Narrowband and Wideband Directional Beamformer with Reduced Side Lobe Level, in: 2019 International Conference on Data Science and Communication (IconDSC), 2019, pp. 1–4.

[7] S. P. Boyd, L. Vandenberghe, Convex Optimization, Cambridge university press, 2004.

[8] L. Zhang, A. Ijaz, P. Xiao, M. M. Molu, R. Tafazolli, Filtered OFDM Systems, Algorithms, and Performance Analysis for 5G and Beyond, IEEE Transactions on Communications 66 (3) (2018) 1205–1218.

[9] J. Terry, J. Heiskala, OFDM Wireless LANs: A Theoretical And Practical Guide, Sams publishing, 2002.

[10] T. Hwang, C. Yang, G. Wu, S. Li, G. Y. Li, OFDM and Its Wireless Applications: A Survey, IEEE Transactions on Vehicular Technology 58 (4) (2008) 1673–1694.

[11] L. Lu, G. Y. Li, A. L. Swindlehurst, A. Ashikhmin, R. Zhang, An Overview of Massive MIMO: Benefits and Challenges, IEEE Journal of Selected Topics in Signal Processing 8 (5) (2014) 742–758.

[12] E. G. Larsson, O. Edfors, F. Tufvesson, T. L. Marzetta, Massive MIMO for Next Generation Wireless Systems, IEEE Communications Magazine 52 (2) (2014) 186–195.

[13] T. L. Marzetta, Massive MIMO: An Introduction, Bell Labs Technical Journal 20 (2015) 11–22.

[14] Y. Saito, Y. Kishiyama, A. Benjebbour, T. Nakamura, A. Li, K. Higuchi, Non-orthogonal Multiple Access (NOMA) for Cellular Future Radio Access, in: 2013 IEEE 77th vehicular technology conference (VTC Spring), IEEE, 2013, pp. 1–5.

[15] T. Kürner, S. Priebe, Towards THz Communications-status in Research, Standardization and Regulation, Journal of Infrared, Millimeter, and Terahertz Waves 35 (1) (2014) 53–62.

[16] U. Madhow, D. R. Brown, S. Dasgupta, R. Mudumbai, Distributed massive MIMO: Algorithms, architectures and concept systems, in: 2014 Information Theory and Applications Workshop (ITA), 2014, pp. 1–7.

[17] Q. Wu, S. Zhang, B. Zheng, C. You, R. Zhang, Intelligent Reflecting Surface Aided Wireless Communications: A Tutorial, IEEE Transactions on Communications (2021).

[18] Y. Liu, L. Zhang, B. Yang, W. Guo, M. A. Imran, Programmable Wireless Channel for Multi-User MIMO Transmission Using Meta-Surface, in: 2019 IEEE Global Communications Conference (GLOBECOM), 2019, pp. 1–6.

[19] S. Gong, X. Lu, D. T. Hoang, D. Niyato, L. Shu, D. I. Kim, Y.-C. Liang, Toward Smart Wireless Communications via Intelligent Reflecting Surfaces: A Contemporary Survey, IEEE Communications Surveys Tutorials 22 (4) (2020) 2283–2314.

[20] W. Wang, B. Zhu, Y. Huang, W. Zhang, Amplitude-Constrained Constellation and Reflection Pattern Designs for Directional Backscatter Communications Using Programmable Metasurface, IEEE Transactions on Wireless Communications 22 (11) (2023) 8498–8511.

[21] C. Liaskos, S. Nie, A. Tsioliaridou, A. Pitsillides, S. Ioannidis, I. Akyildiz, A New Wireless Communication Paradigm through Software-Controlled Metasurfaces, IEEE Communications Magazine 56 (9) (2018) 162–169.

[22] J. Y. Dai, Q. Cheng, T. J. Cui, IRS Hardware Architectures, 2023, pp. 83–98.

[23] Q. Wu, R. Zhang, Towards Smart and Reconfigurable Environment: Intelligent Reflecting Surface Aided Wireless Network, IEEE Communications Magazine 58 (1) (2020) 106–112.

[24] J. Turpin, J. Bossard, K. Morgan, D. Werner, P. Werner, Reconfigurable and Tunable Metamaterials: A Review of the Theory and Applications, International Journal of Antennas and Propagation 2014 (2014) 1–18.

[25] T. Debogovic, J. Perruisseau-Carrier, Dual-polarized Low Loss Reflectarray Cells with MEMS-based Dynamic Phase Control, in: 2015 9th European Conference on Antennas and Propagation (EuCAP), 2015, pp. 1–5.

[26] Y. Liu, J. Kelly, M. Holm, S. Gopal, S. R. Aghdam, Y. Liu, Unit Cell Design for Intelligent Reflecting and Refracting Surface (IRS) With Independent Electronic Control Capability, IEEE Antennas and Wireless Propagation Letters 23 (1) (2024) 414–418.

[27] H. Malau, K.-F. Tong, K.-K. Wong, Intelligent Reflecting Surfaces (IRS) Metasurface-based with Tunable Varactor Diodes for Advanced 6G Wireless Applications, in: 2023 29th International Conference on Telecommunications (ICT), 2023, pp. 1–6.

[28] H. Yang, X. Cao, F. Yang, J. Gao, S. Xu, M. Li, X. Chen, Y. Zhao, Y. Zheng, L. Sijia, A Programmable Metasurface with Dynamic Polarization, Scattering and Focusing Control, Scientific Reports 6 (10 2016).

[29] A. Kwan, J. Dudley, E. Lantz, Who Really Discovered Snell's Law?, Physics World 15 (4) (2002) 64.

[30] S. V. Hum, J. Perruisseau-Carrier, Reconfigurable Reflectarrays and Array Lenses for Dynamic Antenna Beam Control: A Review, IEEE Transactions on Antennas and Propagation 62 (1) (2014) 183–198.

[31] H. Ur Rehman, F. Bellili, A. Mezghani, E. Hossain, Joint Active and Passive Beamforming Design for IRS-Assisted Multi-User MIMO Systems: A VAMP-Based Approach, IEEE Transactions on Communications 69 (10) (2021) 6734–6749.

[32] V. B. Shukla, V. Bhatia, K. Choi, Cascaded Channel Estimator for IRS-Aided mmWave Hybrid MIMO System, IEEE Wireless Communications Letters 13 (3) (2024) 622–626.

[33] R. Kaur, B. Bansal, Performance Analysis of IRS-Assisted Wireless Communication in Presence of Single and Multiple Eavesdroppers, in: 2024 11th International Conference on Signal Processing and Integrated Networks (SPIN), 2024, pp. 155–159.

[34] Y. Song, S. Xu, G. Sun, B. Ai, Weighted Sum-Rate Maximization in Multi-IRS-Aided Multi-Cell mmWave Communication Systems for Suppressing ICI, IEEE Transactions on Vehicular Technology 72 (8) (2023) 10234–10250.

[35] Z. Hou, Y. Huang, J. Chen, G. Li, X. Guan, Y. Xu, R. Chen, Y. Xu, Joint IRS Selection and Passive Beamforming in Multiple IRS-UAV-Enhanced Anti-Jamming D2D Communication Networks, IEEE Internet of Things Journal 10 (22) (2023) 19558–19569.

[36] J. Cheng, C. Shen, Z. Chen, N. Pappas, Robust Beamforming Design for IRS-Aided URLLC in D2D Networks, IEEE Transactions on Communications 70 (9) (2022) 6035–6049.

[37] S. Gong, H. Liu, H. Dai, X. Zhao, C. Xing, Hybrid Analog-Digital Transceiver Design for RIS-Assisted mmWave MIMO Communications, IEEE Wireless Communications Letters 11 (12) (2022) 2620–2624.

[38] R. Liang, J. Fan, Energy-Efficient mmWave IoT Communications With Multihop IRS-Assisted Systems, IEEE Internet of Things Journal 10 (21) (2023) 19344–19355.

[39] H. Ma, H. Wang, Power Minimization Transmission Design for IRS-Assisted Uplink NOMA Systems, in: 2021 IEEE 94th Vehicular Technology Conference (VTC2021-Fall), 2021, pp. 1–4.

[40] X. Guan, Q. Wu, R. Zhang, Joint Power Control and Passive Beamforming in IRS-Assisted Spectrum Sharing, IEEE Communications Letters 24 (7) (2020) 1553–1557.

[41] W. Jiang, Y. Zhang, J. Zhao, Z. Xiong, Z. Ding, Joint Transmit Precoding and Reflect Beamforming Design for IRS-Assisted MIMO Cognitive Radio Systems, IEEE Transactions on Wireless Communications 21 (6) (2022) 3617–3631.

[42] Z. Wan, W. Jiang, J. Nie, D. Niyato, C. Pan, Z. Xiong, Min-Max Fairness Based Joint Optimal Design for IRS-Assisted MEC Systems, IEEE Transactions on Vehicular Technology (2024) 1–15.

[43] A. Bansal, N. Agrawal, K. Singh, C.-P. Li, S. Mumtaz, RIS Selection Scheme for UAV-Based Multi-RIS-Aided Multiuser Downlink Network With Imperfect and Outdated CSI, IEEE Transactions on Communications 71 (8) (2023) 4650–4664.

[44] A. Mohamed, A. Zappone, M. Di Renzo, Bi-Objective Optimization of Information Rate and Harvested Power in RIS-Aided SWIPT Systems, IEEE Wireless Communications Letters 11 (10) (2022) 2195–2199.

[45] J. Yaswanth, M. Katwe, K. Singh, O. Taghizadeh, C. Pan, A. Schmeink, Towards Green Communication: Power-Efficient Beamforming for STAR-RIS-Aided SWIPT, IEEE Transactions on Green Communications and Networking (2024) 1–1.

[46] X. Pei, H. Yin, L. Tan, L. Cao, Z. Li, K. Wang, K. Zhang, E. Björnson, RIS-Aided Wireless Communications: Prototyping, Adaptive Beamforming, and Indoor/Outdoor Field Trials, IEEE Transactions on Communications 69 (12) (2021) 8627–8640.

[47] Y. Cao, T. Lv, W. Ni, Intelligent Reflecting Surface Aided Multi-User mmWave Communications for Coverage Enhancement, in: 2020 IEEE 31st Annual International Symposium on Personal, Indoor and Mobile Radio Communications, 2020, pp. 1–6.

[48] A. M. Tota Khel, K. A. Hamdi, Performance Analysis of IRS-Assisted Full-Duplex Wireless Communication Systems With Interference, IEEE Communications Letters 26 (9) (2022) 2027–2031.

[49] G. R. Mati, S. Das, T. Swami, An Improved Multi-IRS Aided MISO System Using Multivariate Analysis, in: 2021 IEEE 18th India Council International Conference (INDICON), 2021, pp. 1–6.

[50] Z. Ding, H. V. Poor, A Simple Design of IRS-NOMA Transmission, IEEE Communications Letters 24 (5) (2020) 1119–1123.

[51] J. Chen, Y.-C. Liang, Y. Pei, H. Guo, Intelligent Reflecting Surface: A Programmable Wireless Environment for Physical Layer Security, IEEE Access 7 (2019) 82599–82612.

[52] D. Xu, X. Yu, Y. Sun, D. W. K. Ng, R. Schober, Resource Allocation for IRS-assisted Full-duplex Cognitive Radio Systems, IEEE Transactions on Communications 68 (12) (2020) 7376–7394.

[53] Z.-Q. He, X. Yuan, Cascaded Channel Estimation for Large Intelligent Metasurface Assisted Massive MIMO, IEEE Wireless Communications Letters 9 (2) (2020) 210–214.

[54] T. L. Jensen, E. De Carvalho, An Optimal Channel Estimation Scheme for Intelligent Reflecting Surfaces Based on a Minimum Variance Unbiased Estimator, in: ICASSP 2020 - 2020 IEEE International Conference on Acoustics, Speech and Signal Processing (ICASSP), 2020, pp. 5000–5004.

[55] X. Shi, J. Wang, J. Song, Triple-Structured Compressive Sensing-Based Channel Estimation for RIS-Aided MU-MIMO Systems, IEEE Transactions on Wireless Communications 21 (12) (2022) 11095–11109.

[56] Z. Mao, X. Liu, M. Peng, Channel Estimation for Intelligent Reflecting Surface Assisted Massive MIMO Systems—A Deep Learning Approach, IEEE Communications Letters 26 (4) (2022) 798–802.

[57] Z. Chen, J. Tang, X. Y. Zhang, Q. Wu, Y. Wang, D. K. C. So, S. Jin, K.-K. Wong, Offset Learning Based Channel Estimation for Intelligent Reflecting Surface-Assisted Indoor Communication, IEEE Journal of Selected Topics in Signal Processing 16 (1) (2022) 41–55.

[58] J. Zuo, Y. Liu, Z. Qin, N. Al-Dhahir, Resource Allocation in Intelligent Reflecting Surface Assisted NOMA Systems, IEEE Transactions on Communications 68 (11) (2020) 7170–7183.

[59] D. Zhao, H. Lu, Y. Wang, H. Sun, Joint Passive Beamforming and User Association Optimization for IRS-assisted mmWave Systems, in: GLOBECOM 2020 - 2020 IEEE Global Communications Conference, 2020, pp. 1–6.

[60] D. Zhao, H. Lu, Y. Wang, H. Sun, Y. Gui, Joint Power Allocation and User Association Optimization for IRS-Assisted mmWave Systems, IEEE Transactions on Wireless Communications 21 (1) (2022) 577–590.

[61] X. Lin, Z. Zhou, L. Zhang, A. Tukmanov, Q. Abbasi, M. A. Imran, RIS-Assisted Resource Allocation under Base Stations' Non-Cooperation Scheme, in: GLOBECOM 2023 - 2023 IEEE Global Communications Conference, 2023, pp. 7237–7242.

[62] S. Ao, Y. Niu, Z. Han, B. Ai, Z. Zhong, N. Wang, Y. Qiao, Resource Allocation for RIS-Assisted Device-to-Device Communications in Heterogeneous Cellular Networks, IEEE Transactions on Vehicular Technology 72 (9) (2023) 11741–11755.

[63] M. Bashar, K. Cumanan, A. G. Burr, P. Xiao, M. Di Renzo, On the Performance of Reconfigurable Intelligent Surface-Aided Cell-Free Massive MIMO Uplink, in: GLOBECOM 2020 - 2020 IEEE Global Communications Conference, 2020, pp. 1–6.

[64] Y. Ma, Y. Shen, X. Yu, J. Zhang, S. Song, K. B. Letaief, A Low-Complexity Algorithmic Framework for Large-Scale IRS-Assisted Wireless Systems, in: 2020 IEEE Globecom Workshops (GC Wkshps, 2020, pp. 1–6.

[65] V. Kumar, M. Chafii, A. L. Swindlehurst, L.-N. Tran, M. F. Flanagan, SCA-Based Beamforming Optimization for IRS-Enabled Secure Integrated Sensing and Communication, in: GLOBECOM 2023 - 2023 IEEE Global Communications Conference, 2023, pp. 5992–5997.

[66] V. Arun, H. Balakrishnan, Rfocus: Practical beamforming for small devices, arXiv preprint arXiv:1905.05130 (2019).

[67] R. Simons, Guglielmo Marconi and Early Systems of Wireless Communication, Gec Review 11 (1) (1996) 37–55.

[68] H. Cox, R. Zeskind, M. Owen, Robust Adaptive Beamforming, IEEE Transactions on Acoustics, Speech, and Signal Processing 35 (10) (1987) 1365–1376.

[69] Y. Zhao, W. Liu, R. J. Langley, Efficient Design of Frequency Invariant Beamformers with Sensor Delay-Lines, in: 2008 5th IEEE Sensor Array and Multichannel Signal Processing Workshop, Wiley Online Library, 2008.

[70] W. Liu, S. Weiss, Wideband Beamforming: Concepts and Techniques, John Wiley & Sons, 2010.

[71] E. H. Mujammami, I. Afifi, A. B. Sebak, Optimum Wideband High Gain Analog Beamforming Network for 5G Applications, IEEE Access 7 (2019) 52226–52237.

[72] S. Zhang, C. Guo, T. Wang, W. Zhang, ON–OFF Analog Beamforming for Massive MIMO, IEEE Transactions on Vehicular Technology 67 (5) (2018) 4113–4123.

[73] B. Ning, Z. Chen, Low-Complexity Analog Beamforming for mmWave Large-Scale MISOME Wiretap Channel, IEEE Communications Letters 24 (2) (2020) 268–271.

[74] T. Yoo, A. Goldsmith, On the Optimality of Multiantenna Broadcast Scheduling Using Zero-forcing Beamforming, IEEE Journal on Selected Areas in Communications 24 (3) (2006) 528–541.

[75] R. W. Heath, N. González-Prelcic, S. Rangan, W. Roh, A. M. Sayeed, An Overview of Signal Processing Techniques for Millimeter Wave MIMO Systems, IEEE Journal of Selected Topics in Signal Processing 10 (3) (2016) 436–453.

[76] I. Ahmed, H. Khammari, A. Shahid, A. Musa, K. S. Kim, E. De Poorter, I. Moerman, A Survey on Hybrid Beamforming Techniques in 5G: Architecture and System Model Perspectives, IEEE Communications Surveys Tutorials 20 (4) (2018) 3060–3097.

[77] A. F. Molisch, V. V. Ratnam, S. Han, Z. Li, S. L. H. Nguyen, L. Li, K. Haneda, Hybrid Beamforming for Massive MIMO: A Survey, IEEE Communications Magazine 55 (9) (2017) 134–141.

[78] Y. Li, C.-Y.-D. Sim, Y. Luo, G. Yang, 12-Port 5G Massive MIMO Antenna Array in Sub-6GHz Mobile Handset for LTE Bands 42/43/46 Applications, IEEE Access 6 (2018) 344–354.

[79] H. Hu, H. Gao, Z. Li, Y. Zhu, A Sub 6GHz Massive MIMO System for 5G New Radio, in: 2017 IEEE 85th Vehicular Technology Conference (VTC Spring), 2017, pp. 1–5.

[80] M. Rossanese, P. Mursia, A. Garcia-Saavedra, V. Sciancalepore, A. Asadi, X. Costa-Perez, Open Experimental Measurements of Sub-6GHz Reconfigurable Intelligent Surfaces, IEEE Internet Computing 28 (2) (2024) 19–28.

[81] M. Mezzavilla, M. Zhang, M. Polese, R. Ford, S. Dutta, S. Rangan, M. Zorzi, End-to-end Simulation of 5G mmWave Networks, IEEE Communications Surveys & Tutorials 20 (3) (2018) 2237–2263.

[82] S. Rangan, T. S. Rappaport, E. Erkip, Millimeter-wave Cellular Wireless Networks: Potentials and Challenges, Proceedings of the IEEE 102 (3) (2014) 366–385.

[83] T. S. Rappaport, Y. Xing, G. R. MacCartney, A. F. Molisch, E. Mellios, J. Zhang, Overview of Millimeter Wave Communications for Fifth-generation (5G) Wireless Networks — With a Focus on Propagation Models, IEEE Transactions on antennas and propagation 65 (12) (2017) 6213–6230.

[84] M. Shi, K. Yang, Z. Han, D. Niyato, Coverage Analysis of Integrated Sub-6GHz-mmWave Cellular Networks With Hotspots, IEEE Transactions on Communications 67 (11) (2019) 8151–8164.

[85] D. C. Sicker, C. Doerr, The 700 MHz Auction, in: 2008 5th IEEE Annual Communications Society Conference on Sensor, Mesh and Ad Hoc Communications and Networks Workshops, IEEE, 2008, pp. 1–6.

[86] I. C. S. L. S. Committee, et al., IEEE Standard for Information Technology-Telecommunications and Information Exchange between Systems-Local and

Metropolitan Area Networks-Specific Requirements Part 11: Wireless LAN Medium Access Control (MAC) and Physical Layer (PHY) Specifications, IEEE Std 802.11ˆ (2007).

[87] U. Equipment, Technical Specification Group Radio Access Network; NR; User Equipment (UE) Radio Transmission and Reception; Part 1: Range 1 Standalone (Release 15), Part1: Range 1 (2019).

[88] C. J. Hansen, WiGiG: Multi-gigabit wireless communications in the 60 GHz band, IEEE Wireless Communications 18 (6) (2011) 6–7.

[89] S. Sun, G. R. MacCartney, T. S. Rappaport, Millimeter-wave Distance-dependent Large-scale Propagation Measurements and Path Loss Models for Outdoor and Indoor 5G Systems, in: 2016 10th European Conference on Antennas and Propagation (EuCAP), IEEE, 2016, pp. 1–5.

[90] K. Hassan, M. Masarra, M. Zwingelstein, I. Dayoub, Channel Estimation Techniques for Millimeter-Wave Communication Systems: Achievements and Challenges, IEEE Open Journal of the Communications Society 1 (2020) 1336–1363.

[91] D. L. Donoho, A. Maleki, A. Montanari, Message-passing Algorithms for Compressed Sensing, Proceedings of the National Academy of Sciences 106 (45) (2009) 18914–18919.

[92] E. J. Candès, J. Romberg, T. Tao, Robust Uncertainty Principles: Exact Signal Reconstruction from Highly Incomplete Frequency Information, IEEE Transactions on information theory 52 (2) (2006) 489–509.

[93] A. Alkhateeb, O. El Ayach, G. Leus, R. W. Heath, Channel Estimation and Hybrid Precoding for Millimeter Wave Cellular Systems, IEEE journal of selected topics in signal processing 8 (5) (2014) 831–846.

[94] S. Payami, M. Shariat, M. Ghoraishi, M. Dianati, Effective RF Codebook Design and Channel Estimation for Millimeter Wave Communication Systems, in: 2015 IEEE International Conference on Communication Workshop (ICCW), IEEE, 2015, pp. 1226–1231.

[95] Q. Li, T. Shang, T. Tang, Z. Xiong, Adaptive User Association Scheme for Indoor Multi-User NOMA-VLC Systems, IEEE Wireless Communications Letters 12 (5) (2023) 873–877.

[96] K. Zhu, H. Dai, H. Gao, X. Zhou, High Accuracy Discretization-based Integer Programming for the Dubins Multiple Traveling Salesman Problem with Min-max Objective, in: 2022 5th International Conference on Robotics, Control and Automation Engineering (RCAE), 2022, pp. 242–248.

[97] J. Lindsay, S. Gigivi, A Novel way of Training a Neural Network with Reinforcement learning and without Back Propagation, in: 2020 International Joint Conference on Neural Networks (IJCNN), 2020, pp. 1–6.

[98] P. Xiang, G. Wang, D. K. C. Ho, Bias Reduced Semidefinite Relaxation Method for AOA Object Localization in 3-D, in: 2022 IEEE 12th Sensor Array and Multichannel Signal Processing Workshop (SAM), 2022, pp. 91–95.

[99] S. Boyd, S.-J. Kim, L. Vandenberghe, A. Hassibi, A Tutorial on Geometric Programming, Optimization and engineering 8 (2007) 67–127.

[100] L. Diez, G.-P. Popescu, R. Agüero, A Geometric Programming Solution for the Mutual-Interference Model in HetNets, IEEE Communications Letters 20 (9) (2016) 1876–1879.

[101] R. W. Ziolkowski, The Directivity of a Compact Antenna: An Unforgettable Figure of Merit, EPJ Applied Metamaterials (2017).

[102] A. Felix, A. Ayegba, J. J. Olu, A. A. Olufemi, W. D. Fonyuy, H. Ibrahim, Design Of An L-Band Pyramidal Horn Antenna, International Journal For Research & Development In Technology (2017).

[103] C. A. Balanis, Antenna Theory: Analysis and Design, John wiley & sons, 2016.

[104] E. E. Bahingayi, K. Lee, Low-Complexity Beamforming Algorithms for IRS-Aided Single-User Massive MIMO mmWave Systems, IEEE Transactions on Wireless Communications (2022) 1–1.

[105] S. Asaad, Y. Wu, A. Bereyhi, R. R. Müller, R. F. Schaefer, H. V. Poor, Secure Active and Passive Beamforming in IRS-Aided MIMO Systems, IEEE Transactions on Information Forensics and Security 17 (2022) 1300–1315.

[106] Y. Yang, S. Zhang, R. Zhang, IRS-Enhanced OFDMA: Joint Resource Allocation and Passive Beamforming Optimization, IEEE Wireless Communications Letters 9 (6) (2020) 760–764.

[107] W. Cai, R. Liu, M. Li, Y. Liu, Q. Wu, Q. Liu, IRS-Assisted Multicell Multiband Systems: Practical Reflection Model and Joint Beamforming Design, IEEE Transactions on Communications 70 (6) (2022) 3897–3911.

[108] S. H. Hong, J. Park, S.-J. Kim, J. Choi, Hybrid Beamforming for Intelligent Reflecting Surface Aided Millimeter Wave MIMO Systems, IEEE Transactions on Wireless Communications 21 (9) (2022) 7343–7357.

[109] L. Yang, J. Wang, X. Xue, J. Shi, Y. Wang, Secure Hybrid Beamforming for IRS-Assisted Millimeter Wave Systems, IEEE Transactions on Wireless Communications 22 (8) (2023) 5111–5128.

[110] Z. Abdullah, G. Chen, S. Lambotharan, J. A. Chambers, Low-Complexity Antenna Selection and Discrete Phase-Shifts Design in IRS-Assisted Multiuser Massive MIMO Networks, IEEE Transactions on Vehicular Technology 71 (4) (2022) 3980–3994.

[111] S. Abeywickrama, R. Zhang, Q. Wu, C. Yuen, Intelligent Reflecting Surface: Practical Phase Shift Model and Beamforming Optimization, IEEE Transactions on Communications 68 (9) (2020) 5849–5863.

[112] S. Zhou, W. Xu, K. Wang, M. Di Renzo, M.-S. Alouini, Spectral and Energy Efficiency of IRS-Assisted MISO Communication With Hardware Impairments, IEEE Wireless Communications Letters 9 (9) (2020) 1366–1369.

[113] X. Ma, Z. Chen, Y. Chi, W. Chen, L. Du, Z. Li, Channel Estimation for Intelligent Reflecting Surface Enabled Terahertz MIMO Systems, in: 2020 IEEE International Conference on Communications Workshops (ICC Workshops), 2020, pp. 1–6.

[114] J. Xu, C. Yuen, C. Huang, N. Ul Hassan, G. C. Alexandropoulos, M. Di Renzo, M. Debbah, Reconfiguring Wireless Environments via Intelligent Surfaces for 6G: Reflection, Modulation, and Security, Science China Information Sciences 66 (3) (2023) 130304.

[115] Y. Han, W. Tang, S. Jin, C.-K. Wen, X. Ma, Large Intelligent Surface-Assisted Wireless Communication Exploiting Statistical CSI, IEEE Transactions on Vehicular Technology 68 (8) (2019) 8238–8242.

[116] Y. Gao, J. Xu, W. Xu, D. W. K. Ng, M.-S. Alouini, Distributed IRS With Statistical Passive Beamforming for MISO Communications, IEEE Wireless Communications Letters 10 (2) (2021) 221–225.

[117] Y. Sun, K. An, J. Luo, Y. Zhu, G. Zheng, S. Chatzinotas, Outage Constrained Robust Beamforming Optimization for Multiuser IRS-Assisted Anti-Jamming Communications With Incomplete Information, IEEE Internet of Things Journal 9 (15) (2022) 13298–13314.

[118] Q. Deng, G. Yu, X. Liang, F. Shu, J. Wang, IRS-Assisted Cognitive UAV Networks: Joint Sensing Duration, Passive Beamforming, and 3-D Location Optimization, IEEE Internet of Things Journal 11 (2) (2024) 2767–2782.

[119] F. Zhao, W. Hao, X. You, Y. Wang, Z. Chu, P. Xiao, Joint Beamforming Optimization for IRS-Aided THz Communication With Time Delays, IEEE Wireless Communications Letters 13 (1) (2024) 49–53.

[120] J. Tang, Z. Peng, Z. Zhou, D. K. So, X. Zhang, K.-K. Wong, Energy-Efficient Resource Allocation for IRS-aided MISO System with SWIPT, in: GLOBECOM 2022 - 2022 IEEE Global Communications Conference, 2022, pp. 3217–3222.

[121] E. M. Taghavi, R. Hashemi, A. Alizadeh, N. Rajatheva, M. Vu, M. Latva-aho, Joint Active-Passive Beamforming and User Association in IRS-Assisted mmWave Cellular Networks, IEEE Transactions on Vehicular Technology 72 (8) (2023) 10448–10461.

[122] N. Ye, X. Zhuo, J. Li, B. Di, J. An, Secure Directional Modulation in RIS-Aided Networks: A Low-Sidelobe Hybrid Beamforming Approach, IEEE Wireless Communications Letters 11 (8) (2022) 1753–1757.

[123] W. Wang, P. Li, A. Doufexi, M. A. Beach, DRL-Based Sidelobe Suppression for Multi-Focus Reconfigurable Intelligent Surface, in: 2024 18th European Conference on Antennas and Propagation (EuCAP), 2024, pp. 1–5.

[124] X. Tian, N. Gonzalez-Prelcic, R. W. Heath, Variable Beamwidth Near Field Codebook Design for Communications Aided by A Large Scale RIS, in: GLOBECOM 2023 - 2023 IEEE Global Communications Conference, 2023, pp. 2021–2026.

[125] P. Callaghan, P. R. Young, Beam- and Band-Width Broadening of Intelligent Reflecting Surfaces Using Elliptical Phase Distribution, IEEE Transactions on Antennas and Propagation 70 (10) (2022) 8825–8832.

[126] X. Liu, T. Wei, H. Liang, C. Guo, B. Liao, Robust Beamforming for RIS-Assisted NOMA Systems With CSI Imperfection and Low-Resolution Phase Shifters, in: 2023 6th International Conference on Information Communication and Signal Processing (ICICSP), 2023, pp. 654–658.

[127] H. Gao, X. Yang, N. Chen, S. Chen, Y. Yang, C. Yuen, Robust Beamforming for Reconfigurable Intelligent Surface-Assisted Multi-Cell Downlink Transmissions, IEEE Transactions on Vehicular Technology 73 (5) (2024) 6910–6922.

[128] V. Jamali, G. C. Alexandropoulos, R. Schober, H. V. Poor, Low-to-Zero-Overhead IRS Reconfiguration: Decoupling Illumination and Channel Estimation, IEEE Communications Letters 26 (4) (2022) 932–936.

[129] H. Lu, Y. Zeng, S. Jin, R. Zhang, Aerial Intelligent Reflecting Surface: Joint Placement and Passive Beamforming Design With 3D Beam Flattening, IEEE Transactions on Wireless Communications 20 (7) (2021) 4128–4143.

[130] M. He, J. Xu, W. Xu, H. Shen, N. Wang, C. Zhao, RIS-Assisted Quasi-Static Broad Coverage for Wideband mmWave Massive MIMO Systems, IEEE Transactions on Wireless Communications (2022) 1–1.

[131] Y. Liu, L. Zhang, M. A. Imran, Multi-User Beamforming and Transmission Based on Intelligent Reflecting Surface, IEEE Transactions on Wireless Communications 21 (9) (2022) 7329–7342.

[132] L. Di Stefano, S. Mattoccia, A Sufficient Condition Based on the cauchy-schwarz Inequality for Efficient Template Matching, in: Proceedings 2003 International Conference on Image Processing (Cat. No.03CH37429), Vol. 1, 2003, pp. I–269.

[133] A. Mobasher, R. Sotirov, A. K. Khandani, Matrix-lifting Semi-definite Programming for Detection in Multiple Antenna Systems, IEEE Transactions on Signal Processing 58 (10) (2010) 5178–5185.

[134] X. Liu, D. Qiao, Location-fair Beamforming For High Speed Railway Communication Systems, IEEE Access 6 (2018) 28632–28642.

[135] V. Sealey, Definite integrals, Riemann sums, and area under a curve: What is necessary and sufficient, in: Proceedings of the 28th annual meeting of the North American Chapter of the International Group for the Psychology of Mathematics Education, Vol. 2, Citeseer, 2006, pp. 46–53.

[136] H. Laamari, J. Belfiore, N. Ibrahim, Near Maximum Likelihood Detection Using an Interior Point Method and Semidefinite Programming, in: Conference Record of the Thirty-Eighth Asilomar Conference on Signals, Systems and Computers, 2004., Vol. 1, 2004, pp. 223–226 Vol.1.

[137] D. Qiao, H. Qian, G. Y. Li, Broadbeam for Massive MIMO Systems, IEEE Transactions on Signal Processing 64 (9) (2016) 2365–2374.

[138] J. Xue, X. Zhou, C. Wang, D. Wang, Y. Zhao, Z. Li, Hybrid Precoding for IRS-assisted Secure mmWave Communication System with SWIPT, in: 2020 International Conference on Space-Air-Ground Computing (SAGC), IEEE, 2020, pp. 82–86.

[139] C. Lanczos, Linear Differential Operators, SIAM, 1996.

[140] D. Kalman, A Singularly Valuable Decomposition: The SVD of a Matrix, The college mathematics journal 27 (1) (1996) 2–23.

[141] P. D. Tao, L. T. H. An, Convex Analysis Approach to DC Programming: Theory, Algorithms and Applications, Acta mathematica vietnamica 22 (1) (1997) 289–355.

[142] H. Guo, Y.-C. Liang, J. Chen, E. G. Larsson, Weighted Sum-Rate Maximization for Reconfigurable Intelligent Surface Aided Wireless Networks, IEEE Transactions on Wireless Communications 19 (5) (2020) 3064–3076.

[143] S. Zargari, A. Khalili, Q. Wu, M. Robat Mili, D. W. K. Ng, Max-Min Fair Energy-Efficient Beamforming Design for Intelligent Reflecting Surface-Aided SWIPT Systems With Non-Linear Energy Harvesting Model, IEEE Transactions on Vehicular Technology 70 (6) (2021) 5848–5864.

[144] Y. Liu, B. Jiu, H. Liu, ADMM-based Transmit Beampattern Synthesis for Antenna Arrays under a Constant Modulus Constraint, Signal Processing 171 (2020) 107529.

[145] Y.-K. Li, A. Petropulu, Efficient Beamforming Designs for IRS-Aided DFRC Systems, in: 2023 24th International Conference on Digital Signal Processing (DSP), 2023, pp. 1–5.

[146] J. Tranter, N. D. Sidiropoulos, X. Fu, A. Swami, Fast Unit-Modulus Least Squares With Applications in Beamforming, IEEE Transactions on Signal Processing 65 (11) (2017) 2875–2887.

[147] S. Boyd, N. Parikh, E. Chu, B. Peleato, J. Eckstein, et al., Distributed Optimization and Statistical Learning via the Alternating Direction Method of Multipliers, Foundations and Trends® in Machine learning 3 (1) (2011) 1–122.

[148] P. Gupta, D. Ghosh, User Fairness based Energy Efficient Power Allocation for Downlink Cellular NOMA System, in: 2020 5th International Conference on Computing, Communication and Security (ICCCS), 2020, pp. 1–5.

[149] L.-N. Tran, M. F. Hanif, A. Tolli, M. Juntti, Fast Converging Algorithm for Weighted Sum Rate Maximization in Multicell MISO Downlink, IEEE Signal Processing Letters 19 (12) (2012) 872–875.

[150] K. Shen, W. Yu, Fractional Programming for Communication Systems—Part I: Power Control and Beamforming, IEEE Transactions on Signal Processing 66 (10) (2018) 2616–2630.

[151] M. R. Akdeniz, Y. Liu, M. K. Samimi, S. Sun, S. Rangan, T. S. Rappaport, E. Erkip, Millimeter Wave Channel Modeling and Cellular Capacity Evaluation, IEEE Journal on Selected Areas in Communications 32 (6) (2014) 1164–1179.

[152] G. Zhou, C. Pan, H. Ren, K. Wang, M. D. Renzo, Fairness-Oriented Multiple RIS-Aided mmWave Transmission: Stochastic Optimization Methods, IEEE Transactions on Signal Processing 70 (2022) 1402–1417.

[153] T. Van Chien, E. Björnson, E. G. Larsson, Joint Power Allocation and User Association Optimization for Massive MIMO Systems, IEEE Transactions on Wireless Communications 15 (9) (2016) 6384–6399.

[154] N. Jindal, W. Rhee, S. Vishwanath, S. Jafar, A. Goldsmith, Sum Power Iterative Water-filling for Multi-antenna Gaussian Broadcast Channels, IEEE Transactions on Information Theory 51 (4) (2005) 1570–1580.

[155] B. Khamidehi, A. Rahmati, M. Sabbaghian, Joint Sub-Channel Assignment and Power Allocation in Heterogeneous Networks: An Efficient Optimization Method, IEEE Communications Letters 20 (12) (2016) 2490–2493.

[156] A. Nemirovski, Interior Point Polynomial Time Methods in Convex Programming, Lecture notes 42 (16) (2004) 3215–3224.

[157] H. Kim, C. Tepedelenlioglu, Performance Bounds on Average Error Rates Using the AM-GM Inequality and Their Applications in Relay Networks, IEEE Transactions on Wireless Communications 11 (8) (2012) 2986–2995.

[158] Y. Su, X. Pang, S. Chen, X. Jiang, N. Zhao, F. R. Yu, IRS-UAV Relaying Networks for Spectrum and Energy Efficiency Maximization, in: ICC 2022 - IEEE International Conference on Communications, 2022, pp. 2834–2839.

[159] W. Wang, X. Liu, J. Tang, N. Zhao, Y. Chen, Z. Ding, X. Wang, Beamforming and Jamming Optimization for IRS-Aided Secure NOMA Networks, IEEE Transactions on Wireless Communications 21 (3) (2022) 1557–1569.

[160] X. Pang, N. Zhao, J. Tang, C. Wu, D. Niyato, K.-K. Wong, IRS-Assisted Secure UAV Transmission via Joint Trajectory and Beamforming Design, IEEE Transactions on Communications 70 (2) (2022) 1140–1152.

[161] H. Li, R. Liu, M. Liy, Q. Liu, X. Li, IRS-Enhanced Wideband MU-MISO-OFDM Communication Systems, in: 2020 IEEE Wireless Communications and Networking Conference (WCNC), 2020, pp. 1–6.

[162] Y. Lin, S. Jin, M. Matthaiou, X. You, Channel Estimation and User Localization for IRS-Assisted MIMO-OFDM Systems, IEEE Transactions on Wireless Communications 21 (4) (2022) 2320–2335.

[163] W. Wu, F. Yang, F. Zhou, H. Hu, Q. Wu, R. Q. Hu, Intelligent Resource Allocations for IRS-Assisted OFDM Communications: A Hybrid MDQN-DDPG Approach, in: ICC 2022 - IEEE International Conference on Communications, 2022, pp. 2047–2052.

[164] B. Wang, F. Gao, S. Jin, H. Lin, G. Y. Li, Spatial- and Frequency-Wideband Effects in Millimeter-Wave Massive MIMO Systems, IEEE Transactions on Signal Processing 66 (13) (2018) 3393–3406.

[165] Y. Chen, D. Chen, T. Jiang, Beam-Squint Mitigating in Reconfigurable Intelligent Surface Aided Wideband Mmwave Communications, in: 2021 IEEE Wireless Communications and Networking Conference (WCNC), 2021, pp. 1–6.

[166] S. Ma, W. Shen, J. An, L. Hanzo, Wideband Channel Estimation for IRS-Aided Systems in the Face of Beam Squint, IEEE Transactions on Wireless Communications 20 (10) (2021) 6240–6253.

[167] R. Borralho, A. Mohamed, A. U. Quddus, P. Vieira, R. Tafazolli, A Survey on Coverage Enhancement in Cellular Networks: Challenges and Solutions for Future Deployments, IEEE Communications Surveys Tutorials 23 (2) (2021) 1302–1341.

[168] H. Han, Y. Liu, L. Zhang, On Half-Power Beamwidth of Intelligent Reflecting Surface, IEEE Communications Letters 25 (4) (2021) 1333–1337.

[169] T. K. Ishii, Handbook of Microwave Technology, Elsevier, 1995.

[170] S. Rajagopal, Beam Broadening for Phased Antenna Arrays using Multi-beam Subarrays, in: 2012 IEEE International Conference on Communications (ICC), 2012.

[171] B. Xiong, Z. Zhang, C. Pan, J. Wang, Performance Analysis of Aerial RIS Auxiliary mmWave Mobile Communications With UAV Fluctuation, IEEE Wireless Communications Letters (2024) 1–1.

[172] R. Su, L. Dai, D. W. K. Ng, Wideband Precoding for Ris-Aided THz Communications, IEEE Transactions on Communications 71 (6) (2023) 3592–3604.

[173] T. Chao, C. C. Fung, Z.-E. Ni, M. Servetnyk, Joint Beamforming and Aerial IRS Positioning Design for IRS-Assisted MISO System With Multiple Access Points, IEEE Open Journal of the Communications Society 5 (2024) 612–632.

[174] Z. Li, H. Shen, W. Xu, D. Chen, C. Zhao, Deep Learning-Based Adaptive Phase Shift Compression and Feedback in IRS-Assisted Communication Systems, IEEE Wireless Communications Letters 13 (3) (2024) 766–770.

[175] Y. Liu, L. Zhang, F. Gao, M. A. Imran, Intelligent Reflecting Surface Networks With Multiorder-Reflection Effect: System Modeling and Critical Bounds, IEEE Transactions on Communications 70 (10) (2022) 6992–7005.

[176] H. Cao, S. Garg, G. Kaddoum, S. Singh, M. S. Hossain, Softwarized Resource Management and Allocation With Autonomous Awareness for 6G-Enabled Cooperative Intelligent Transportation Systems, IEEE Transactions on Intelligent Transportation Systems 23 (12) (2022) 24662–24671.

[177] H. Cao, S. Wu, Y. Hu, F. Tian, L. Yang, Secure Virtual Resource Allocation in Heterogeneous Networks for Intelligent Transportation, in: 2020 IEEE 91st Vehicular Technology Conference (VTC2020-Spring), 2020, pp. 1–5.

[178] V. Govindraj, M. Sathiyanarayanan, B. Abubakar, Customary Homes to Smart Homes Using Internet of Things (IoT) and Mobile Application, in: 2017 International Conference On Smart Technologies For Smart Nation (SmartTechCon), 2017, pp. 1059–1063.

[179] T. Malapane, W. Doorsamy, B. Paul, An Intelligent IoT-based Health Monitoring System, in: 2020 International Conference on Intelligent Data Science Technologies and Applications (IDSTA), 2020, pp. 95–100.